

# **LATERAL TORSIONAL BUCKLING OF RECTANGULAR REINFORCED CONCRETE BEAMS**

A Dissertation  
Presented to  
The Academic Faculty

by

Ilker Kalkan

In Partial Fulfillment  
Of the Requirements for the Degree  
Doctor of Philosophy in the  
School of Civil and Environmental Engineering

Georgia Institute of Technology  
December 2009

Copyright © 2009 by Ilker Kalkan

# **LATERAL TORSIONAL BUCKLING OF RECTANGULAR REINFORCED CONCRETE BEAMS**

Approved by:

Dr. Abdul-Hamid Zureick, Advisor  
School of Civil and Environmental  
Engineering  
*Georgia Institute of Technology*

Dr. Lawrence F. Kahn  
School of Civil and Environmental  
Engineering  
*Georgia Institute of Technology*

Dr. Kenneth M. Will  
School of Civil and Environmental  
Engineering  
*Georgia Institute of Technology*

Dr. Bruce R. Ellingwood  
School of Civil and Environmental  
Engineering  
*Georgia Institute of Technology*

Dr. George Kardomateas  
School of Aerospace Engineering  
*Georgia Institute of Technology*

Date Approved: September 28<sup>th</sup>, 2009

*To my family...*

## **ACKNOWLEDGEMENTS**

The author is grateful to his advisor Dr. Abdul-Hamid Zureick for his help, guidance, patience and encouragement throughout this project.

The author would like to express his sincere gratitude to Dr. Lawrence Kahn, whose technical expertise and guidance contributed greatly to the success of the experimental program. The author is also grateful to the other thesis committee members Dr. Kenneth M. Will, Dr. Bruce R. Ellingwood and Dr. George Kardomateas for their time and suggestions.

The experiments of the present study were carried out at the Structural Engineering and Materials Laboratory of Georgia Institute of Technology. The author feels grateful to the facility manager Jeremy Mitchell; former research engineer Marcus Millard; mechanical specialist Michael R. Sorenson; senior facilities manager Andrew Udell; fellow graduate students Yavuz Menten, Jong Han Lee, Jonathan Hurff, Victor Garas, Robert Moser, Brett Holland, Jennifer Dunbeck, Katherine Snedeker and Kennan Crane; former fellow graduate students Murat Engindeniz and Felix Kim; former undergraduate assistants Andrew Cao and Luis Fajardo and other people without whose helping hand the author could not conduct the experiments. Special thanks are due to fellow graduate students Mustafa Can Kara and Towhid Bhuiyan for their tremendous help and support during the course of the experiments.

This dissertation is dedicated to the family of the author, whose support and love made this dream possible. The author feels indebted to his parents Müzeyyen and İsmail

Kalkan and his brother Murat Kalkan for their unconditional love and unlimited support particularly at difficult times.

Financial support provided for the experiments by Georgia Department of Transportation (GDOT) is gratefully acknowledged. The author would like to express his appreciation to Kırıkkale Üniversitesi, Turkey for providing financial support to the author during the course of his dissertation. Thanks are also due to Dr. Mustafa Y. Kılınç, Dr. Osman Yıldız and Dr. Orhan Doğan for their support during this study.

# TABLE OF CONTENTS

	Page
ACKNOWLEDGEMENTS	iv
LIST OF TABLES	x
LIST OF FIGURES	xii
LIST OF SYMBOLS	xx
LIST OF ABBREVIATIONS	xxvii
SUMMARY	xxviii
<u>CHAPTERS</u>	
I INTRODUCTION	1
1.1 Introduction	1
1.2 Project Objectives	4
1.3 Organization of the Study	4
1.4 Previous Studies	6
1.4.1 Review of Previous Experimental Work	7
1.4.2 Analytical Methods for Predicting Lateral Torsional Buckling	28
1.4.3 Summary	56
II SPECIMENS AND MATERIAL PROPERTIES	57
2.1 Specimens	57
2.1.1 Specimen Descriptions	57
2.1.2 Experiment Design	58
2.2 Concrete Material Properties	62
III EXPERIMENTAL SET-UP, INSTRUMENTATION AND PROCEDURE	69
3.1 Experimental Setup	69

3.1.1 Loading Mechanism	69
3.1.2 Supports	75
3.1.3 Load, Deflection and Strain Measurements	88
3.1.3.1 LVDT Strain Measurements	93
3.1.3.2 Strain Measurements through Electrical Resistance Strain Gauges	95
3.2 Test Procedure	98
3.3 Summary of the Test Results	99
IV LATERAL BENDING RIGIDITY OF RECTANGULAR REINFORCED CONCRETE BEAMS AND INFLUENCE OF SHRINKAGE CRACKING ON THE RIGIDITY	101
4.1 Introduction	101
4.2 Available Lateral Bending Rigidity Expressions	102
4.3 Proposed Lateral Bending Rigidity Expression	105
4.3 Influence of Shrinkage Cracking on the Lateral Bending Rigidity	121
V TORSIONAL RIGIDITY OF RECTANGULAR REINFORCED CONCRETE BEAMS	131
5.1 Torsional Behavior of Reinforced Concrete Beams	131
5.2 Torsional Rigidity of Rectangular Reinforced Concrete Beams	137
5.2.1 Uncracked Torsional Rigidity Expressions	137
5.2.2 Post-Cracking Torsional Rigidity	141
5.3 Experimental Torsional Rigidities of the Test Beams	145
5.4 Proposed Torsional Rigidity Expression	151
VI CRITICAL MOMENT CALCULATIONS AND INFLUENCES OF THE INITIAL GEOMETRIC IMPERFECTIONS ON THE LATERAL STABILITY OF REINFORCED CONCRETE BEAMS	153
6.1 Introduction	153
6.2 Critical Moment Calculations	153

6.3 Influences of Sweep and Initial Twisting Angle on the Lateral Stability of Reinforced Concrete Beams	156
VII EXPERIMENTAL RESULTS AND OBSERVATIONS AND CORRELATION OF THE ANALYTICAL AND EXPERIMENTAL RESULTS	173
7.1 Experimental Results and Observations	173
7.1.1 Crack Patterns of the Specimens	173
7.1.2 Experimental Results	181
7.2 Correlation of the Analytical and Experimental Results	183
VIII SUMMARY AND CONCLUSIONS	195
8.1 Summary	195
8.2 Conclusions	200
8.3 Futures Research	203
APPENDIX A: NOMINAL AND MEASURED DIMENSIONS OF THE SPECIMENS	205
APPENDIX B: MEASURED INITIAL GEOMETRIC IMPERFECTIONS AND PERMANENT DEFORMATIONS OF THE SPECIMENS	213
APPENDIX C: MIDSPAN STRAIN DISTRIBUTIONS OF THE BEAMS AT DIFFERENT LOAD LEVELS	229
APPENDIX D: EXPERIMENTAL LOAD-DEFLECTION PLOTS OF THE SPECIMENS	249
APPENDIX E: METHOD FOR THE EVALUATION OF THE CENTROIDAL DEFLECTIONS AND ROTATION OF A BEAM	265
APPENDIX F: CRITICAL MOMENT CALCULATIONS OF THE SPECIMENS	273
APPENDIX G: CONSTRUCTION DETAILS OF THE SPECIMENS	283
G.1 Compression Reinforcement	283
G.2 Tilt-up and Lifting Mechanisms for the Specimens	284
APPENDIX H: DETERMINATION OF THE EXPERIMENTAL BUCKLING LOADS OF THE SPECIMENS	289



REFERENCES	297
VITA	304

## LIST OF TABLES

	Page
Table 1.1: Nominal dimensions of the beams tested by Hansell and Winter (1959).	7
Table 1.2: Results of the tests by Hansell and Winter (1959).	8
Table 1.3: Beams tested by Sant and Bletzacker (1961).	15
Table 1.4: Results of the tests by Sant and Bletzacker (1961).	16
Table 1.5: Specimens tested by Massey and Walter (1969).	21
Table 1.6: Beams tested by Konig and Pauli (1990).	23
Table 1.7: Midspan initial imperfections of the beams tested by Konig and Pauli (1990).	23
Table 1.8: Loads, midspan deformations and rotations at failure of the beams tested by Konig and Pauli (1990).	23
Table 2.1: Specimens of the present experimental program.	58
Table 2.2: Mechanical properties of concrete.	64
Table 3.1: Experimental results of the specimens.	100
Table 4.1: Experimental and calculated cracking moments of the second set of specimens.	113
Table 4.2: Descriptions of the shrinkage specimens from the concrete mixtures used in B44 and B36L.	126
Table 5.1: Maximum torsional moments of the specimens at the initiation of buckling and the cracking torques.	149
Table 5.2: Torsional rigidities of the specimens.	150
Table 7.1: Experimental and analytical critical load values of the specimens.	186
Table 7.2: Experimental-to-analytical load ratios of the specimens.	187
Table 7.3: Measured sweeps and angles of twist at limit load of the specimens at midspan.	189
Table A.1: Nominal and measured heights of the first set of specimens.	206

Table A.2: Nominal and measured heights of the second set of beams.	207
Table A.3: Nominal and measured widths of the first set of specimens along the span.	209
Table A.4: Widths of the first set of specimens along the depth of midspan section.	209
Table A.5: Nominal and measured widths of the second set of beams.	211
Table A.6: Nominal and measured span lengths of first set of specimens.	212
Table A.7: Nominal and measured total lengths of the second set of specimens.	212
Table B.1: Measured sweeps of Specimens B18.	214
Table B.2: Measured sweeps of Specimens B30 and B36.	214
Table B.3: Measured sweeps of Specimens B44.	216
Table B.4: Measured sweeps of Specimens B36L.	217
Table H.1: Critical loads from the classical and Meck's (1977) version of the Southwell (1932) plots for the second set of beams.	295

## LIST OF FIGURES

	Page
Figure 1.1: (a) Lateral torsional buckling of a beam subjected to a concentrated load at midspan; (b) Lateral and vertical deflections and torsional rotation of the midspan section	2
Figure 1.2: Load-lateral deflection curve of a reinforced concrete beam.	3
Figure 1.3: Comparison of the vertical deflections at yield point of the companion beams tested by Hansell and Winter (1959).	9
Figure 1.4: Comparison of the lateral top deflections at yield point of the companion beams tested by Hansell and Winter (1959).	9
Figure 1.5: Comparison of the lateral bottom deflections at yield point of the companion beams tested by Hansell and Winter (1959).	10
Figure 1.6: Experimental-to-calculated ultimate moment ratios of the beams Tested Hansell and Winter (1959).	10
Figure 1.7: Loading mechanism used by Hansell and Winter (1959).	12
Figure 1.8: Undeformed and deformed configurations of the loading mechanism.	12
Figure 1.9: Direction of the torsional moments induced by the eccentric application of the load.	13
Figure 1.10: Web sidesway buckling failure of the specimen due to the lateral restraining forces in the loading mechanism.	15
Figure 1.11: Experimental-to-predicted buckling moment ratios of the beams in the first three specimen groups, B36, B30 and B24.	17
Figure 1.12: Loading frame used by Sant and Bletzacker (1961).	18
Figure 1.13: Deformed configuration of the loading mechanism used by Sant and Bletzacker (1961).	19
Figure 1.14: Cross-sectional details of the specimens tested by Konig and Pauli (1990).	22
Figure 1.15: Ratio of the buckling load of each Specimen to the buckling load of Specimen 2.	25

Figure 1.16: Loading mechanism used by Konig and Pauli (1990).	27
Figure 1.17: Stress-strain curve of normal-strength concrete and the tangent moduli of elasticity at different stress levels.	31
Figure 1.18: Secant modulus of elasticity corresponding to the extreme compression fiber strain.	34
Figure 1.19: (a) Stress distribution in the compression zone of the beam section in the plastic state; (b) Stress-strain curve of concrete; assumed by Siev (1960).	40
Figure 1.20: Strain distribution at midspan section and the corresponding reduced modulus of elasticity.	42
Figure 1.21: Definition of the variables in the expressions proposed by Massey (1967).	45
Figure 1.22: Effect of the vertical location of the applied load with respect to the shear center of beam section.	48
Figure 1.23: Definition of area and perimeters in Equations (1.30) - (1.32)	54
Figure 2.1: First set of specimens (B36, B30, B22, and B18)	59
Figure 2.2: Second set of specimens (B44, B36L)	60
Figure 2.3: Congested reinforcement in B36	63
Figure 2.4: Application of self-consolidating concrete	63
Figure 2.5: Stress-strain curves of concrete in the first set of beams	67
Figure 2.6: Stress-strain curves of concrete in B44	67
Figure 2.7: Stress-strain curves of concrete in B36L	68
Figure 3.1: Undeformed and deformed configurations of the loading frame and loading cage.	70
Figure 3.2: Loading frame	71
Figure 3.3: Undeformed and deformed shapes of the Gravity Load Simulator	72
Figure 3.4: (a) Undeformed; and (b) Deformed configurations of the Gravity Load Simulator.	72
Figure 3.5: Ball-and-socket joint	73

Figure 3.6: Vertical orientation of the loading cage (a) Before the test; (b) After buckling.	74
Figure 3.7: Minor-axis rotations at the supports	75
Figure 3.8: Lateral deformations and torsional rotations restrained at the supports.	76
Figure 3.9: In-plane support conditions: (a) In analysis models; (b) Hinged-hinged; (c) Roller-hinged; (d) Roller-roller.	77
Figure 3.10: Roller supports at the beam ends in the second set of experiments.	81
Figure 3.11: Behavior of the beams with: (a) Roller supports; (b) Hinged supports in lateral direction.	82
Figure 3.12: (a) Support frame in the first set of experiments; (b) A ball roller in contact with the beam.	83
Figure 3.13: Bending of the ball roller	84
Figure 3.14: Lateral support frame in the second set of experiments.	84
Figure 3.15: Rigid caster in contact with the specimen.	85
Figure 3.16: Support frame in the second set of tests: (a) B44-1; (b) B44-2.	87
Figure 3.17: Distortion in the cross-section at the beam end.	87
Figure 3.18: Deviation of the Initial Orientations of the Potentiometers.	89
Figure 3.19: Coupling between the in-plane and out-of-plane deflection measurements for a lateral string potentiometer with varying distances from the specimen.	90
Figure 3.20: Lateral torsional buckling (a) with; (b) without distortions in the cross-sectional shape of the beam.	91
Figure 3.21: Lateral deflection potentiometers in the first set of experiments.	92
Figure 3.22: Lateral deflection potentiometers in the second set of experiments.	92
Figure 3.23: Strain measurement using LVDT's in the first set of tests.	93
Figure 3.24: Strain measurement through strain gages in the second set of tests.	94
Figure 3.25: 2-element cross strain gage on the side face of B44-1.	96

Figure 3.26: Longitudinal strain gages along the depth of north face of Specimen B44-2 at midspan.	97
Figure 3.27: Strain gages on an aluminum strip to measure the longitudinal strain in the tension zone.	98
Figure 4.1: Spring models defining (a) Branson's (1963); (b) Bischoff's (2005) effective moment of inertia expression.	109
Figure 4.2: In-plane deflections of Beams B44-1 at midspan.	110
Figure 4.3: In-plane deflections of Beams B44-2 at midspan.	110
Figure 4.4: In-plane deflections of Beams B44-3 at midspan.	111
Figure 4.5: In-plane deflections of Beams B36L-1 at midspan.	111
Figure 4.6: In-plane deflections of Beams B36L-2 at midspan.	112
Figure 4.7: Moduli of elasticity corresponding to the fibers in the compression zone of a beam section.	114
Figure 4.8: Proposed spring model for the lateral bending behavior of reinforced concrete beams.	117
Figure 4.9: Shrinkage cracking in B30 prior to the test.	123
Figure 4.10: Length changes of specimens with and without SRA from the concrete mixture of B44.	126
Figure 4.11: Delta rosette for principal strain measurement at a point.	128
Figure 4.12: Principal strains on the side face of B36L-2.	129
Figure 4.13: Principal strains on the side face of B36L-3.	129
Figure 5.1: Torque-twist curve of a reinforced concrete beam with shear reinforcement.	132
Figure 5.2: Components of the axial torque on the failure surface of a concrete beam according to the skew-bending theory.	134
Figure 5.3: Comparison of the coefficients $\beta_c$ calculated from different equations.	142
Figure 5.4: Thin-walled tube space truss model.	144
Figure 5.5: Experimental torque-twist curve of Specimen B44-1.	146
Figure 5.6: Experimental torque-twist curve of Specimen B36L-1.	146

Figure 5.7: Approximation of the torque-twist curve of B44-2 into a series of line segments.	148
Figure 6.1: Lateral centroidal deflections of B44-1 and B44-2 at midspan.	158
Figure 6.2: Lateral centroidal deflections of B36L-1 and B36L-2 at midspan.	158
Figure 6.3: Longitudinal strain distributions in a cross-section from major-axis and minor-axis bending moments.	161
Figure 6.4: Extreme compression fiber strains of B44-1 and B44-2 from major-axis bending	163
Figure 6.5: Extreme compression fiber strains of B36L-1 and B36L-2 from major-axis bending	163
Figure 6.6: Extreme top strains on the convex faces of B44-1 and B44-2 caused by minor-axis bending	165
Figure 6.7: Top strains on the convex faces of B36L-1 and B36L-2 caused by minor-axis bending	167
Figure 6.8: Rotation of the major and minor axes of a section due to twist.	169
Figure 6.9: (a) Southwell (1932) Plot; (b) Load-Deflection Plot for Specimen B44-1.	169
Figure 7.1: Typical crack pattern on the convex faces of the specimens after buckling	174
Figure 7.2: Typical crack pattern on the concave faces of the specimens after buckling	174
Figure 7.3: Flexural cracks on the concave face of B44-3 at midspan before buckling	175
Figure 7.4: Vertical cracks on the convex face of B44-2 at midspan after buckling	176
Figure 7.5: Directions of the shear and principal stresses due to the shear forces.	178
Figure 7.6: Directions of the shear and principal stresses due to the torsional moments.	179
Figure 7.7: Diagonal tension cracks on the convex face of B36L-1 after buckling.	180
Figure 7.8: Diagonal tension cracks on the concave face of B18-2 after buckling.	180



Figure 7.9: Diagonal tension cracks continuing on the top surface of B44-2 after buckling	181
Figure 7.10: Maximum compressive strains in the first set of beams, illustrated on the stress-strain curve of concrete.	182
Figure 7.11: Maximum compressive strains in B44 at the instant of buckling.	182
Figure 7.12: Maximum compressive strains in B36L at the instant of buckling.	183
Figure 7.13: Experimental to analytical critical load ratios of the specimens according to different formulae.	188
Figure A.1: Height measurement points along the lengths of the beams.	208
Figure A.2: Width measurement points along the lengths of the specimens.	210
Figure A.3: Length measurement depths of the specimens.	212
Figure B.1: Imperfection measurement points on Beams (a) B18; (b) B30 and B36; (c) B44 and B36L.	215
Figure B.2: Sweep at midheight of B18-1.	219
Figure B.3: Sweep at midheight of B18-2.	219
Figure B.4: Sweep at midheight of B30.	220
Figure B.5: Sweep at midheight of B36.	220
Figure B.6: Sweep at midheight of B44-1.	221
Figure B.7: Sweep at midheight of B44-2.	221
Figure B.8: Sweep at midheight of B44-3.	222
Figure B.9: Sweep at midheight of B36L-1.	222
Figure B.10: Sweep at midheight of B36L-2.	223
Figure B.11: Permanent lateral deformation at midheight of B30.	223
Figure B.12: Permanent lateral deformation at midheight of B44-1.	224
Figure B.13: Permanent lateral deformation at midheight of B44-2.	224
Figure B.14: Permanent lateral deformation at midheight of B44-3.	225
Figure B.15: Permanent lateral deformation at midheight of B36L-2.	225

Figure B.16: Permanent torsional rotations of B30.	226
Figure B.17: Permanent torsional rotations of B44-1.	226
Figure B.18: Permanent torsional rotations of B44-2.	227
Figure B.19: Permanent torsional rotations of B44-3.	227
Figure B.20: Permanent torsional rotations of B36L-1.	228
Figure C.1: Loads and lateral deflections corresponding to the strain distributions in Figures C.2 to C.4.	230
Figure C.2: Midspan strain distributions of B44-1 at the initial stages of loading.	231
Figure C.3: Midspan strain distributions of B44-1 close to buckling.	232
Figure C.4: Midspan strain distributions of B44-1 after buckling.	233
Figure C.5: Loads and lateral deflections corresponding to the strain distributions in Figures C.6 and C.7.	233
Figure C.6: Midspan strain distributions of B44-2 at the initial stages of loading.	234
Figure C.7: Midspan strain distributions of B44-2 at the initiation of buckling.	235
Figure C.8: Loads and lateral deflections corresponding to the strain distributions in Figures C.9 to C.11.	235
Figure C.9: Midspan strain distributions of B44-3 at the initial stages of loading.	236
Figure C.10: Midspan strain distributions of B44-3 at different load levels.	237
Figure C.11: Midspan strain distributions of B44-3 close to buckling.	238
Figure C.12: Loads and lateral deflections corresponding to the strain distributions in Figures C.13 and C.14.	239
Figure C.13: Midspan strain distributions of B36L-1 at the initial stages of loading.	240
Figure C.14: Midspan strain distributions of B36L-1 close to buckling.	241
Figure C.15: Loads and lateral deflections corresponding to the strain distributions in Figures C.16 to C.18.	242
Figure C.16: Midspan strain distributions of B36L-2 at the initial stages of loading.	243
Figure C.17: Midspan strain distributions of B36L-2 at different load levels.	244

Figure C.18: Midspan strain distributions of B36L-2 prior to and after buckling.	245
Figure C.19: Depthwise strains along the midspan section of B44-1 at the initial stages of loading.	246
Figure C.20: Depthwise strains along the midspan section of B44-1 at the final stages of loading.	247
Figure C.21: Depthwise strains along the midspan section of B44-1 during unloading.	248
Figure D.1: Out-of-plane deflections of B18-2 at midspan.	250
Figure D.2: Out-of-plane deflections of B22-1 at midspan.	250
Figure D.3: Out-of-plane deflections of B22-2 at midspan.	251
Figure D.4: Out-of-plane deflections of B30 at midspan.	251
Figure D.5: Out-of-plane deflections of B36 at midspan.	252
Figure D.6: Out-of-plane deflections of B44-1 at midspan.	252
Figure D.7: Out-of-plane deflections of B44-2 at midspan.	253
Figure D.8: Out-of-plane deflections of B44-3 at midspan.	253
Figure D.9: Out-of-plane deflections of B36L-1 at midspan.	254
Figure D.10: Out-of-plane deflections of B36L-2 at midspan.	254
Figure D.11: Lateral centroidal deflections of Beams B44 at midspan.	255
Figure D.12: Lateral centroidal deflections of Beams B36L at midspan.	255
Figure D.13: In-plane deflections of Beam B18-2 at midspan.	258
Figure D.14: In-plane deflections of Beams B22 at midspan.	258
Figure D.15: In-plane deflections of Beams B30 at midspan.	259
Figure D.16: In-plane deflections of Beams B36 at midspan.	259
Figure D.17: In-plane deflections of Beams B44-1 at midspan.	260
Figure D.18: In-plane deflections of Beams B44-2 at midspan.	260
Figure D.19: In-plane deflections of Beams B44-3 at midspan.	261

Figure D.20: In-plane deflections of Beams B36L-1 at midspan.	261
Figure D.21: In-plane deflections of Beams B36L-2 at midspan.	262
Figure D.22: Experimental torque-twist curve of Specimen B44-1.	262
Figure D.23: Experimental torque-twist curve of Specimen B44-2.	263
Figure D.24: Experimental torque-twist curve of Specimen B44-3.	263
Figure D.25: Experimental torque-twist curve of Specimen B36L-1.	264
Figure D.26: Experimental torque-twist curve of Specimen B36L-2.	264
Figure E.1: Potentiometer configuration in the tests.	266
Figure E.2: Angle of twist calculations.	269
Figure E.3: Centroidal deflection calculations.	272
Figure G.1: Reinforcement in Specimen B36.	285
Figure G.2: Lifting mechanism in the first set of beams.	285
Figure G.3: Use of spreader beams to lift the beams.	287
Figure G.4: The lifting point in the second set of beams connected to the spreader beam.	288
Figure H.1: Southwell (1932) Plots for Specimen B44-2.	292
Figure H.2: Meck's (1977) Version of the Southwell (1932) Plots for Specimen B44-2.	293
Figure H.3: Massey's (1963) Version of the Southwell (1932) Plots for Specimen B44-2.	294

## LIST OF SYMBOLS

$A_c$	Gross area of the cross-section (Figure 1.24)
$A_e$	Area bounded by the centerline of the effective wall
$A_o$	Area bounded by the shear flow zone
$A_s$	Total cross-sectional area of the longitudinal reinforcement
$A_t$	Cross-sectional area of one leg of a stirrup
$A_l$	Area bounded by the centerline of a closed stirrup (Figure 1.24)
$A_2$	Area of the rectangle formed by the lines connecting the centroids of the corner longitudinal bars (Figure 1.24)
$B$	Lateral bending rigidity
$E$	Modulus of elasticity
$E_c$	Elastic modulus of concrete
$E_{it}$	Initial tangent modulus of elasticity
$E_o$	Overall modulus of elasticity $[= (E_{sec}+E_c)/2]$
$E_r$	Reduced modulus of elasticity $\left[ = 4 \cdot E_c \cdot E_{tan} / \left( \sqrt{E_c} + \sqrt{E_{tan}} \right)^2 \right]$
$E_s$	Modulus of elasticity of steel
$E_{sec}$	Secant modulus of elasticity
$E_{tan}$	Tangent modulus of elasticity
$E_{tano}$	Tangent modulus of elasticity corresponding to the extreme compression fiber strain (Figure 1.17)
$EC_w$	Warping rigidity
$EI_x$	In-plane bending rigidity
$EI_y$	Out-of-plane bending rigidity

$G$	Modulus of rigidity
$G_c$	Modulus of rigidity of concrete
$G'_c$	Reduced modulus of rigidity of concrete $\left[ = E_{\text{sec}}/2 \cdot (1 + \nu) \right]$
$G_{cr}C_{cr}$	Post-cracking torsional rigidity (Figure 5.1)
$G_o$	Overall modulus of rigidity of concrete
$G_s$	Modulus of rigidity of steel
$(GC)$	Torsional rigidity
$I_{cr}$	Cracked moment of inertia about the major axis
$I_e$	Effective moment of inertia
$I_g$	Moment of inertia of the gross cross-section about the major axis
$I_x$	Moment of inertia about the major axis
$I_{ucr}$	Uncracked moment of inertia about the major axis considering the contribution of the longitudinal reinforcement
$I_y$	Moment of inertia about the minor axis
$J$	Torsional constant
$L$	Unbraced length
$M_x$	In-plane bending moment
$M_y$	Out-of-plane bending moment
$M_a$	Maximum in-plane bending moment along the span of a beam
$M_c$	Calculated ultimate moment
$M_{cr}$	Critical moment
$M_{cra}$	Cracking Moment
$M_L$	Limit moment
$M_{ex}$	Experimental ultimate moment
$P$	Applied load

$P_{an}$	Analytical ultimate or critical load
$P_{cr}$	Critical load
$P_L$	Limit load
$T$	Torsional moment
$T_a$	Applied torque
$T_b$	Maximum torsional moment in the beam at the instant of buckling
$T_{cr}$	Cracking torque
$T_{max}$	Maximum torsional moment in a beam
$T_n$	Torsional strength of a reinforced concrete member
$T_{np}$	Torsional strength of a plain concrete member
$a$	Moment lever arm of a section
$b$	Beam width
$b_s$	Width of the longitudinal reinforcement layer (Figure 1.18)
$b_1$	Width of the area bounded by the centerline of a closed stirrup (Figure 1.18)
$b_2$	Width of the rectangle formed by the lines connecting the centroids of the longitudinal reinforcing bars (Figure 1.24)
$c$	Neutral axis depth from the compression face
$c_u$	Neutral axis depth at the ultimate flexural moment level
$c_v$	Percent coefficient of variation
$d$	Depth of the centroid of the tension reinforcement from the compression face
$d_1$	Depth of the area bounded by the centerline of a closed stirrup (Figure 1.18)
$e$	Vertical distance of the point of application of load from the centroid of the beam section
$f$	Stress
$f_c$	Concrete stress
$f'_c$	Compressive strength of concrete

$f_r$	Modulus of rupture of concrete
$f_t$	Splitting tensile strength of concrete
$h$	Beam height
$k_{cr}$	Lateral bending rigidity of the cracked portion of a concrete beam (Figure 4.1)
$k_{eq}$	Lateral bending rigidity of a concrete beam (Figure 4.1)
$k_{ucr}$	Lateral bending rigidity of the uncracked portion of a concrete beam (Figure 4.1)
$n$	Modular ratio of steel to concrete [= $E_s/E_c$ ]
$p_e$	Perimeter of the area bounded by the centerline of the effective wall
$p_o$	Perimeter of the area bounded by the shear flow zone
$p_1$	Perimeter of the area bounded by the centerline of a closed stirrup (Figure 1.24)
$p_2$	Perimeter of the rectangle formed by the lines connecting the centroids of the corner longitudinal bars (Figure 1.24)
$s$	Spacing of the stirrups
$t_i$	Wall thickness of a tube
$t_s$	Thickness of the longitudinal reinforcement layer (Figure 1.18)
$u_c$	Out-of-plane deflection of the centroid of midspan section
$u_o$	Sweep at midheight of a beam at midspan
$u_t$	Out-of-plane deflection at the top of midspan section
$u_{to}$	Sweep at the top of a beam at midspan
$u(z)$	Centroidal sweep at a distance $z$ from the end of a beam
$v$	Lateral deflection of the centroid of midspan section in the direction of the major axis of the twisted configuration of a beam (Figure 6.8)
$v_c$	In-plane deflection of the centroid of midspan section
$v_o$	Initial imperfection at the center of a beam in the direction of the major axis of the initial configuration of midspan section
$w$	Self-weight per unit length of a beam



$w_{cr}$	Critical self-weight per unit length of a beam causing buckling
$\bar{y}$	Depth of the center of gravity of the transformed beam section from the compression face (Equation 4.6)
$\Sigma I_{sy}$	Moment of inertia of the longitudinal reinforcement about the minor axis of the beam section
$\beta$	Coefficient for St. Venant's torsional constant
$\varepsilon$	Strain
$\varepsilon_c$	Strain of the compression fibers at an arbitrary depth from the compression face created by the major-axis bending (Figure 1.17)
$\varepsilon_{co}$	Extreme compression fiber strain from major-axis bending
$\varepsilon_{cl}$	Compressive strain on the concave face of the beam originating from the lateral bending moment only (Figure 1.17)
$\varepsilon_{cr}$	Cracking strain of concrete
$\varepsilon_o$	Strain at peak stress
$\varepsilon_{to}$	Strain at the centroid of the tension reinforcement from major-axis bending
$\varepsilon_{tl}$	Tensile strain on the convex face of the beam originating from the lateral bending moment only (Figure 1.17)
$\varepsilon_y$	Yielding strain of steel
$\theta$	Twist
$\theta_{cri}$	Twist at the initiation of diagonal cracking (Figure 5.1)
$\theta_{crp}$	Twist at the end of diagonal cracking (Figure 5.1)
$\theta_u$	Twist at ultimate torque (Figure 5.1)
$\mu$	Mean value
$\nu$	Poisson's ratio
$\nu_c$	Poisson's ratio of concrete
$\rho_l$	Volumetric ratio of the longitudinal reinforcement $[= A_s/A_c]$
$\rho_t$	Volumetric ratio of the transverse reinforcement $[= A_t \cdot p_1/(A_c \cdot s)]$

$\rho_{to}$	Total volumetric ratio of the transverse and longitudinal reinforcement [= $\rho_l + \rho_t$ ]
$\sigma$	Standard deviation
$\sigma_c$	Extreme compression fiber stress
$\varphi_c$	Angle of twist of the beam at midspan
$\varphi_o$	Initial twisting angle of a beam at midspan
$\varphi_{ult}$	Twisting angle of a beam at midspan at the instant when the limit load is reached
$\varphi(z)$	Twisting angle at a distance $z$ from the end of a beam

## LIST OF ABBREVIATIONS

DEMEC	Demountable mechanical strain gage
HRWR	High range water reducing admixture
LVDT	Linear variable differential transducer
NA	Neutral axis
OC	Conventionally vibrated ordinary concrete
SCC	Self-compacting concrete
SRA	Shrinkage reducing admixture
WWR	Welded wire reinforcement

## SUMMARY

The study presents the results of an investigation aimed at examining the lateral stability of rectangular reinforced concrete slender beams. A total of eleven reinforced concrete beams having a depth to width ratio between 10.20 and 12.45 and a length to width ratio between 96 and 156 were tested. Beam thickness, depth and unbraced length were 1.5 to 3.0 in., 18 to 44 in., and 12 to 39.75 ft, respectively. The initial geometric imperfections, shrinkage cracking conditions and material properties of the beams were carefully determined prior to the tests.

Each beam was subjected to a single concentrated load applied at mid-span by means of a gravity load simulator that allowed the load to always remain vertical when the section displaces out of plane. The loading mechanism minimized the lateral translational and rotational restraints at the point of application of load to simulate the nature of gravity load.

Each beam was simply-supported in and out of plane at the ends. The supports allowed warping deformations, yet prevented twisting rotations at the beam ends.

In the experimental part of the study, reinforced concrete beams with initial imperfections (sweep) failed under loads lower than the critical loads corresponding to the geometrically perfect configuration of the respective beams. The maximum load carried by an imperfect beam is known as the limit load ( $P_L$ ). In the present study, the limit load ( $P_L$ ) and the critical load ( $P_{cr}$ ) were distinguished.

In the first part of the analytical investigation, a formula was developed for determining the critical loads corresponding to the lateral torsional buckling of

rectangular reinforced concrete beams. The effects of shrinkage cracking and inelastic stress-strain properties of concrete and the contribution of longitudinal reinforcement to the lateral stability are accounted for in the critical load formula. The second part of the investigation focused on developing a formula for the estimation of limit loads of reinforced concrete beams with initial lateral imperfections. The proposed limit load formula was obtained by introducing the destabilizing effect of sweep as a reduction term to the critical load equation.

Finally, the experimental results were compared to the proposed analytical solution and to various lateral torsional buckling solutions in the literature. The formulation proposed in the present study was found to agree well with the experimental results. The good correlation with the experimental results and the incorporation of the geometric and material nonlinearities into the formula makes the proposed solution, given below for a simply supported rectangular reinforced concrete beam loaded with a concentrated load at midspan, practical for design purposes:

$$P_{cru} = \frac{4 \cdot M_{cr}}{L} - \frac{u_{to} \cdot (48 \cdot E_c \cdot I_y)}{\sin(\phi_{ult}) \cdot L^3} \quad (1)$$

where  $P_L$  is the limit load;  $L$  is the unbraced length of the beam;  $u_{to}$  is the sweep at the top of the beam at midspan;  $E_c$  is the elastic modulus of concrete;  $I_y$  is the second moment of area of the beam section about the minor axis;  $\phi_{ult}$  is the angle of twist of the beam at midspan corresponding to the limit load ( $P_L$ ).  $M_{cr}$  is the critical moment corresponding to the geometrically perfect configuration of the beam, obtained from Equation (2):

$$M_{cr} = \frac{4.23}{L} \cdot \left( 1 - 1.74 \cdot \frac{e}{L} \cdot \sqrt{\frac{B_o}{(GC)_o}} \right) \cdot \sqrt{B_o \cdot (GC)_o} \quad (2)$$

where  $B_o$  is the lateral bending rigidity, obtained from Equation (3);  $(GC)_o$  is the torsional rigidity, calculated from Equation (4);  $e$  is the vertical distance of the load application point from the centroid of the midspan cross section.

$$B_o = \left[ \left( \frac{b^3 \cdot c}{12} \right) \cdot \frac{1}{1 + \left( \frac{\omega \cdot M_{cra}}{M_{cr}} \right)^2 \cdot \left( \frac{c}{h} - 1 \right)} \right] \cdot \left( \frac{E_{sec} + E_c}{2} \right) \quad (3)$$

$$(GC)_o = \frac{E_{sec} + E_c}{4 \cdot (1 + \nu)} \cdot \left[ \frac{b^3 \cdot h}{3} \cdot \left( 1 - 0.63 \cdot \frac{b}{h} \right) \right] \quad (4)$$

where  $b$  and  $h$  are the width and height of the beam, respectively;  $c$  is the depth of the neutral axis from the compression face;  $M_{cra}$  is the cracking moment;  $\omega$  is a constant, which has a value of 1 in the absence of restrained shrinkage cracks in concrete and a value of 2/3 in the presence of restrained shrinkage cracks and  $\nu$  is Poisson's ratio of concrete.  $E_{sec}$  is the secant modulus of elasticity of concrete corresponding to the extreme compression fiber strain at midspan at the instant when  $M_{cr}$  is reached.

# INTRODUCTION

## 1.1 Introduction

Due to the increasing use of slender structural concrete beams in long-span bridges and other structures, lateral stability is becoming an important criterion in the design of structural concrete girders. Lateral-torsional buckling of long-span precast concrete girders is a matter of concern, particularly during bridge construction.

Bridge girders are laterally supported by diaphragms and the bridge deck after the completion of a bridge. Nonetheless, lateral stability of the precast bridge girders should be assured also during fabrication, lifting, transportation and erection stages. Accordingly, precast concrete girders should be designed to remain stable even under the most unfavorable loading and support conditions of the transitory phases of construction.

Lateral instability of a beam arises from the compressive stresses in the beam resulting from flexure due to transverse loading. The compression zone of the beam tends to buckle about the minor axis of the overall cross-section of the beam while the tension zone tends to remain stable. When the load reaches a certain “critical” value, the beam buckles out of plane and twists (Figure 1.1) as a result of the differential lateral displacements of the compression and tension zones.

For assessing the stability, the critical moment of a concrete girder should be evaluated for the loading and support conditions of different phases of construction. A beam free from initial geometric imperfections does not undergo out-of-plane deflections and rotations before reaching a critical moment value. When the maximum moment in the beam reaches the critical moment value, the beam experiences sudden excessive out-

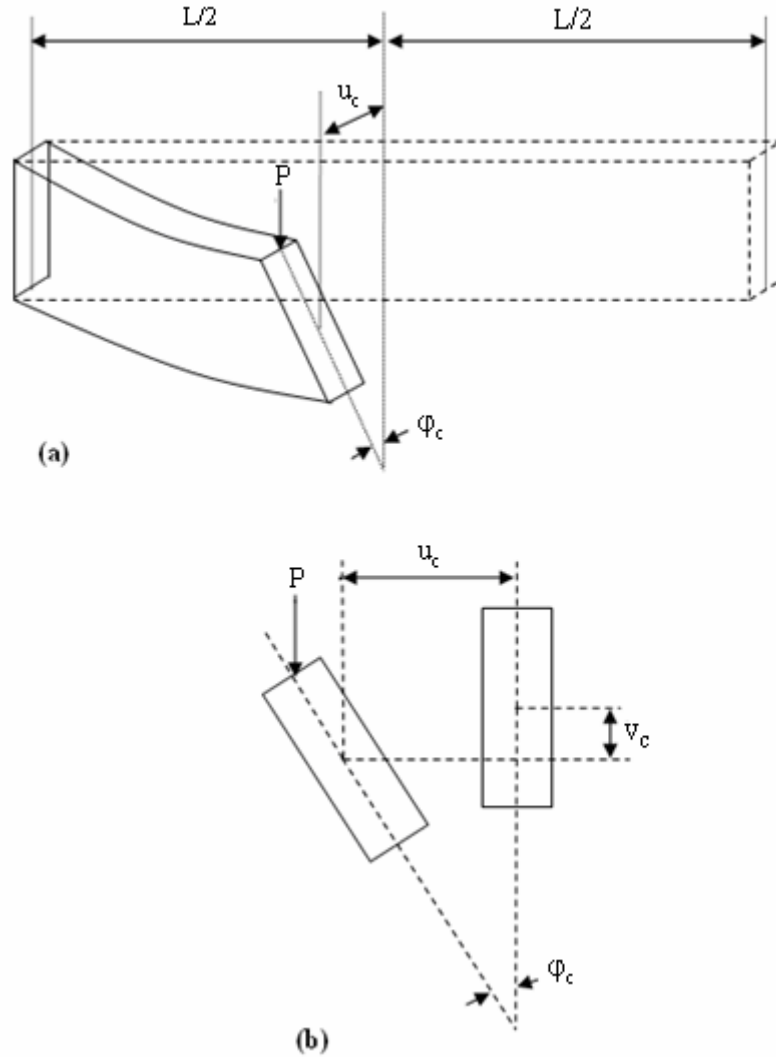


Figure 1.1 – (a) Lateral torsional buckling of a beam subjected to a concentrated load at midspan; (b) Lateral and vertical deflections and rotation of the midspan section

of-plane deformations and torsional rotations. This type of buckling is known as bifurcation instability and the moment at which the beam loses its stability and experiences rapid and excessive deformations at a constant load level is known as the critical moment ( $M_{cr}$ ).

A beam having initial geometric imperfections, on the contrary, does not bifurcate at the limit load. The beam undergoes deformations and rotations throughout the whole



course of loading, even prior to buckling. The moment carried by the beam reaches an ultimate value, called the limit moment ( $M_L$ ), beyond which greater lateral deformations and rotations take place while the moment-carrying capacity of the beam slowly decreases (Figure 1.2). This type of instability is known as limit load instability.

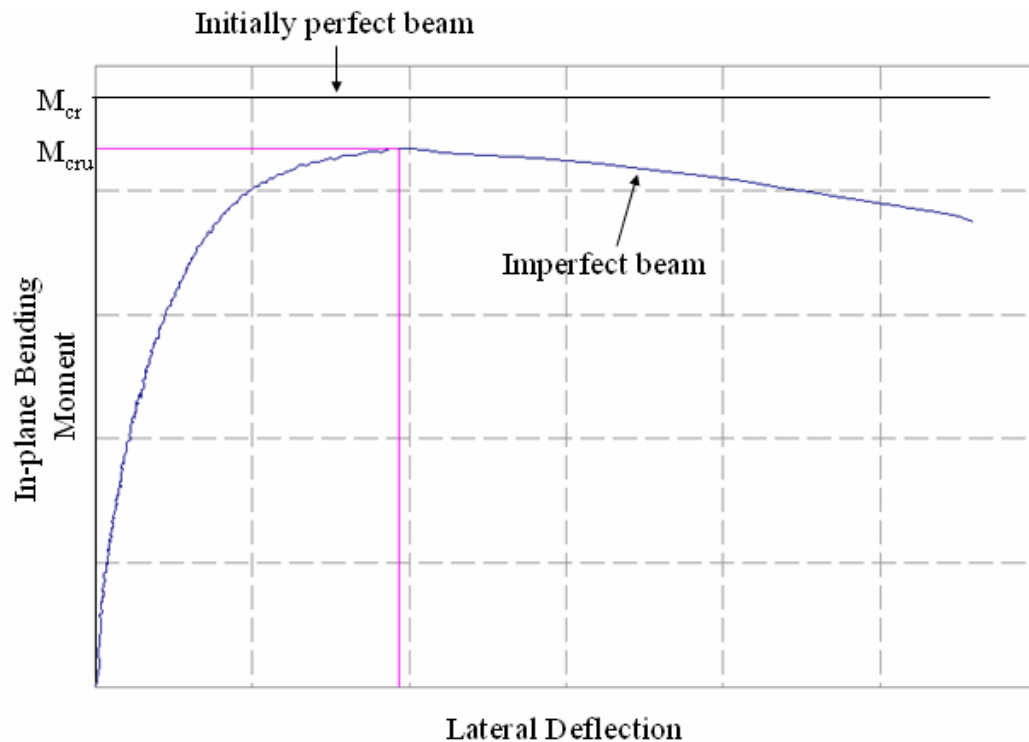


Figure 1.2 – Load-lateral deflection curve of a slender reinforced concrete beam

In reinforced concrete beams, the difference between the critical moment ( $M_{cr}$ ) and the limit moment ( $M_L$ ) is more pronounced since cracking in an imperfect concrete beam due to the lateral displacements prior to buckling decreases the moment-carrying capacity of the beam significantly.

ACI 318-05 (2005) does not include an analytical method for the calculation of the critical moment of a concrete beam. The only provision regarding the stability is given in Section 10.4, which limits the ratio of beam span to beam width,  $L/b$ , to less than 50.

AASHTO LRFD (2005) specifies in Section 5.5.4.3 that: “Buckling of precast members during handling, transportation, and erection shall be investigated.” However, no analytical method is given for the calculation of the critical moment of a reinforced concrete beam

## **1.2 Project Objectives**

The research described herein investigates the lateral stability of rectangular reinforced concrete beams experimentally and analytically. The analytical study was carried out to develop an analytical method to estimate critical moments of rectangular reinforced concrete beams. In the experimental part of the study, a total of eleven slender rectangular reinforced concrete beams were tested to produce experimental data for supporting the analytical methods proposed for examining the lateral-torsional buckling of reinforced concrete beams.

Attention is given to the effects of the initial geometric imperfections and shrinkage on the lateral stability of reinforced concrete beams.

## **1.3 Organization of the Study**

Section 1.4 summarizes the previous studies in the literature on lateral stability of reinforced concrete beams. Chapter II introduces the specimens of the experimental program and mechanical properties of the concrete mixtures used in the specimens.

Chapter III presents the experimental setup used to test the beams and summarizes the test procedure.

Chapter IV summarizes the previously developed formulae concerning the lateral bending rigidity of rectangular reinforced concrete beams and introduces the new lateral bending rigidity equation proposed in this study. The chapter also presents the spring systems used to model a reinforced concrete beam when developing the flexural rigidity expressions. Finally, the effect of restrained shrinkage cracking on the lateral bending rigidity of a concrete beam is examined in the last section of Chapter IV, where a modification to the proposed lateral bending rigidity expression is introduced to account for the reduction in the rigidity due to the presence of possible shrinkage cracks in concrete.

In Chapter V, the torsional rigidity expressions for rectangular reinforced concrete beams available in the literature are presented. Later, the slopes of the experimental torque-twist curves of the specimens are compared to the analytical values obtained from the torsional rigidity expressions given in the chapter. The torsional rigidity expression giving the closest agreement with the experimental results is modified to account for the possible inelastic material behavior of concrete at the time of buckling.

Chapter VI presents the critical moment calculations of reinforced concrete beams. In Section 6.2, effects of the initial geometric imperfections on the ultimate moment and the out-of-plane deformations and twisting rotations of an imperfect reinforced concrete beam are explained and modifications to the critical moment expression are proposed to account for the effects of geometric nonlinearities.

In Chapter VII, the crack patterns of the specimens and some experimental results are presented, and the analytical critical load values obtained from the formulae given in Chapter VI are compared to the experimental buckling loads of the specimens to determine the degree of correlation between the analytical and experimental results.

Finally, conclusions of the study are summarized in the last chapter.

In the present study, limit moments of the specimens were taken as the greatest moments in the experimental load-deflection plots of the specimens. There are some other methods given in the literature for obtaining the buckling moments of beams by using the experimental data. The methods developed by Southwell (1932), Meck (1977) and Massey (1963) and their applications to reinforced concrete beams are explained in Appendix H.

#### **1.4 Previous Studies**

This section reviews the previous studies on lateral torsional buckling of rectangular reinforced concrete beams. The experimental studies in the literature are presented in Section 1.4.1. Next, the analytical methods in the literature for predicting the critical loads of reinforced concrete beams are explained in Section 1.4.2. Finally, the contributions of the previous studies to the field of lateral stability of reinforced concrete beams are summarized in Section 1.4.3, where the factors that remained uninvestigated in the literature are also emphasized to support the need for the present research.

#### 1.4.1 Review of Previous Experimental Work

Hansell and Winter (1959) studied the lateral stability of reinforced concrete beams both experimentally and analytically. The main goal of the experimental study was to investigate any possible reductions in the flexural capacities of reinforced concrete beams with increasing  $L/b$  ratios. Hansell and Winter (1959) tested five different groups of beams, namely B6, B9, B12, B15 and B18. Two companion beams for each group of specimens were made and tested to failure. Nominal dimensions of the beams are presented in Table 1.1. All specimen groups except B6 violated the slenderness criterion, given in the 1956 Edition of ACI Building Code, which limited the  $L/b$  ratio to less than 32 for reinforced concrete beams.

Table 1.1 – Nominal dimensions of the beams tested by Hansell and Winter (1959)

Specimen	Height, $h$ (in.)	Width, $b$ (in.)	Length, $L$ (ft)	$d/b$ ratio	$L/b$ ratio
B18	13	2.5	18	4.5	86.4
B15	13	2.5	15	4.5	72.0
B12	13	2.5	12	4.5	57.6
B9	13	2.5	9	4.5	43.2
B6	13	2.5	6	4.5	28.8

All specimens tested by Hansell and Winter (1959) failed in in-plane bending compression failure after the yielding of tension reinforcement and developed their ultimate flexural strength prior to lateral torsional buckling. Experimental ultimate moments of the specimens are presented in Table 1.2 together with the calculated ultimate flexural moments. The experimental-to-calculated ultimate moment ratio of each test beam is also given in the table. The experimental ultimate moments are in good

Table 1.2 – Results of the tests by Hansell and Winter (1959)

Specimen	Failure Mode	Experimental Ultimate Moment, $M_{ex}$ (in-kips)	Calculated Ultimate Moment, $M_c$ (in-kips)	Experimental- to-Calculated Moment Ratio $M_{ex}/M_c$
<b>B6-1</b>	Flexure	216	196.7	1.10
<b>B6-2</b>	Flexure	199	196.7	1.01
<b>B9-1</b>	Flexure	201	196.7	1.02
<b>B9-2</b>	Flexure	205	196.7	1.04
<b>B12-1</b>	Flexure	193	197.0	0.98
<b>B12-2</b>	Flexure	199	197.0	1.01
<b>B15-1</b>	Flexure	192	195.9	0.98
<b>B15-2</b>	Flexure	198	195.9	1.01
<b>B18-1</b>	Flexure	190	196.2	0.97
<b>B18-2</b>	Flexure	196	196.2	1.00

agreement with the calculated moment values. The mean and the coefficient of variation of  $M_{ex}/M_c$  are 1.01 and 3.5%, respectively.

Hansell and Winter (1959) also reported the midspan vertical, lateral top and lateral bottom deflections of the specimens at the onset of yielding of the flexural reinforcement. These are shown in Figures 1.3, 1.4 and 1.5, respectively. The test results of the identical (companion) beams are also shown in the figures. It is to be noted in these figures that the vertical deflections corresponding to the onset of steel yielding and the ultimate moments (Figure 1.6) are in close agreement among the companion beams while the lateral top and bottom deflections show significant variations among the companion beams. For instance, out-of-plane deflections of the companion beams in Specimen Groups B12, B15 and B18 display considerable variation.

Hansell and Winter (1959) loaded the specimens at quarter points to have constant in-plane flexural moment over the middle part of the span. Under the loading and support conditions reported by Hansell and Winter (1959), the bottom portions of the beams at

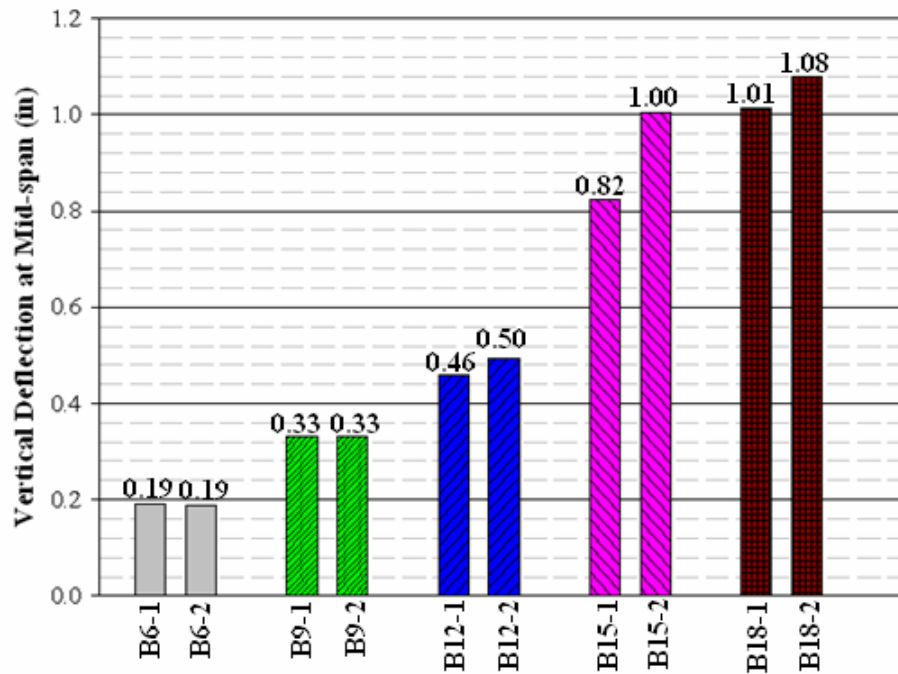


Figure 1.3 – Comparison of the vertical deflections at yield point of the companion beams tested by Hansell and Winter (1959)

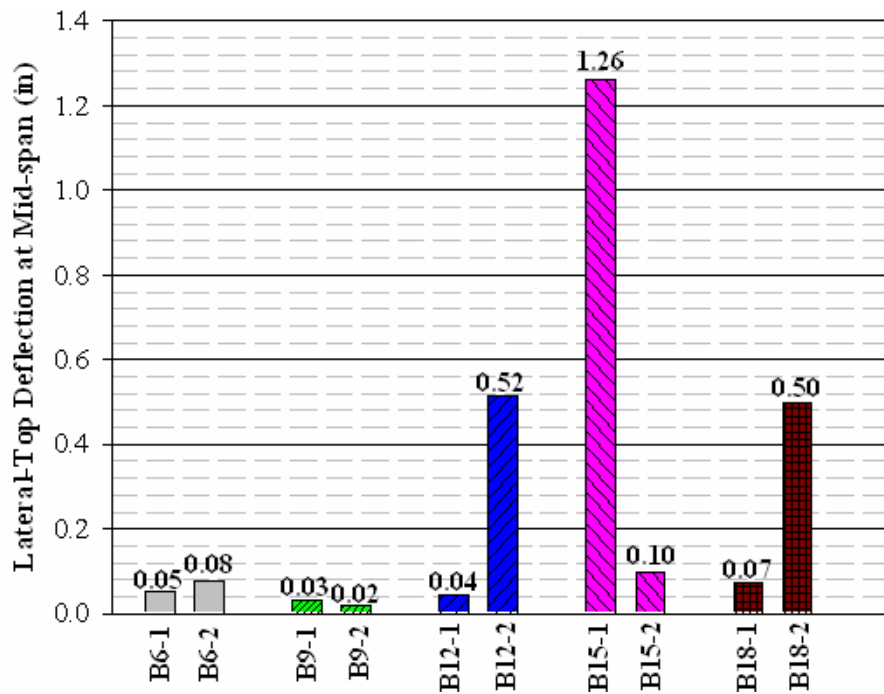


Figure 1.4 –Comparison of the lateral top deflections at yield point of the companion beams tested by Hansell and Winter (1959)

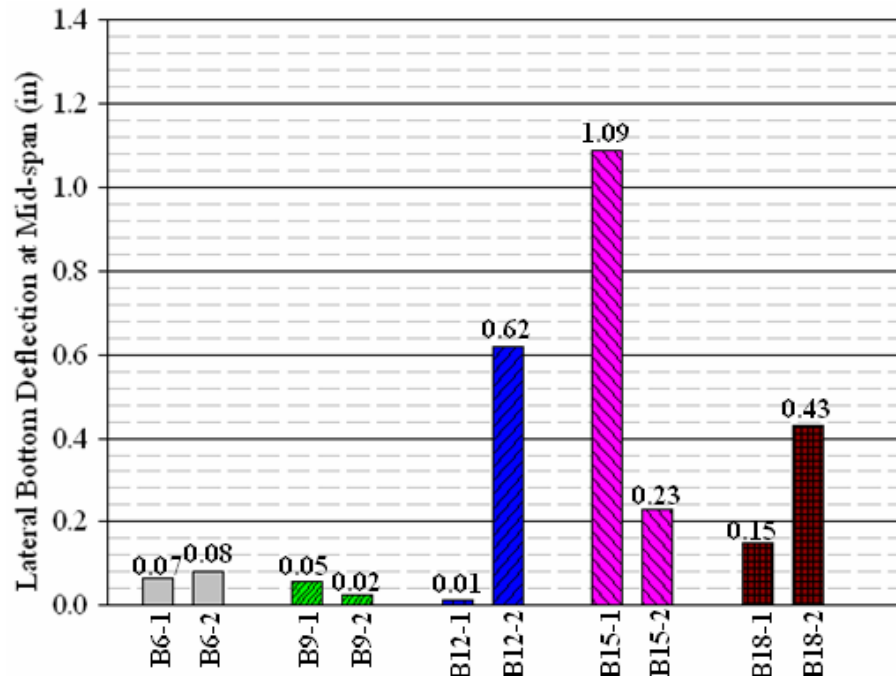


Figure 1.5 – Comparison of the lateral bottom deflections at yield point of the companion beams tested by Hansell and Winter (1959)

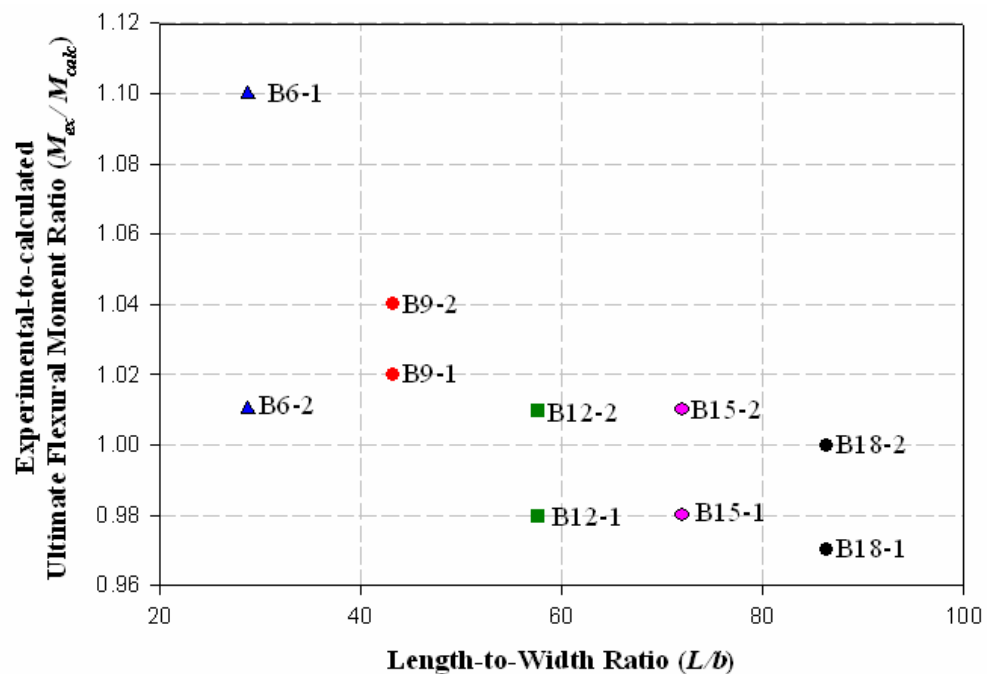


Figure 1.6 – Experimental -to- calculated ultimate moment ratios of beams tested by Hansell and Winter (1959)



midspan were subjected to tensile stresses from major-axis bending while the top portions were subjected to compressive stresses. In lateral torsional buckling, the compression zone of a beam is prone to undergo greater lateral deflections than the tension zone due to the stabilizing effect of the tensile stresses from in-plane bending. Nevertheless, the midspan lateral bottom deflections of some test specimens of Hansell and Winter (1959) exceeded the lateral top deflections.

Figure 1.7 shows the mechanism used by Hansell and Winter (1959) to convey the load from the head of a universal testing machine to the test beam. Hansell and Winter (1959) used a loading ball for the rotational freedom and a roller assembly to provide lateral translational freedom at the loading point. When the test beam deflected out of plane, the parts of the loading mechanism below the roller assembly were supposed to move with the rollers in the lateral direction (Figure 1.8), preventing any lateral restraint to the test beam. Furthermore, the loading cage around the beam was expected to rotate with the beam about the loading ball, preventing any torsional restraint to the beam at the loading point. The specimens were loaded using a universal testing machine. The load was transmitted to the loading points (quarter points of the span) through a steel beam connected to the specimen at each loading point, through the loading mechanism shown in Figure 1.7.

An examination of the loading fixture (Figure 1.8) used by Hansell and Winter (1959) reveals that the steel beam transmitting the load to the specimen does not displace in the lateral direction while the beam deforms out of plane. Therefore, the line of action

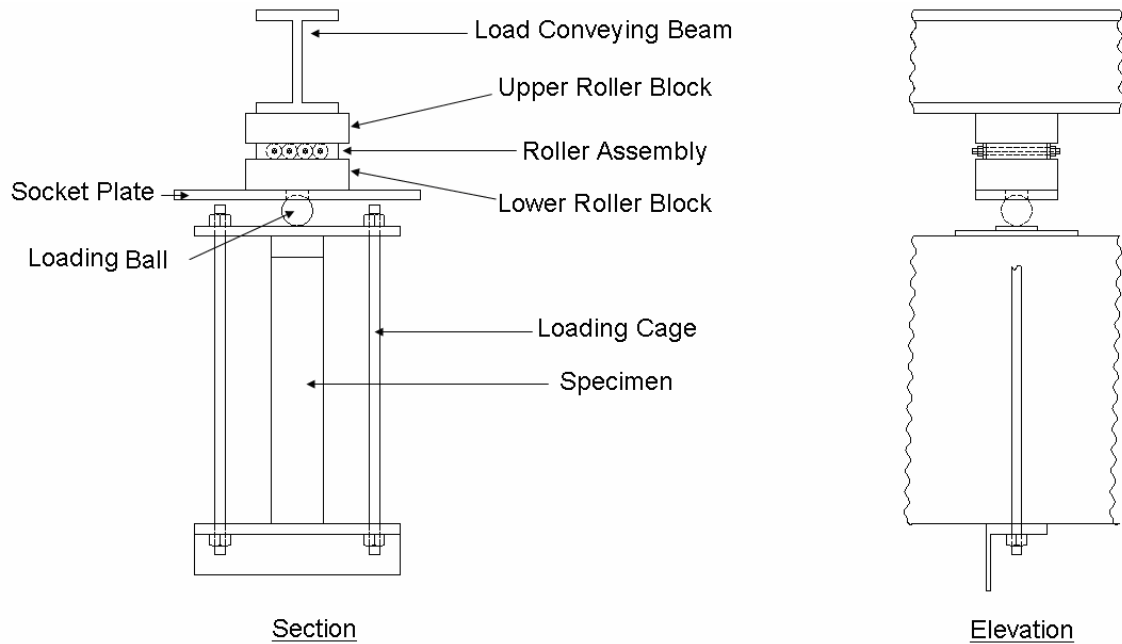


Figure 1.7 – Loading mechanism used by Hansell and Winter (1959)

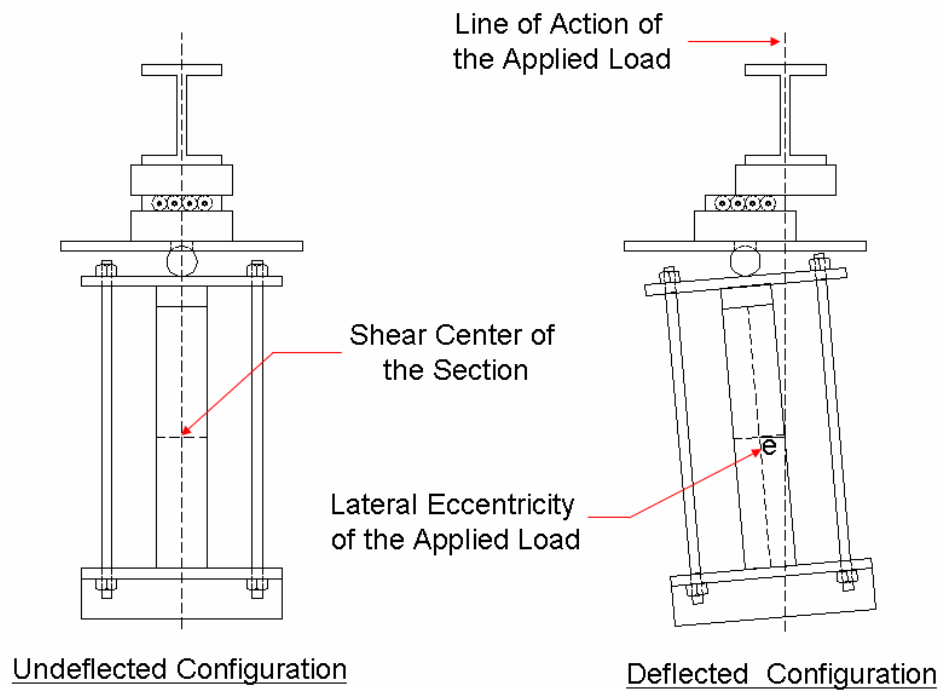


Figure 1.8 –Undeformed and expected deflected configurations of the loading mechanism

of the vertical load, initially passing through the shear center of the beam section, becomes eccentric with respect to the shear center as the specimen deforms out of plane. The eccentricity of the applied load creates larger and larger torsional moments in the beam as the applied load increases in the course of the test.

Figure 1.9 depicts the position of the line of the applied load relative to the beam when the beam undergoes lateral deflections and torsional rotations. The roller assemblies allow free out-of-plane deflections in the beam at the loading points while the steel beam remains stationary in the lateral direction. Hence, the line of action of the applied load stays in its original position, rendering the applied load eccentric relative to the shear center, which results in torsional moments in opposite direction to the torsional rotations from instability. The accidental torsions constitute a restraint to lateral torsional buckling.

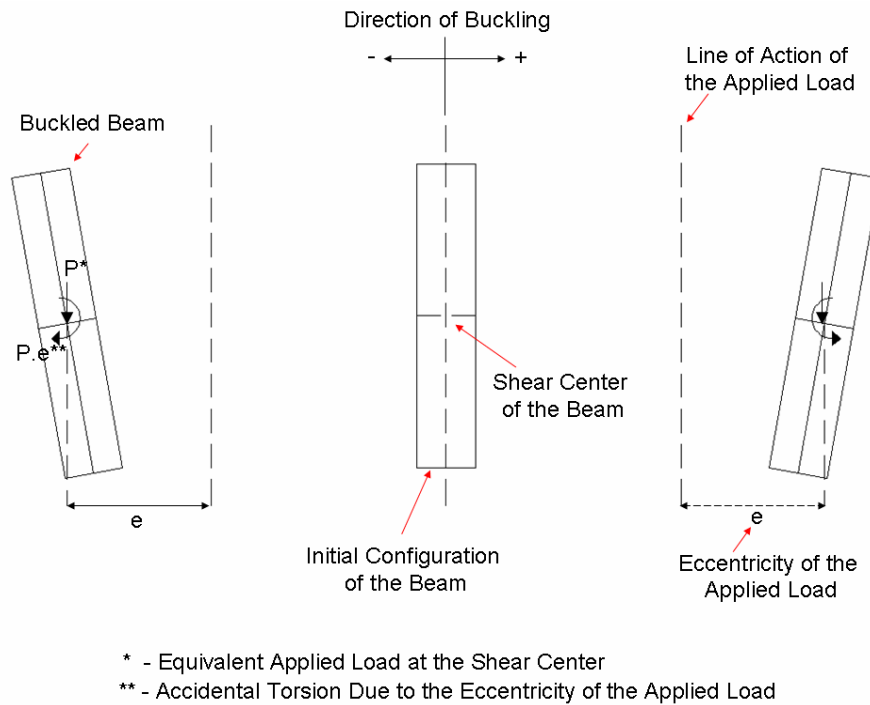


Figure 1.9 –Direction of the torsional moments induced by the eccentric application of the load

In the loading fixture used by Hansell and Winter (1959), the loading ball right above the specimen, the socket plate, the lower roller block and the roller assembly (Figure 1.7) move with the specimen in the lateral direction when the specimen undergoes out-of-plane deflections. The loading ball, moving with the specimen in lateral direction, applies lateral forces to the socket plate (Figure 1.10). If there is rolling friction in the roller assembly, the lateral translation of the roller assembly and the socket plate is restrained and the socket plate applies reaction forces to the loading ball, which restrains the lateral deflection of the top portion of the beam. Significant friction forces in the roller assembly can cause the top portion of the beam to be more stable than the bottom portion, which has no lateral translational restraint. In this case, the bottom portion undergoes greater lateral deformations than the top portion (Figure 1.10) and the beam experiences a different type of buckling called the web sidesway buckling. Hansell and Winter (1959) stated that all rolling surfaces in their setup was cleaned and oiled prior to each test to minimize the rolling friction in the loading fixture and the lateral translation restraint to the top portion of the beam.

Considering the good agreement between the experimental ultimate moments and the analytical values calculated according to Eq. (A.1) in 1956 Edition of the ACI Building Code, Hansell and Winter (1959) concluded that there were no reductions in the experimental ultimate moments of the beams due to the slenderness effects.

Sant and Bletzacker (1961) tested four different groups of beams, denoted B36, B30, B24 and B12 whose nominal dimensions are specified in Table 1.3. Three identical beams of each of the first three groups, B36, B30 and B24 and two identical beams of the fourth group, B12 were tested to failure. Table 1.4 summarizes the test results. The mean

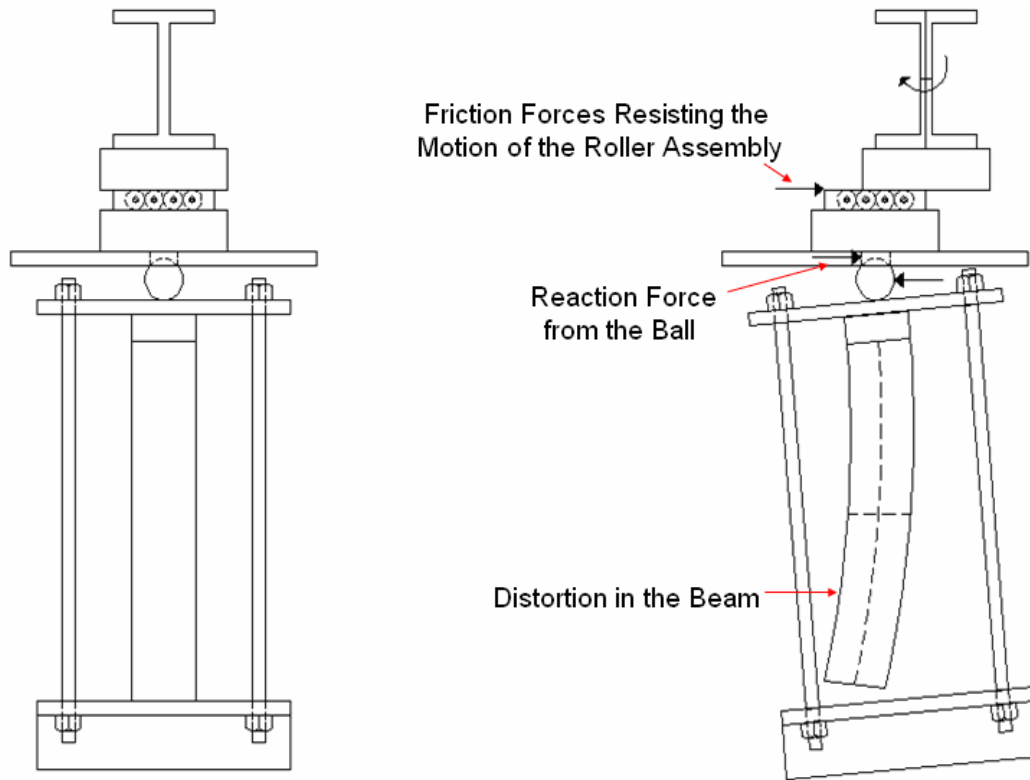


Figure 1.10 –Web sidesway buckling failure of the specimen due to the lateral restraining forces in the loading mechanism

Table 1.3 – Beams tested by Sant and Bletzacker (1961)

Specimen Group	Number of Samples	Height, h (in.)	Width, b (in.)	Length, L (ft)	d/b ratio	L/b ratio
<b>B36</b>	3	36	2.5	20	12.45	96
<b>B30</b>	3	30	2.5	20	10.20	96
<b>B24</b>	3	24	2.5	20	8.13	96
<b>B12</b>	2	12	2.5	20	3.78	96

value of the test results of identical beams are included in the table.

Table 1.4 – Results of the tests by Sant and Bletzacker (1961)

Group	Test Specimen	Failure Mode	Test Moment, $M_{test}$ (in-kips)
I	B36-1	Stability	1620
	B36-2	Stability	1845
	B36-3	Stability	1350
	$\mu^*$		1605
II	B30-1	Stability	2040
	B30-2	Stability	2160
	B30-3	Stability	1402
	$\mu$		1867
III	B24-1	Stability	1260
	B24-2	Stability	1350
	B24-3	Stability	1440
	$\mu$		1350
IV	B12-1	Flexure	300
	B12-2	Flexure	210
	$\mu$		255

\* - Mean value of the test moments of the beams in the same group

Test results show considerable variation. For instance, the experimental buckling moment of Specimen B30-2 is 54% larger than the experimental moment value obtained by testing its companion, B30-1. In Fig. 1.11, the experimental-to-predicted buckling moment ratios of the beams in specimen groups B36, B30 and B24 are shown to reveal the variation in the test results of companion beams. Since B12-1 and B12-2 did not experience lateral torsional buckling, they are not included in the figure.

Sant and Bletzacker (1961) used a steel loading ball to provide rotational freedom and a rolling mechanism to provide lateral-translational freedom at the point of application of load (Figure 1.12). The specimens were loaded through a hydraulic load cylinder, placed right above the beam and connected to the beam through threaded rods.

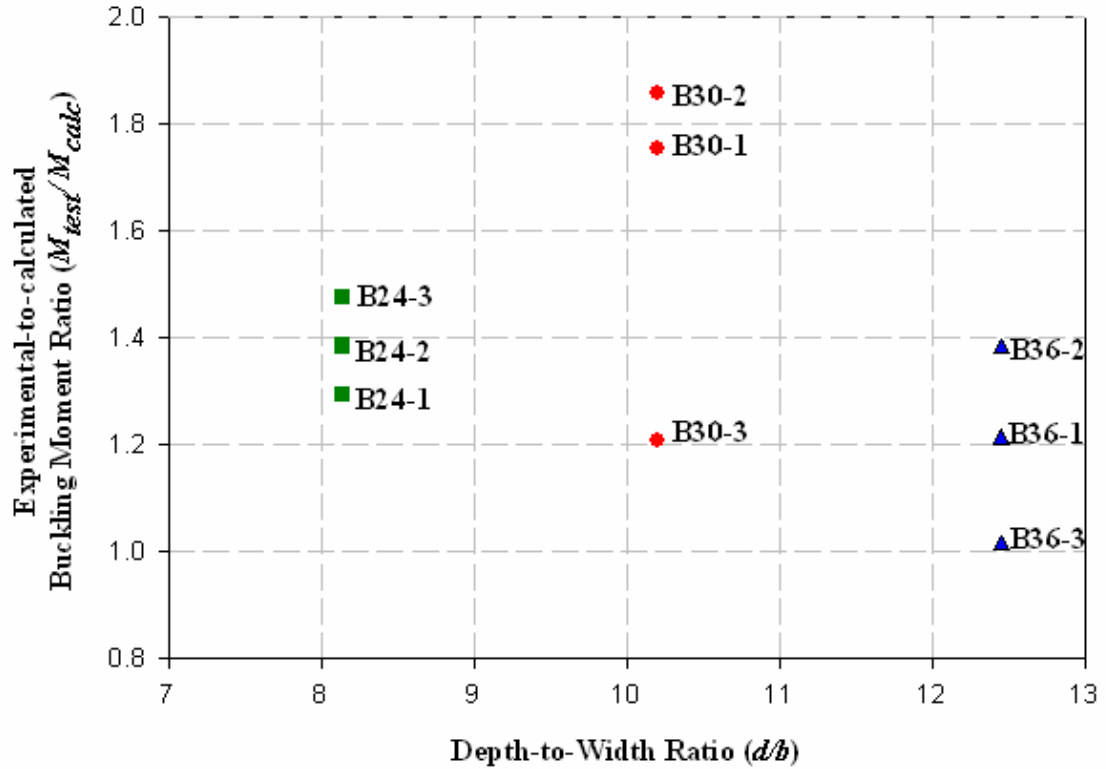


Figure 1.11 – Experimental-to-predicted buckling moment ratios of the beams in the first three specimen groups, B36, B30 and B24

The loading ball was located on the head of the load cylinder in a ball-and-socket joint. Finally, the roller assembly was placed above a load cell, which was located adjacent to the top surface of the socket plate of the ball-and-socket assembly.

A ball-and-socket joint allows free angular motion of the connecting parts relative to each other. When a beam experiences torsional rotations in the test setup used by Sant and Bletzacker (1961), the beam and the load cylinder, connected to it, rotate relative to the top portion of mechanism above the loading ball. The loading ball rotates in the socket with the specimen and cylinder, preventing any rotational restraint to the beam at loading point. As illustrated in Figure 1.13, the load cylinder is also free to rotate relative

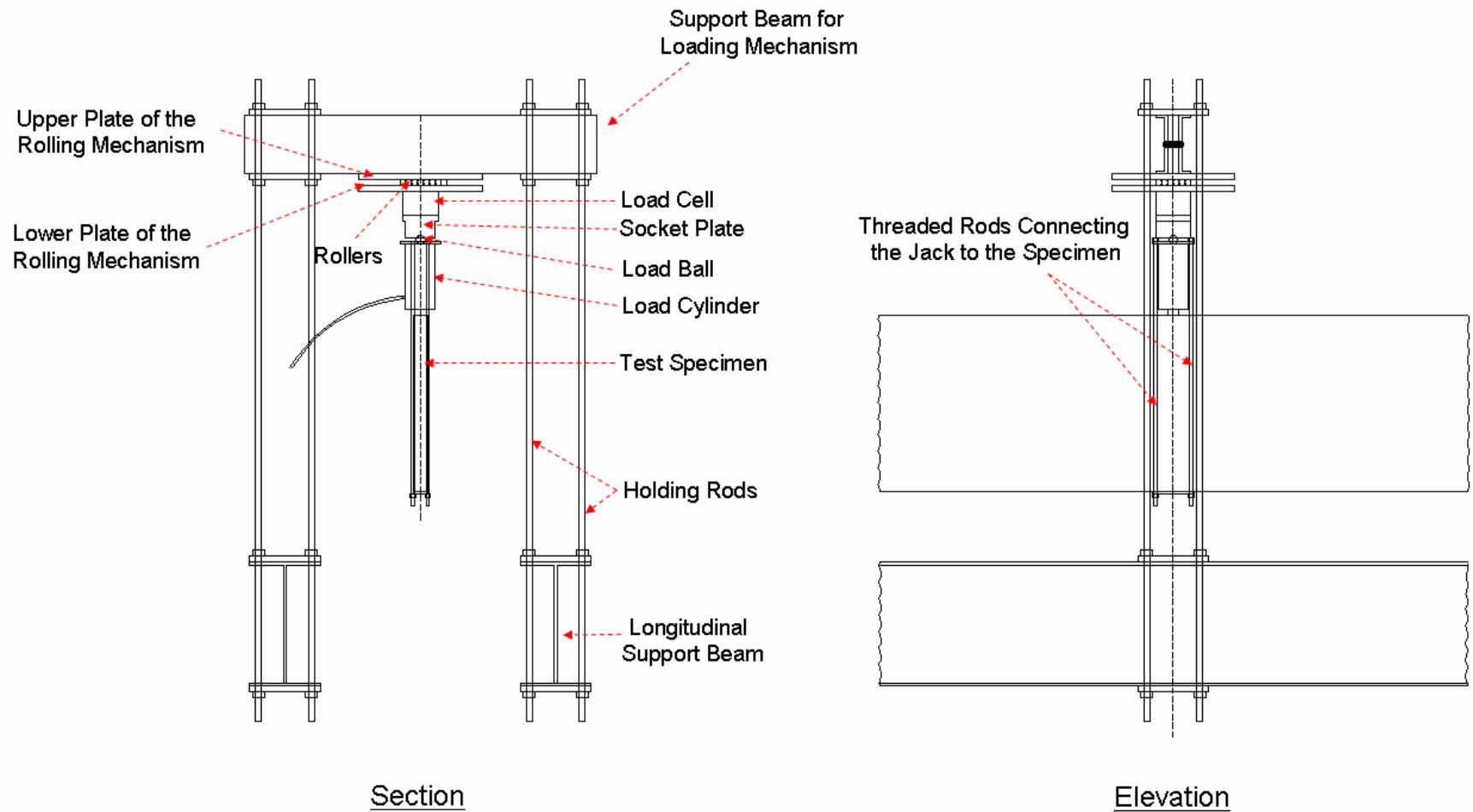


Figure 1.12 – Loading frame used by Sant and Bletzacker (1961)



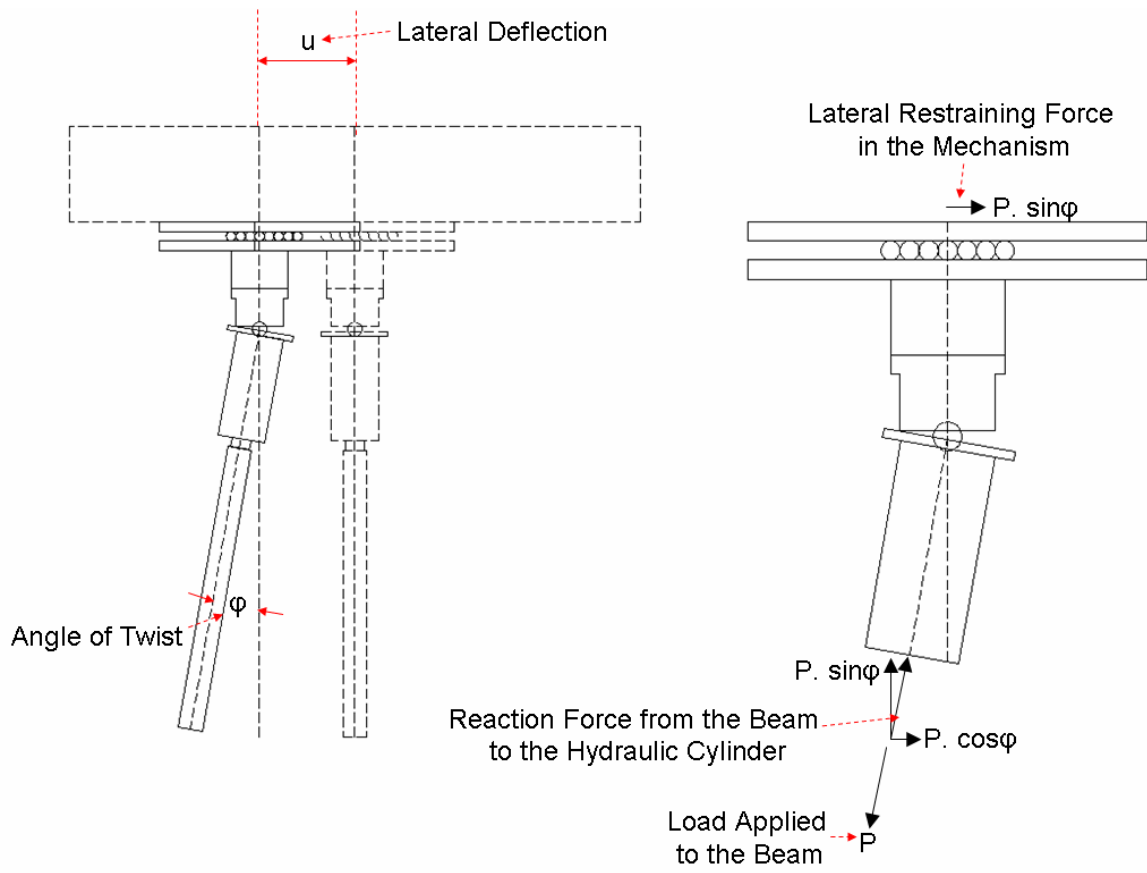


Figure 1.13 – Deflected configuration of the loading mechanism used by Sant and Bletzacker (1961)

to the top portion of the mechanism, since the cylinder is placed between the specimen and the ball-and-socket joint. Therefore, the cylinder ceases to be oriented vertically once the specimen experiences torsional rotations. The deviation of the applied load from the vertical axis induces lateral restraining force to the loading mechanism, which prevents the rollers in the rolling mechanism to move freely in the lateral direction. The lateral-translational restraint at the loading point increases the buckling load of a beam and decreases the out-of-plane deformations and the torsional rotations.

The verticality of the applied load in a lateral-torsional buckling test is crucial, particularly in the case of geometrically imperfect beams. Theoretically, a geometrically

perfect beam experiences little or no out-of-plane deformations and torsional rotations prior to buckling. On the contrary, a beam with initial geometric imperfections undergoes lateral deformations and torsional rotations throughout the entire course of loading. Therefore, the vertical orientation of the load applied by the loading mechanism used by Sant and Bletzacker (1961) is lost at the very early stages of the test of an imperfect beam. The inclination of the applied load with respect to the vertical axis continuously increases in the course of loading, introducing greater and greater lateral restraining forces to the roller mechanism. This lateral-translational restraint affects the experimental results.

Massey and Walter (1969) tested five small-scale beams with the details given in Table 1.5. The table also includes the experimental buckling loads of the specimens. The specimens were simply-supported in plane and out of plane and subjected to a concentrated load at mid-span. Massey and Walter (1969) used a special method of loading. The specimens were loaded through a water tank connected to the beam at the centroid of the mid-span section. Using dead weights hung from the specimen is a proper method of loading in lateral-torsional buckling experiments for two reasons. First, a dead weight hanging from the beam travels with the beam and does not induce any lateral-translational and rotational restraint to the beam at the load application point. Secondly, the vertical orientation of the dead weight does not change regardless of the rotations in the beam, since the gravitational forces are always vertical. Loading a beam with dead weights is also a quite economical and convenient method of loading. Nevertheless, this method of loading has a limitation preventing it to be applicable to large-scale beam tests, particularly if water is used as the means of loading. Water has a low unit weight (0.0624

kip/ft<sup>3</sup>). Therefore, large volumes of water are needed to load large-scale beams up to the failure.

Table 1.5 – Specimens tested by Massey and Walter (1969)

Specimen	Effective Depth, $d$ (in.)	Width, $b$ (in.)	Length, $L$ (ft)	Tension Reinforcement	Experimental Buckling Load, $P_{cr}$
1	12	1	10	$\frac{1}{2} \times \frac{1}{2}$ square bar	3.77
2	12	1	12	$\frac{1}{2} \times \frac{1}{2}$	3.68
3	15	$\frac{3}{4}$	12	$1 \times \frac{1}{4}$	2.20
4	15	$\frac{3}{4}$	12	$\frac{3}{4} \times \frac{1}{4}$	1.42
5	12	$\frac{3}{4}$	14	$\frac{3}{4} \times \frac{1}{4}$	0.60

Due to the limitations of the loading method, Massey and Walter (1969) tested small-scale beams, which are also easier to fabricate and to test, compared to the large-scale ones. Nevertheless, due to their relatively small lateral-flexural and torsional rigidities, the experimental results of the beams with smaller scales are more sensitive to the parameters associated with the test setup (tolerance errors). For instance, restraints from the loading mechanism, accidental deviations from vertical and eccentricities of the applied load have more pronounced influences on the behavior and test results of a small-scale beam, as opposed to a beam with larger scale.

Konig and Pauli (1990) carried out an extensive experimental study in which they tested six reinforced and prestressed concrete beams. The first five beams were T-shaped and they were designed in a way that each specimen was distinct from the other four specimens in an individual parameter, influencing the lateral stability of concrete beams. The sixth beam was totally different from the other five specimens in cross-sectional shape, dimensions and reinforcement (Figure 1.14). In the following discussion, the

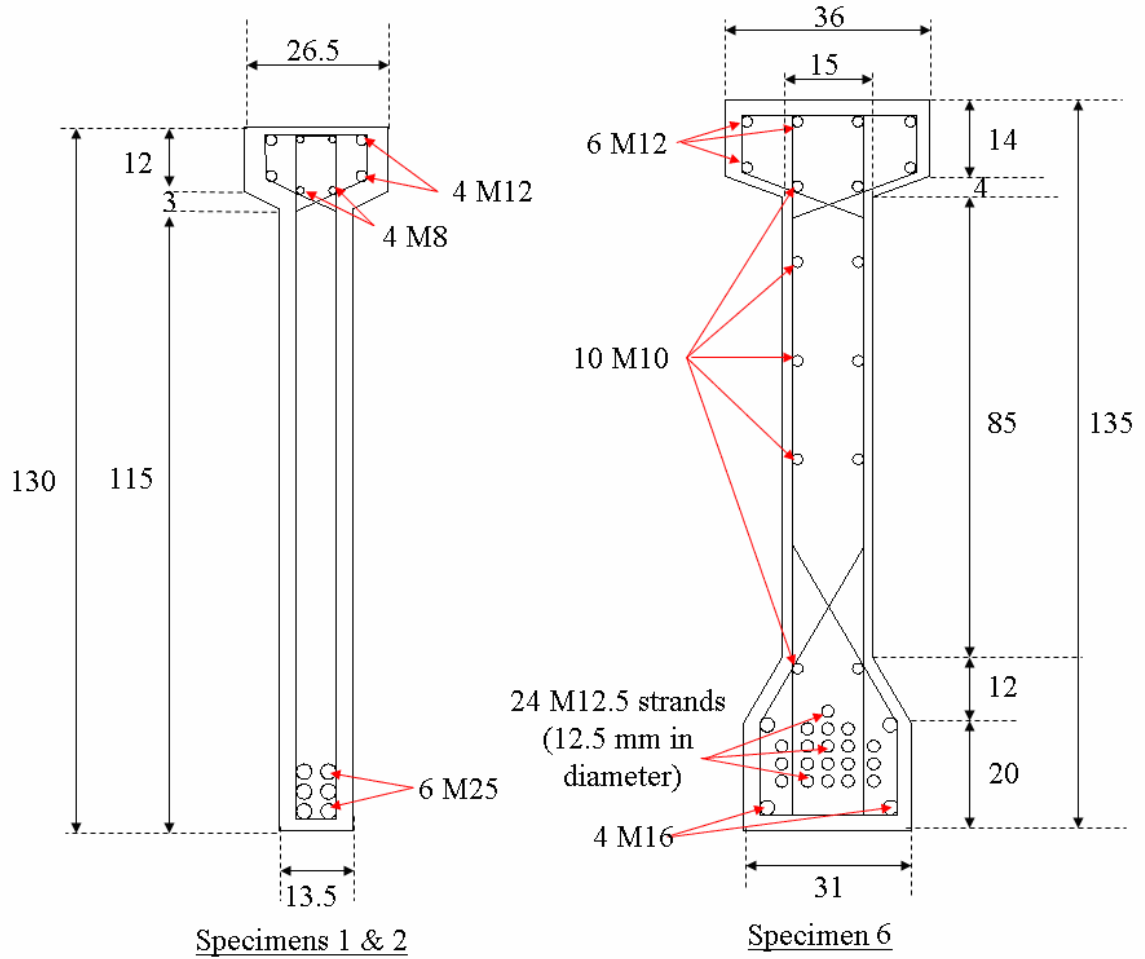


Figure 1.14– Cross-sectional details of the specimens tested by Konig and Pauli (1990)

specimens are introduced by emphasizing the individual parameters whose effects were examined. Then, the influence of each parameter will be discussed in the light of the experimental results obtained by Konig and Pauli (1990). The nominal dimensions and the flexural reinforcement of the test specimens are presented in Table 1.6 and the initial geometric imperfections are tabulated in Table 1.7. Finally, the experimental buckling loads and deformations of the specimens are given in Table 1.8.

Table 1.6 –Beams tested by Konig and Pauli (1990)

Specimen	Span Length, L (ft)	Top Flange Width, b (in)	Beam Height, h (in)	Tension Reinforcement	Compression Reinforcement
1	59	10.4	51.2	6 M25	4 M12 & 4 M8
2	59	10.2	51.2	6 M25	4 M12 & 4 M8
3	59	14.2	51.2	6 M25	4 M12 & 4 M8
4	59	10.2	51.2	6 M25	4 M25 & 4 M8
5	59	10.2	51.2	14 M12.5 strands	4 M12 & 2 M12.5
6	84	14.2	53.1	24 M12.5 strands	4 M12 & 4 M8

Table 1.7 – Midspan initial imperfections of the beams tested by  
Konig and Pauli (1990)

Specimen	Initial Sweep at Midheight, $u_o$ (in.)	Angle of twist, $\phi_o$ (radian %)
1	0.79	0
2	0.12	0.30
3	0.24	0.30
4	0.10	0.15
5	0.63	0.30
6	0.43	0.40

Table 1.8 – Loads, midspan deformations and rotations at failure of the beams  
tested by Konig and Pauli (1990)

Specimen	Critical Load, $P_{cr}$ (kips)	Mid-span Deformation (in.)		Midspan Angle of Rotation (%)
		Lateral Top	Vertical	
1	42.7	6.4	4.6	0.5
2	44.5	3.3	2.4	0
3	57.0	5.6	4.6	1.0
4	53.4	1.9	3.7	0
5	45.1	7.2	2.8	0
6	50.9	8.8	5.5	0

Specimens 1 and 2 had the base nominal dimensions, reinforcement and cross-sectional details. They only differed in the initial geometric imperfections. Specimen 3 was identical to the first two specimens, except the width of the top flange. The top flange of the third specimen was made stockier than the first two specimens by increasing the breadth from 10.4 in. (25 cm) to 14.2 in. (35 cm). Specimen 4 had heavier compression reinforcement than the first three beams. The M12 bars in the top flanges of the first three beams were replaced with M25 bars in the fourth specimen while keeping the nominal dimensions identical to the first two specimens. Specimen 5 was reinforced with prestressing strands instead of rebars to examine the influence of prestressing of reinforcement on the lateral stability of concrete beams. The M8 bars in the top flanges and the M25 bars in the bottom portions of the first four specimens (Figure 1.14) were replaced with M12.5 strands in the fifth specimen. Specimen 6 was tested to investigate the lateral stability of prestressed concrete beams with I-section to observe the influence of the cross-sectional shape on the stability.

Specimen 2 had a smaller initial lateral deformation, sweep, than the first specimen. Accordingly, the test results of the second specimen are closer to reflect the behavior of an initially-perfect beam with the base dimensions. Therefore, the results of each of the five specimens are compared to the experimental values of Specimen 2 (Figure 1.15) when discussing the influence of an individual parameter on the lateral stability of concrete beams.

Specimen 1 with the greater sweep (0.79 in. at mid-height of the mid-span section) failed at an applied load, 4 % lower than the buckling load of Specimen 2, whose sweep was measured as 0.12 in. Although the midspan sweep of one of the specimens

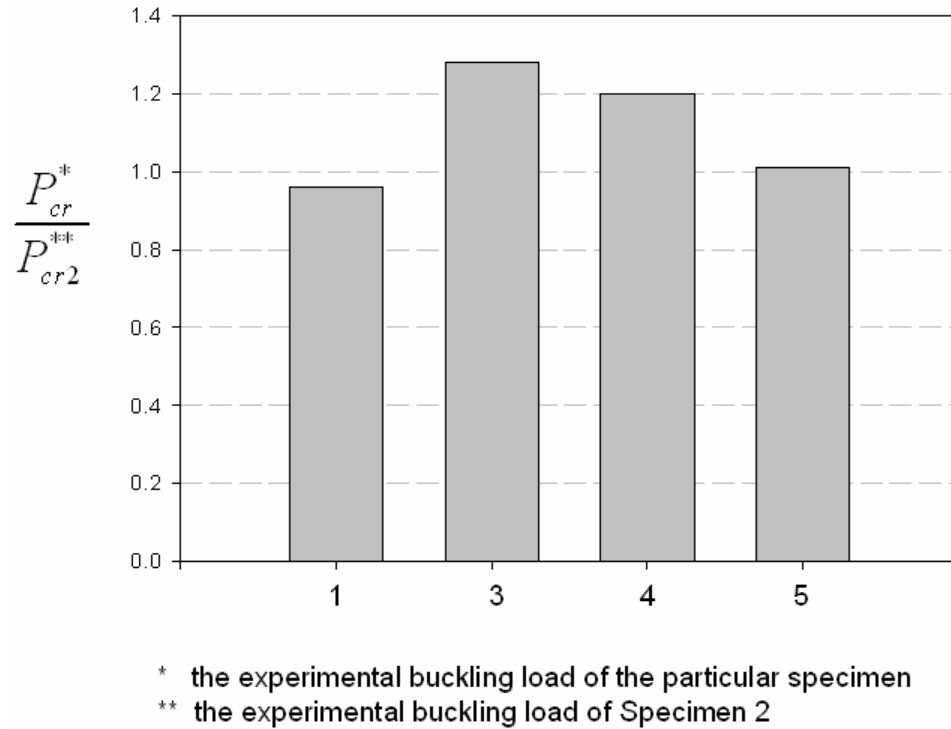


Figure 1.15 – Ratio of the buckling load of each specimen to the buckling load of Specimen 2

was almost seven times greater than the sweep of the other beam, the reduction in the buckling load was only 4 %, implying that the influence of the initial imperfections was not quite significant.

The loading and support conditions reported by Konig and Pauli (1990) suggests that the top flanges of the specimens were subjected to compressive stresses while the bottom portions were under tension in the tests. Specimen 3, which had a wider top flange than the first two beams, buckled under an applied load of 57 kips, which is 28 % greater than the buckling load of the second specimen. The significant increase in the failure load depicts the major stabilizing effect of a wider compression flange on the beam.

The test results of Specimen 4 indicated that the stabilizing effect of the compression reinforcement was two-fold. First, the buckling load increased to 53.4 kips, corresponding to an increase of 20 % with regard to the second specimen. Secondly, the lateral-top deflection of Specimen 4 at failure was smaller than the top deflections of the first three beams. Both the increase in the failure load and the decrease in the lateral-top deflection were bound up with the increase in the out-of-plane rigidity of the top flange. The M12 bars in the top flanges of the first three beams were placed 3.5 in. away from the weak axis of the section (Figure 1.14). Owing to the distance from the minor axis, the reinforcing bars significantly contributed to the lateral bending rigidity. The use of M25 bars in Specimen 4 in replacement of the M12 bars increased the resistance of the beam to lateral-torsional buckling by further constraining the top flange from deforming out of plane.

The buckling load of Specimen 5 was only 1.3 % greater than the buckling load of Specimen 2. Accordingly, Konig and Pauli (1990) concluded that the stabilizing effect of prestressing was not as pronounced as the effects of the top flange width and the compression reinforcement. However, the type of reinforcement was not the only difference between Specimen 5 and Specimen 2. Specimen 5 had a significantly larger sweep than Specimen 2. The buckling load of Specimen 5 might have been reduced by the major sweep, causing the experimental results not to reflect the actual degree of stabilization provided by prestressing. To evaluate the influence of prestressing on the lateral stability of concrete beams, more experimental results are needed.

Konig and Pauli (1990) used the loading mechanism illustrated in Figure 1.16 in their experiments. A water tank was connected to the beam at the one-third points of the



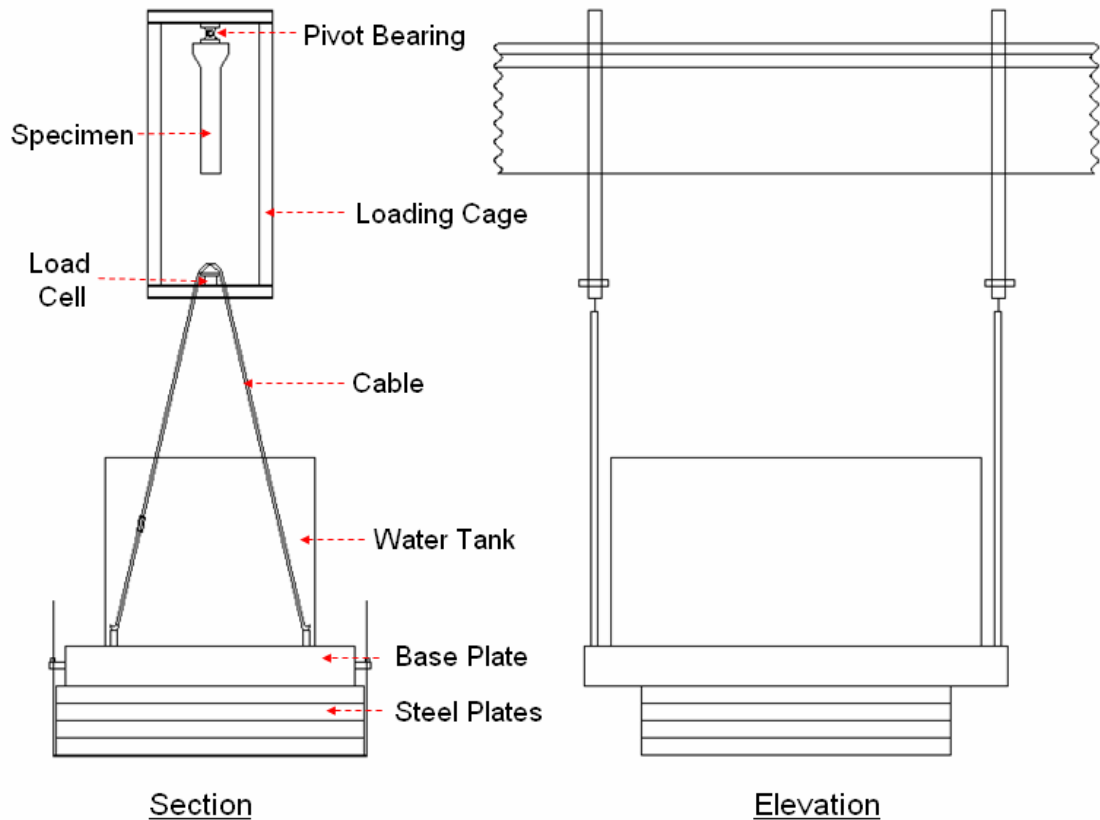


Figure 1.16 – Loading mechanism used by König and Pauli (1990)

span. Steel plates were attached to the tank. The use of steel plates in addition to the water tank reduced the need for excessive volumes of water in the tests and enabled the researchers to use a tank of smaller capacity to attain the buckling loads of the beams. The water tank was connected to a loading cage through cables. The loading cage transmitted the load to the top of the beam. A pivot bearing, joining the beam and the loading cage, provided the beam with the rotational freedom at the point of application of load.

The loading mechanism used by König and Pauli (1990) was clearly superior to the mechanisms used by Hansell and Winter (1959) and Sant and Bletzacker (1961). When introducing the loading mechanism used by Massey and Walter (1969), the

efficiency of dead weights, hung from the specimen, in minimizing the lateral-translational and rotational restraining forces at the loading point was discussed. Konig and Pauli (1990) also overcame the need for a spacious water tank in the setup by using steel plates. By considering the nature of the dead loads, the test results obtained by Konig and Pauli (1990) can be considered reliable to be used in the analytical studies.

The beams tested by Konig and Pauli (1990) were simply supported in and out of plane at the ends. The boundary conditions of a simply-supported beam are explained in the third chapter of the present text in detail. One of the conditions that need to be fulfilled to achieve the simple support conditions is the absence of a major restraint from the supports against the displacement in longitudinal direction. The lateral supports used by Konig and Pauli (1990) allowed the longitudinal displacements at the beam ends. The top flanges of the beams were supported laterally through ball-bearings. The bottommost portions of the beam ends were also supported in lateral direction to preserve the integrity of the support sections. Sliding pads were placed between the beam and the bottom supports. The ball bearings at the top and the sliding pads at the bottom minimized the longitudinal friction forces from the lateral supports and allow the ends to rotate in plane with no major restraint.

#### **1.4.2 Analytical Methods for Predicting Lateral Torsional Buckling**

One of the first investigations on the lateral stability of reinforced concrete beams was conducted by Marshall (1948). The analytical study aimed at developing critical load expressions for a laterally-unsupported beam under three different loading conditions:

1. Concentrated load at mid-span;
2. Uniformly distributed load throughout the span;

3. Equal and opposite bending moments at the beam ends;

Marshall (1948) obtained the critical load equations (1.1) and (1.2) for the loading cases 1 and 2, respectively. Equation (1.3) gives the critical moment of a beam subjected to the equal and opposite end moments (loading case 3):

$$P_{cr} = \frac{16.93}{L^2} \cdot \sqrt{B \cdot (GC)} \quad (1.1)$$

$$w_{cr} = \frac{28.6}{L^3} \cdot \sqrt{B \cdot (GC)} \quad (1.2)$$

$$M_{cr} = \frac{8.47}{L} \cdot \sqrt{B \cdot (GC)} \quad (1.3)$$

where  $P_{cr}$ ,  $w_{cr}$  and  $M_{cr}$  are the critical concentrated load, the critical unit load and the critical moment of a laterally unsupported beam, respectively;  $L$  is the unbraced length of the beam;  $B$  and  $GC$  are the out-of-plane flexural and the torsional rigidities of the beam, respectively. Marshall (1948) proposed the use of the following lateral flexural and torsional rigidity expressions for rectangular reinforced concrete beams:

$$B = 2.5 \cdot 10^6 \cdot \frac{b^3 \cdot d}{12} \quad (1.4)$$

$$GC = 0.9 \cdot 10^6 \cdot \frac{b^3 \cdot d}{3} \quad (1.5)$$

where  $b$  and  $d$  are the width and the effective depth of the beam, respectively. The multipliers  $2.5 \times 10^6$  and  $0.9 \times 10^6$  in Equations (1.4) and (1.5) are the modulus of elasticity and the modulus of rigidity of concrete, respectively. Marshall (1948) assumed the

modulus of elasticity and the modulus of rigidity to be constant for the concrete fibers throughout the length and depth of the beam at the time of buckling. This assumption disregards the inelastic lateral-torsional buckling behavior of reinforced concrete beams. Figure 1.17 illustrates the stress-strain curve of a normal-strength concrete. The moduli of elasticity corresponding to different stress values are shown on the curve. The first portion of the curve up to the proportional limit stress ( $0.4f_c'$  for normal-strength concrete) is linear. The slope of this line represents the initial tangent modulus of elasticity ( $E_{it}$ ), and it is calculated according to Equation (1.6), given in ACI 318-05 (2005) for normal-weight concrete.

$$E_{it} = 57000 \cdot \sqrt{f_c'} \quad (1.6)$$

where  $E_{it}$  and  $f_c'$  are the initial tangent modulus of elasticity and the compressive strength of concrete in psi, respectively.

If all the compression fibers throughout the depth and length of a beam are stressed below the proportional limit (elastic limit in many cases) of concrete at the instant of buckling, the beam experiences elastic lateral-torsional buckling. In the case of elastic buckling, the initial tangent modulus of elasticity of concrete provides a good estimate for the rigidity of all the compression fibers in the beam. The constant modulus of elasticity value,  $2.5 \times 10^6$ , proposed by Marshall (1948) corresponds to a concrete compressive strength of 1920 psi according to Equation (1.6). 1920 psi is a low concrete strength compared to the compressive strength values encountered in today's practice. Therefore, the constant modulus of elasticity value proposed by Marshall (1948) will

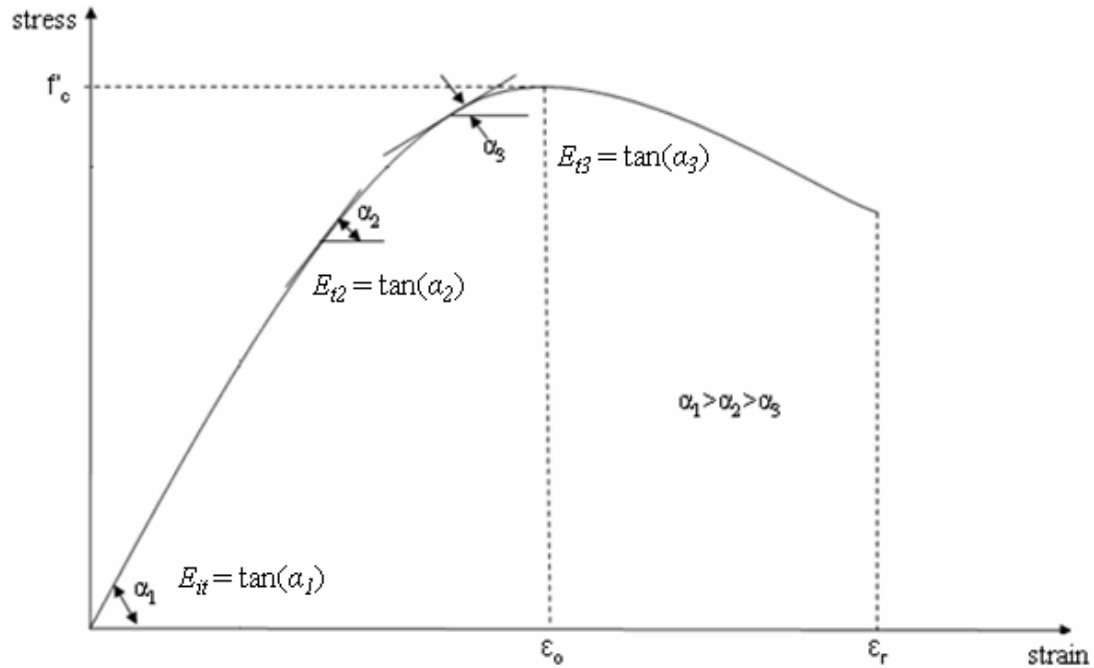


Figure 1.17 – Stress-strain curve of normal-strength concrete and the tangent moduli of elasticity at different stress levels (from Nawy 2005)

result in low estimates when computing the load associated with the elastic lateral torsional buckling of a reinforced concrete beam.

In the case of inelastic lateral-torsional buckling, however, some compression fibers of the beam are stressed beyond the proportional limit of concrete at the time of buckling. Figure 1.17 indicates that the slope of the stress-strain curve reduces as the stress and strain increase beyond the proportional limit [ $\tan(\alpha_1) > \tan(\alpha_2) > \tan(\alpha_3)$ ]. Particularly, if the concrete is stressed to more than  $0.7f'_c$ , it loses its rigidity to a major extent and the modulus drops drastically vanishing at ultimate stress. Depending on the stresses reached at the initiation of buckling, the modulus of elasticity values for highly-stressed fibers at the outermost parts of the compression zone can be significantly lower than the initial tangent modulus of elasticity of concrete ( $E_{it} > E_{t2} > E_{t3}$ ), reducing the overall modulus of the beam used in the evaluation of the lateral bending rigidity.

To summarize, the modulus of elasticity value used in the calculation of the flexural rigidity about the minor axis varies significantly along the length and depth of the beam at the instant of buckling. Therefore, a constant value of the elastic modulus should not be used when computing the lateral flexural rigidity.

The multiplier  $0.9 \times 10^6$  in Equation (1.5) is the assumed modulus of rigidity value of the concrete. By using a Poisson's ratio of 0.3, this value can be calculated from Equation (1.7):

$$G = \frac{E}{2 \cdot (1 + \nu)} \quad (1.7)$$

where  $E$  and  $G$  are the modulus of elasticity and the modulus of rigidity, respectively;  $\nu$  is the Poisson's ratio. Similar to the elastic modulus term in the lateral bending rigidity expression, Marshall (1948) proposed the use of a constant modulus of rigidity value in the torsional rigidity calculations, which disregards the inelastic material behavior of concrete and the variation of the modulus of rigidity along the length and depth of the beam at the time of buckling.

The use of the effective depth  $d$  in Equations (1.4) and (1.5) suggests that Marshall (1948) assumed that all fibers of the beam from the compression face to the centroid of the tension reinforcement contribute to the resistance of the beam against lateral-torsional buckling. Only the portion of the beam below the centroid of the tension reinforcement is neglected in the critical load calculations. Using  $d$  in the critical load calculations is based on a very general assumption that the concrete above the centroid of the tension reinforcement remains uncracked until buckling. Depending on the strain distribution in the tension zone of the beam, the flexural cracks may propagate upward

close to the compression zone before buckling, rendering the cracked zone ineffective in resisting buckling. Particularly, in the case of inelastic lateral-torsional buckling, many tension fibers in the beam reach strains higher than the cracking strain of concrete in tension. Therefore, extension of the flexural cracks in the tension zone should be well-established to determine the portion of the beam providing rigidity against buckling. The use of  $d$  in the critical load calculations may overestimate the portion of the beam effective in resisting lateral buckling at the time of failure.

Marshall (1948) used uncracked, elastic and homogeneous material assumption in the critical load calculations. Consequently, the rigidity expressions given in the study do not reflect the true behavior of reinforced concrete beams, especially if the buckling takes place close to the ultimate flexural load levels. Marshall (1948) also inferred that the stability criteria based on  $L/b$  ratio only is not factual and the lateral stability of a beam should be evaluated based on  $d/b$  ratio as well as the  $L/b$  ratio. The study included the stability analysis of both singly- and doubly-reinforced concrete beams. Marshall (1948) did not investigate the effects of initial geometric imperfections on the lateral stability of reinforced concrete beams.

Hansell and Winter (1959) conducted an analytical study to investigate the lateral stability of an initially perfect rectangular reinforced concrete beam. In their study, Hansell and Winter (1959) found that the secant modulus of elasticity corresponding to the extreme compression fiber strain at the instant of buckling reflects the material behavior of concrete in the compression zone, and therefore, the secant modulus of elasticity should be used as the material rigidity term when evaluating the critical moments of rectangular reinforced concrete beams. Secant modulus of elasticity is the

slope of the line on the stress-strain curve connecting the origin to the point corresponding to the extreme compression fiber strain (Figure 1.18). The modulus of rigidity used in the assessment of the torsional rigidity of a beam is calculated from the secant modulus of elasticity according to Equation 1.7.

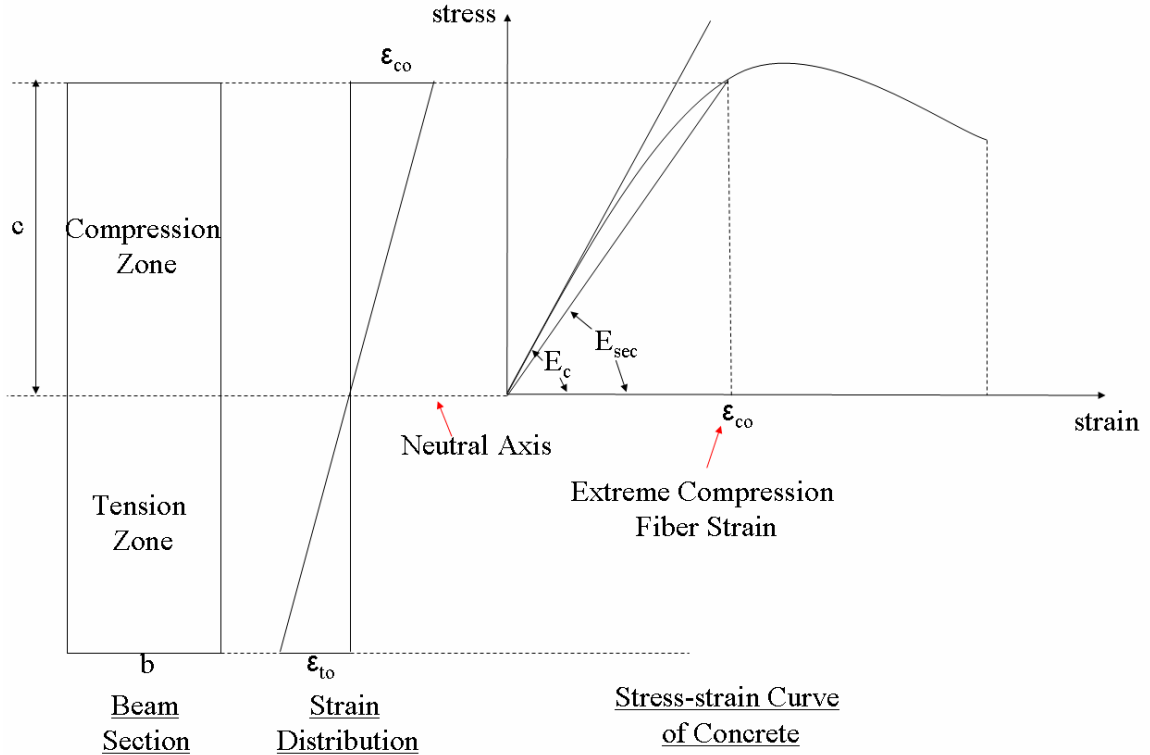


Figure 1.18 – Secant modulus of elasticity corresponding to the extreme compression fiber strain

Hansell and Winter (1959) conservatively assumed that the concrete below the neutral axis is fully cracked at the time of buckling and its contribution to the resistance to lateral-torsional buckling should be disregarded. By only taking the compression zone of the section into account, Hansell and Winter (1959) obtained the following lateral bending and torsional rigidity expressions for rectangular reinforced concrete beams:



$$B = E_{\text{sec}} \cdot \frac{b^3 \cdot c}{12} \quad (1.8)$$

$$GC = \frac{E_{\text{sec}}}{2 \cdot (1 + \nu)} \cdot \left[ \frac{b^3 \cdot c}{3} \cdot \left( 1 - 0.35 \cdot \frac{b}{d} \right)^2 \right] \quad (1.9)$$

where  $c$  is the neutral axis depth,  $b$  is the beam width,  $d$  is the effective depth to the centroid of reinforcement and  $E_{\text{sec}}$  is the secant modulus of elasticity corresponding to the extreme compression fiber strain at the instant of buckling.

The use of the neutral axis depth in the equations is appropriate in the case of inelastic lateral-torsional buckling. When a beam fails in inelastic buckling, many portions along the depth of the tension zone exceed the cracking strain of concrete. Hence, the flexural cracks in the tension zone propagate towards the compression zone rendering an important portion of tension zone ineffective at the time of buckling. On the other hand, a considerable portion of the tension zone can be still effective in resisting the instability failure in the case of elastic lateral-torsional buckling, particularly if the buckling takes place at the early stages of loading when only some fibers in the outermost portion of the tension zone reach the cracking strain of concrete. Thus, use of the neutral-axis depth results in low buckling load estimates for slender concrete beams subject to elastic lateral-torsional buckling.

Another noteworthy detail in the rigidity expressions proposed by Hansell and Winter (1959) is the use of a constant  $c$  value for different sections along the span. When the in-plane bending moment is constant throughout the span of a beam, the neutral axis depth ( $c$ ) of each section along the span is the same. Nevertheless, the neutral axis depths of different cross-sections of a beam are different in the case of non-uniform in-plane

bending moment along the span. For design purposes, Hansell and Winter (1959) proposed the use of a single  $c$  value for the entire beam independent of the in-plane bending moment distribution in the span. Hansell and Winter (1959) recommended the use of the rigidity values corresponding to the beam section with maximum bending moment along the span (for example the midspan section of a beam subjected to a concentrated load at midspan), since the rigidities in a concrete beam are minimum at the maximum moment locations.

Siev (1960) identified three different states of a reinforced concrete beam along the loading history; uncracked elastic, cracked elastic and cracked plastic states. A different lateral-bending rigidity expression was developed for each state. Nonetheless, Siev (1960) advocated the use of a single torsional rigidity expression for reinforced concrete beams independent of the state of the beam at the time of buckling.

In his study, Siev (1960) analyzed a beam simply supported in and out of plane at the ends and subjected to a concentrated load at mid-span. Under the specified loading and support conditions, the largest in-plane bending moments occur at mid-span of the beam, while the end portions of the beam are subjected to minor bending moments. Therefore, few or no flexural cracks form in the tension zone of the beam near the end supports. Since the largest torsional moments are resisted by the end portions of the beam, Siev (1960) included the contribution of the tension zone to the torsional rigidity and proposed the following rigidity expression:

$$GC = \frac{E_c}{2 \cdot (1 + \nu)} \cdot \left[ \frac{b^3 \cdot h}{3} \cdot \left( 1 - 0.63 \cdot \frac{b}{h} \right) \right] \quad (1.10)$$

where  $h$  is the overall depth of the beam and  $\nu$  is the Poisson's ratio.

In the uncracked state, Siev (1960) considered the reinforced concrete as a homogeneous material and disregarded the contribution of the flexural and shear reinforcement to the lateral-flexural rigidity. The uncracked flexural rigidity ( $B_u$ ) is given by Equation (1.11):

$$B_u = \frac{b^3 \cdot h}{12} \cdot E_c \quad (1.11)$$

The second state of a reinforced concrete beam was identified as the cracked elastic state. In the cracked elastic state, flexural cracks form and propagate in the tension zone of the beam while the concrete in the compression zone is still linearly elastic. Siev (1960) approximated the stress-strain curve of concrete into a linearly elastic and a plastic portion. The lateral-bending rigidity of the beam in the cracked elastic state was obtained by dividing the out-of-plane bending moment to the out-of-plane bending curvature induced by the moment. The curvature of the beam was determined from the stresses and strains in the cross-section. Siev (1960) considered the fact that the neutral axis of a cross-section of the beam deviates from horizontal in the presence of biaxial moments, namely the in-plane and out-of-plane bending moments. Based on a linear stress-strain relationship in the compression zone of the section and a rotated neutral axis due to the presence of lateral bending moments in addition to the major-axis bending moments, Siev (1960) developed the following lateral-flexural rigidity expression for the cracked elastic state of the beam:

$$B_c = \frac{M}{\sigma_c} \cdot \frac{c \cdot E_c}{a} \cdot \left( \frac{b^2}{6 \cdot c} + \frac{b_o^2}{4 \cdot (d - c)} \right) \quad (1.12)$$

where  $M$  is the in-plane bending moment;  $\sigma_c$  is the extreme compression fiber stress corresponding to  $M$ ;  $b_o$  is the horizontal distance between the centroids of the reinforcing bars and  $a$  is the internal moment arm of the section. As a result of assuming a triangular stress distribution in the compression zone of the section,  $a$  is equal to  $d-c/3$ .

The lateral-flexural rigidity in the cracked elastic state ( $B_c$ ) is a function of the in-plane bending moment ( $M$ ) the extreme compression stress ( $\sigma_c$ ) and the neutral axis depth ( $c$ ) corresponding to  $M$ . Therefore, the rigidity value at the time of buckling can only be calculated by knowing the critical moment and the stress and strain distributions in the section corresponding to the critical moment. The evaluation of the critical moment based on the rigidity expressions given by Siev (1960) requires an iterative approach. First, an initial value of  $M$  is assumed and the lateral-flexural rigidity corresponding to the initial value of  $M$  is calculated. Subsequently, the critical moment is computed from the calculated lateral-flexural and torsional rigidity values, using Equation (1.13).

$$M_{cr} = \frac{C_1}{C_2 \cdot L} \cdot \sqrt{B \cdot C} \quad (1.13)$$

where  $C_1$  and  $C_2$  are the constants corresponding to the loading and support conditions of the beam, respectively. The iterations are then continued until the moment value converges.

Finally, Siev (1960) proposed a lateral-flexural rigidity expression for the cracked plastic state of the beam. In the plastic state, some fibers in the compression zone of the beam are strained beyond the elastic limit of concrete (Figure 1.19). Since an elastic-perfectly plastic stress-strain behavior was assumed for concrete, a uniform stress

distribution is reached within the outermost portion of the compression zone. Siev (1960) derived the following lateral-flexural rigidity expression for the plastic state of the beam:

$$B_p = \frac{b^2 \cdot M}{12 \cdot \epsilon_c \cdot a} \cdot \frac{c_p + c_e}{c_p + \frac{c_e}{2}} \quad (1.14)$$

where  $c_p$  and  $c_e$  are the depths of the plastic and elastic portions of the compression zone, respectively (Figure 1.19);  $\epsilon_c$  is the strain at the extreme compression fibers.

Sant and Bletzacker (1961) also carried out an analytical study on the lateral torsional buckling of rectangular reinforced concrete beams. The following lateral-flexural and torsional rigidity expressions were proposed:

$$B = E_r \cdot \frac{b^3 \cdot d}{12} \quad (1.15)$$

$$GC = \frac{E_r}{2 \cdot (1 + \nu)} \cdot \frac{b^3 \cdot d}{3} \quad (1.16)$$

where  $E_r$  is the reduced modulus of elasticity of concrete corresponding to the extreme compression fiber strain.

Equations (1.15) and (1.16) are different from the rigidity expressions adopted by Hansell and Winter (1959) mainly in two aspects. First, Sant and Bletzacker (1961) assumed that only the concrete above the centroid of the tension reinforcement contributes to the resistance of a beam against buckling. Therefore, the effective depth ( $d$ ) is used in the rigidity expressions instead of the neutral axis depth ( $c$ ) presuming that the concrete below the centroid of the tension reinforcement is ineffective at the time of

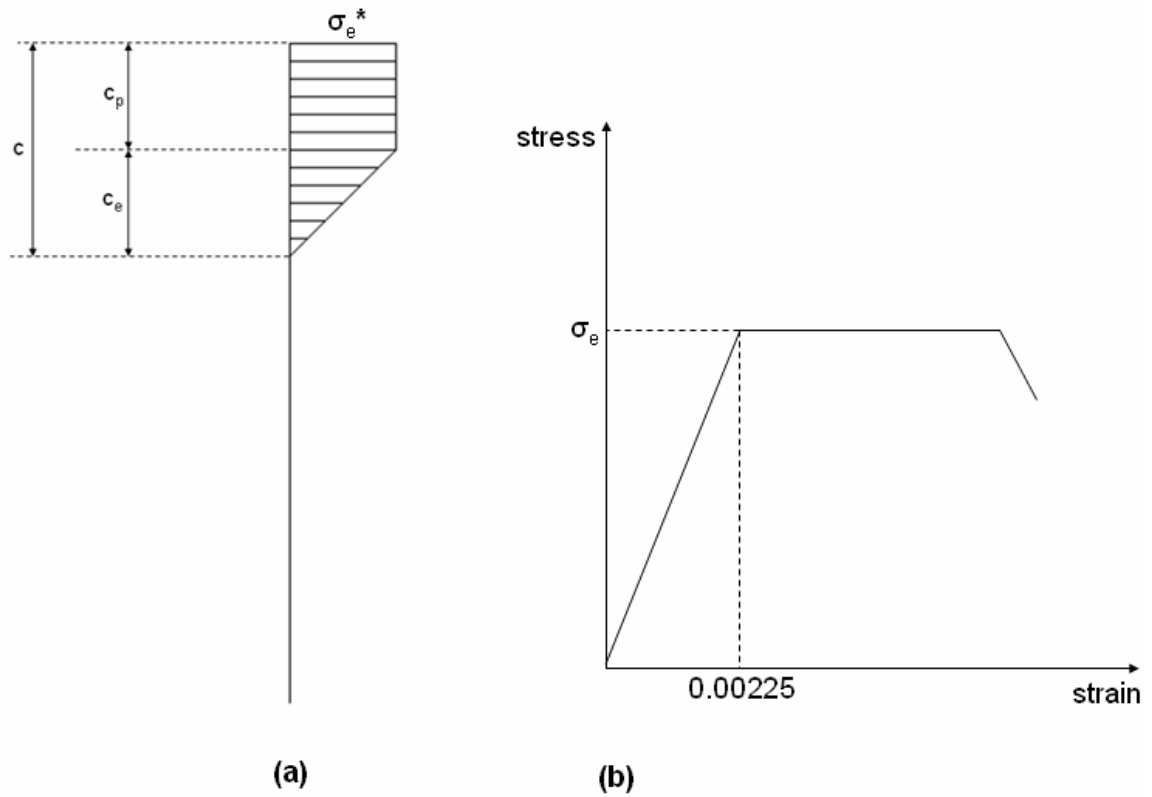


Figure 1.19 – (a) Stress distribution in the compression zone of the beam section in the plastic state; (b) Stress-strain curve of concrete; assumed by Siev (1960)

(\*  $\sigma_e$  = elastic limit stress)

buckling due to cracking. The portion of a beam effective in resisting lateral torsional buckling is determined according to the strain distribution in the section and in the span of the beam at the onset of buckling. The fibers in the tension zone strained beyond the cracking strain of concrete are not taken into consideration in critical load calculations. According to the moment levels reached prior to buckling and the cross-sectional and material properties of the beam, the use of  $c$  or  $d$  or a value between them might be more appropriate to account for the effective portion of the beam in buckling resistance.

However, the use of  $c$  in critical load calculations results in lower buckling load estimates than the use of  $d$ , proposed by Sant and Bletzacker (1961).

In addition, Sant and Bletzacker (1961) argued that the reduced modulus of elasticity reflects the material rigidity of concrete at the time of buckling. The reduced modulus of elasticity expression used by Sant and Bletzacker was first derived by Considère (1891) and Engesser (1895) and later supported by the experimental and analytical studies on inelastic column buckling by Von Karman (1910). The application of the reduced modulus theory to lateral torsional buckling is briefly explained in the following discussion.

In the double modulus theory for lateral-torsional buckling, the strain distributions along the depth as well as the width of the midspan section of a beam at the time of buckling are established as in Figure 1.20. For simplification, the beam is assumed not to experience out-of-plane bending deformations prior to buckling. Accordingly, the beam is only strained as a result of the in-plane bending deformations at the onset of buckling. When the beam loses its stability and bends out of plane, the fibers in the concave half of the section are compressed further. On the other hand, the out-of-plane deformations after buckling introduce tensile stresses and strains to the fibers in the convex half of the beam. In other words, the compressive strains resulting from the in-plane and out-of-plane bending moments add up in the concave side of the compression zone, while the tensile strains caused by the lateral bending cancel the compressive strains resulting from the vertical bending in the convex side of the compression zone of the section. The formation of the tensile strains in the compression zone of the beam is named as strain reversals. As shown in Figure 1.20, the further loading of the fibers in the concave side of the section

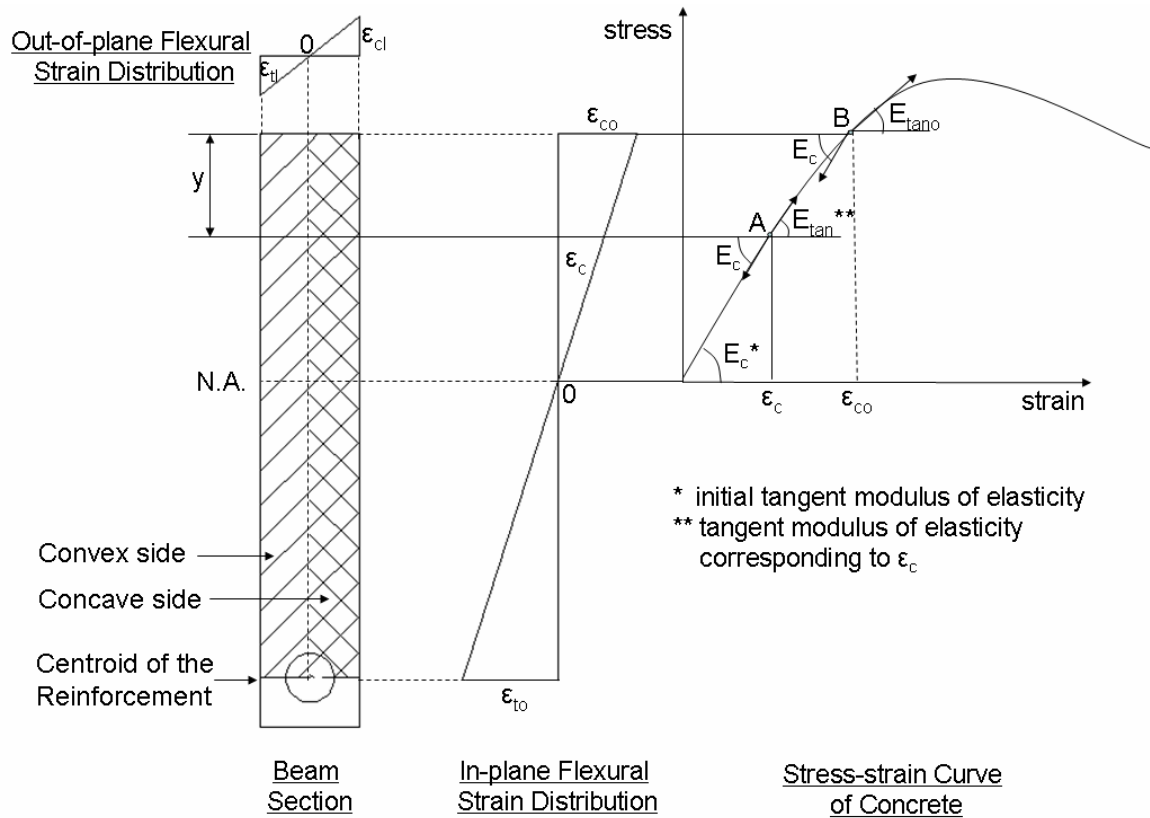


Figure 1.20 – Strain distribution at midspan section and the corresponding reduced modulus of elasticity

takes place along the line tangent to the curve at point A. On the other hand, the unloading of the fibers in the convex side takes place along a line parallel to the initial straight portion of the stress-strain curve. Therefore, the modulus of elasticity of the loading fibers is the tangent modulus of elasticity,  $E_{tan}$  corresponding to the compressive strain of the fibers at the onset of buckling, while the modulus of elasticity valid for the unloading fibers is the initial tangent modulus of elasticity of concrete,  $E_c$ .

The reduced modulus (double modulus) theory is based on the presumption that the load increase in the beam due to additional compressive strains in the concave side of the beam is equal to the decrease in the load due to tensile strains developed in the



convex side of the beam after buckling. Thus, the load-carrying capacity of the beam is constant during buckling. Based on the constant load assumption, the following expression is developed for the reduced modulus of elasticity:

$$E_r = \frac{4 \cdot E_c \cdot E_{\tan}}{\left(\sqrt{E_c} + \sqrt{E_{\tan}}\right)^2} \quad (1.17)$$

Since the tangent modulus of elasticity depends on the strain of the fibers at the onset of buckling, the reduced modulus of elasticity is a function of the strain in the fibers at the initiation of buckling. Equation (1.17) was developed for the buckling of a column, subjected to equal concentrated loads at the ends. In column buckling, the axial strain is assumed to be constant across the width and the length of the column. Therefore, all fibers in the concave side of the column have the same tangent modulus of elasticity at the onset of buckling. On the other hand, the strains resulting from the in-plane bending vary throughout the depth and the length of a beam, subjected to a concentrated load at mid-span. Consequently, the tangent and reduced moduli of elasticity change along the depth and the length of the beam. Therefore, the use of a constant tangent modulus of elasticity along the depth of the concave half of the compression zone does not actually reflect the material rigidity of the beam at the time of buckling. However, the rigidity and critical load calculations considering the variations in the reduced modulus of elasticity in the section and in the span of the beam are not practical and quite time-consuming. Thus, Sant and Bletzacker (1961) proposed the use of the smallest reduced modulus of elasticity corresponding to the most-strained compression fibers in the beam, which are the extreme compression fibers of the midspan section, in the case of midspan loading. As indicated in Figure 1.20, the smallest reduced modulus of elasticity corresponds to the

outermost side of the compression zone of the midspan section because the slope of the loading line (the tangent modulus of elasticity) reduces as the strain in the fibers increases.

The double modulus theory makes use of the assumption that strain reversals take place in the convex part of the compression zone of the beam. The strain measurements taken by Sant and Bletzacker (1961) validated the presence of the strain reversals, i.e. the formation of the additional tensile strains, in the convex side of the compression zone after buckling.

In contrast to the previous researchers, Massey (1967) included the contribution of the longitudinal reinforcement to the lateral-bending and torsional rigidities and the contribution of the shear reinforcement to the torsional rigidity of a reinforced concrete beam and proposed the Equations (1.18) and (1.19):

$$B = E_{\text{sec}} \cdot \frac{b^3 \cdot c}{12} + E_s \cdot \Sigma I_{sy} \quad (1.18)$$

$$GC = G'_c \cdot \beta \cdot b^3 \cdot h + \frac{1}{3} \cdot (G_s - G'_c) \cdot \Sigma b_s^3 \cdot t_s + \frac{\gamma \cdot b_l^2 \cdot d_l \cdot A_t \cdot E_s}{2 \cdot \sqrt{2} \cdot s} \quad (1.19)$$

where  $h$  is the height of the section;  $\Sigma I_{sy}$  is the moment of inertia of the longitudinal steel about the minor axis of the section;  $b_s$  and  $t_s$  are the width and the thickness of the longitudinal reinforcement layer, respectively, as illustrated in Figure 1.21;  $\gamma$  is a constant defined by Cowan (1953);  $b_l$  and  $d_l$  are the breadth and the depth of the cross-sectional area enclosed by a closed stirrup, respectively (Figure 1.21);  $s$  is the spacing of the stirrups;  $A_o$  is the cross-sectional area of one leg of the stirrup;  $\beta$  is the coefficient for St. Venant's torsional constant;  $E_s$  and  $G_s$  are the modulus of elasticity and the modulus of

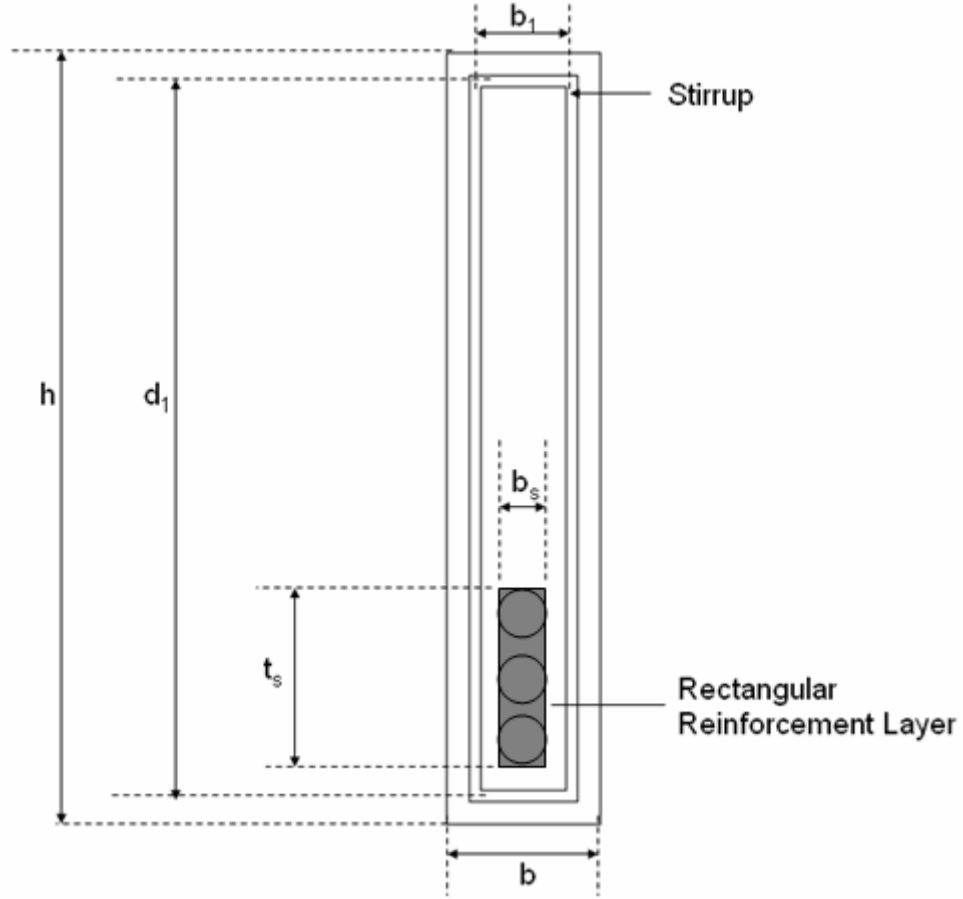


Figure 1.21 – Definition of the variables in the expressions proposed by Massey (1967)

rigidity of steel, respectively;  $G'_c$  is the reduced modulus of rigidity of concrete, calculated according to Equation (1.20):

$$G'_c = G_c \cdot \frac{E_{sec}}{E_c} \quad (1.20)$$

where  $E_c$  and  $G_c$  are the modulus of elasticity and the modulus of rigidity of concrete, respectively.

Massey (1967) modified the lateral-bending rigidity expression developed by Hansell and Winter (1959) by adding the second term,  $E_s \cdot \Sigma I_{sy}$ , corresponding to the out-

of-plane bending resistance provided by the longitudinal reinforcement. According to Equation (1.18), the contribution of the longitudinal reinforcement is only of concern if the lateral-torsional buckling takes place prior to the yielding of the flexural reinforcement. When the steel yields, its modulus of elasticity becomes zero and the second term vanishes. After yielding of the flexural reinforcement, only the uncracked concrete above the neutral axis provides the out-of-plane flexural resistance.

According to Massey (1967), the torsional rigidity of a reinforced concrete beam is calculated by the summation of the three different rigidity terms given in Equation (1.19). The first two terms correspond to the contributions of the concrete and the flexural reinforcement, respectively. The rectangular concrete section and the thin-walled rectangular reinforcement layer (the gray area in Figure 1.21), consisting of the longitudinal reinforcing bars, are considered as the two main components of the non-homogeneous concrete beam. The last term, on the other hand, is the contribution of the shear reinforcement and is taken into account only if the stirrups are closed.

The inelastic behavior of the concrete is taken into consideration by the use of the secant modulus of elasticity and the reduced modulus of rigidity in the lateral-flexural and torsional rigidity expressions, respectively. Similar to Equation (1.18), yielding of the longitudinal reinforcement nullifies its contribution to the torsional rigidity of the beam.

Stiglat (1991) investigated the agreement of the critical moment predictions based on an approximate method proposed by Stiglat (1971) with the experimental results obtained by König and Pauli (1990). The approximate method suggests that the critical moment calculated for an elastic and uncracked concrete beam should be modified using the stresses at the extreme compression fibers at the onset of buckling to account for the

inelastic material properties. To begin with, an initial critical moment value is calculated, neglecting the inelastic material properties of concrete. The following initial critical moment expressions were presented for a simply-supported beam with three different loading conditions: uniformly-distributed load along the span (Equation 1.21), a single concentrated load at mid-span (Equation 1.22) and equal concentrated loads at one-third points of the span (Equation 1.23).

$$M_{cri} = \frac{3.54}{L} \cdot \left( 1 - 1.44 \cdot \frac{e}{L} \cdot \sqrt{\frac{2.5 \cdot I_y}{J}} \right) \cdot \sqrt{E_c \cdot G_c \cdot I_y \cdot J \cdot \frac{I_x - I_y}{I_x}} \quad (1.21)$$

$$M_{cri} = \frac{4.23}{L} \cdot \left( 1 - 1.74 \cdot \frac{e}{L} \cdot \sqrt{\frac{2.5 \cdot I_y}{J}} \right) \cdot \sqrt{E_c \cdot G_c \cdot I_y \cdot J \cdot \frac{I_x - I_y}{I_x}} \quad (1.22)$$

$$M_{cri} = \frac{3.25}{L} \cdot \left( 1 - 1.44 \cdot \frac{e}{L} \cdot \sqrt{\frac{2.5 \cdot I_y}{J}} \right) \cdot \sqrt{E_c \cdot G_c \cdot I_y \cdot J \cdot \frac{I_x - I_y}{I_x}} \quad (1.23)$$

where  $M_{cri}$  is the initial (uncorrected) critical moment;  $I_x$  and  $I_y$  are the moments of inertia about the major and minor axes, respectively;  $J$  is the torsional constant;  $L$  is the unbraced length of the beam;  $e$  is the initial vertical distance of the load from the shear center of the beam section.

The terms in the parenthesis in each equation correspond to the stabilizing or destabilizing effect of the vertical location of the load with respect to the shear center. Figure 1.22 illustrates the deflected and undeflected configurations of a beam with a concentrated load, applied at the top, at the shear center and at the bottom of the cross-section. In all three cases, the line of action of the applied load passes through the shear center prior to torsional rotations. When the beam experiences torsional rotations, the line

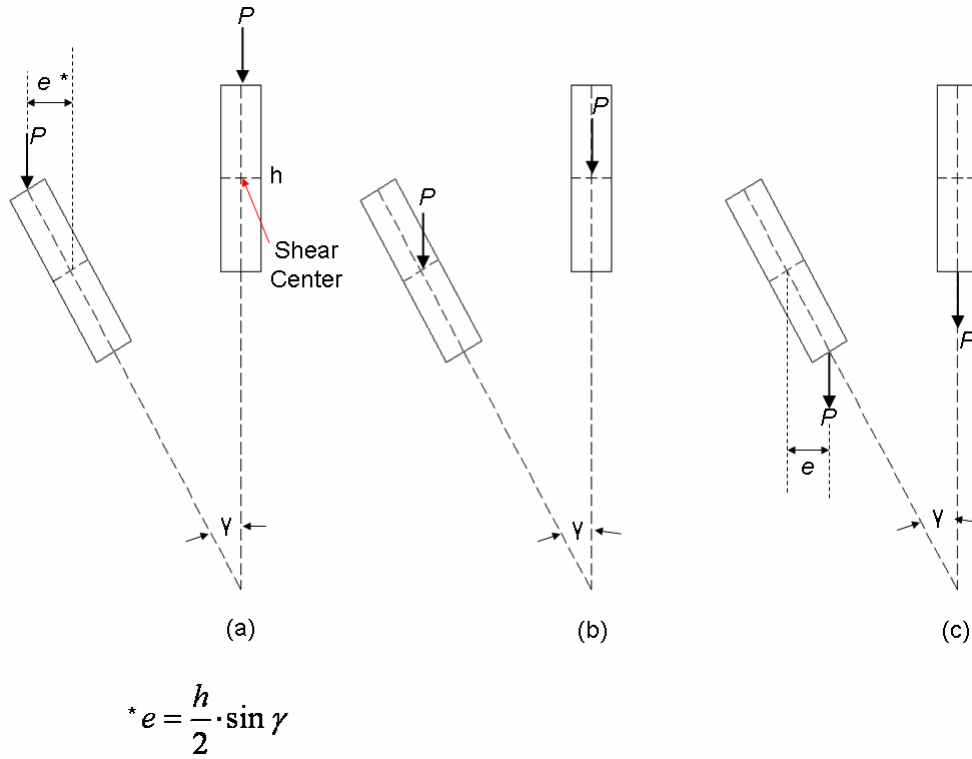


Figure 1.22 – Effect of the vertical location of the applied load with respect to the shear center of beam section

of action of the load continues to pass through the shear center in case (b). In cases (a) and (c), on the other hand, torsional rotations in the beam render the applied load laterally eccentric with respect to the shear center. A load acting above the shear center creates torsional moments, in the same direction as the existing torsional rotations due to instability. Therefore, the applied load increases the rotations in the beam, having a destabilizing effect. On the contrary, the torsional moments induced by the load applied below the shear center oppose the torsional rotations due to instability. Consequently, a load acting below the shear center has a stabilizing effect on the beam.

In Equations (1.21) - (1.23), the term “ $e$ ” is taken positive, when the load acts above the shear center. For a positive value of  $e$ , the expression in the parenthesis is less than unity, so the critical moment is reduced due to the destabilizing effect of the load.

When the load acts below the shear center, on the other hand,  $e$  is negative, increasing the buckling moment in account for the stabilizing influence of the applied load in the deflected configuration of the beam.

Stiglat (1991) recommended using a value of 60 % of the uncracked torsional constant of the beam section in Equations (1.21) - (1.23). Using reduced values for the torsional constant takes into consideration the zones in the beam which are already cracked at the onset of buckling.

Next, the critical moment calculated based on the elastic material properties should be corrected for the material nonlinearities of concrete. The correction is done using the comparative slenderness parameters. First, the stress at the extreme compression surface of the most-stressed beam section (for instance, the midspan section in the case of a concentrated load at midspan) is calculated according to Equation (1.24):

$$\sigma_{cri} = M_{cri} \cdot \frac{e_o}{I_x} \quad (1.24)$$

where  $\sigma_{cri}$  is the stress corresponding to the extreme compression fibers of the most-stressed section along the span;  $e_o$  is the vertical distance of the outermost compression fibers from the centroid of the section. The comparative slenderness parameter is obtained using  $\sigma_{cri}$  in Equation (1.25):

$$\lambda_v = \pi \cdot \sqrt{\frac{E_c}{\sigma_{cri}}} \quad (1.25)$$

where  $\lambda_v$  is the comparative slenderness parameter. The slenderness parameter, defined by Stiglat (1991), is a function of the modulus of elasticity of concrete and the maximum

compressive stress in the beam. The initial critical moment, calculated with the modulus of elasticity and modulus of rigidity corresponding to the initial portion of the stress-strain curve of concrete below the proportional limit stress, is corrected using  $\lambda_v$  to account for the reduced modulus of elasticity, valid for the fibers stressed beyond the elastic limit of concrete. Later, an equivalent stress value,  $\sigma_T$ , is obtained from the comparative slenderness parameter using tables presented by Stiglat (1991). Finally, the critical moment of the beam is calculated by correcting the initial critical moment according to Equation (1.26):

$$M_{cr} = M_{cri} \cdot \frac{\sigma_T}{\sigma_{cri}} \quad (1.26)$$

Stiglat (1991) reported that the analytical critical moment values according to the proposed approximate method were in close agreement with the experimental results obtained by Konig and Pauli (1990). Moreover, Stiglat (1991) stated that the use of the reduced torsional constant in Equations (1.21) - (1.23) resulted in conservative critical moment predictions since all analytical critical moment values were smaller than the experimental buckling moments.

Revathi and Mennon (2006) modified the effective moment of inertia expression in ACI 318-05 (2005) Section 9.5.2.3 for the case of out-of-plane bending. The original form of the expression is given in Equation (1.27):

$$I_e = \left( \frac{M_{cra}}{M_a} \right)^3 \cdot I_g + \left[ 1 - \left( \frac{M_{cra}}{M_a} \right)^3 \right] \cdot I_{cr} \leq I_g \quad (1.27)$$



where  $I_g$ ,  $I_{cr}$  and  $I_e$  are the uncracked, the cracked and the effective moments of inertia, respectively;  $M_a$  is the maximum moment in the span at the particular applied load level;  $M_{cra}$  is the cracking moment of the beam.

Equation (1.27) is the weighted average of the uncracked and cracked moments of inertia of a concrete beam. The uncracked moment of inertia corresponds to the early stages of loading when the cracking moment of the beam is not exceeded and the entire beam section contributes to the in-plane bending resistance. When the cracking moment is exceeded, flexural cracks form in the outermost layers of the tension zone of a beam. Later, the flexural cracks propagate in the tension zone towards the compression zone and the moment of inertia of the beam decreases as the applied load increases. When the flexural cracks render the entire tension zone ineffective, the moment of inertia reaches a minimum limit, called the cracked moment of inertia. Equation (1.27), which is the moment of inertia of a concrete beam when the maximum moment in the span is  $M_a$ , reflects the variation in the moment of inertia of a concrete beam from the uncracked state to the fully cracked state as the flexural cracks propagate in the tension zone.

The out-of-plane bending rigidity expression proposed by Revathi and Mennon (2006) is given in Equation (1.28):

$$B = E_c \cdot \left\{ \left[ \left( \frac{M_{cra}}{0.8 \cdot M_{ult}} \right)^3 \cdot \left( \frac{b^3 \cdot h}{12} \right) + \left[ 1 - \left( \frac{M_{cra}}{0.8 \cdot M_{ult}} \right)^3 \right] \cdot \left[ \frac{b^3 \cdot c_u}{12} + \psi \cdot \left( \frac{E_s}{E_c} \cdot \Sigma I_{sy} \right) \right] \right] \right\} \quad (1.28)$$

where  $M_{ult}$  is the ultimate flexural moment of the beam;  $c_u$  is the neutral axis depth of the beam at ultimate flexural load;  $\Sigma I_{sy}$  is the moment of inertia of the longitudinal

reinforcement about the minor axis;  $\psi$  is a multiplier, which is taken 0 for under-reinforced beams and 1 for over-reinforced beams. The first term in the parenthesis,  $b^3h/12$ , is the uncracked moment of inertia of a reinforced concrete beam about the minor axis. The term  $b^3c_u/12 + \psi \cdot \left( (E_s / E_c) \Sigma I_{sy} \right)$  is the moment of inertia of a concrete section at the ultimate flexural load. Accordingly, Revathi and Mennon (2006) proposed a lateral bending rigidity at the time of buckling, which is a weighted average of the uncracked moment of inertia and the moment of inertia of the beam at ultimate load.

Equation 1.27 uses the maximum moment in the span at a particular load to average the uncracked and cracked moments of inertia. In the case of lateral bending, the maximum moment at the time of buckling is the buckling moment of the beam. Hence, the buckling moment should be known to calculate the out-of-plane flexural rigidity of the beam at the buckling moment. To avoid an iterative procedure, Revathi and Mennon (2006) proposed the use of the lateral bending rigidity corresponding to 80% of the ultimate flexural moment. Although the use of  $0.8.M_{ult}$  is a close approximation in the case of inelastic lateral-torsional buckling, it can underestimate the lateral bending rigidity in the case of elastic lateral torsional buckling. When the buckling moment is much smaller than  $0.8.M_{ult}$  as in the case of elastic lateral torsional buckling, there are less flexural cracks in the beam and the rigidity of the beam at the instant of buckling is significantly greater than the value calculated from Equation (1.28).

Revathi and Mennon (2006) also proposed the use of initial tangent modulus of elasticity,  $E_c$ , in the rigidity calculations. As shown in Figure 1.17, the initial tangent modulus of elasticity is used when concrete is in the elastic range of stress-strain curve. Since all compression fibers throughout the beam are stressed below the elastic limit, the

use of  $E_c$  is appropriate when the beam undergoes elastic lateral-torsional buckling. In the case of inelastic lateral-torsional buckling, nonetheless, some compression fibers in highly-stressed portions of the beam are strained beyond the elastic range, where the modulus of elasticity of concrete is smaller than  $E_c$ . Consequently,  $E_c$  is not applicable for all compression fibers in the beam, buckling inelastically, contrary to the assumption in Equation (1.28).

Finally, Revathi and Mennon (2006) proposed the following torsional rigidity expression:

$$C = \frac{4 \cdot \mu' \cdot E_s \cdot A_2^2 \cdot A_c}{p_2^2 \cdot \left( \frac{1}{\rho_l} + \frac{1}{\rho_t} \right)} \quad (1.29)$$

where  $A_c$  is the area of the gross cross-section of the beam;  $A_2$  and  $p_2$  are the area and the perimeter of the rectangle connecting the centers of the corner longitudinal bars (Figure 1.23);  $\mu'$  is a rigidity multiplier taken as 1.2 for under-reinforced and 0.8 for over-reinforced sections;  $\rho_l$  and  $\rho_t$  are the volumetric ratios of the longitudinal and transverse reinforcement, respectively, calculated from Equations (1.30) and (1.31):

$$\rho_l = \frac{A_s}{A_c} \quad (1.30)$$

$$\rho_t = \frac{A_t \cdot p_l}{A_c \cdot s} \quad (1.31)$$

where  $A_s$  is the area of the longitudinal reinforcement in the cross-section;  $A_t$  is the cross-sectional area of one leg of a stirrup;  $p_l$  is the perimeter of the centerline of a stirrup (Figure 1.23);  $s$  is the spacing of the stirrups.

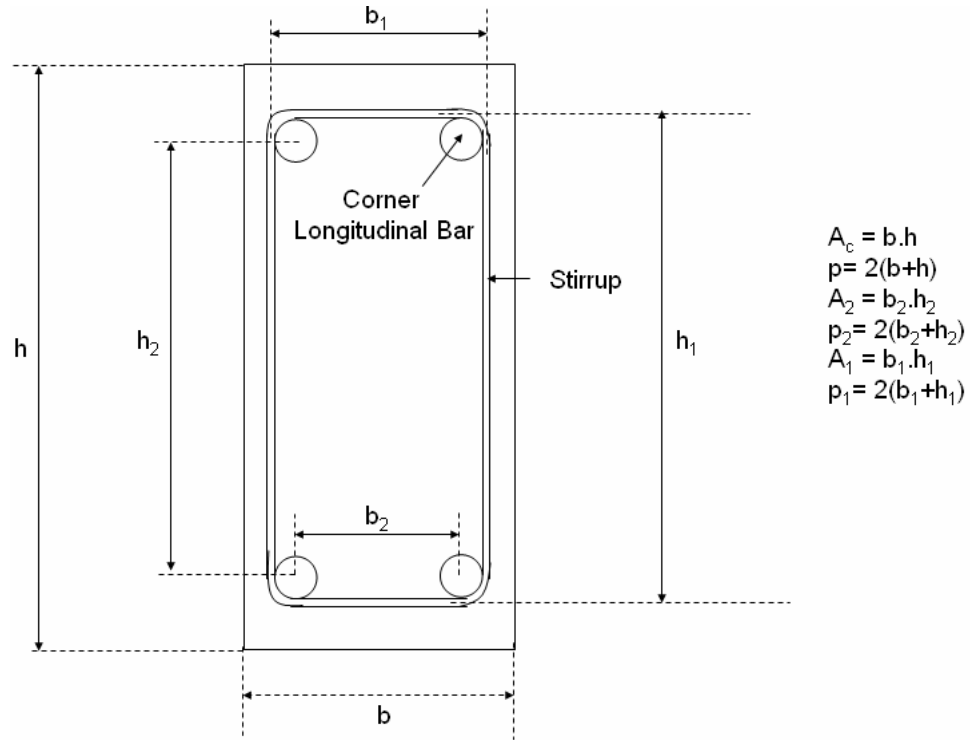


Figure 1.23 – Definition of area and perimeters in Equations (1.29) - (1.31)

The torsional rigidity of a reinforced concrete beam before torsional cracking is given by Equation (1.32) according to St. Venant's theory.

$$C = G_c \cdot \beta \cdot b^3 \cdot h \quad (1.32)$$

where  $\beta$  is the coefficient for St. Venant's torsional constant, obtained from Equation (1.33):

$$\beta = 1 - \frac{192}{\pi^5} \cdot \frac{b}{h} \cdot \sum_{n=0}^{\infty} \frac{1}{(2n+1)^5} \cdot \tanh \frac{(2n+1)\pi h}{2b} \quad (1.33)$$

The torsional rigidity expressions, adopted by Hansell and Winter (1959) (Equation 1.9), Siev (1960) (Equation 1.10) and Sant and Bletzaker (1961) (Equation 1.16), all correspond to the uncracked stage of a concrete beam, and they are derived from

Equation 1.32. Equation 1.29, on the other hand, is the torsional rigidity of a reinforced concrete beam in the early post-cracking stage, meaning right after the formation of diagonal tension cracks due to torsion.

The post-cracking torsional rigidity of a concrete beam is provided by the outer thin-walled layer of concrete surrounding the corner longitudinal bars and stirrups. A three-dimensional model called the thin-walled tube, space truss model was used by Lampert (1973) and Hsu (1973) to develop the post-cracking torsional rigidity of rectangular reinforced concrete beams. Later, Tavio and Teng (2004) simplified the rigidity expression developed by Hsu (1973) and proposed a new expression. Equation (1.29) is a modified version of the torsional rigidity expression proposed by Tavio and Teng (2004), which is presented in Chapter V (Equation 5.27).

Equation (1.29) is the torsional rigidity of a concrete beam right after cracking. Using the equation in critical moment calculations suggests that the whole concrete beam is cracked diagonally at the time of buckling. In the presence of lateral supports at the beam ends, torsional moments resulting from the out-of-plane deformations increase from zero at midspan to a maximum value at the ends. Therefore, the middle portion of the beam remains diagonally uncracked throughout the loading while the end portions, under significant torsional moments, are cracked to a major degree at the time of buckling, particularly in the case of a geometrically-imperfect beam, experiencing major lateral deformations prior to buckling. The uncracked torsional rigidity of the beam reasonably reflects the torsional resistance of the middle portion of the beam, yet the ends possess torsional rigidities close to or even smaller than the post-cracking torsional rigidity. Adopting the post-cracking torsional rigidity for the whole beam in the

calculations is overly-conservative while using the uncracked torsional rigidity overestimates the resistance of a beam, leading to unsafe results. If a single torsional rigidity expression is desired to be valid for the whole span, it should be an average of the maximum and minimum values of the torsional rigidity of the beam along the span.

### **1.4.3 Summary**

The analytical methods for predicting lateral torsional buckling loads of reinforced concrete beams, presented in Section 1.4.2, considered the elastic-inelastic stress-strain behavior of concrete and steel, the contribution of the longitudinal and shear reinforcement to the stability and the flexural cracking of concrete. Nevertheless, the influences of the initial geometric imperfections and the restrained shrinkage cracking of concrete on the lateral stability of reinforced concrete beams have not been studied yet. The analytical part of this study aimed at incorporating all the factors, including the initial geometric imperfections and restrained shrinkage cracking of concrete, into the formula.

For an exact analysis of the lateral stability of a reinforced concrete beam, the initial geometric imperfections, the initial cracking condition (presence or absence of shrinkage cracks), the experimental stress-strain curves of concrete and steel and the cross-sectional details of the beam should be fully known. In none of the experimental studies presented in Section 1.4.1, all of the aforementioned properties of the test specimens were reported. Therefore, reinforced concrete beams, whose geometric and material properties are fully known, were tested in the present study for a better evaluation of the analytical methods presented in Section 1.4.2 and the method proposed in the present study.

## **CHAPTER II**

### **SPECIMENS AND MATERIAL PROPERTIES**

#### **2.1 Specimens**

##### **2.1.1 Specimen Descriptions**

In the experimental program, two sets of specimens were tested. The first set of specimens was composed of six beams of four types, B36, B30, B22 and B18. The second set of beams consisted of five beams of two different types, B44, B36L. Table 2.1 presents the specimens of the entire experimental program. Figure 2.1 and Figure 2.2 illustrate the nominal cross-sectional details of the specimens.

Each beam is denoted with the letter “B”, followed by two numbers. The first number corresponds to the depth of the specimen in inches, while the second number is used for the identification of the specimen. For instance, B44-1 corresponds to the first of the identical beams having a depth of 44 inches. Additionally, specimen group B36L has the letter “L” (representing the longer span) to distinguish it from the specimen B36.

Companion beams were identical to each other in dimensions and amount of flexural and shear reinforcement. Furthermore, concrete from the same batch was used in companion beams to minimize the influence of the mechanical properties of concrete on the experimental results. Similarly, reinforcing steel of the companion beams was from the same batch with the exception of specimen groups B22 and B18. Flexural reinforcing bars in specimens B22-1 and B18-1 were Grade 60 while the bars in specimens B22-2 and B18-2 were Grade 40 (ASTM A615/A, 2007). Since Beams B22 and B18 buckled

Table 2.1 – Specimens tested in the experimental program

<b>Specimen Group</b>	<b>Number of Samples</b>	<b>Height, h (in)</b>	<b>Width, b (in)</b>	<b>Span Length, L (ft)</b>	<b>d/b ratio</b>	<b>L/b ratio</b>
<b>B36</b>	1	36	2.5	20	12.45	96
<b>B30</b>	1	30	2.5	20	10.20	96
<b>B22</b>	2	22	1.5	12	12.45	96
<b>B18</b>	2	18	1.5	12	10.20	96
<b>B44</b>	3	44	3.0	39	12.45	156
<b>B36L</b>	2	36	3.0	39	10.20	156

before yielding of flexural reinforcement, grade of the reinforcing bars had no influence on the buckling behavior of the beams.

Shear reinforcement was needed in the specimens to prevent shear failure. Due to the small widths of the specimens, welded wire reinforcement (WWR) sheets were used instead of bent reinforcing bars. Two 2x6-W2.5xW3.5 sheets, one on each side of the flexural reinforcement, constituted the shear reinforcement of each specimen (Figures 2.1 and 2.2).

### 2.1.2 Experiment Design

The first set of tests was carried out to evaluate the performance of the experimental setup. Thus, any potential shortcomings in the loading and support systems could be discovered and corrected before the second set of experiments. Another goal of the first set of tests was to observe the lateral-torsional buckling behavior of reinforced concrete beams and to detect the factors affecting the lateral stability. Therefore, the first set of specimens was designed to be quite slender so that the beams would certainly fail by lateral-torsional buckling.



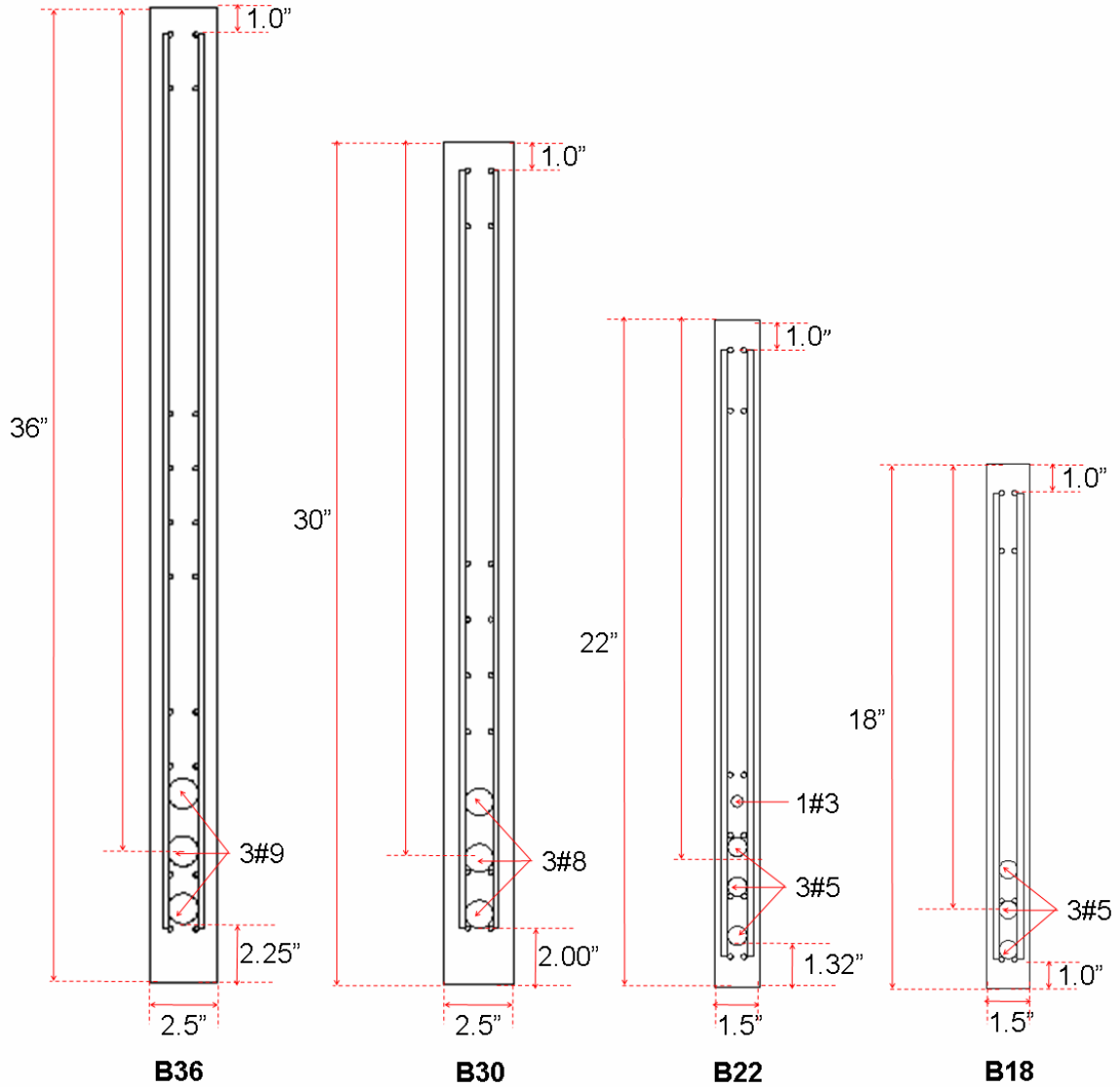


Figure 2.1 – First set of specimens (B36, B30, B22, and B18)

Beams B30 and B36 were tested in the first stage of the experimental program. They had similar dimensions and cross-sectional details to the beams tested by Sant and Bletzacker (1961), whose experimental work formed the basis of the slenderness limitation specified in Section 10.4 of ACI 318-05 (2005) together with the experimental study carried out by Hansell and Winter (1959). To understand scale effects, four smaller beams of two types, B22 and B18 were tested in the first stage.

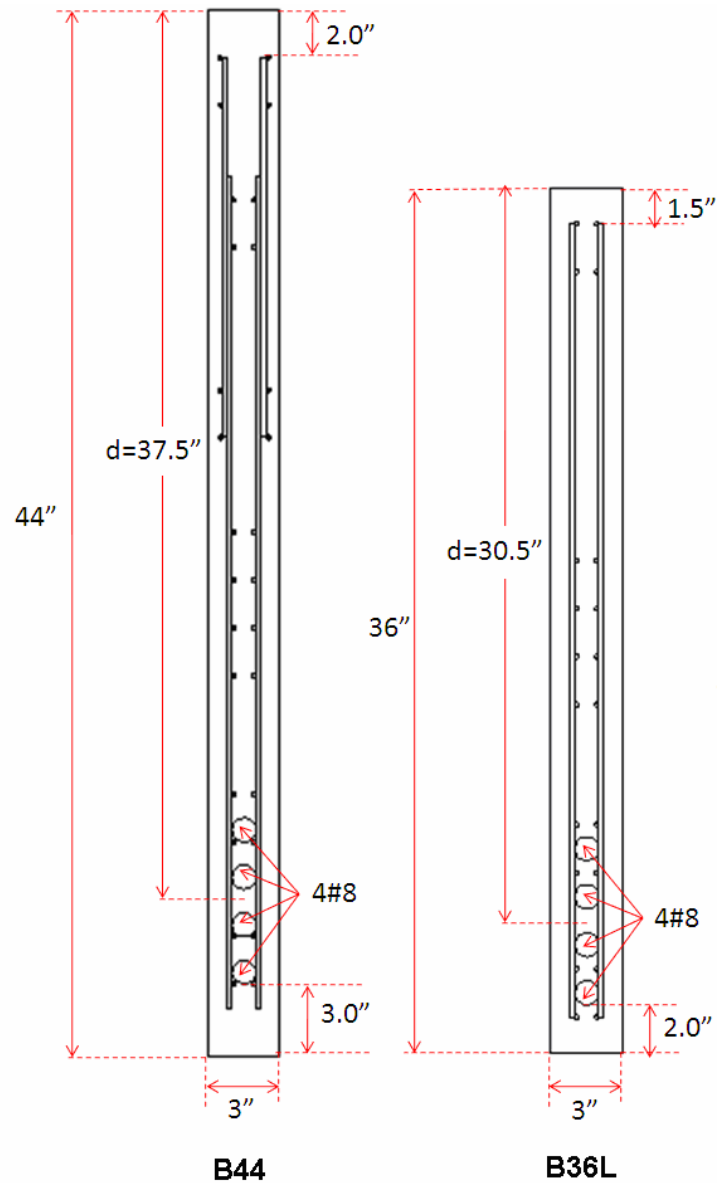


Figure 2.2 – Second set of specimens (B44, B36L)

In the first stage of the experimental program, several observations were made leading to the design of the second set of specimens. The second set of beams was constructed at a larger scale than the first set for two reasons. First, tests on B22 and B18 demonstrated that small-scale beams were extremely sensitive to experimental errors, such as eccentricities in the applied load and deviations from vertical in the orientation of

the load. The smaller lateral-flexural and torsional rigidities of small-scale beams cause the experimental results of such beams to be excessively influenced by the accidental torsions resulting from the slight eccentricities and deviations of the applied loads. As the scales of the specimens were increased, the slight tolerance errors became less influential. Secondly, all specimens were constructed in the same lab environment, using the same type of materials. Therefore, the initial geometric imperfections of the specimens of different sizes were of the same order of magnitude. Since large-scale beams were expected to be less affected than the small-scale beams by imperfections of the same order of magnitude, testing beams with greater scales was preferred in the second stage of the experimental program.

All specimens were designed to undergo elastic lateral torsional buckling, so that the influences of the factors other than inelasticity on the lateral stability of reinforced concrete beams could be examined. Elastic lateral torsional buckling of reinforced concrete beams takes place when both concrete and reinforcement in the beams are strained in the elastic portions of their respective stress-strain curves. In a simply-supported beam, subjected to a concentrated load at midspan, the extreme compression fibers at midspan are the most-stressed portion of the concrete beam. If the extreme compression fiber strain at initiation of buckling is within the initial elastic portion of the stress-strain curve of concrete, the entire compression zone of the beam behaves elastically at initiation of buckling. Similarly, the strain in the tension reinforcement at initiation of buckling does not reach the yield strain of steel in elastic lateral torsional buckling of reinforced concrete beams.

## 2.2 Concrete Material Properties

The small dimensions and congested reinforcement (Figure 2.3) in the first set of beams rendered the mechanical vibration of concrete difficult. To overcome the consolidation problems, Self-Consolidating Concrete (SCC) was used in the first set of specimens. SCC is a flowable type of concrete which spreads into the form and consolidates under its own weight (Figure 2.4). The high-range water-reducing (HRWR) admixtures in SCC decrease the viscosity of concrete and eliminate the need for mechanical vibration. The spread of SCC was measured as 25 in. according to the slump flow test, described in ASTM C1611 (2005). The SCC used a 3/8-in maximum size aggregate.

Mechanical properties of concrete and reinforcing steel influence the lateral buckling behavior of reinforced concrete beams significantly. Concrete from the same batch and reinforcing bars from the same batch of steel were used in the companion beams to reduce differences.

For the concrete used in the first set of beams, three 6 in. x 12 in. cylinder samples were tested on the 7<sup>th</sup> day, on the 28<sup>th</sup> day and on each test day to obtain the compressive strength of concrete ( $f'_c$ ) according to ASTM C39-05 (2005). Furthermore, three more cylinder tests were conducted on each day to determine the modulus of elasticity ( $E_c$ ) and the Poisson's Ratio ( $\nu_c$ ) of the concrete according to ASTM C469 (2002). Different from the first set of beams, cylinder tests were only conducted on the test days in the second set of beams. Table 2.3 tabulates the means and the standard deviations of the test results of each test day.



Figure 2.3 – Congested reinforcement in B36



Figure 2.4 – Application of self-consolidating concrete

Table 2.2 – Mechanical properties of concrete

Test Day	Age at Test (days)	$f'_c$ (psi)		$E_c$ (ksi)		$v_c$	
		Sample Size	$\mu^1$	Sample Size	$\mu$	Sample Size	$\mu$
<b>B22-1</b>	119	3	11730	3	5200	3	0.16
<b>B22-2</b>	129	3	11000	3	4850	3	0.17
<b>B18-1</b>	145	3	11460	3	5000	2	0.13
<b>B18-2</b>	160	3	11320	3	5000	3	0.16
<b>B30</b>	220	3	12220	3	5950	3	0.20
<b>B36</b>	249	3	12780	3	5850	3	0.17
<b>B44-1</b>	179	3	8470	3	4450	3	0.16
<b>B44-2</b>	225	3	8540	3	4450	3	0.15
<b>B44-3</b>	234	3	8560	3	4550	3	0.14
<b>B36L-1</b>	192	3	7900	3	4300	3	0.15
<b>B36L-2</b>	201	3	7940	3	4500	3	0.15
<sup>1</sup> Sample Mean							

In critical and ultimate bending moment calculations, the stress-strain curves of concrete used in the specimens were needed. Therefore, compression tests were conducted on 6 in. x 12 in. concrete cylinders to determine the experimental stress-strain curves of concrete. Figure 2.5 to Figure 2.7 illustrate the experimental stress-strain curves of concrete, obtained from cylinder tests. Critical moment and ultimate flexural moment calculations of the specimens are simplified if the stress-strain curve of concrete is expressed in a mathematical form. For this purpose, several analytical models for the stress-strain curve of high-strength concrete were examined.

Analytical stress-strain curves from the models proposed by Carreira and Chu (1985), Tomaszewicz (1984) and Wee et al. (1996) were included in the plots to determine the model giving the best agreement with the experimental stress-strain curves.

Carreira and Chu (1985) proposed Equation (2.1) for the stress-strain relationship high-strength concrete.

$$f_c = f'_c \cdot \left[ \frac{\beta \cdot \left( \frac{\varepsilon}{\varepsilon_o} \right)}{\beta - 1 + \left( \frac{\varepsilon}{\varepsilon_o} \right)^\beta} \right] \quad (2.1)$$

where  $\varepsilon$  and  $f_c$  are the concrete strain and stress, respectively;  $\varepsilon_o$  is the strain at peak stress and  $f'_c$  is the compressive strength of concrete according to the cylinder tests;  $\beta$  is a material parameter, given by

$$\beta = \frac{1}{1 - f'_c / \varepsilon_o \cdot E_c} \quad (2.2)$$

The model proposed by Tomaszewicz (1984) adopts Equation (2.1) for the ascending branch of the stress-strain curve. For the descending branch of the curve, on the other hand, Equation (2.3) was developed with the introduction of a new parameter,  $k$  to Equation (2.1).

$$f_c = f'_c \cdot \left[ \frac{\beta \cdot \left( \frac{\varepsilon}{\varepsilon_o} \right)}{\beta - 1 + \left( \frac{\varepsilon}{\varepsilon_o} \right)^{k \cdot \beta}} \right] \quad (2.3)$$

where  $k = f'_c / 2.90$  with  $f'_c$  given in ksi.

Similar to the formulation given by Tomaszewicz (1984), Wee et al. (1996) recommended the use of Equation (2.1) for the ascending branch and a modified form of Equation (2.1), given below, for the descending branch.

$$f_c = f'_c \cdot \left[ \frac{k_1 \cdot \beta \cdot \left( \frac{\varepsilon}{\varepsilon_o} \right)}{k_1 \cdot \beta - 1 + \left( \frac{\varepsilon}{\varepsilon_o} \right)^{k_2 \cdot \beta}} \right] \quad (2.4)$$

where  $k_1 = (7.26/f'_c)^{3.0}$  and  $k_2 = (7.26/f'_c)^{1.3}$  with  $f'_c$  given in ksi.

All three models adopt the same equation (2.1) for the ascending branch of the stress-strain curve. Figure 2.5 to Figure 2.7 indicate that Equation (2.1) closely estimates the ascending portions of the experimental curves. Since the stresses in all specimens were within the initial portions of the stress-strain curves of concrete, only the ascending portions of the curves were determined in the cylinder tests.



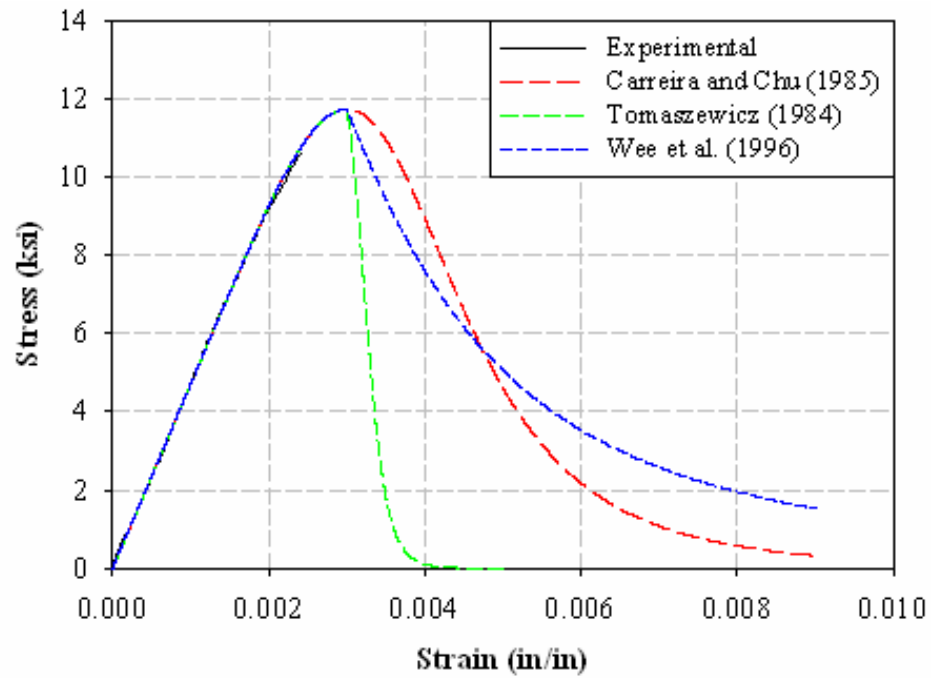


Figure 2.5 –Stress-strain curves of concrete in the first set of beams

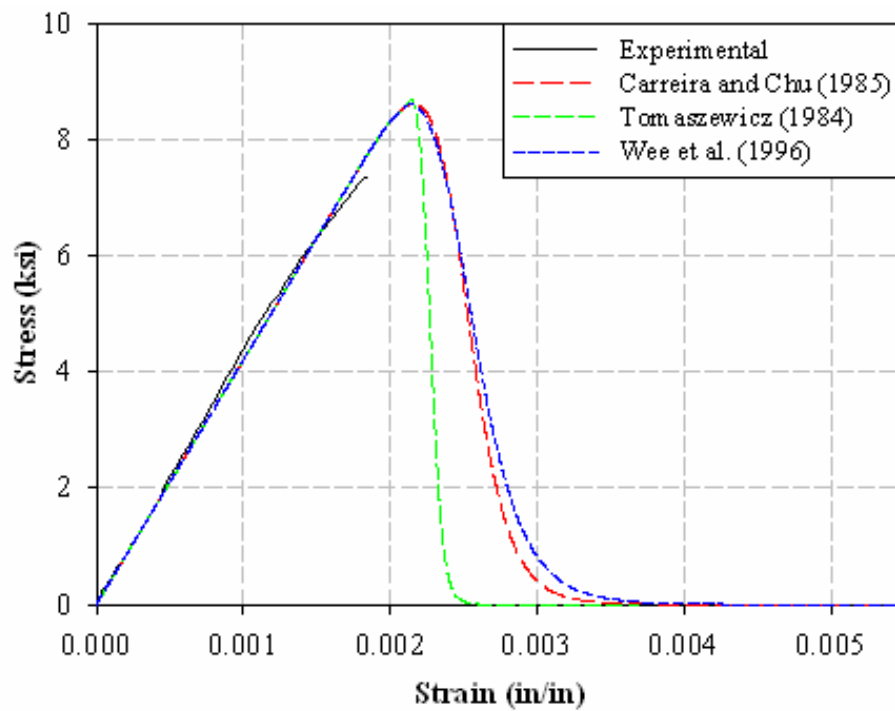


Figure 2.6 –Stress-strain curves of concrete in B44

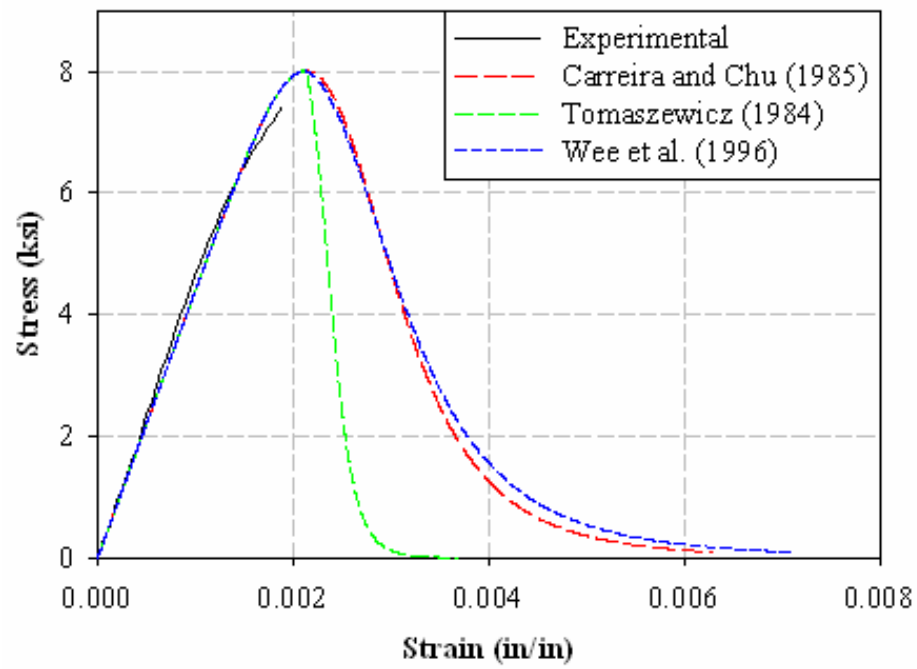


Figure 2.7 –Stress-strain curves of concrete in B36L

# **CHAPTER III**

## **EXPERIMENTAL SET-UP, INSTRUMENTATION AND PROCEDURE**

### **3.1 Experimental Set-up**

#### **3.1.1 Loading Mechanism**

The loading frame used for testing the beams of the present study consisted of a loading mechanism, called the gravity load simulator, a tension jack mounted to the center pin of the simulator, a loading cage and a ball-and-socket joint conveying the load from the cage to the beam (Figures 3.1 and 3.2).

Gravity load simulator was first developed by Yarimci et al. (1967) and used in sway-permitted testing of large scale frames, later in lateral torsional buckling tests of steel I-beams by Yura and Phillips (1992) and lateral stability of polymer composite I-shaped members by Stoddard (1997). In the present experimental program, the gravity load simulator designed and applied by Stoddard (1997) was used.

The gravity load simulator is composed of two inclined arms and a rigid triangular frame connected to the arms through pins. The pin connections at both ends of the arms cause the mechanism to be unstable. The instantaneous center of the mechanism at any configuration of the simulator is the intersection point of the extensions of the inclined arms (Figure 3.3). The center pin (bottom pin) of the triangular frame moves in an approximately horizontal line for certain limits of mechanism motion. Since the center pin is directly below the instantaneous center at any configuration of the simulator, the line of action of the load applied by a loading device connected to the center pin has a vertical orientation passing through the instantaneous center. The applied load has

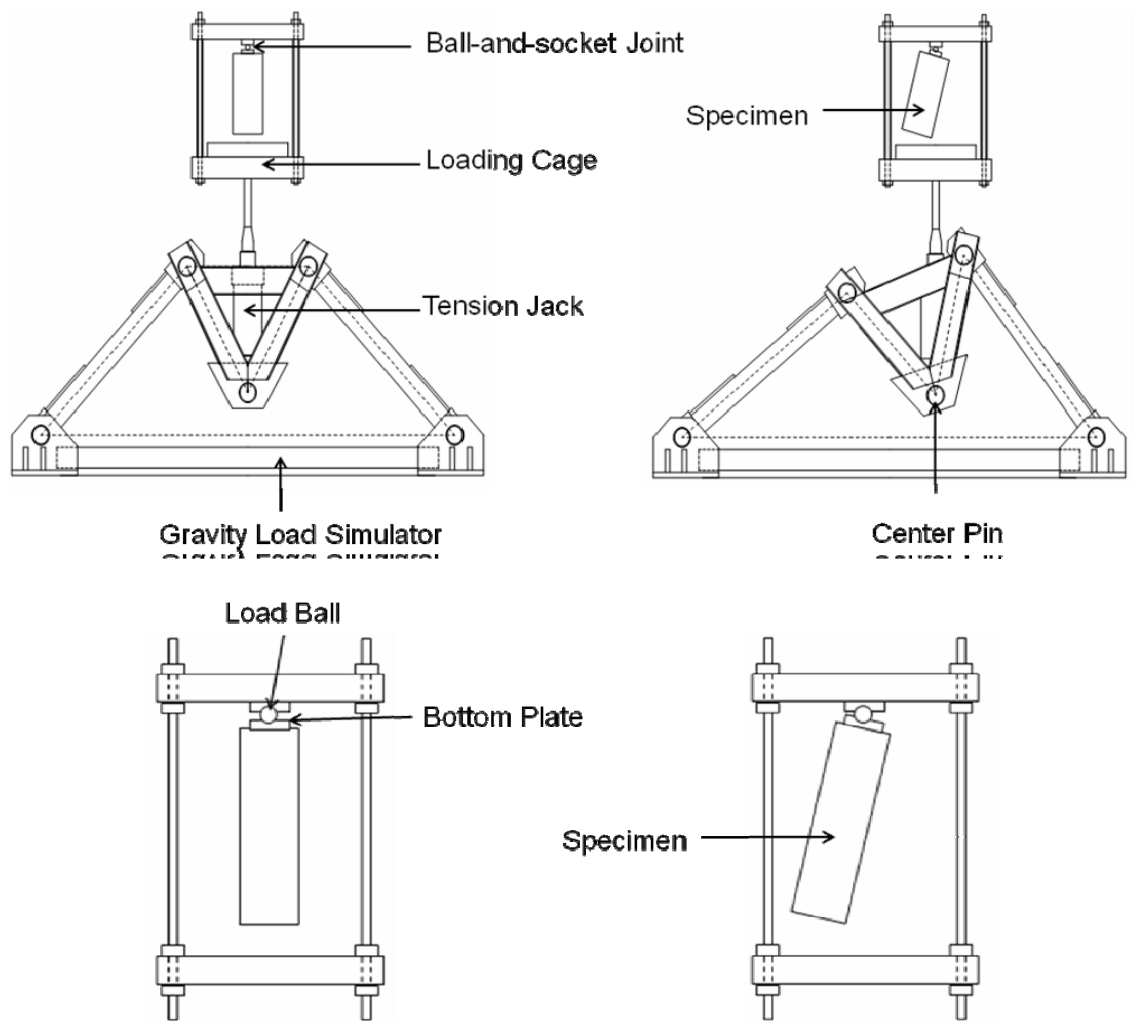


Figure 3.1 – Undeformed and deformed configurations of the loading frame and loading cage

insignificant deviations from the vertical orientation in a certain range of lateral displacement of the center pin. In the present study, a hydraulic cylinder mounted to the center pin of the triangular frame loaded the beams vertically throughout the entire test and did not restrain the out-of-plane translation of the loading point owing to the lateral motion of the center pin of the simulator with the beam (Figure 3.4).

The rotational freedom of the loading point was achieved with the help of the ball-and-socket joint (Figure 3.5), which was composed of two steel plates and a steel

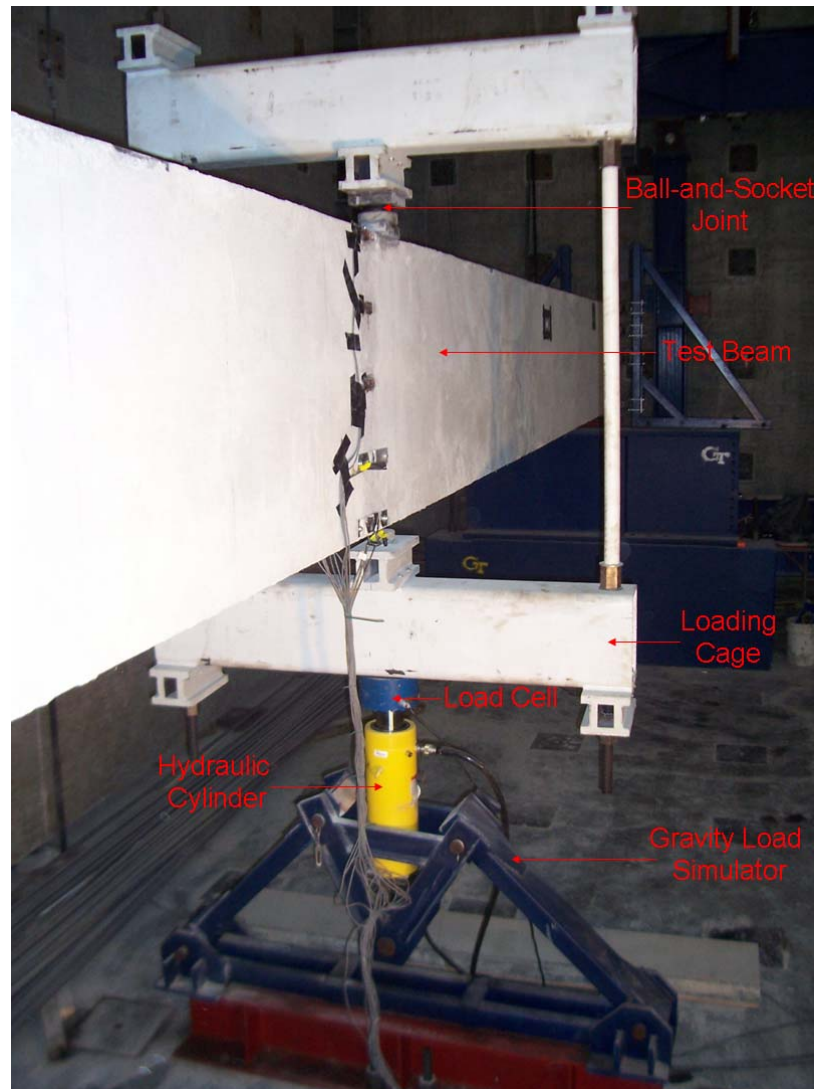


Figure 3.2 – Loading frame

ball between them, positioned in a socket. Bottom plate of the joint, which was epoxied to the top surface of the beam, rotated with the beam allowing the loading cage (Figure 3.6) and the hydraulic cylinder to preserve their vertical orientation. Consequently, the applied load, transferred from the loading cage to the beam by the steel ball, continued to have a vertical orientation even after the rotations of the beam. The socket was lightly oiled prior to each test to diminish the friction between ball and plates.

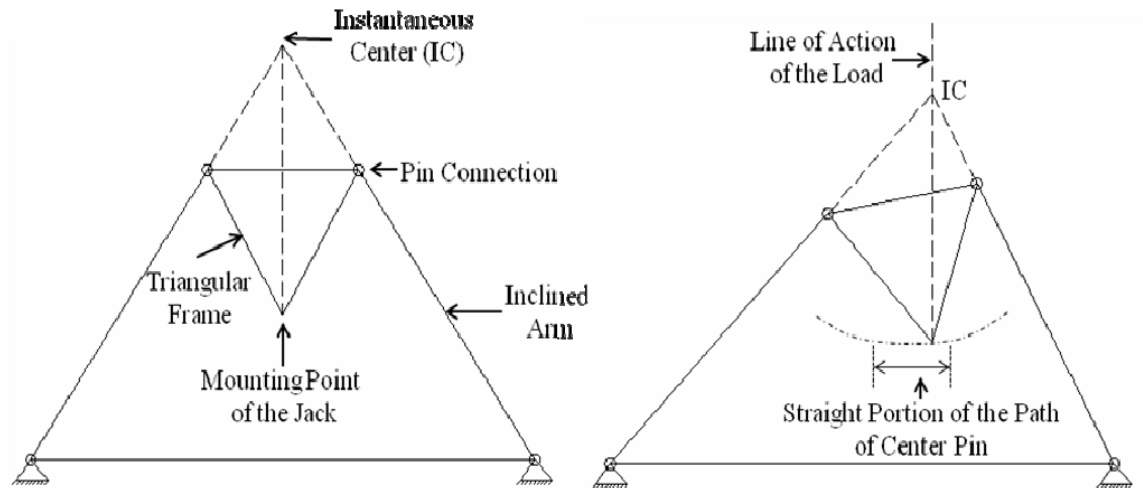


Figure 3.3 – Undeformed and deflected shapes of the gravity load simulator



(a)

(b)

Figure 3.4 – (a) Undeformed and (b) Deflected configurations of the gravity load simulator



Figure 3.5 – Ball-and-socket joint





(a)

(b)

Figure 3.6 –The vertical orientation of the loading cage (a) before the test; (b) after buckling



### 3.1.2 Supports

In the design of the experimental setup, the in-plane and out-of-plane supports were selected and designed to obtain simple support conditions about the major and minor axes of the beam. The end supports allowed rotations about the major and minor axes (Figure 3.7) while restraining rotation about the longitudinal axis of the beam (Figure 3.8). Furthermore, the end supports restrained the in-plane (vertical) and out-of-plane (lateral) translations (Figure 3.8), yet allowed longitudinal translation and warping deformations.

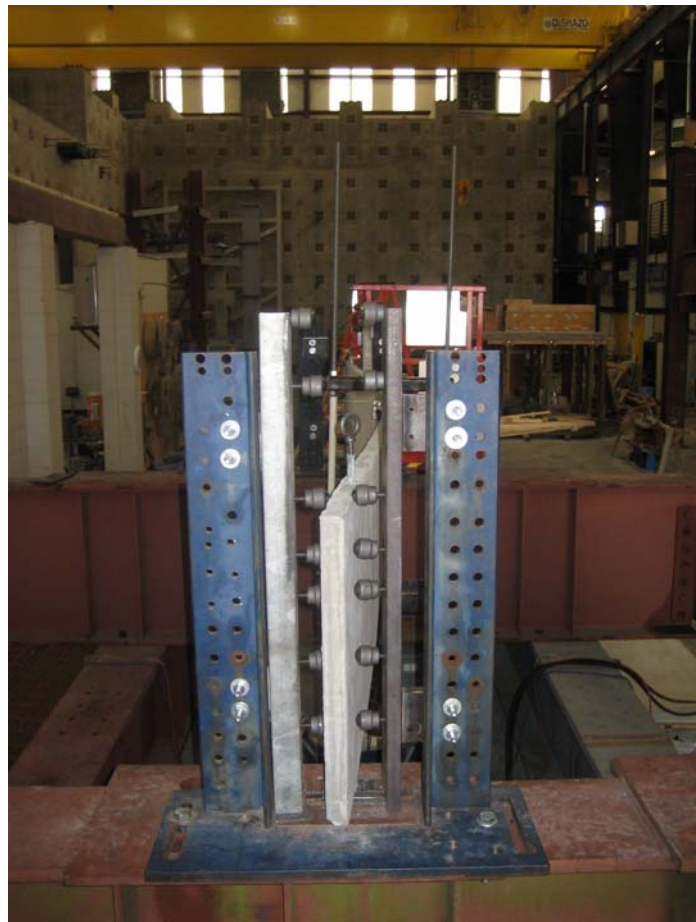


Figure 3.7 – Minor-axis rotations at the supports



Figure 3.8 – Lateral deformations and torsional rotations restrained at the supports

Longitudinal deformations of the beams played an important role in the design of in-plane and out-of-plane supports. Restraining the displacements of the support sections in longitudinal direction changes the behavior of a beam completely. When the longitudinal displacements of a beam are prevented at the support locations, the in-plane support conditions deviate from simple support conditions.

When analyzing beams subjected to in-plane loading, through one-dimensional models, the supports are located at the centroids of the support sections [Figure 3.9(a)]. In

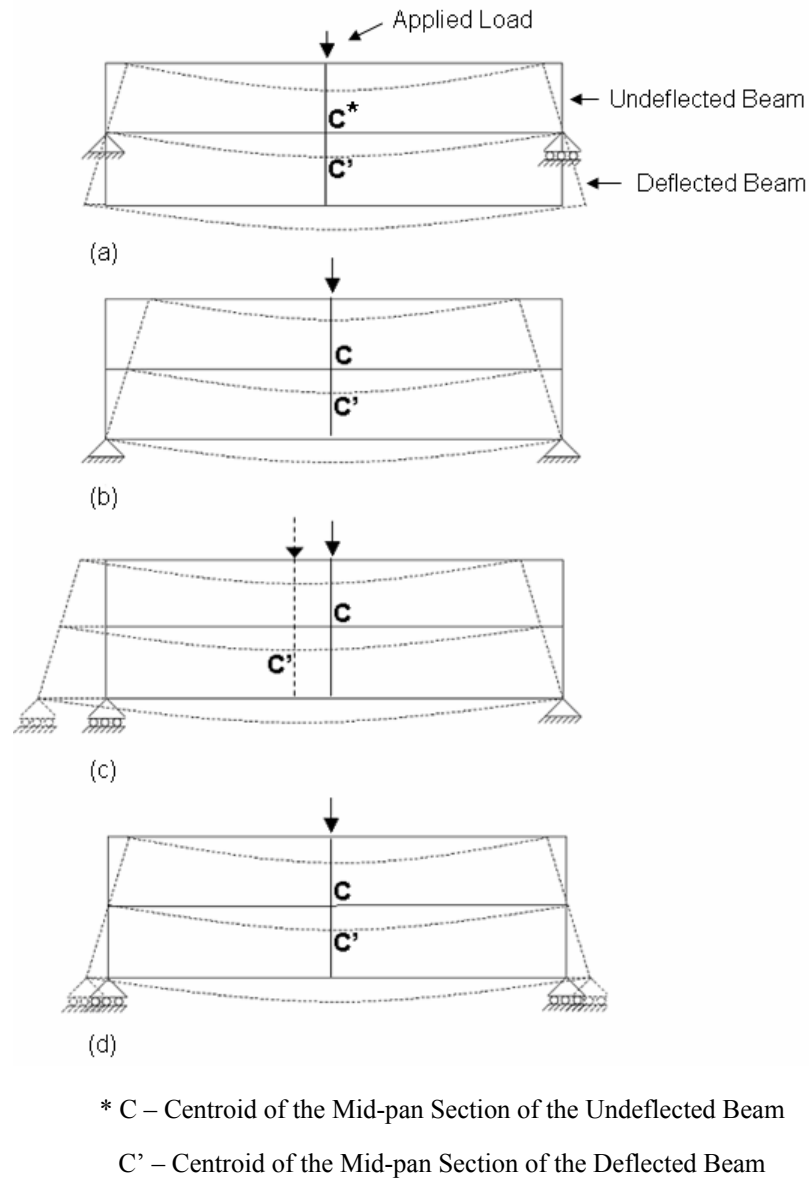


Figure 3.9 – In-plane support conditions: (a) in analysis models; (b) Hinged-hinged; (c) Roller-hinged; (d) Roller-roller.

the following discussion, the centerline of the beam is assumed to be coincident with the neutral axis. According to this assumption, the centerline continues to be unstrained as the beam deforms in plane. In a simply-supported beam, the support sections rotate in plane about the line of contact of the support with the beam. In a beam with support

conditions as in Figure 3.9(a), the end sections rotate about the horizontal centroidal axis (major axis) of the section. Therefore, the portion above the centroidal axis displaces longitudinally towards the mid-span of the beam while the portion below the centroidal axis displaces outwards. In other words, the top portion of the beam shortens while the bottom portion elongates due to the in-plane bending rotations. The centroids of the end sections remain at their initial positions maintaining the longitudinal distance between them. Furthermore, the centerline and the initial midspan of the beam do not undergo translations in longitudinal direction. The in-plane flexural deformations of the beam take place symmetrically about the mid-span of the undeflected configuration of the beam.

The in-plane support conditions are somewhat different in an experiment. The supports are located underneath the beam. Using rollers or hinges or a combination of them at the support locations influences the in-plane behavior and deformations of a beam when the supports are beneath the beam. Figures 3.9(b)-(d) illustrate the in-plane deformations of a beam with hinges at both ends, a hinge at one end and a roller at the other end and rollers at both ends, respectively.

A beam exhibits completely different in-plane flexural behaviors under the three different boundary conditions shown in Figures 3.9(b)-(d). The three cases are investigated to find the boundary conditions under which a beam has an in-plane flexural behavior in closest agreement with the case considered in the one-dimensional analysis [Figure 3.9(a)].

In Figure 3.9(b), both ends of the beam are supported with hinges. Since the hinges at the ends restrain the longitudinal displacement, the bottommost portions of the end sections remain at their original positions as the beam bends in plane. The end

sections undergo major-axis rotations about the supports and the centroids of the end sections displace towards mid-span. The longitudinal displacements of the centroids of the end sections constitute a clear distinction from the in-plane flexural deformations of the beam supported as in Figure 3.9(a). Hence, providing fixtures simulating hinges at both ends was not adopted in the experiments.

In Figure 3.9(c), the beam is hinge-supported at one end and roller-supported at the other end. The roller support translates in longitudinal direction while the hinge remains in its original position when the beam bends in plane. The roller-supported end of the beam experiences longitudinal translations as well as flexural rotations; yet the hinged end of the beam only rotates in-plane about the support. As the beam ends undergo bending rotations, the roller translates in longitudinal direction to assure that the initial distance between the centroids of the end sections is preserved. The in-plane flexural behavior of a beam with a hinge at one end and a roller at the other end matches with the behavior in Figure 3.9 (a) in the preservation of the initial longitudinal distance between the centroids of the end sections. Nevertheless, there are differences between the in-plane deformations of a beam supported as in Figure 3.9(c) and a beam supported as in Figure 3.9(a). The midspan section of the beam in Figure 3.9(c) translates in the longitudinal direction towards the roller-supported end as the beam flexes. Hence, the location of the midspan load also shifts longitudinally with the beam, constituting a significant difference from the behavior of the beam supported at the centroids of the end sections.

In Figure 3.9(d), both ends of the beam are roller-supported. The beam is statically unstable since there is no restraining force at the support locations preventing

the beam from undergoing rigid-body translation in the longitudinal direction. However, the lack of the longitudinal restraining force at the beam ends was not significant in the present study since the longitudinal displacements and in-plane bending deformations of the specimens were estimated to be small due to the large major-axis bending rigidities possessed by the slender beams. Furthermore, the loading frame prevented significant longitudinal translation of the beams. The bending rigidity of the loading frame would provide a longitudinal force at the load point, restraining the tilting of the loading frame due to the longitudinal translation of the beam.

Figure 3.9(d) depicts that the roller supports at both ends of the beam translate in longitudinal direction, allowing the stretched bottom portions of the end sections to displace outwards as the beam bends in plane. Since the centroids of the end sections do not displace in longitudinal direction, the initial longitudinal distance between the centroids of the end sections is maintained as the beam ends rotate in plane. Unlike a beam with a hinge at one end and a roller support at the other end, the centerline of a beam with roller supports at both ends does not move in longitudinal direction.

Based on the above discussion, the in-plane flexural behavior of a beam with roller in-plane supports at both ends is closest to the behavior of a beam with the support conditions as in a one-dimensional analysis. Therefore, each specimen was roller-supported at both ends to have similar support conditions to a one-dimensional analysis (Figure 3.10).

Lateral stability of a beam is also influenced by the longitudinal restraint at the lateral supports. Figure 3.11 illustrates the two lateral support conditions in the aspect of longitudinal restraint. Lateral support (shown with crosses in the figure) was provided at



Figure 3.10 – Roller supports at the beam ends in the second set of experiments

five points along the depth of the beam ends. In Figure 3.11 (a), lateral supports allowed free translation in longitudinal direction while preventing the beam from deflecting in lateral direction. On the other hand, lateral supports in Figure 3.11 (b) restrain the longitudinal displacements as well as the lateral displacements at the beam ends. Hence, lateral supports are shown as rollers in Figure 3.11 (a) and as hinges in Figure 3.11 (b).

If the lateral supports prevent the ends from rotating in plane by restraining the longitudinal displacements, the beam ends become fixed rather than simply-supported. Since the lateral stability of a beam is closely related to its in-plane flexural behavior, the longitudinal restraining forces at the lateral supports should be minimized to achieve simple support conditions in and out of plane.

In the present experimental program, out-of-plane supports were designed in a way that the points in contact with lateral supports were allowed to translate in longitudinal direction with insignificant levels of restraint. In that way, the beam ends were provided with rotational freedom about the major axis.

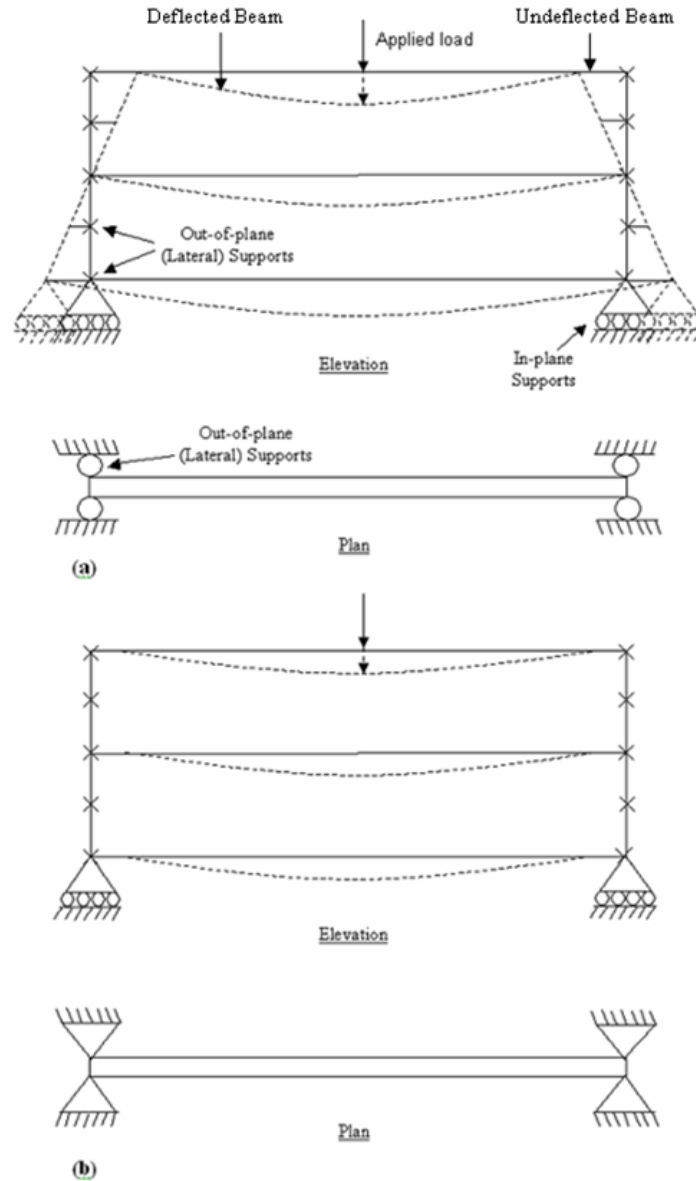


Figure 3.11 – Behavior of the beams with: (a) roller supports; (b) hinged supports in lateral direction

Two different support frames were built in the two stages of experimental program to achieve the aforementioned lateral support conditions. In the first stage, ball rollers were employed to support the beams laterally (Figure 3.12). A ball roller [Figure 3.12(b)] is a special type of caster, whose wheel is a steel ball capable of swiveling freely in a socket. The rotational freedom of the ball allows free motion in any direction. The



use of ball rollers in the first set of experiments assured that the points on the beam in contact with the lateral supports were not restrained from translating in longitudinal direction. So, the lateral supports provided the support sections of the beams with in-plane rotational freedom to achieve the simple support conditions. The ball rollers were mounted to the support frames through threaded studs [Figure 3.12(b)].

Although the ball rollers were observed to prevent the beam ends from rotating about the longitudinal axis of the beam and from deflecting laterally, the support forces transferred from the beam to the ball rollers were noticed to cause the threaded rods of the ball rollers to bend during the tests (Figure 3.13). Therefore, a new lateral support frame (Figure 3.14) was designed prior to the second set of experiments. Rigid casters (Figure 3.15) were used instead of the ball casters.

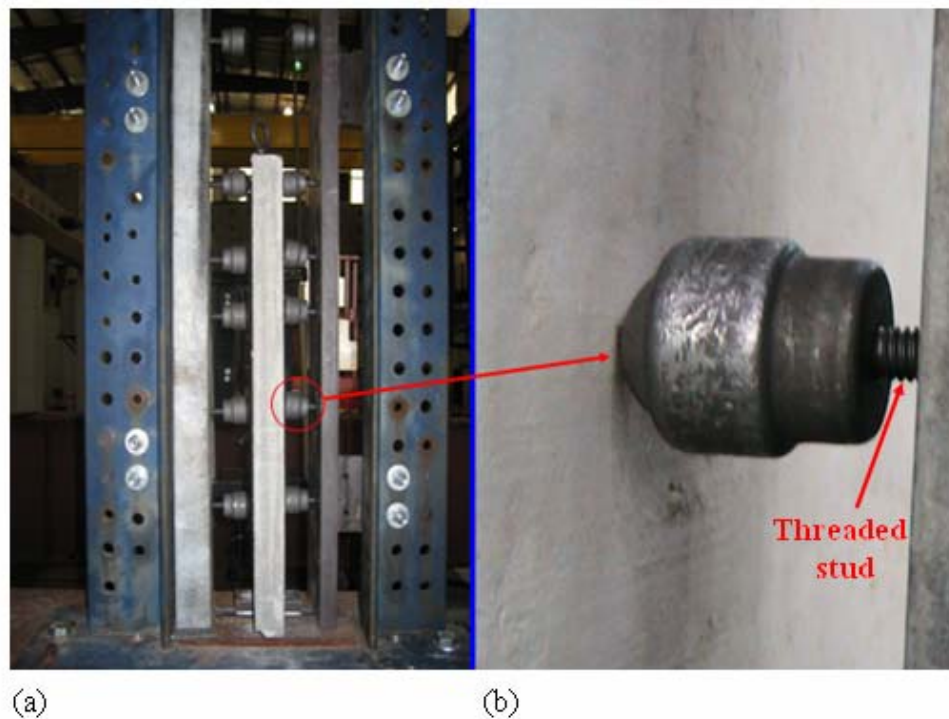


Figure 3.12 – (a) Support frame in the first set of experiments; (b) A ball roller in contact with the beam



Figure 3.13 – Bending of the ball roller

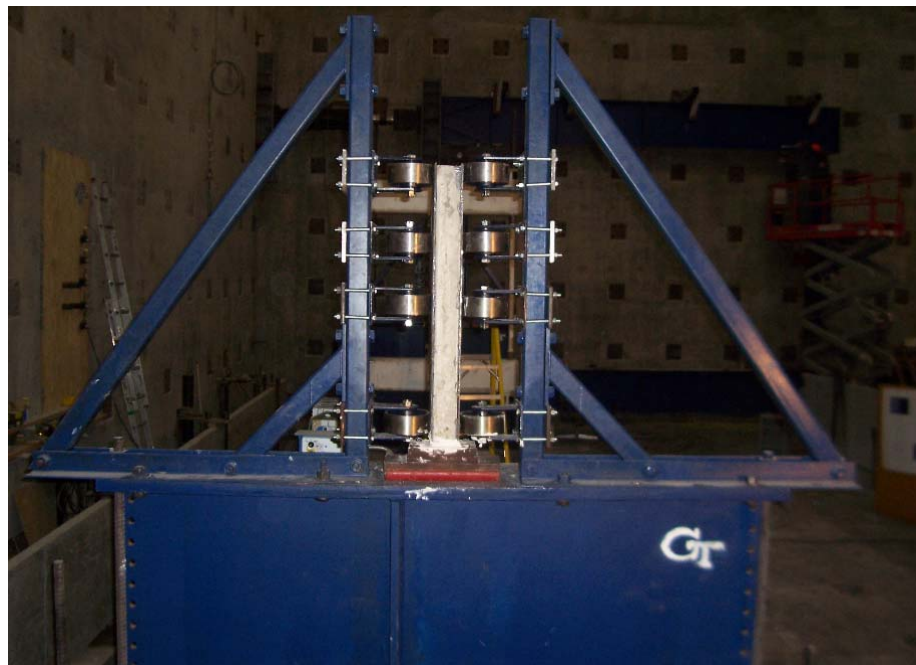


Figure 3.14 – Lateral support frame in the second set of experiments

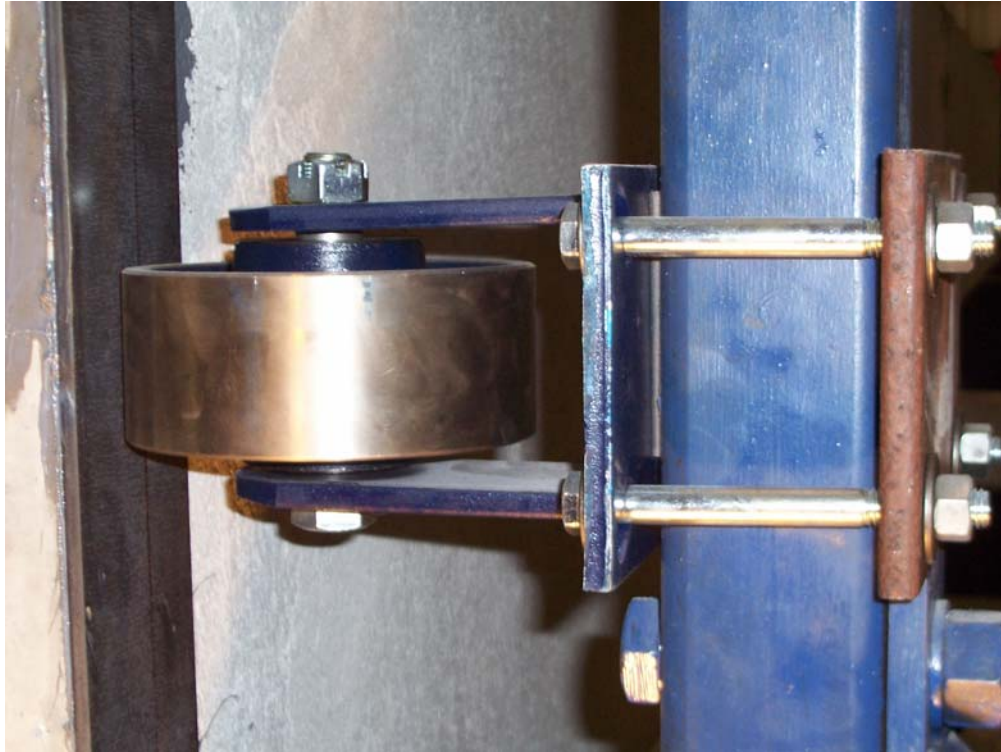


Figure 3.15 – Rigid caster in contact with the specimen

The rigid casters had a wheel rotating about an axle passing through the center of the wheel. The casters were mounted to the lateral support frames in a way that the wheel rotations allowed longitudinal displacements of the points of contact of the beams with the casters (Figure 3.15). Therefore, the in-plane flexural rotations of the end sections were not restrained to satisfy the simple support conditions about the major axis.

The casters had a mounting plate with four corner holes to bolt the caster to a frame. Instead of bolting the casters directly to the support frame, the mounting plate of each caster was connected edge to edge to a steel plate adjacent to the other side of the frame (Figure 3.15) to allow the casters to move to the desired level along the height of the frame to accommodate different beam depths. The four  $\frac{1}{2}$ -in diameter bolts connecting the casters to the support system provided adequate rigidity to the casters

against the bending moments induced by the vertical friction forces between the beams and the caster wheels.

The support frames in the second set of experiments were mainly composed of two HSS 3x3x1/4 structural tubes, one on each side of the beam (Figure 3.14). Each of these tubes was supported by two diagonal knee braces. One of these braces was extended to the top of the support member (HSS 3x3x1/4) while the other brace was connected to the tube at one-third of the height of the tube.

In the first test of the second stage (Specimen B44-1), two casters were used on each side of the beam to support the beam ends laterally [Figure 3.16(a)]. One of the casters supported the topmost portion of the beam while the other caster was touching the beam at the two-third of the height. Although two casters had sufficient capacity to withstand the lateral forces in the tests, problems associated with deformations and distortions at the beam ends were encountered. Since lateral support was provided at the top halves of the beam ends only, the bottom portions of the ends displaced in the opposite direction to the lateral deformations, after buckling (Figure 3.17). The top portions, on the contrary, remained in their initial positions owing to the adequate lateral support at the top. Displacement of the bottom parts of the end portions relative to the top resulted in distortions in the cross-sectional shape of the beam. Figure 3.17 illustrates the distortion. The distortions in the support regions did not affect the buckling moment and the deformations in the beam prior to buckling since the bottom parts of the end sections started moving laterally as a result of the excessive out-of-plane deformations in the post-buckling stage. Two additional casters on each side, supporting the bottom halves of the beam ends were used in the following experiments [Figure 3.16(b)]. The beam ends were



supported by four casters on each side of the beam to provide lateral translational and rotational restraint along the depth of the beam.

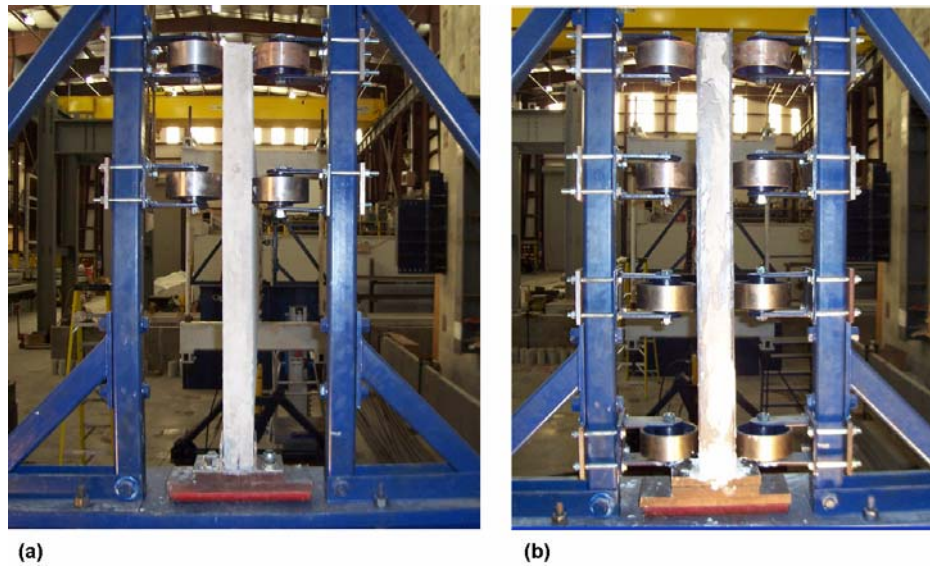


Figure 3.16 – Support frame in the second set of tests: (a) B44-1; (b) B44-2



Figure 3.17 – Distortion in the cross-section at the beam end

### **3.1.3 Load, Deflection and Strain Measurements**

A 50-kip load cell in the first set of experiments and a 100-kip load cell in the second set of experiments were used. The load cells were placed in line with the jack and loading cage in order to measure the applied load. String potentiometers were utilized to determine the in-plane and out-of-plane deflections, the torsional rotations and distortions at midspan.

In a lateral-torsional buckling test, the in-plane deflections of a beam are accompanied by out-of-plane deflections. Each point along the span of a slender beam undergoes lateral displacements as well as vertical displacements. Therefore, the cable of a potentiometer, having horizontal or vertical orientation at the beginning of the test, deviates from its initial orientation once the beam starts deforming out of plane (Figure 3.18). Since a geometrically imperfect beam deflects out of plane and experiences rotations even at the initial stages of loading, uncoupled lateral and vertical deflections cannot be measured directly by using horizontally- and vertically-oriented potentiometers even prior to the buckling of the beam.

In the first set of experiments, the coupled deflection measurements from the potentiometers were converted into in-plane and out-of-plane deflections and rotations at the shear center (centroid in rectangular sections), through a modified approach presented by Zhao (1994) and extended by Stoddard (1997). This approach, presented in Appendix E, is based on geometric relations linking the deflection measurements from three potentiometers to deflections and rotation of the centroid.

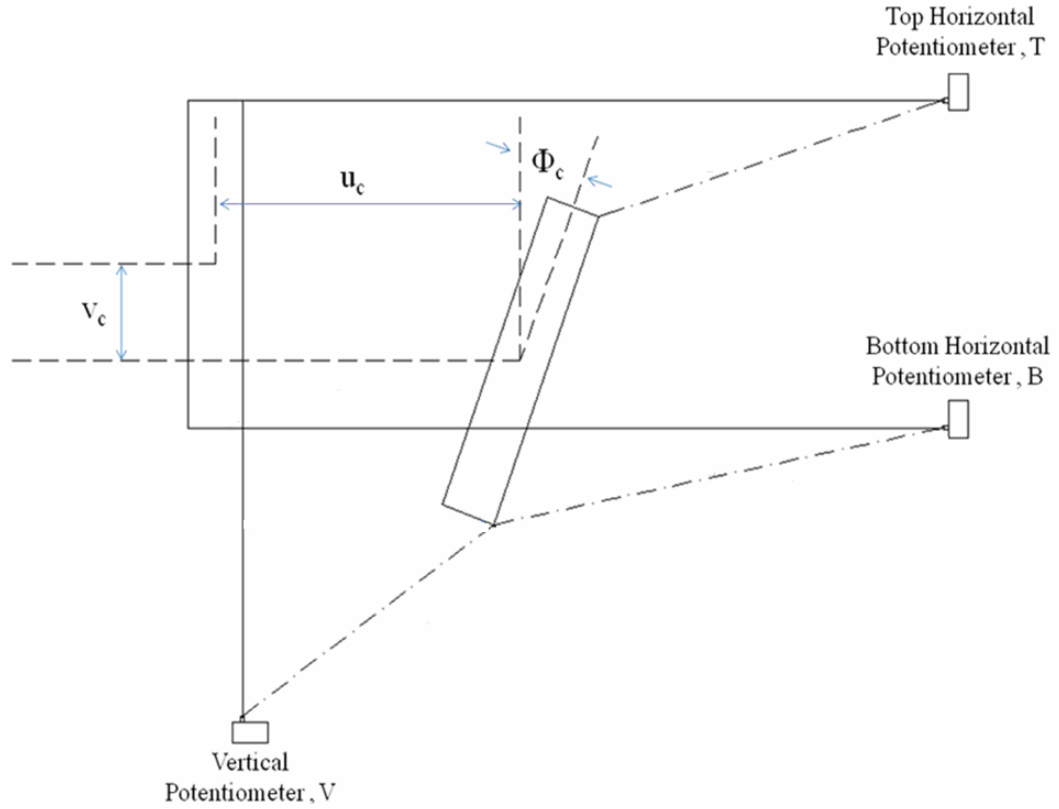


Figure 3.18 – Deviation of the Initial Orientations of the Potentiometers

In the second set of experiments, the distances of the lateral and vertical potentiometers to the beam were increased to minimize the coupling between the lateral and vertical deflection readings. This is illustrated in Figure 3.19, which shows that the angle of the measuring cable from horizontal (vertical in the case of a vertical string potentiometer) in the twisted configuration of the beam decreases as the distance between the potentiometer and the beam increases. Accordingly, the difference between the horizontal component of the measuring cable ( $L \cdot \cos \alpha$  in Figure 3.19) and the length of the measuring cable ( $L$ ) decreases with an increase in the distance of the potentiometer to the beam. This means that the change in length of the measuring cable, measured by the

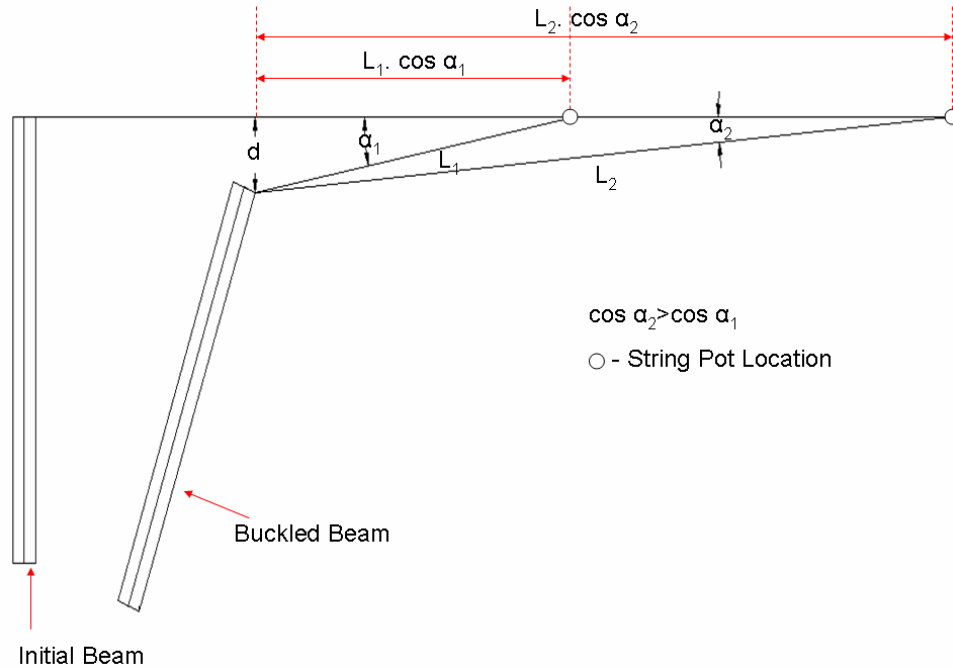


Figure 3.19 – Coupling between the in-plane and out-of-plane deflection measurements for a lateral string potentiometer with varying distances from the specimen

potentiometer, becomes closer to the lateral deflection of the cable-attachment point on the beam, as the distance of the potentiometer increases.

The cross-section of a concrete beam might distort when the beam buckles in a lateral torsional mode. As shown in Figure 3.20(a), two lateral potentiometers are adequate to determine the rotated configuration of the midspan section after buckling when the cross-section of a beam does not distort. Nonetheless, distortions in the cross-section of a beam cannot be detected by only measuring the out-of-plane deflections at two different depths along the midspan section. Therefore, lateral deflections were measured at three or more different points along the depth of each specimen at midspan [Figure 3.20(b)] to assess the shape of the midspan section throughout the test and to detect any possible distortion in the cross-section. Three lateral potentiometers in the first



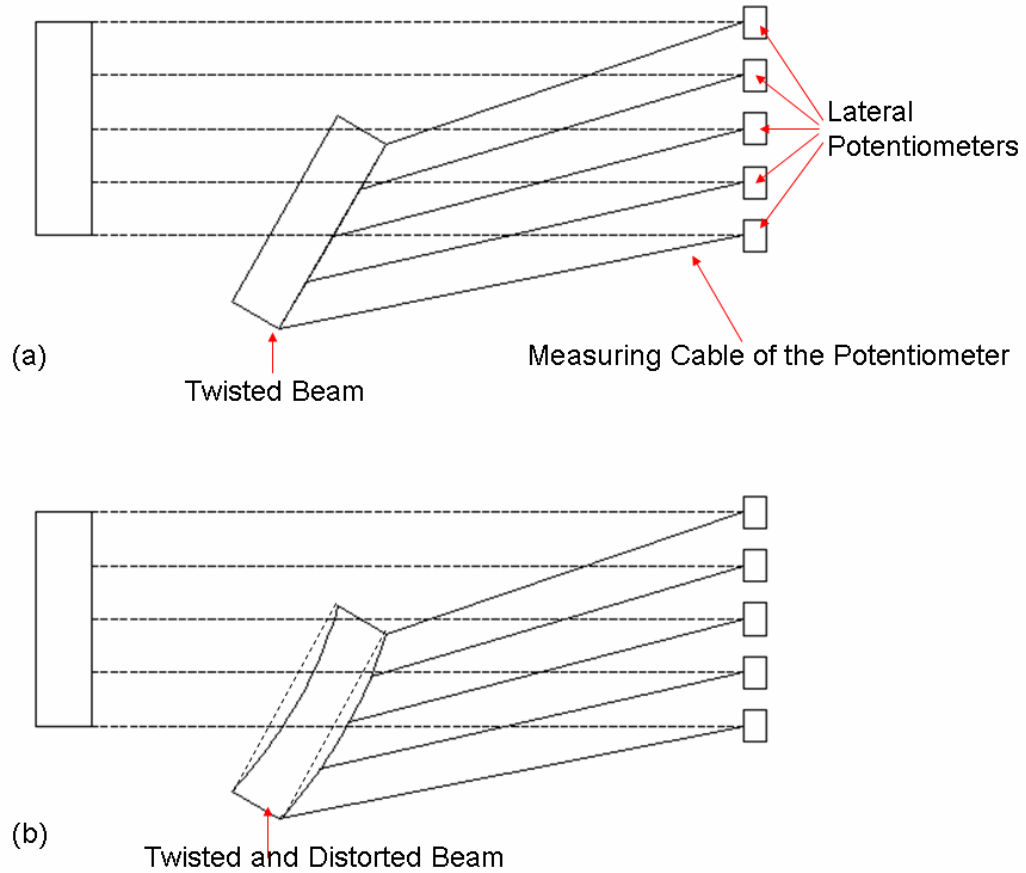


Figure 3.20 – Lateral-torsional buckling (a) with; (b) without distortions in the cross-sectional shape of the beam

stage of the experimental program (Figure 3.21) and five lateral potentiometers in the second stage of the experimental program (Figure 3.22) were used.

During the first stage of the experimental program, Linear Variable Differential Transducers (LVDT's) were used for obtaining the strain distributions through the depth of the convex and concave faces of each specimen at midspan (Figure 3.23). These LVDT's were replaced with electrical resistance strain gauges (Figure 3.24) during the second stage of the experimental program.



Figure 3.21 – Lateral deflection potentiometers in the first set of experiments



Figure 3.22 – Lateral deflection potentiometers in the second set of experiments

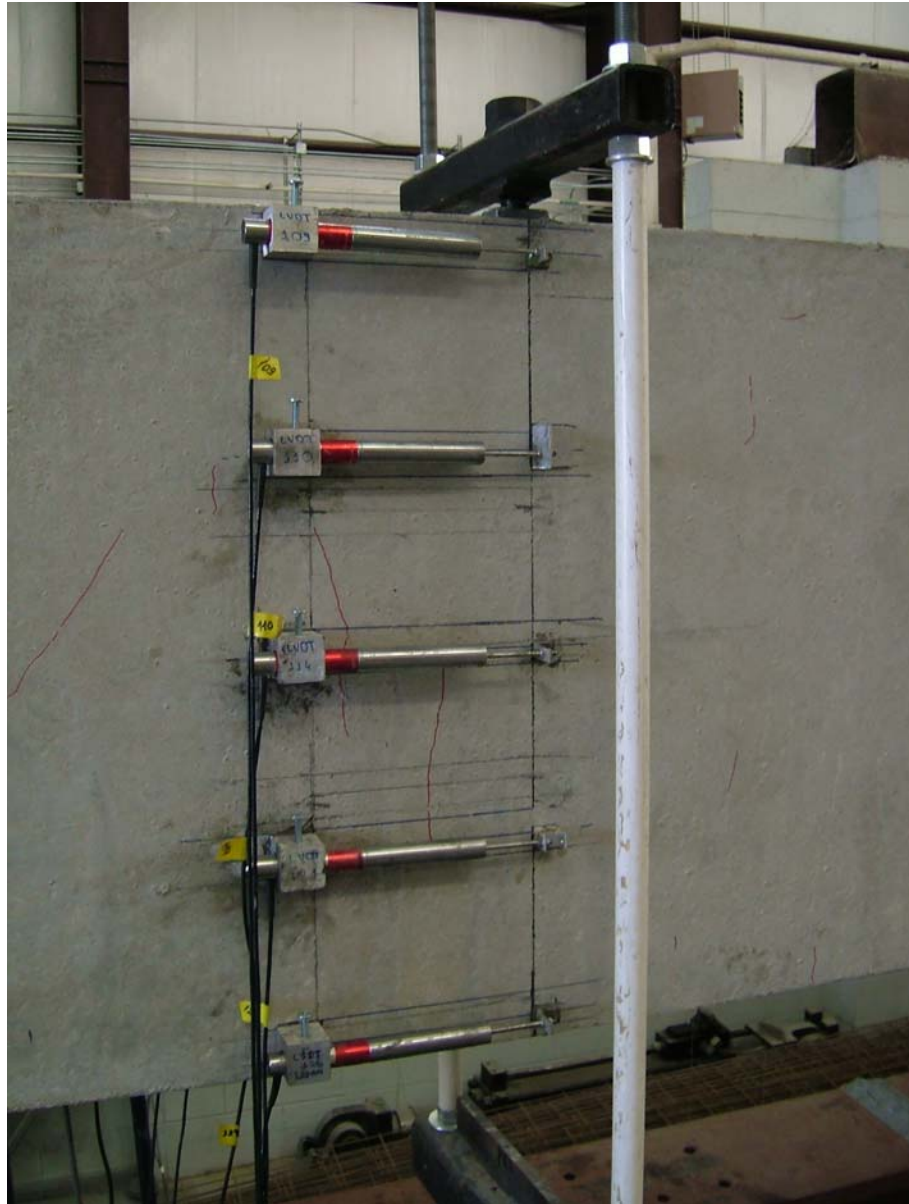


Figure 3.23 – Strain measurement using LVDT's in the first set of tests

#### 3.1.3.1 LVDT Strain Measurements

Each LVDT was placed in an aluminum box glued to the side face of the specimen (Figure 3.23). The extension rod of the LVDT core (armature) was attached to an aluminum plate bonded to the side face of the specimen. The initial longitudinal distance between the box and plate was the gage length, over which the strain was measured. As



Figure 3.24 – Strain measurement through electrical resistance strain gauges in the second set of tests

the beam bent in and out of plane, the longitudinal distance between the box and plate changed, causing the armature to slide inside the LVDT tube. The strain was calculated from the slide of the armature. Nevertheless, it was found out that the slide of the armature was not equal to the change in the longitudinal distance between the box and plate. The out-of-plane bending deformations in the beam caused the extension rod, connecting the armature to the plate, to bend and lose its initial straightness, which

caused the measurement taken by the LVDT to be different from the axial elongation or shortening of beam at the LVDT location. Therefore, LVDT's were not used for measuring the strains in the second set of experiments.

#### 3.1.3.2 Strain Measurements through Electrical Resistance Strain Gauges

In the first test of the second stage of the experimental program (Specimen B44-1), the longitudinal strains from in-plane and out-of-plane bending and the depthwise strains from the possible distortions in the cross-section of the beam were measured through two-element cross strain gauges, attached to the side faces of the beam at mid-span (Figure 3.25). The strain gage oriented in the depthwise direction was used for detecting the possible distortions in the cross-section of the beam. Three-element rosettes were not needed since the longitudinal and depthwise strains were estimated to be the principal strains due to negligible shear stresses from shear forces and torsional moments at midspan.

Strain was measured at five points along the depth of the beam (Figure 3.26) to determine the strain distributions on the convex and concave faces of the beam. Appendix C presents the longitudinal strain distributions along the convex and concave faces of the second set of specimens at midspan. The depthwise strains measured at midspan of B44-1 are also given in the appendix.

The strain measurements in the first test (B44-1) indicated that the depthwise strains did not reach significant levels prior to buckling. Therefore, in the remaining tests individual gauges, measuring the longitudinal strains only, were used instead of cross gauges (Figure 3.26).



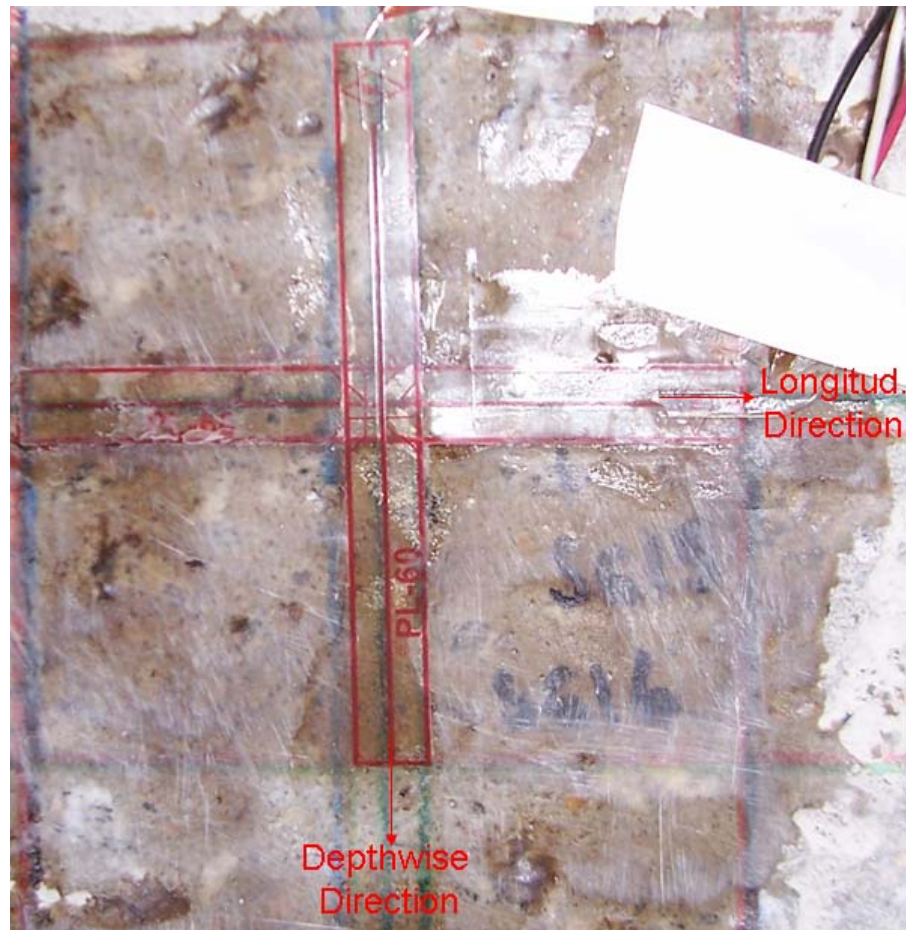


Figure 3.25 - 2-element cross strain gauge on the side face of B44-1

In the test of B44-1, strain measurements in the tension zone were greatly influenced by flexural cracking. Cracks which formed directly under the gauges caused the measured strain values to be extremely high. To measure the tensile strains in the remaining tests, the strain gauges on the tension side of the beam were installed on aluminum strips, which were attached to the face of the beam by means of concrete drop-in anchors and bolts (Figure 3.27) to prevent the slip of the strips during the tests. The strain gauges installed on the aluminum strips measured the average tensile strain between the two points, where the strip was attached to the side face of the beam.

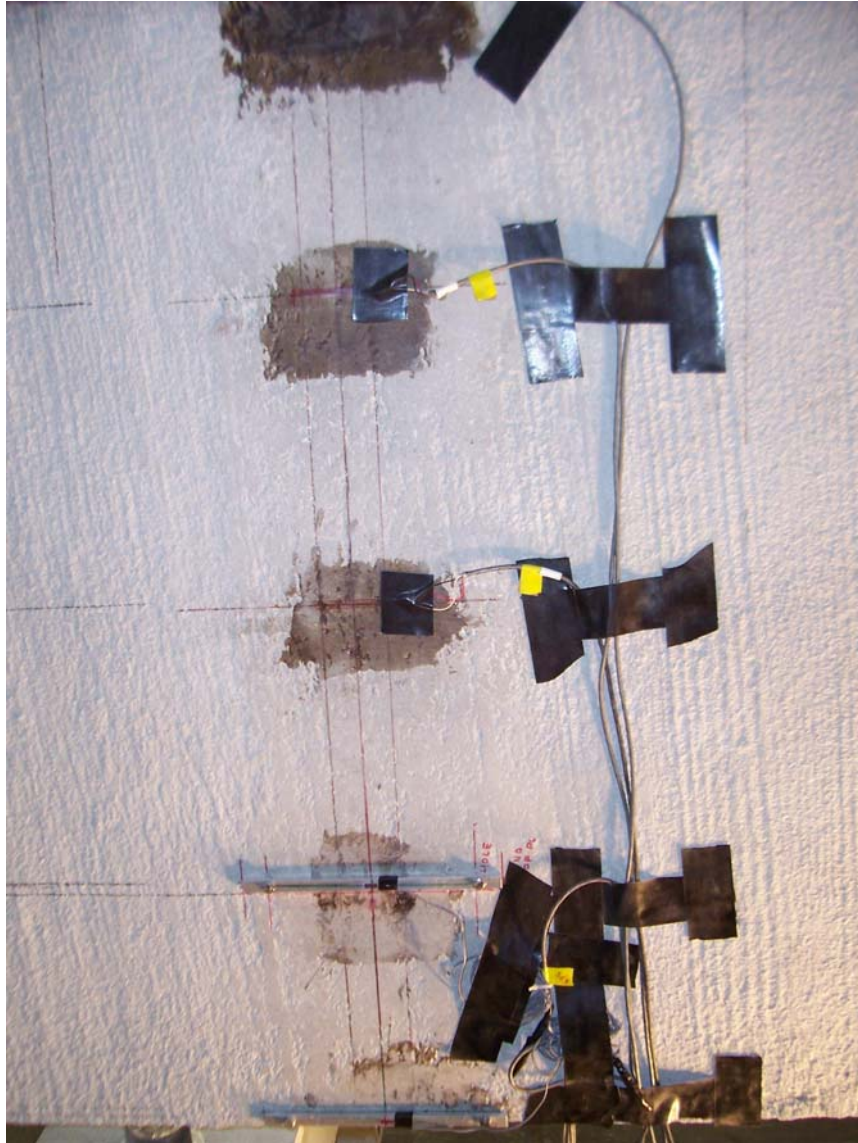


Figure 3.26 – Longitudinal strain gauges along the depth of north face of specimen B44-2 at midspan

Consequently, the tensile strain measurements were not affected from the flexural cracking in the tension zone. Full-bridge strain gauge circuits (Figure 3.27) composed of two transverse and two longitudinal gages were installed on some of the aluminum strips to cancel the accidental bending strains in the strips and to measure the axial strains only.

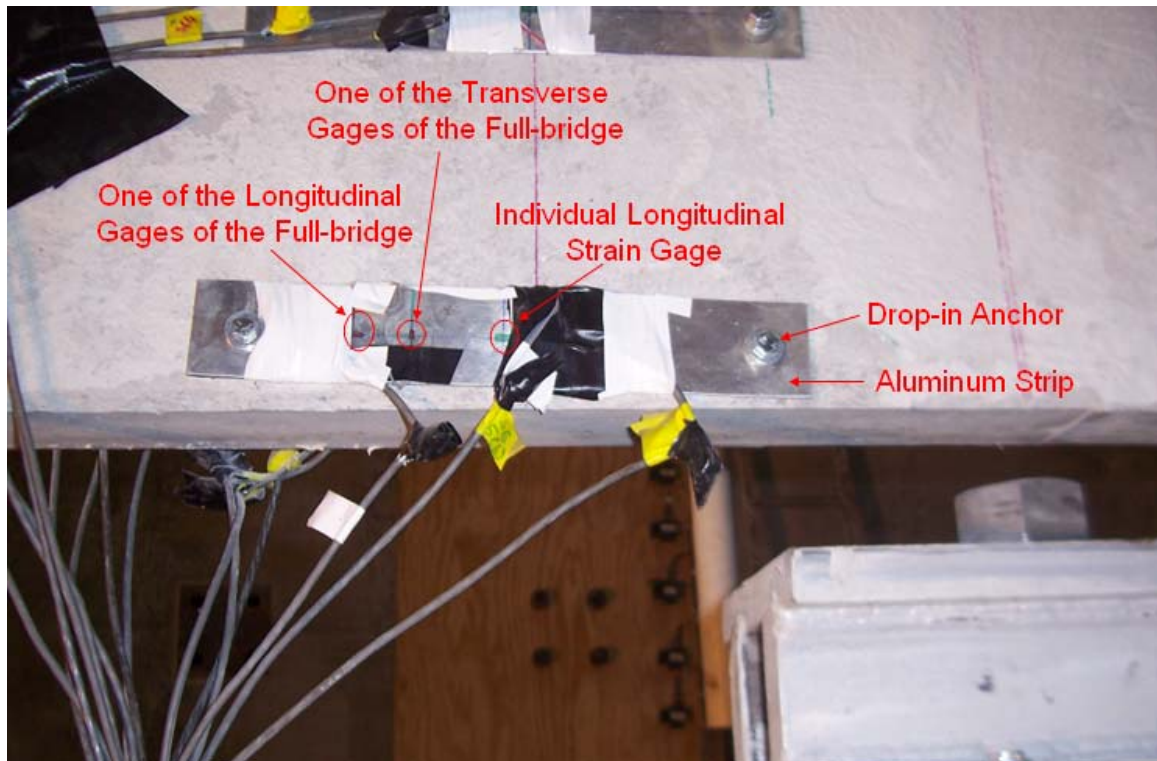


Figure 3.27 –Electrical resistance strain gauges on an aluminum strip for measuring the longitudinal strain in the tension zone

### 3.2 Test Procedure

The beams were positioned on their sides during the construction stage. After the concrete was set, each specimen was tilted into the vertical position and moved to the test setup through a special lifting method which is explained in Appendix G. The sweep and initial twisting angles of the specimens were measured prior to the tests (Appendix B).

The beams were loaded to failure. To detect the experimental cracking load of each specimen and to explore the extension of in-plane flexural cracks, loading was stopped at every 1-to-2 kip load increment at the initial stages of the test. Once the rate of increase in the out-of-plane deflections and torsional rotations became large, the beams were loaded to failure without interruption.



### **3.3 Summary of the Test Results**

All specimens of the present experimental program failed in lateral torsional buckling. Table 3.1 presents the experimental buckling loads of the specimens and the centroidal lateral and vertical deflections and the torsional rotations at midspan at the instant of buckling.

In all specimens, the typical crack pattern of lateral torsional buckling, which is explained in Chapter VII, was observed. The experimental load-lateral (out-of-plane) deflection, load-vertical (in-plane) deflection and torque-twist curves of the specimens are presented in Appendix D. The midspan strain distributions of the beams throughout the test are presented in Appendix C.

The tests indicated that the initial geometric imperfections, sweep (initial lateral deflection) in particular, significantly influence the lateral stability of a reinforced concrete beam. Section 6.3 explains the effects of the initial geometric imperfections on the lateral stability and load-lateral deflection behavior of reinforced concrete beams in the light of the results of the present experimental program.

Table 3.1 – Experimental Results of the Specimens

<b>Specimen</b>	<b>Buckling Load (kips)</b>	<b>Lateral Deflection at Centroid (in.)</b>	<b>Vertical Deflection at Centroid (in.)</b>	<b>Angle of Twist (degrees)</b>
<b>B18-1</b>	12.4	1.12	0.37	1.17
<b>B18-2</b>	12.0	1.18	0.35	0.45
<b>B22-1</b>	8.7	2.06	0.24	1.66
<b>B22-2</b>	11.0	1.44	0.22	0.90
<b>B30</b>	22.0	1.82	0.48	0.86
<b>B36</b>	39.2	0.39	0.40	0.52
<b>B44-1</b>	15.2	2.81	0.55	0.77
<b>B44-2</b>	12.0	2.12	0.48	0.55
<b>B44-3</b>	21.0	2.58	0.78	0.66
<b>B36L-1</b>	13.5	2.82	0.84	0.70
<b>B36L-2</b>	21.7	1.48	1.37	0.65

## **CHAPTER IV**

### **LATERAL BENDING RIGIDITY OF RECTANGULAR REINFORCED CONCRETE BEAMS AND INFLUENCE OF SHRINKAGE CRACKING ON THE RIGIDITY**

#### **4.1 Introduction**

Rigidity of a beam against bending moments about the minor axis is termed as the lateral (or out-of-plane) bending rigidity. Lateral bending rigidity is the product of two variables: (1) the second moment of area about the minor axis of the section ( $I_y$ ); and (2) the modulus of elasticity ( $E$ ), reflecting the overall material resistance of the beam at the initiation of buckling. Determination of the lateral bending rigidity of a reinforced concrete beam is not straightforward due to the variation in  $I_y$  and  $E$  as loading progresses. The flexural cracks in a beam render some portions of the beam ineffective in resisting flexural moments. Therefore, sectional response of a concrete beam to lateral bending ( $I_y$ ) is not constant throughout the test. Secondly, the stress-strain behavior of concrete is linear and elastic only up to the elastic limit, assuming that the proportionality limit of concrete is equal to the elastic limit. If a reinforced concrete beam or some portions of it is strained beyond the elastic limit of concrete, the material response of the beam cannot be reflected through  $E$  and another modulus of elasticity should be used to account for the inelastic material behavior of concrete. Accordingly, the lateral bending rigidity expression proposed for reinforced concrete beams should take into account the elastic-inelastic material behavior of concrete, the non-homogeneous nature of a reinforced concrete beam, and the reduction due to cracking in the cross-sectional area of the beam providing the bending rigidity.

Different lateral bending expressions for reinforced concrete beams in the literature are summarized in Section 1.3. In the following section, only the lateral bending rigidity expressions that are used in the analysis of the experimental results are explained in more detail. In Section 4.3, the lateral bending rigidity expression proposed in the present study is presented. The proposed rigidity expression is developed based on modeling a reinforced concrete beam with a system of springs. Section 4.3 also discusses the spring system models used by Bischoff (2007) and Bischoff and Scanlon (2007) in explaining the differences between the effective moment of inertia expressions proposed by Branson (1963) and Bischoff (2005). Finally, influence of restrained shrinkage cracking on the lateral bending rigidity of reinforced concrete beams is explained in Section 4.4, where the lateral bending rigidity expression, proposed in the present study, is modified to account for the effect of shrinkage cracks. Furthermore, factors that promoted the formation of the shrinkage cracks in the first set of beams and the measures taken to prevent shrinkage cracking in the second set of beams are also discussed in Section 4.4.

## 4.2 Available Lateral Bending Rigidity Expressions

In the analytical study, four different lateral flexural rigidity expressions were used in addition to the rigidity expression proposed in the present study. The first expression is the lateral flexural rigidity of a homogeneous and elastic beam:

$$B_{eh} = E_c \cdot \frac{b^3 \cdot h}{12} \quad (4.1)$$

where  $E_c$  is the elastic modulus of concrete;  $b$  and  $h$  are the width and height of the beam, respectively.

Equation (4.1) takes into account the contribution of the entire cross-section of a beam to lateral bending rigidity and therefore neglects the reduction in the bending rigidity due to flexural cracking. Furthermore, the use of  $E_c$  in the equation reveals that the entire beam is assumed to be stressed in the elastic range of the stress-strain curve of concrete, up to buckling, which is true in elastic lateral torsional buckling of reinforced concrete beams only. In the case of inelastic buckling,  $E_c$  does not represent the overall material rigidity of concrete in a beam at the time of buckling.

Although Equation (4.1) neglects the contribution of the reinforcement to the bending rigidity, ignores the reduction in the rigidity due to the presence of flexural cracks and considers the elastic buckling only, the equation was included in the analytical study to determine the influence of flexural cracking, reinforcement and inelastic material behavior of concrete on the lateral stability of concrete beams.

Equations (4.2), (4.3) and (4.4) are the lateral bending rigidity expressions proposed by Hansell and Winter (1959), Sant and Bletzacker (1961) and Massey (1967), respectively. The expressions were previously presented in Section 1.3 of Chapter I.

$$B_{hw} = E_{\text{sec}} \cdot \frac{b^3 \cdot c}{12} \quad (4.2)$$

$$B_{sb} = E_r \cdot \frac{b^3 \cdot d}{12} \quad (4.3)$$

$$B_m = E_{\text{sec}} \cdot \frac{b^3 \cdot c}{12} + E_s \cdot \Sigma I_{sy} \quad (4.4)$$

where  $B_{hw}$ ,  $B_{sb}$ ,  $B_m$  are the lateral flexural rigidities according to Hansell and Winter (1959), Sant and Bletzacker (1961) and Massey (1967), respectively;  $c$  is the neutral axis depth of the midspan section of a beam at the initiation of buckling;  $d$  is the effective depth of the beam;  $E_s$  is the elastic modulus of the reinforcing steel;  $\Sigma I_{sy}$  is the moment of inertia of the longitudinal reinforcing bars about the minor axis of the section;  $E_{sec}$  and  $E_r$  are the secant and reduced modulus of elasticity of concrete corresponding to the extreme compression fiber strain at the instant of bifurcation, respectively.  $E_r$  is calculated from Equation (4.5):

$$E_r = \frac{4 \cdot E_c \cdot E_{tan}}{\left(\sqrt{E_c} + \sqrt{E_{tan}}\right)^2} \quad (4.5)$$

where  $E_{tan}$  is the tangent modulus of elasticity of concrete corresponding to the extreme compression fiber strain at the instant of buckling.

Equations (4.2)-(4.4) offer different approaches to account for the possible inelastic material behavior of concrete at the instant of buckling, by proposing the use of different types of modulus of elasticity ( $E_{sec}$  and  $E_r$ ). Equations (4.2) and (4.4) account for the destabilizing effect of flexural cracks, by considering the minor axis moment of inertia of the compression zone only. Finally, Equation (4.4) accounts for the contribution of the longitudinal reinforcement to the lateral bending rigidity through the use of the second term on the right hand side of the equation ( $E_s \cdot \Sigma I_{sy}$ ). Equations (4.1)-(4.4) are included in the study to compare the results obtained from these equations to the lateral bending rigidity values obtained from the rigidity equation proposed in the present study.

### 4.3 Proposed Lateral Bending Rigidity Expression

The proposed lateral bending rigidity expression was developed through spring models. The idea of using springs in modeling the bending behavior of beams originated from the works of Bischoff and Scanlon (2007) and Bischoff (2007), who used spring models to justify the effective moment of inertia ( $I_e$ ) expression developed by Bischoff (2005). For a better understanding of the spring model used in the present study, the effective moment of inertia expression proposed by Bischoff (2005) and the spring model corresponding to this expression is explained in the following discussion.

Prior to the formation of flexural cracks in the tension zone of a beam, the entire cross-section of the beam contributes to the moment of inertia, which is obtained from Equation (4.6) by also considering the contribution of the flexural reinforcement:

$$I_{ucr} = \frac{1}{12} \cdot b \cdot h^3 + b \cdot h \cdot \left( \bar{y} - \frac{h}{2} \right)^2 + (n-1) \cdot A_s \cdot (d - \bar{y})^2 \quad (4.6)$$

where  $A_s$  is the cross-sectional area of the flexural reinforcement;  $n$  is the modular ratio of steel to concrete;  $\bar{y}$  is the depth of the center of gravity of the transformed section from the top surface of the beam. When calculating the uncracked moment of inertia,  $I_{ucr}$ , the flexural reinforcement is transformed into an equivalent concrete area in accordance with the modular ratio of steel to concrete,  $n$ . The gross moment of inertia of a concrete beam ( $I_g$ ), on the other hand, is calculated from Equation (4.7):

$$I_g = \frac{1}{12} \cdot b \cdot h^3 \quad (4.7)$$

The contribution of the flexural reinforcement to the moment of inertia can be neglected and  $I_{ucr}$  can be simplified to  $I_g$  in reinforced concrete beams with low reinforcement ratios.

When the bending moment at a cross-section reaches the cracking moment ( $M_{cra}$ ), flexural cracks form in the outermost layers of the tension zone. As the bending moment increases, the flexural cracks propagate upwards, rendering a greater area in the tension zone ineffective in resisting bending. Therefore, moment of inertia of the section decreases as loading progresses and the moment of inertia reaches a minimum limit, called the cracked moment of inertia ( $I_{cr}$ ) in serviceability limits.  $I_{cr}$  is calculated from Equation (4.8):

$$I_{cr} = \frac{1}{12} \cdot b \cdot c^3 + n \cdot A_s \cdot (d - c)^2 \quad (4.8)$$

where  $c$  is the neutral axis depth when all fibers in the compression zone are stressed below the elastic limit of concrete.

Bending moments exceeding  $M_{cra}$  result in discrete cracks along the length of a concrete beam. The difference in the moments of inertia of the cracked parts and the uncracked parts of a beam causes variation in the flexural rigidity along the span. Concrete between the discrete cracks contributes to resist the tensile stresses in the beam and increases the overall flexural rigidity. The tensile contribution of the concrete between the cracks is called tension stiffening. Formation of discrete flexural cracks along the span and tension stiffening raise a gradual transition of the moment of inertia of a beam from the uncracked moment of inertia ( $I_{ucr}$ ) to the cracked moment of inertia ( $I_{cr}$ ), as the applied moment ( $M_a$ ) increases beyond  $M_{cra}$ . The gradual transition in the post-



cracking stage was taken into account by Branson (1963), who proposed an effective moment of inertia expression, which is a weighted average of the moment of inertia of the gross cross-section ( $I_g$ ) and the moment of inertia of the fully cracked transformed cross-section ( $I_{cr}$ ):

$$I_{eb} = \left( \frac{M_{cra}}{M_a} \right)^3 \cdot I_g + \left[ 1 - \left( \frac{M_{cra}}{M_a} \right)^3 \right] \cdot I_{cr} \quad (4.9)$$

where  $I_{eb}$  is the effective moment of inertia according to Branson (1963);  $M_a$  is the maximum bending moment along the span; and  $M_{cra}$  is the cracking moment of the beam. Equation 4.9 is the effective moment of inertia expression recommended in ACI 318-05 (2005) Section 9.5.2 to compute the immediate vertical deflections of reinforced concrete beams.

Branson's (1963) expression concerning the effective moment of inertia is an empirical equation, which is based on test results of simply-supported rectangular reinforced concrete beams with a reinforcement ratio of 1.65 %. Later, Bischoff (2005) found that Equation (4.9) overestimates the effective moment of inertia of concrete beams with low steel reinforcement ratios ( $\rho_f < 1\%$ ) and concrete beams reinforced with fiber-reinforced polymer bars. Using the tension stiffening strain approach, Bischoff (2005) was able to develop the following alternative effective moment of inertia expression:

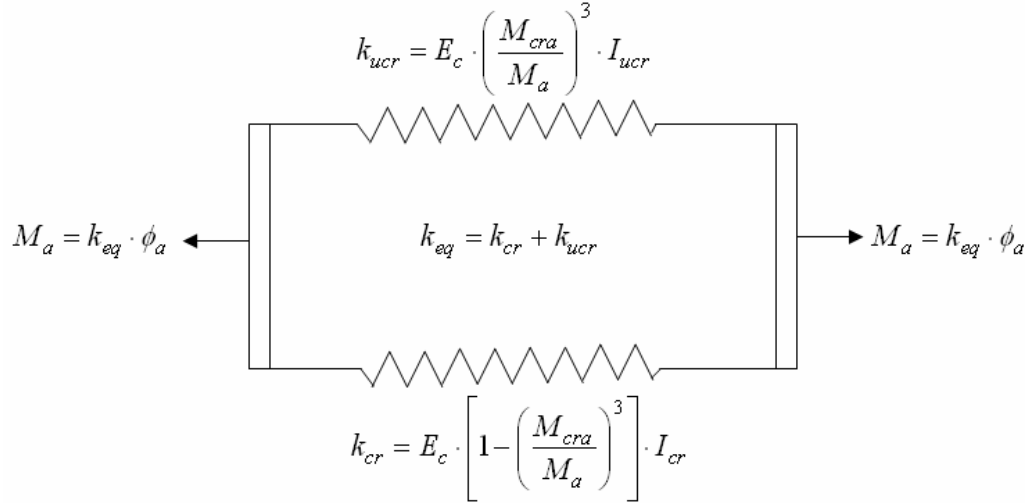
$$\frac{1}{I_{ebi}} = \left( \frac{M_{cra}}{M_a} \right)^2 \cdot \frac{1}{I_g} + \left[ 1 - \left( \frac{M_{cra}}{M_a} \right)^2 \right] \cdot \frac{1}{I_{cr}} \quad (4.10)$$

Equation (4.10) is different from the expression of Branson (1963), which is an average of the rigidities of the uncracked and cracked portions of a beam. Bischoff's (2005) effective moment of inertia was developed through averaging the flexibilities of the uncracked and cracked parts.

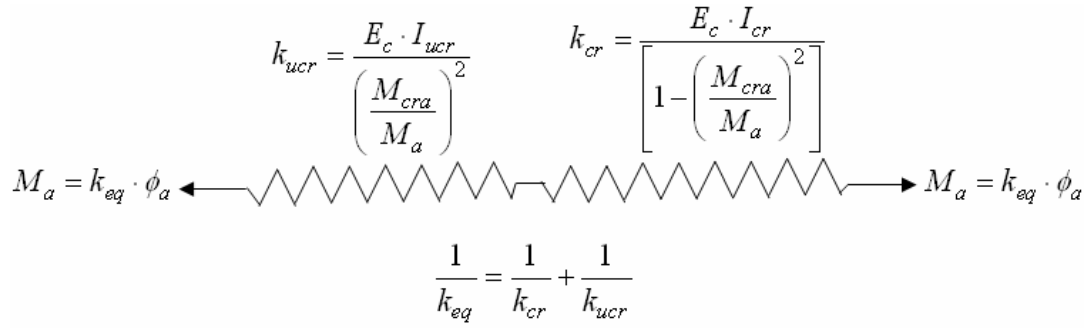
According to Bischoff and Scanlon (2007), the difference between Branson's (1963) effective moment of inertia ( $I_{eb}$ ) and Bischoff's (2005) effective moment of inertia ( $I_{ebi}$ ) can be explained through spring models.  $I_{eb}$ , which is the weighted average of the rigidities, can be obtained by modeling the uncracked and cracked parts of a beam through springs in parallel [Figure 4.1(a)].  $I_{ebi}$ , nevertheless, is obtained by modeling the uncracked and cracked portions of a beam with springs in series [Figure 4.1(b)].

Figure 4.1 (b) illustrates that springs in series carry the same load (applied moment,  $M_a$  in this case), whereas the parallel connection of springs in Figure 4.1(a) implies that the load is distributed to the springs in accordance with their rigidities. A discrete crack in the span and an uncracked portion right adjacent to it are subjected to approximately the same bending moment and therefore modeling the uncracked and cracked parts of a beam with springs in series is more appropriate.

Later, the experiments carried out by Gilbert (2006) on simply-supported rectangular one-way slabs revealed that the sectional resistance of reinforced concrete flexural members with low reinforcement ratios ( $\rho_f < 1\%$ ) was overestimated by Branson's (1963) effective moment of inertia expression, while Bischoff's (2005) effective moment of inertia expression produced immediate vertical deflections in close agreement with the experimental deflections of the specimens.



(a)



(b)

Figure 4.1- Spring models defining (a) Branson's (1963); (b) Bischoff's (2005) effective moment of inertia expression

For the present study, Figures (4.2) to (4.6) compare the experimental vertical deflections of the second set of specimens (B44 and B36L) with the analytical values calculated using Branson's (1963) and Bischoff's (2005) effective moment of inertia expressions.

According to Bischoff and Scanlon (2007), the analytical deflection estimates based on both Equations (4.8) and (4.9) are in close agreement with each other when the steel reinforcement ratio of a concrete beam is above 1%. Specimens B44 and B36L had

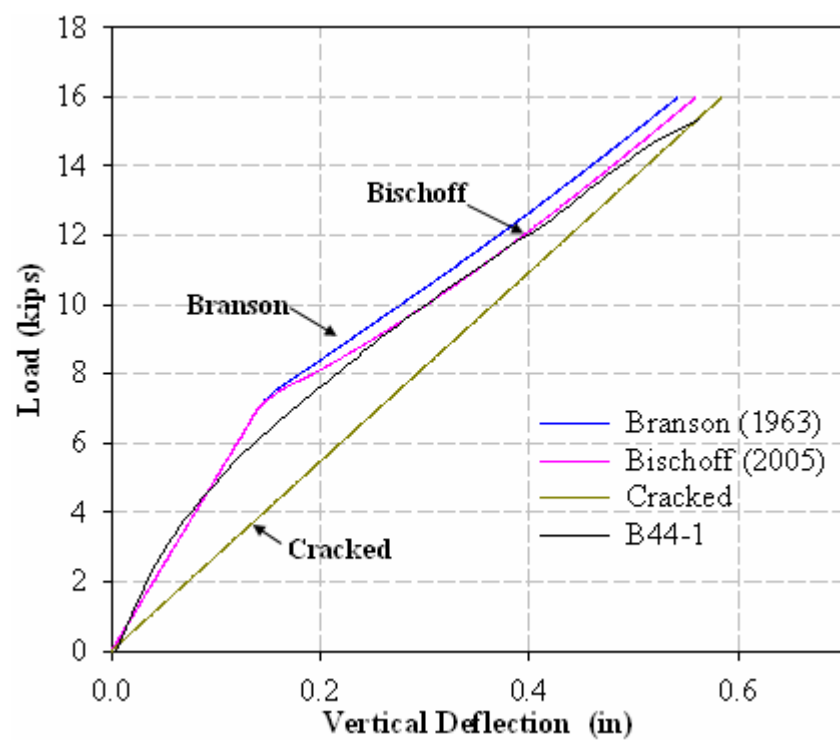


Figure 4.2 – In-plane deflections of B44-1 at midspan

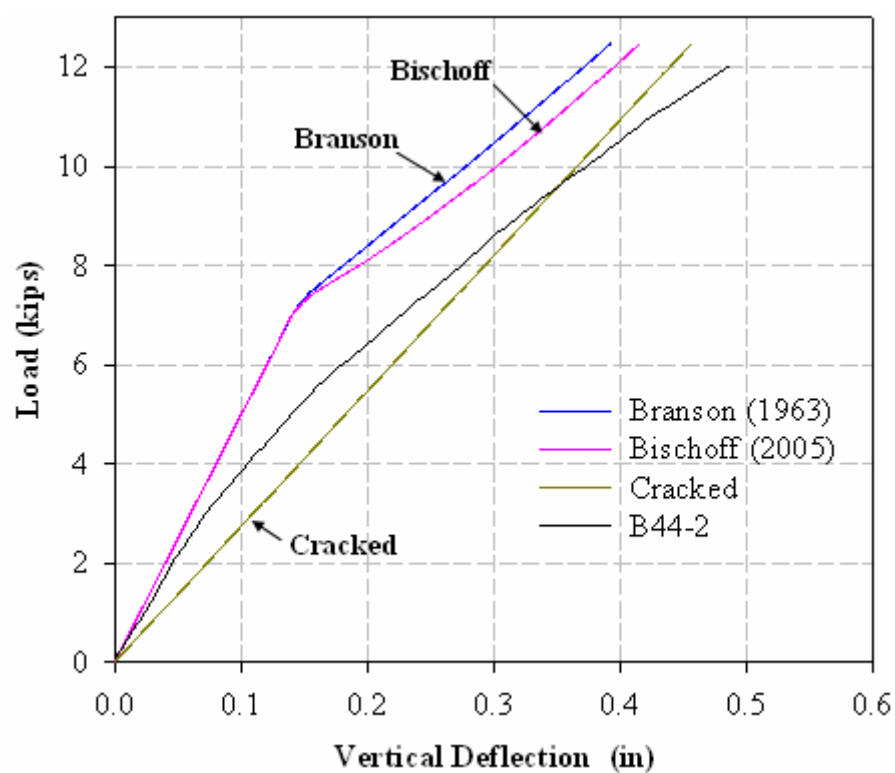


Figure 4.3 – In-plane deflections of B44-2 at midspan

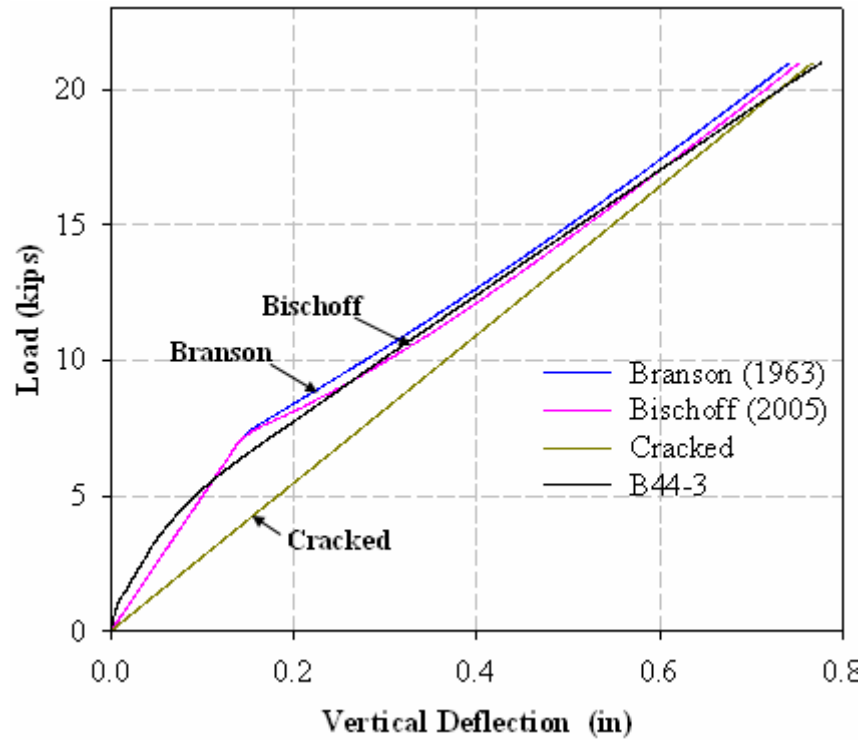


Figure 4.4 – In-plane deflections of B44-3 at midspan

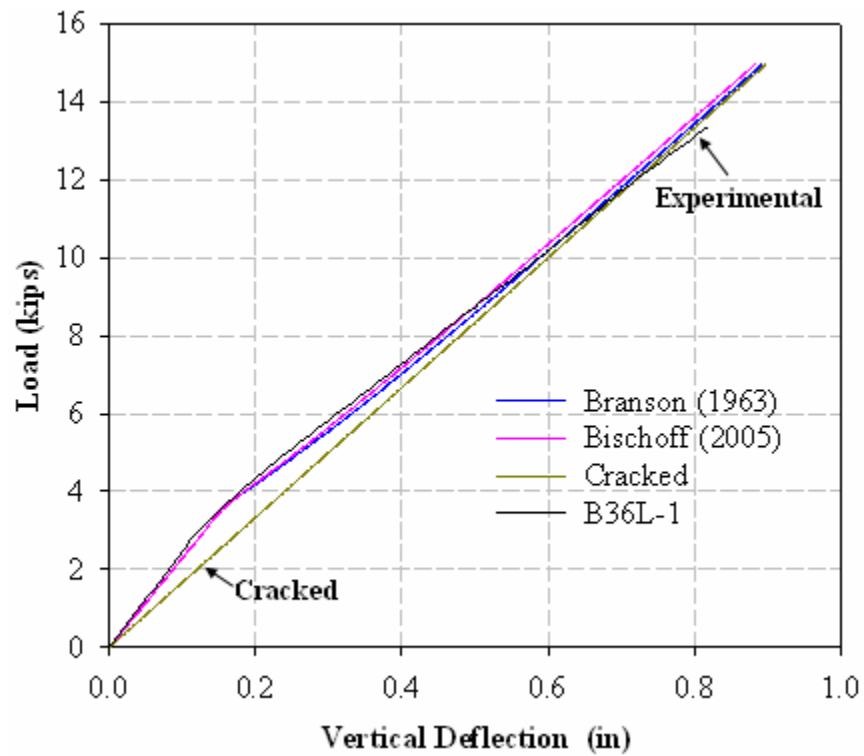


Figure 4.5 – In-plane deflections of B36L-1 at midspan

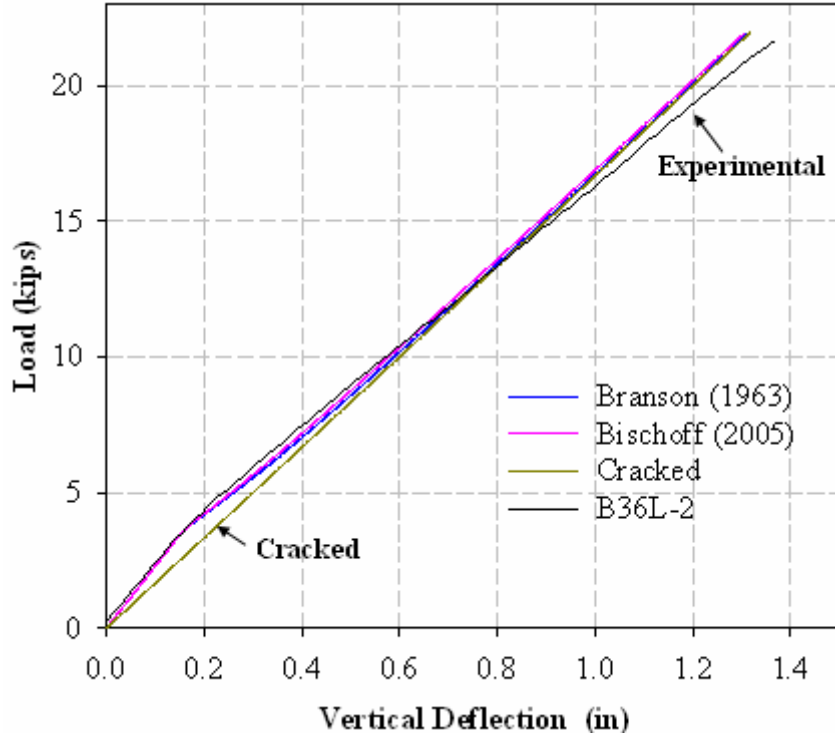


Figure 4.6 – In-plane deflections of B36L-2 at midspan

reinforcement ratios of 2.5% and 2.8%, respectively. Although in Figures 4.5 and 4.6, the analytical deflection curves corresponding to  $I_{eb}$  and  $I_{ebi}$  are only slightly different from each other, Figures 4.2 to 4.4 reveals that Bischoff's (2005) effective moment of inertia expression ( $I_{ebi}$ ) produces closer estimates to the experimental values.

The experimental curves of B36L-1 and B36L-2 in Figures 4.5 and 4.6 are in close agreement with the analytical curves corresponding to  $I_{eb}$  and  $I_{ebi}$ . Nevertheless, the experimental curves of B44-1, B44-2 and B44-3 in Figures 4.2 to 4.4 do not show a good agreement with the analytical curves due to the significant differences between the experimental cracking moment values of the specimens (Table 4.1) and the cracking moment values obtained from Equation (4.11), which was used for obtaining the analytical curves corresponding to  $I_{eb}$  and  $I_{ebi}$ .

$$M_{cra} = \frac{I_{ucr} \cdot (7.5 \cdot \sqrt{f'_c})}{h - \bar{y}} \quad (4.11)$$

where  $7.5 \cdot \sqrt{f'_c}$  is the modulus of rupture of normal-weight concrete, given in ACI 318-05 (2005) Section 9.5.2.3.

Table 4.1 – Experimental and calculated cracking moments of the second set of specimens

Specimen	Experimental $M_{cra}$ (in-kips)	Calculated $M_{cra}$ (in-kips)
<b>B44-1</b>	470	870
<b>B44-2</b>	530	870
<b>B44-3</b>	480	870
<b>B36L-1</b>	420	610
<b>B36L-2</b>	540	600

Previously, Bischoff and Scanlon (2007) and Bischoff (2007) showed that spring models well represent the in-plane bending behavior of reinforced concrete beams. Accordingly, the lateral bending behavior of reinforced concrete beams can also be represented by a spring system, if the contributions of different portions of a concrete beam can be reasonably evaluated.

The proposed spring model for the lateral bending behavior of reinforced concrete beams makes use of the reduced modulus theory [Considère (1891) and Engesser (1895)]. Here, the reduced modulus theory and its use in the proposed model are explained in detail with the help of Figure 4.7.

The proposed model is based on a geometrically perfect beam, which does not experience lateral deformations and torsional rotations prior to bifurcation. Figure 4.7 (c)

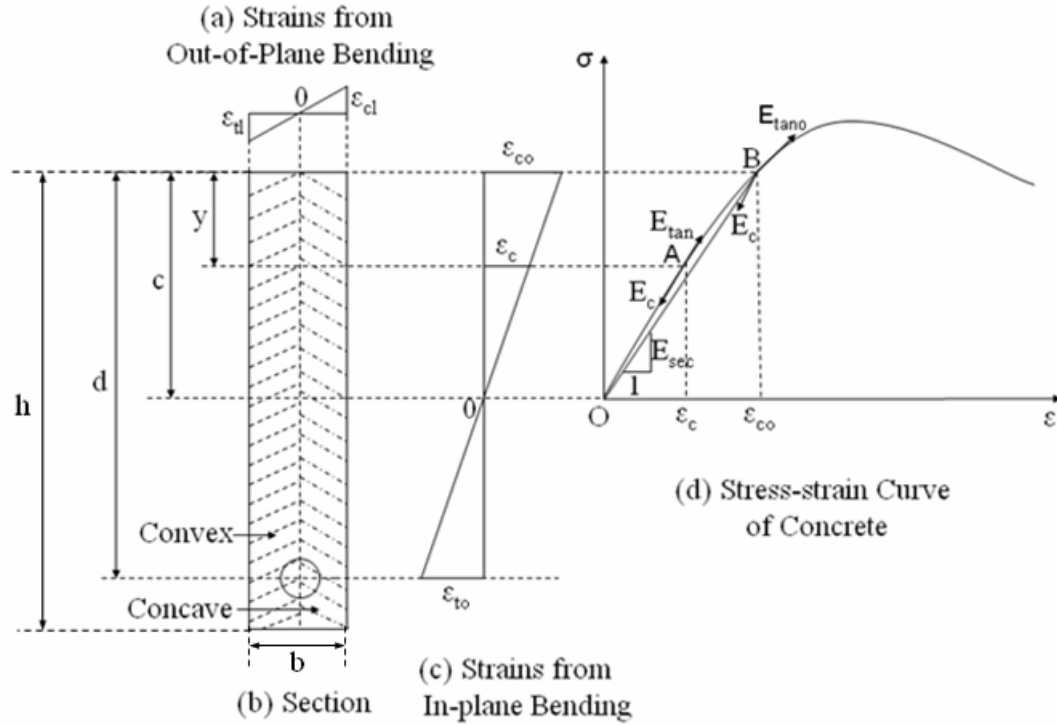


Figure 4.7 – Moduli of elasticity corresponding to the fibers in the compression zone of a beam section

is the longitudinal strain distribution along the depth of a cross-section of the beam before buckling. The longitudinal strains in the pre-buckling stage of the beam solely originate from in-plane bending moments. The compressive strain varies linearly from zero at the neutral axis to maximum ( $\epsilon_{co}$ ) at the extreme fibers and the strain at an arbitrary depth  $y$  from the compression face of the beam is denoted as  $\epsilon_c$ . Figure 4.7(d) is the stress-strain curve of concrete in compression. Since the longitudinal strain is not constant along the depth of the compression zone, compression fibers at different depths are at different points on the stress-strain curve. For instance, Point A on the curve corresponds to the fibers at a depth  $y$  while Point B corresponds to the outermost fibers. When bifurcation takes place, the concave part of the section is subjected to additional compressive strains from lateral bending while the convex part is subjected to tensile strains, as shown in



Figure 4.7(a). The longitudinal strain from out-of-plane bending increases from zero at the minor axis, which is the vertical centroidal axis in symmetric sections, to maximum ( $\epsilon_{tl}$  and  $\epsilon_{cl}$ ) at sides. Tensile strains from lateral bending cause the fibers on the convex side of the compression zone to be unloaded, while the additional compressive strains result in further loading of the compression fibers on the concave side of the section. Figure 4.7(d) illustrates that unloading of the compression fibers takes place along a line parallel to the initial linear portion of the stress-strain curve of concrete. In other words, the elastic modulus,  $E_c$  is valid for all unloading fibers in the compression zone, independent of the longitudinal strain ( $\epsilon_c$ ) of a fiber prior to buckling. The further loading of a compression fiber at an arbitrary depth  $y$ , on the other hand, takes place along a line tangent to the stress-strain curve of concrete at Point A. Since the slope of the line tangent to the curve changes along the stress-strain curve, the tangent modulus of elasticity corresponding to the loading fibers changes along the depth of the compression zone of the section.

Hansell and Winter (1959) analytically showed that the secant modulus of elasticity corresponding to the extreme compression fiber strain ( $\epsilon_{co}$ ) should be used as the material rigidity term if the entire compression zone of a section continues to be loaded after buckling. Secant modulus of elasticity ( $E_{sec}$ ) corresponding to the extreme compression fiber is the slope of the line connecting Point B on the stress-strain curve to the origin O as shown in Figure 4.7 (d). The origin of the stress-strain curve corresponds to the fibers at the neutral axis depth, which have zero longitudinal strain at the initiation of buckling. Point B, on the other hand, corresponds to the most-stressed fibers of the compression zone. Therefore, the line connecting Point B to the origin represents the

entire compression zone if all compression fibers of the section are further loaded in the post-buckling stage.

In the present study, the compression zone of a section is divided into a loading and an unloading portion after buckling, according to the reduced modulus theory. The secant modulus of elasticity,  $E_{sec}$  corresponding to the extreme compression fiber strain at the instant of bifurcation is used as the modulus of the loading part of the compression zone.

The spring model proposed in the present study is shown in Figure 4.8. A reinforced concrete beam is composed of uncracked and cracked parts along the length. Each of the uncracked and cracked portions of the beam is partitioned into a loading and an unloading segment when buckling takes place. Applied moment is distributed to the loading and unloading segments of a portion. Since a cracked portion along the span and an uncracked portion adjacent to it bear approximately the same lateral bending moment, the cracked and uncracked parts of the beam are modeled with springs in series. The loading and unloading segments of a cracked or an uncracked portion of the beam contribute to the resistance of the lateral bending moments in accordance with their flexural rigidities about the minor axis of the beam section. Hence, loading and unloading segments of a portion are modeled with springs in parallel.

In an uncracked section, the entire section contributes to resistance to the minor-axis bending moments. Therefore,  $k_1$  and  $k_2$  contain the term  $h$ . In a cracked section, on the other hand, concrete below the neutral axis is assumed not to contribute to the flexural rigidity of the beam due to the flexural cracks in the tension zone of the section.

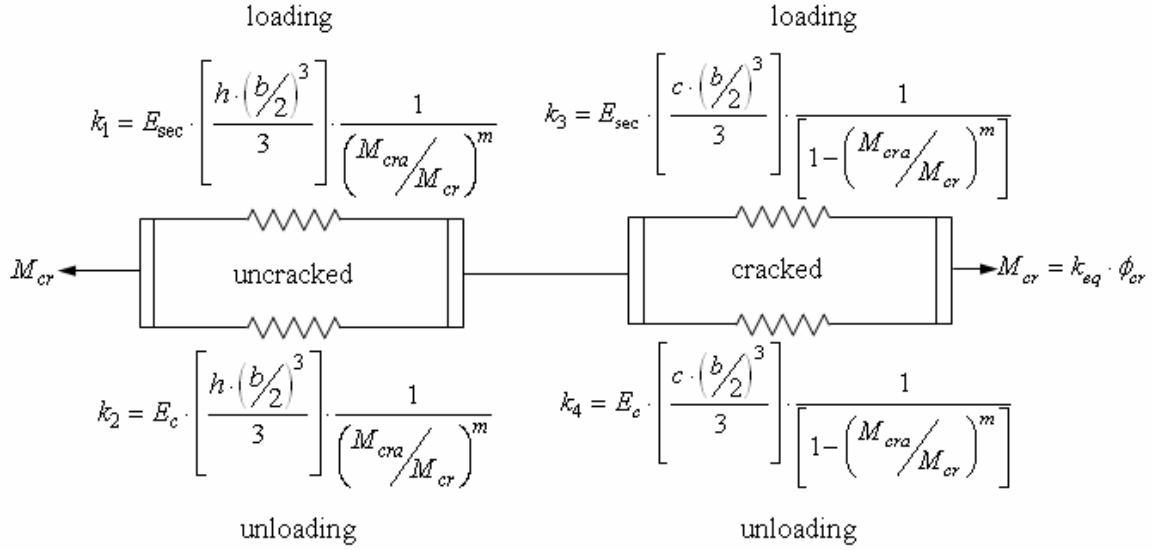


Figure 4.8 – Proposed spring model for the lateral bending behavior of reinforced concrete beams

Therefore, the neutral axis depth of the section at the initiation of buckling ( $c$ ) is used in  $k_3$  and  $k_4$ .

In the rigidity expressions  $k_1$ ,  $k_2$ ,  $k_3$  and  $k_4$ ,  $b/2$  was adopted as the width of each of the loading and unloading segments of a section. The widths of the loading and unloading segments are equal if the secant modulus of concrete ( $E_{sec}$ ) corresponding to the extreme compression fiber strain at the initiation of buckling is equal to the elastic modulus of concrete ( $E_c$ ). Having  $E_{sec}$  equal to  $E_c$  is possible only if the entire beam is stressed in the linear elastic range of concrete, which is known as the elastic lateral-torsional buckling. In the case of inelastic lateral-torsional buckling, nevertheless,  $E_{sec}$  can be much lower than  $E_c$ , causing the widths of the loading part and the unloading part of a section to be different. However,  $b/2$  was used in the equations to simplify the lateral-flexural rigidity expression.

The equivalent rigidity ( $k_{eq}$ ) of the spring system in Figure 4.8 is obtained from Equation (4.12) by also using the weight factors for the cracked and uncracked parts of a beam, previously employed by Branson (1963) and Bischoff (2005):

$$\frac{1}{k_{eq}} = \left( \frac{M_{cra}}{M_{cr}} \right)^m \cdot \frac{1}{k_1 + k_2} + \left[ 1 - \left( \frac{M_{cra}}{M_{cr}} \right)^m \right] \cdot \frac{1}{k_3 + k_4} \quad (4.12)$$

where  $M_{cra}$  and  $M_{cr}$  are the cracking moment and the critical moment of a beam, respectively. Using the expressions for  $k_1$ ,  $k_2$ ,  $k_3$  and  $k_4$ , given in Figure 4.8

$$\frac{1}{k_{eq}} = \left( \frac{M_{cra}}{M_{cr}} \right)^m \cdot \frac{1}{E_{sec} \cdot \frac{h \cdot b^3}{24} + E_c \cdot \frac{h \cdot b^3}{24}} + \left[ 1 - \left( \frac{M_{cra}}{M_{cr}} \right)^m \right] \cdot \frac{1}{E_{sec} \cdot \frac{c \cdot b^3}{24} + E_c \cdot \frac{c \cdot b^3}{24}} \quad (4.13)$$

After simplifications, the lateral flexural rigidity of a reinforced concrete beam,  $k_{eq}$  is obtained from Equation (4.14):

$$k_{eq} = \frac{b^3 \cdot c}{24} \cdot \frac{E_{sec} + E_c}{1 + \left( \frac{M_{cra}}{M_{cr}} \right)^m \cdot \left( \frac{c}{h} - 1 \right)} \quad (4.14)$$

ACI 318-05 (2005) suggests the use of a value of 3 for the power  $m$  in Equation 4.9 to obtain an average rigidity for the entire span of a reinforced concrete beam with discrete cracks along the span. Bischoff (2005), on the other hand, stated that a value of  $m=2$  in his effective moment of inertia expression (Equation 4.10) correlates well with Branson's original equation. In the present study, the spring system (Figure 4.8) models the cracked and uncracked portions of a concrete beam with springs in series, similar to

the spring model used by Bischoff (2005). Therefore, using a value of  $m=2$  was assumed to be more appropriate.

The lateral bending rigidity in Equation (4.14) can be formulated as the product of the modulus of elasticity of concrete and the effective moment of inertia of the beam about the minor axis, leading to Equation (4.15):

$$k_{eq} = \left[ \left( \frac{b^3 \cdot c}{12} \right) \cdot \frac{1}{1 + \left( \frac{M_{cra}}{M_{cr}} \right)^m \cdot \left( \frac{c}{h} - 1 \right)} \right] \cdot \left( \frac{E_{sec} + E_c}{2} \right) \quad (4.15)$$

The expression in the square brackets in Equation (4.15) is the effective moment of inertia of the beam about the minor axis. The remaining part of the equation, on the other hand, is the overall modulus of elasticity of concrete ( $E_o$ ) of the beam, calculated from Equation (4.16):

$$E_o = \left( \frac{E_{sec} + E_c}{2} \right) \quad (4.16)$$

Considering the contribution of the longitudinal reinforcement to the lateral bending rigidity is meaningful if two criteria are satisfied. First, the longitudinal rebars in a beam should remain unyielded till the buckling moment to contribute to the lateral bending resistance. Secondly, longitudinal rebars should be located close to the sides of the beam to increase the lateral distance from the minor axis, which constitutes the moment arm of the bars in lateral bending. Previously, the contribution of the longitudinal rebars to the lateral bending rigidity was taken into account by Massey (1967) and by Revathi and Menon (2006). The second term in Equation (4.4), proposed

by Massey (1967), and the term  $\psi \cdot ((E_s/E_c) \cdot \Sigma I_{sy})$  in Equation (1.29), proposed by Revathi and Mennon (2006) correspond to the longitudinal reinforcement. In the spring model employed in the present study, rigidity contributions of the longitudinal rebars to the lateral bending rigidities of the uncracked and cracked sections of a beam can be represented by a spring connected in parallel to the other two springs of each of the cracked and uncracked parts of the beam. In other words, the number of parallel springs in each of the cracked and uncracked portions should be increased to three if the contribution of the longitudinal reinforcement is desired to be included in the rigidity expression. Accordingly, the lateral bending rigidity expression is modified, giving Equation (4.17):

$$k_{eq} = \frac{\left[ (E_{sec} + E_c) \cdot (h \cdot b^3 / 24) + E_s \cdot \Sigma I_{sy} \right] \cdot \left[ (E_{sec} + E_c) \cdot (c \cdot b^3 / 24) + E_s \cdot \Sigma I_{sy} \right]}{(E_{sec} + E_c) \cdot (b^3 / 24) \cdot \left[ c \cdot (M_{cra} / M_{cr})^m + \left( 1 - (M_{cra} / M_{cr})^m \right) \cdot h \right] + E_s \cdot \Sigma I_{sy}} \quad (4.17)$$

where  $E_s$  is the elastic modulus of the reinforcing steel;  $\Sigma I_{sy}$  is the total moment of inertia of the longitudinal reinforcing bars about the minor axis of the section. When the longitudinal reinforcement yields prior to buckling,  $E_s$  becomes zero and Equation (4.17) reduces to Equation (4.15). Similarly, the contribution of the longitudinal reinforcement ( $E_s \Sigma I_{sy}$ ) vanishes and the equation simplifies to Equation (4.15) if the longitudinal reinforcing bars are located along the minor axis of the beam section ( $\Sigma I_{sy}=0$ ). In the specimens of the present experimental program, for example, the longitudinal rebars were located along the vertical centroidal axis of the beam, which coincides with the minor axis in the case of elastic lateral-torsional buckling. Therefore, Equation (4.15) was used in the critical moment calculations of the beams, buckling elastically.

#### 4.4 Influence of Shrinkage Cracking on the Lateral Bending Rigidity

Shrinkage is defined as the volume change in a concrete member due to the loss of water arising from the difference in relative humidity between concrete and the surrounding environment. If a concrete member is allowed to shrink freely, it will experience longitudinal deformations. If the shrinkage deformations of a beam are restrained, on the other hand, tensile stresses develop in the beam, resulting in cracking of concrete. Restrained shrinkage cracks may reduce the lateral bending resistance of a concrete beam considerably.

Influence of shrinkage restraint stresses on the flexural rigidity of concrete beams was studied by Scanlon and Bischoff (2008), who stated that shrinkage restraint stresses in a beam reduce the cracking moment. Scanlon and Bischoff (2008) proposed the use of a reduced effective cracking moment in Equation (4.10) in the presence of restrained shrinkage cracks in a beam. The reduced cracking moment value proposed by Scanlon and Bischoff (2008) is equal to 2/3 of  $M_{cr}$ . Scanlon and Bischoff (2008) also stated that the influence of shrinkage cracks on the flexural rigidity becomes more pronounced when a beam has a low longitudinal reinforcement ratio ( $\rho_l < 0.8\%$ ).

Considering the influence of the shrinkage cracks on the cracking moment, Equation (4.14) can be modified, leading to Equation (4.18):

$$k_{eq} = \left[ \left( \frac{b^3 \cdot c}{12} \right) \cdot \frac{1}{1 + \left( \frac{\omega \cdot M_{cra}}{M_{cr}} \right)^2 \cdot \left( \frac{c}{h} - 1 \right)} \right] \cdot \left( \frac{E_{sec} + E_c}{2} \right) \quad (4.18)$$

where  $\omega$  is equal to 1 in the absence of restrained shrinkage cracks in a beam and  $\omega$  is equal to 2/3 in the presence of restrained shrinkage cracks.

Shrinkage restraint comes from several sources. For instance, free shrinkage of a beam can be prevented by the structure (slab, beams) surrounding the beam. Longitudinal reinforcement in a beam and the formwork in the construction stage also have restraining effects on the shrinkage deformations of a beam.

In the first set of specimens of the present experimental program, shrinkage cracking of concrete was observed (Figure 4.9). To overcome the cracking problem in the second set of beams, the reasons for the formation of the shrinkage cracks were investigated. According to the investigation, the use of self-compacting concrete (SCC) instead of the conventionally vibrated ordinary concrete (OC) in the first set of beams might have enhanced the degree of shrinkage cracking of the beams.

Previously, various researchers investigated the vulnerability of SCC to shrinkage cracking. Loser and Leemann (2008) stated that shrinkage of a concrete mixture is primarily related to the volume of the paste in the mixture. Owing to the higher paste volume and lower aggregate content, SCC has greater total shrinkage and a higher shrinkage rate, and therefore, an earlier age of cracking than OC with comparable compressive strength if rapid drying of concrete takes place. Loser and Leemann (2008) also recommended the use of shrinkage reducing admixtures (SRA) in SCC to reduce shrinkage and increase the age of cracking of concrete. Turcry et al. (2006) conducted an experimental study, through which they concluded that an SCC mixture cracks earlier than the OC mixture with the same compressive strength due to the higher shrinkage rate. Turcry and Loukili (2006) explained the higher shrinkage rate of SCC with its lower



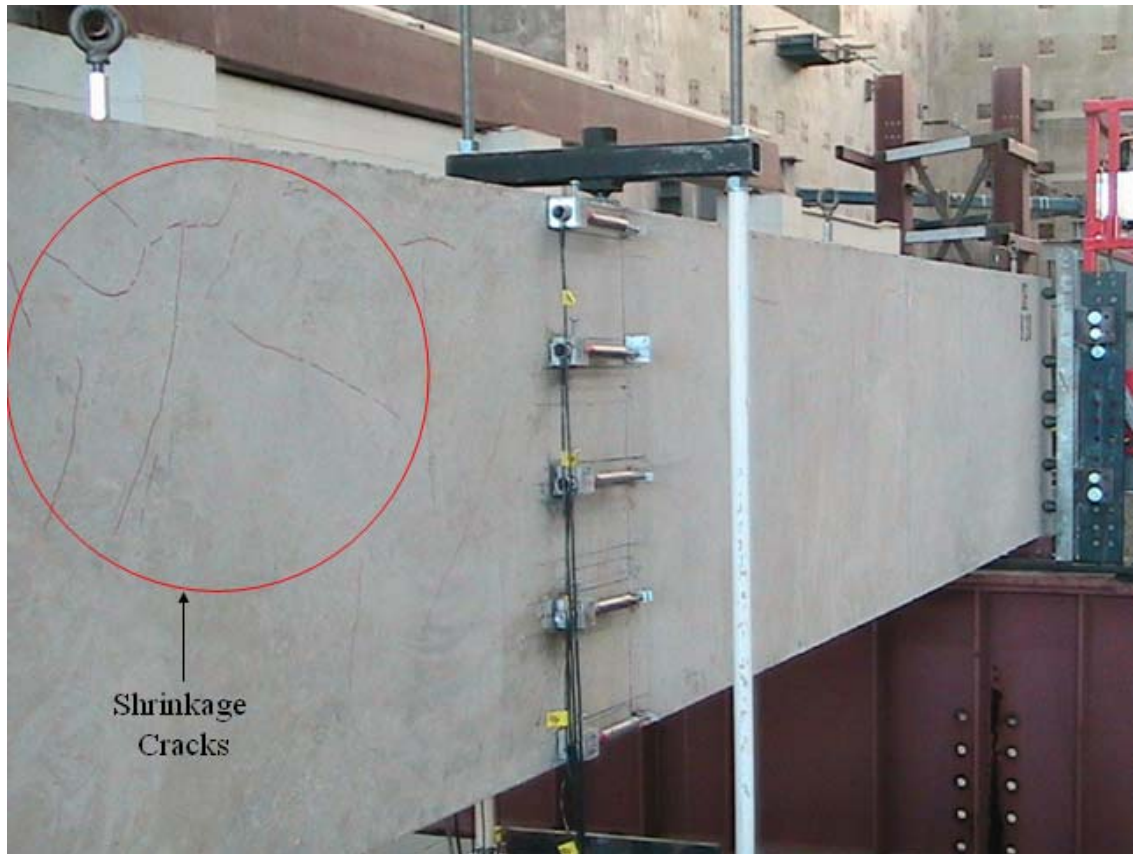


Figure 4.9 – Shrinkage cracking in B30 prior to the test

bleeding capacity than OC as a result of the higher binder content in SCC. Similarly, Leemann and Hoffmann (2005) found out that SCC has a shrinkage rate 30% higher than OC with the same compressive strength.

The high shrinkage rate of SCC might have reduced the age of shrinkage cracking of concrete and caused shrinkage cracks to form before the removal of the first set of beams from the forms. Surfaces of the beams exposed to air were kept moist using wet burlaps. However, the lower bleeding capacity and the higher shrinkage rate of SCC might have resulted in rapid drying of the surface and induced tensile stresses to concrete before the subsequent rewetting of the burlaps on the beams.

Another potential stimulus for the shrinkage cracking of the first set of beams was the late removal of the beams from their forms. The first set of beams was kept in the forms for approximately two weeks. Formwork of a concrete beam constitutes a restraint for the free shrinkage deformations. Although the open surfaces of the beams were maintained wet till the dismantling of the forms, the forms might have caused restrained shrinkage cracks to form due to higher shrinkage rate of SCC.

The early cracking age of the first set of beams in the forms was also related to the specimen geometry. The beams were cast on their sides to facilitate the concrete pour. Position of the beams in the formwork caused one of the lateral faces of each beam to be uncovered, providing a large surface for the evaporation of the bleeding water. Furthermore, the small widths of the specimens facilitated the drying to reach the internal regions and affect the entire beam rapidly. Weiss and Shah (2001) carried out an experimental study in which they observed that thinner concrete sections are less resistant to shrinkage cracking and the age of cracking decreases as the specimen thickness decreases.

In the second set of specimens, some measures were taken to prevent shrinkage cracking of concrete. First, conventionally vibrated ordinary concrete (OC) was used rather than SCC to increase the age of shrinkage cracking of concrete through the lower shrinkage rate. Secondly, the beams were removed from the forms in less than a week to eliminate the shrinkage restraint for concrete as early as possible.

Addition of the Eclipse Shrinkage Reducing Admixture (SRA), produced by Grace Construction Products, was another protective measure against restrained shrinkage cracking of concrete. Studies done by several researchers indicated the

favorable influence of SRA on the reduction of the total shrinkage and the shrinkage rate of concrete. The experimental study conducted by Shah et al. (1992) indicated that addition of SRA's to concrete greatly reduced the free shrinkage deformations and the widths of the shrinkage cracks in the case of restrained shrinkage. Lura et al. (2007) experimentally showed that the addition of SRA's to mortar reduces the evaporation of water from the surface of the mortar and causes smaller tensile stresses to develop at the surface. Therefore, mortar mixtures with SRA have fewer and narrower shrinkage cracks than the mixtures without SRA under the same environmental conditions.

Efficiency of the measures taken to avoid shrinkage cracking of concrete was examined through some methods. First, shrinkage cracks could not be detected in any of the beams constructed in the second phase of experimental program. Nevertheless, the presence of micro-cracks in concrete cannot be observed through visual inspection. Hence, two more methods were used to measure the shrinkage strains in the beams to investigate shrinkage cracking of concrete at the micro level. First, prismatic specimens with and without SRA were prepared from the concrete mixtures used in the beams. Sampling of concrete was done according to ASTM C192 (2007). Length changes of specimens were measured according to the test method described in ASTM C157 (2006). Six specimens were prepared from each of the concrete mixtures used in Beams B44 and B36L. The SRA contents and curing conditions of the specimens are tabulated in Table 4.2.

In Figure 4.10, the percent length changes of Specimens 3, 4 and 5 are compared to illustrate the influence of SRA on the volume change of concrete. According to the plot, the length change of the specimen without SRA (Specimen 5) was measured to be

Table 4.2 – Descriptions of the shrinkage specimens from the concrete mixtures used in B44 and B36L

Specimen	Addition of SRA	Curing Conditions
1	Yes	Same Conditions as the Beams
2	Yes	Same Conditions as the Beams
3	Yes	In the moist room for 28 days
4	Yes	In the moist room for 28 days
5	No	In the moist room for 28 days
6	No	In the moist room for 28 days

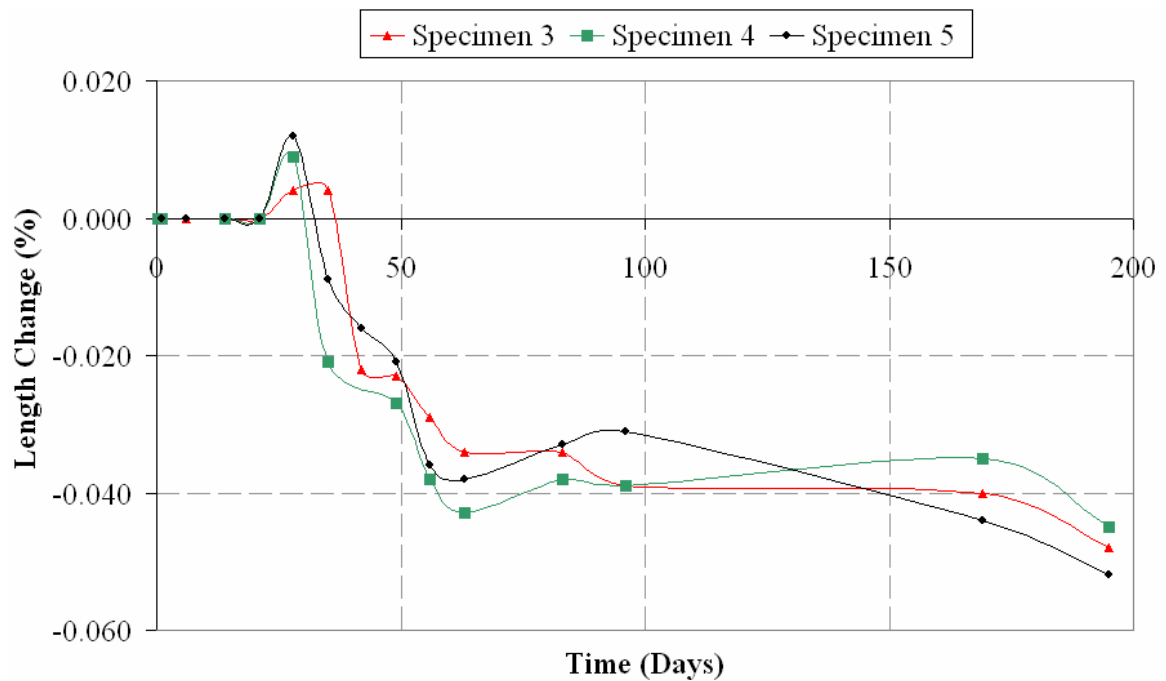


Figure 4.10 – Length changes of specimens with and without SRA from the concrete mixture of B44

close to the length changes of the specimens with SRA (Specimens 3, 4) in the first 120 days after the concrete pour. Later, Specimen 5 experienced greater length changes than the other two specimens.

Secondly, strains on the lateral faces of the specimens were continuously measured through DEMEC (Demountable Mechanical) gages to determine the restrained shrinkage stresses in the beams for monitoring for the formation of shrinkage cracks in concrete. Directions of the principal stresses originating from restrained shrinkage are not known. Hence, three independent strain measurements in different directions are needed to determine the principal strains and stresses at a certain point. To measure the stresses at the surfaces of the specimens, delta strain rosettes were formed at two different locations on the side face of each specimen in specimen group B36L.

A DEMEC gage is a mechanical device which measures the distance between two points. The gage has two conical points, one at each end of an invar bar. One of the conical points is fixed and the other conical point can move in a certain range. To measure the distance between two fixed points on a surface, the conical points of the gage are inserted into the holes drilled at the fixed point. The initial distance between the two fixed points on the beam is the gage length over which the strain is measured.

In the present study, four screw anchors were embedded into the fresh concrete at each strain measurement location according to the pattern shown in Figure 4.11. Four screws positioned in this pattern form a delta strain rosette. Strain in each direction is obtained by dividing the change in the distance between two points to the initial distance between the points, measured on the concrete pour day.

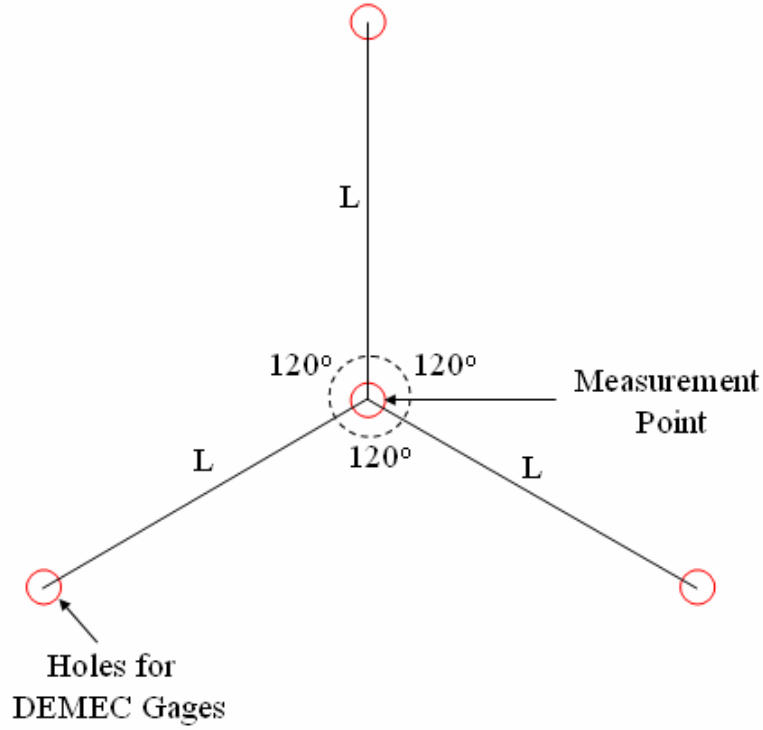


Figure 4.11 – Delta rosette for principal strain measurement at a point

Variation of the two principal strains in time is illustrated in Figures 4.12 and 4.13 for Specimens B36L-2 and B36L-3, respectively. Cracking strain of concrete ( $\epsilon_{cr}$ ) in uniaxial tension is also shown in each plot.  $\epsilon_{cr}$  is calculated from Equation (4.19):

$$\epsilon_{cr} = \frac{f_t}{E_c} \quad (4.19)$$

where  $f_t$  is the splitting tensile strength of concrete, which is obtained from Equation (4.20):

$$f_t = 6.4 \cdot \sqrt{f'_c} \quad (4.20)$$

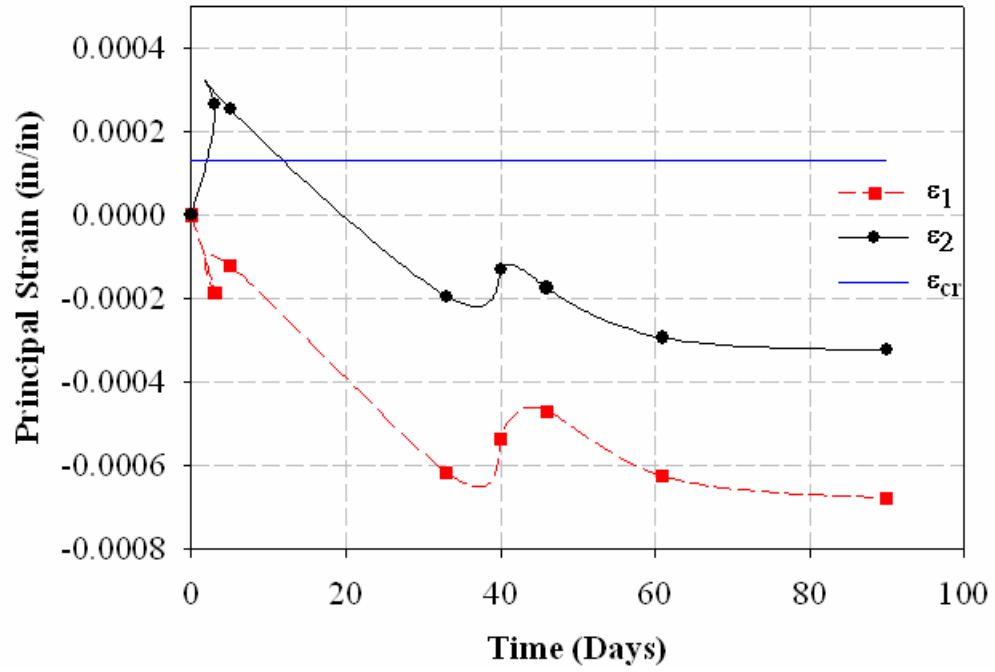


Figure 4.12 – Principal strains on the side face of B36L-2

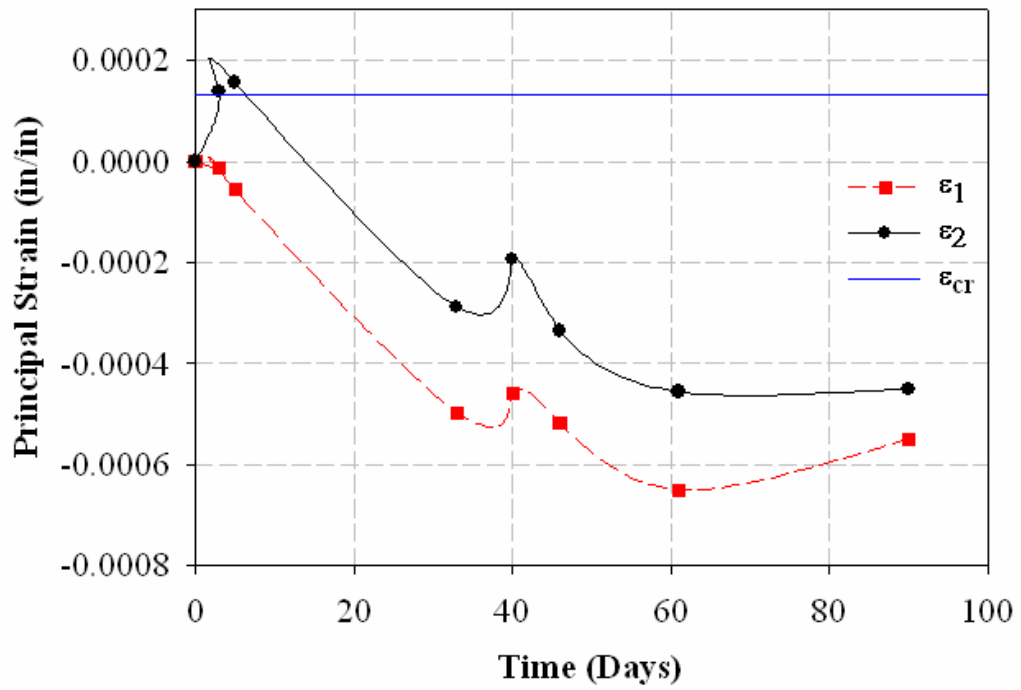


Figure 4.13 – Principal strains on the side face of B36L-3

Equation (4.20) is the tensile strength of concrete in uniaxial tension according to Mirza et al. (1979). Although the tensile strength of concrete reduces in the presence of a compressive stress in the perpendicular direction the reduction is ignorable considering the small values of the compressive principal strains in Figures 4.12 and 4.13 on the day when the tensile principal strains reached the peak values.

The plots indicate that tensile strains developed at the surfaces of the beams till the removal of the beams from the formwork, which constituted a restraint for the free shrinkage deformations. After the removal of the beams from the forms, on the other hand, the beams were subjected to compressive strains originating from the free shrinkage deformations of concrete. The tensile principal strains in the beams prior to the dismantling of the forms only slightly exceeded the cracking strain of concrete for a short period of time. Therefore, the potential shrinkage cracks in the beams are expected to be narrow and small in number.

Since the specimens of the present study did not experience significant restrained shrinkage cracking according to the aforementioned measurements, the multiplier  $\omega$  in Equation (4.18) was taken 1 in the evaluation of the lateral bending rigidities of the specimens.  $\omega$  can be taken 2/3 as a conservative assumption when the restrained cracking condition of concrete in a beam is not known.



## **CHAPTER V**

### **TORSIONAL RIGIDITY OF RECTANGULAR REINFORCED CONCRETE BEAMS**

Resistance of a beam to lateral torsional buckling is determined by the lateral bending rigidity and the torsional rigidity of the beam. The present chapter briefly introduces the torsional behavior of reinforced concrete beams and explains the evaluation of the torsional rigidity of a concrete beam in the light of the experimental torque-twist curves of the test specimens.

#### **5.1 Torsional Behavior of Reinforced Concrete Beams**

The torsional behavior of reinforced concrete beams is explained with the help of Figure 5.1, which is the typical torque-twist curve of a reinforced concrete beam with shear reinforcement. The torque-twist curve in the figure can be divided into three distinct segments: OA, AB and BC. The initial linear segment (OA) ends at point A, which corresponds to the initiation of the diagonal cracking in the beam. The slope of the line OA is termed as the uncracked torsional rigidity of the beam,  $(GC)_u$ . Prior to the formation of the diagonal tension cracks, the torsional rigidity is related to the shear strains around the perimeter of the cross-section of a beam. The entire beam behaves as a solid and homogeneous body and the contribution of the flexural and shear reinforcement to the torsional rigidity can be neglected. The uncracked torsional rigidity expressions existing in the literature are presented in Section 5.2.1.

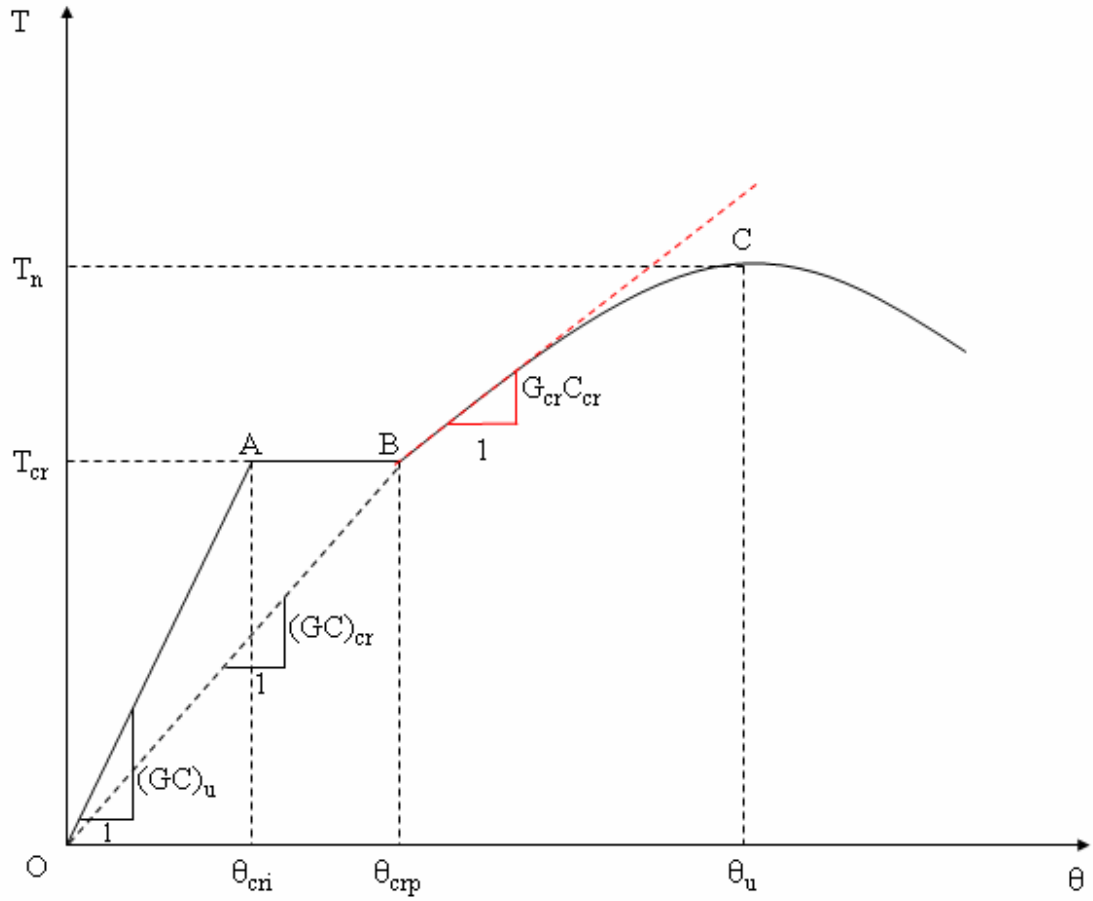


Figure 5.1 – Typical torque-twist curve of a reinforced concrete beam with shear reinforcement

The second segment (AB) starts when the applied torque reaches the cracking torque,  $T_{cr}$ . According to ACI 318R-05 Section 11.6.1,  $T_{cr}$  can be determined from Equation (5.1):

$$T_{cr} = 4 \cdot \sqrt{f'_c} \cdot \left( \frac{A_{cp}^2}{p_{cp}} \right) \quad (5.1)$$

where  $f'_c$  is the cylinder compressive strength of concrete in psi;  $A_{cp}$  is the gross cross-sectional area of the beam and  $p_{cp}$  is the perimeter of the cross-section.

Cracking torque of a reinforced concrete beam is the torsional strength of the plain concrete beam with the same dimensions. Equation (5.1) was developed based on the assumption that a plain concrete beam fails in torsion when the principal tensile stress in the beam becomes equal to the tensile strength of concrete ( $f'_t$ ), which can be obtained from Equation (5.2):

$$f'_t = 4 \cdot \sqrt{f'_c} \quad (5.2)$$

Equation (5.2) is the tensile strength of concrete under biaxial tension and compression. It was used instead of Equation (4.20), which is the tensile strength of concrete under uniaxial tension, to account for the compressive and tensile principal stresses in a beam under pure torsion.

Hsu (1984) developed a criterion for the torsional failure of plain concrete members, which is based on the skew-bending theory, developed by Hsu (1968) to explain the torsional behavior of concrete beams. According to the skew-bending theory, the failure plane of a concrete beam, loaded in pure torsion, makes a 45-degree angle with the longitudinal axis of the beam. The applied torque can be decomposed into two components: a component parallel to the failure surface (bending component,  $T_b$  in Figure 5.2) and a component perpendicular to the surface (twisting component,  $T_t$  in Figure 5.2). According to Hsu (1984), torsional failure of a plain concrete beam takes place when the tensile stress on the lateral face of the beam ( $\sigma_t$  in Figure 5.2) induced by the bending component of the applied torque reaches the modulus of rupture of concrete. Accordingly, the torsional strength of a plain concrete member is obtained from Equation (5.3).

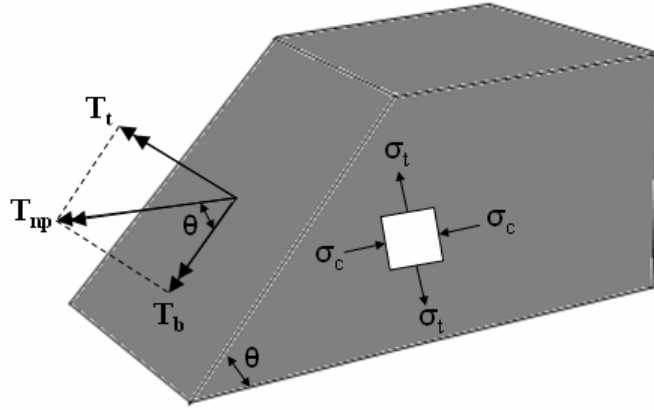


Figure 5.2 – Components of the axial torque on the failure surface of a concrete beam according to the skew-bending theory

$$T_{np} = \frac{b^2 \cdot h}{3} \cdot (0.85 \cdot f_r) \quad (5.3)$$

where  $f_r$  is the modulus of rupture of concrete, expressed in terms of  $f'_c$  according to Equation (5.4):

$$f_r = 21 \cdot \left( 1 + \frac{10}{b^2} \right) \sqrt[3]{f'_c} \quad (5.4)$$

The multiplier  $0.85$  in Equation (5.3) is the reduction in the modulus of rupture of concrete resulting from the stresses induced by the twisting component of the applied torque. The compressive stresses ( $\sigma_c$  in Figure 5.2) from the twisting component are in perpendicular direction to the tensile stresses from the bending component on the lateral face of the beam. Interaction of the tensile and compressive stresses induces a 15-percent reduction in the modulus of rupture.

Based on previous experimental results [Hsu (1968)], Hsu (1984) established that torsional reinforcement in a beam (including both longitudinal and shear reinforcement) increases the cracking torque of the beam, although it does not influence the uncracked torsional rigidity. The cracking torque of a concrete beam reinforced with longitudinal reinforcement and closed stirrups is obtained from the torsional strength of the plain concrete beam with the same dimensions,  $T_{np}$  (Equation 5.3), using Equation (5.5):

$$T_{cr} = (1 + 4 \cdot \rho_t) \cdot T_{np} \quad (5.5)$$

where  $\rho_t$  is the total volumetric reinforcement ratio of the beam, calculated from Equation (5.6):

$$\rho_t = \rho_l + \rho_s \quad (5.6)$$

Volumetric ratio of the longitudinal reinforcement,  $\rho_l$ , and volumetric ratio of the shear reinforcement,  $\rho_s$ , are determined according to Equations (5.7) and (5.8), respectively.

$$\rho_l = \frac{A_l}{A_{cp}} \quad (5.7)$$

$$\rho_s = \frac{A_t \cdot p_l}{A_{cp} \cdot s} \quad (5.8)$$

where  $A_l$  is the total cross-sectional area of the longitudinal reinforcement;  $A_t$  is the cross-sectional area of one leg of a stirrup;  $p_l$  is the perimeter of the area bounded by the centerline of a stirrup;  $s$  is the spacing of the stirrups.

In Section 5.3 of the present chapter, the maximum torsional moments in the specimens at the initiation of buckling will be compared to the cracking torques, obtained from Equation (5.1) and (5.5), to determine the cracking conditions of the beams at the instant of buckling.

In the uncracked stage, the entire solid section is effective in resisting the torsional moments. Upon diagonal cracking, the concrete core of the section becomes ineffective. In the post-cracking stage, therefore, torsional rigidity of a reinforced concrete beam is provided by the outer skin of the section enclosing the closed stirrups and the longitudinal corner bars. The horizontal plateau (AB) in Figure 5.1 corresponds to the redistribution of the shear forces in the beam as the transition from the uncracked condition to the post-cracking condition takes place. Segment AB becomes less pronounced as the torsional reinforcement ratio of a concrete beam increases.

Initial portion of the post-cracking segment (BC) of the torque-twist curve is linear. The slope of the initial linear portion is denoted as the post-cracking torsional rigidity of the beam ( $G_{cr}C_{cr}$  in Figure 5.1). The post-cracking torsional rigidity expressions in the literature are introduced in Section 5.2.2.

Beyond the linear portion of BC, the torque-twist curve curves gradually to horizontal until the applied torque reaches the torsional strength of the beam,  $T_n$ . In the curved portion of BC, torsional rigidity decreases with an increase in the torque. At the torsional strength level, the beam does not possess torsional rigidity, and thus, torsional failure takes place after a short time.

## 5.2 Torsional Rigidity of Rectangular Reinforced Concrete Beams

Torsional cracking changes the behavior of a reinforced concrete beam completely. Different distributions of the strains from torsion in the pre- and post-cracking stages of loading create different equilibrium conditions. Owing to the differences in the torsional behavior of a concrete beam before and after diagonal cracking, the following discussion classifies the torsional rigidity expressions, existing in the literature, into two separate groups: the uncracked torsional rigidity expressions and the post-cracking torsional rigidity expressions for reinforced concrete beams.

### 5.2.1 Uncracked Torsional Rigidity Expressions

A reinforced concrete beam is considered as an elastic and homogeneous body prior to the formation of the diagonal tension cracks. The torsion of elastic and homogeneous beams was studied by St. Venant (1856), who developed a semi-inverse method to solve the equations from the theory of elasticity, defining the torsion of noncircular sections. Using Fourier series, St. Venant (1856) reached the torsional rigidity expression for the rectangular sections:

$$(GC)_u = \beta_c \cdot b^3 \cdot h \cdot G_c \quad (5.9)$$

where  $G_c$  is the modulus of rigidity of concrete, calculated from Equation (5.10) and  $\beta_c$  is the coefficient for St. Venant's torsional constant, obtained from Equation (5.11):

$$G_c = \frac{E_c}{2 \cdot (1 + \nu)} \quad (5.10)$$

where  $\nu$  is the Poisson's ratio of concrete and  $E_c$  is the elastic modulus of concrete.

$$\beta_c = \frac{1}{3} \cdot \left( 1 - \frac{192}{\pi^5} \cdot \frac{b}{h} \cdot \sum_{n=0}^{\infty} \frac{1}{(2n+1)^5} \cdot \tanh \frac{(2n+1)\pi h}{2b} \right) \quad (5.11)$$

Equation (5.11) indicates that St. Venant's torsional constant depends on the height-to-width ( $h/b$ ) ratio of a cross-section.

In discussing the torsional rigidity of rectangular sections, Wang (1953) stated that the first term of the infinite series in Equation (5.11) gives the value of the sum to within 0.5 percent. Therefore, for practical purposes,  $\beta_c$  can be approximated to a simpler form, considering the first term of the series only:

$$\beta_c = \frac{1}{3} \cdot \left( 1 - \frac{192}{\pi^5} \cdot \frac{b}{h} \cdot \tanh \frac{\pi h}{2b} \right) \quad (5.12)$$

According to Timoshenko and Goodier (1970), for narrow rectangular cross-sections

$$\tanh \frac{\pi h}{2b} = 1 \quad (5.13)$$

Accordingly, Equation (5.12) can be simplified to Equation (5.14), if the beam has a narrow rectangular cross-section:

$$\beta_c = \frac{1}{3} \cdot \left( 1 - 0.63 \cdot \frac{b}{h} \right) \quad (5.14)$$

The torsional rigidity expression adopted by Siev (1960) uses the above form of  $\beta_c$ . Assuming that the modulus of rigidity of concrete ( $G_c$ ) obtained from Equation (5.10) is valid at the time of buckling, Siev (1960) proposed Equation (5.15):



$$(GC)_s = G_c \cdot \left[ \frac{b^3 \cdot h}{3} \cdot \left( 1 - 0.63 \cdot \frac{b}{h} \right) \right] \quad (5.15)$$

Another approximate form of Equation (5.11) was presented by Yen (1975), based on the studies of Kollbrunner and Bassler (1969):

$$\beta_c = \frac{1}{3} \cdot \left( 1 - 0.630 \cdot \frac{b}{h} + 0.052 \frac{b^5}{h^5} \right) \quad (5.16)$$

Hansell and Winter (1959) simplified Equation (5.11) to the following form:

$$\beta_c = \frac{1}{3} \cdot \left( 1 - 0.35 \cdot \frac{b}{d} \right)^2 \quad (5.17)$$

Using the above form of  $\beta_c$ , Hansell and Winter (1959) proposed a torsional rigidity expression for rectangular reinforced concrete beams:

$$(GC)_{hw} = G'_c \cdot \left[ \frac{b^3 \cdot c}{3} \cdot \left( 1 - 0.35 \cdot \frac{b}{d} \right)^2 \right] \quad (5.18)$$

where  $G'_c$  is the reduced modulus of rigidity of concrete according to Hansell and Winter (1959), calculated from Equation (5.19):

$$G'_c = \frac{E_{sec}}{2 \cdot (1 + \nu)} \quad (5.19)$$

where  $E_{sec}$  is the secant modulus of elasticity of concrete corresponding to the extreme compression fiber strain at the initiation of buckling.

Equation (5.19) takes into account both elastic and inelastic lateral torsional buckling of reinforced concrete beams. Elastic modulus of concrete ( $E_c$ ) and the modulus of rigidity calculated from  $E_c$  (Equation 5.10) do not reflect the true material rigidity of a beam if some fibers of the beam are stressed beyond the elastic limit of the stress-strain curve of concrete, as in the case of inelastic lateral torsional buckling. Hansell and Winter (1959) suggested to use the reduced shear modulus ( $G'_c$ ) to account for the reduction in the overall material rigidity of the beam when the beam buckles inelastically. In the case of elastic lateral torsional buckling, on the other hand,  $G'_c$  becomes equal to  $G_c$  since all fibers throughout the beam are stressed within the elastic range of the stress-strain curve of concrete and  $E_{sec}$  is equal to  $E_c$ .

Sant and Bletzacker (1961) approximated the parameter  $\beta_c$  to  $1/3$ , which is commonly used in thin-walled sections and proposed the following torsional rigidity expression for narrow rectangular reinforced concrete beams:

$$(GC)_{sb} = G_r \cdot \frac{b^3 \cdot d}{3} \quad (5.20)$$

where  $G_r$  is the reduced modulus of rigidity of concrete according to Sant and Bletzacker (1961), calculated from Equation (5.21):

$$G_r = \frac{E_r}{2 \cdot (1 + \nu)} \quad (5.21)$$

where  $E_r$  is the double modulus of concrete corresponding to the extreme compression fiber strain at the instant of buckling, calculated from Equation (5.22):

$$E_r = \frac{4 \cdot E_c \cdot E_{tan}}{\left(\sqrt{E_c} + \sqrt{E_{tan}}\right)^2} \quad (5.22)$$

where  $E_{tan}$  is the tangent modulus of concrete corresponding to the extreme compression fiber strain at the instant of buckling.

Equation (5.20) depicts that Sant and Bletzacker (1961) preferred to relate the shear modulus of concrete to the double modulus of elasticity,  $E_r$  to account for the possible inelastic material behavior at the initiation of buckling.

In the above discussion, simplified versions of St. Venant's torsional constant were presented. Equations (5.12), (5.14), (5.16) and (5.17) are the simplified forms of Equation (5.11). Figure 5.3 compares the values obtained from the simplified forms of Equation (5.11) to the actual values of  $\beta_c$  obtained from Equation (5.11).

Figure 5.3 shows that Equations (5.12), (5.14), (5.16) and (5.17) are in good agreement with Equation (5.11) for  $b/h$  smaller than unity. However, the use of a constant value of 1/3 for  $\beta_c$ , proposed by Sant and Bletzacker (1961), is meaningful only when the section is quite narrow. For  $b/h > 0.1$ , assuming  $\beta_c = 1/3$  will introduce significant errors to the calculations. To conclude, the aforementioned simplified versions of Equation (5.11) can be used instead of Equation (5.11) to facilitate the uncracked torsional rigidity calculations.

### 5.2.2 Post-Cracking Torsional Rigidity

In the post-cracking stage of loading, the torsional rigidity of a reinforced concrete beam is provided by the outer skin concrete, since the concrete core is rendered ineffective by

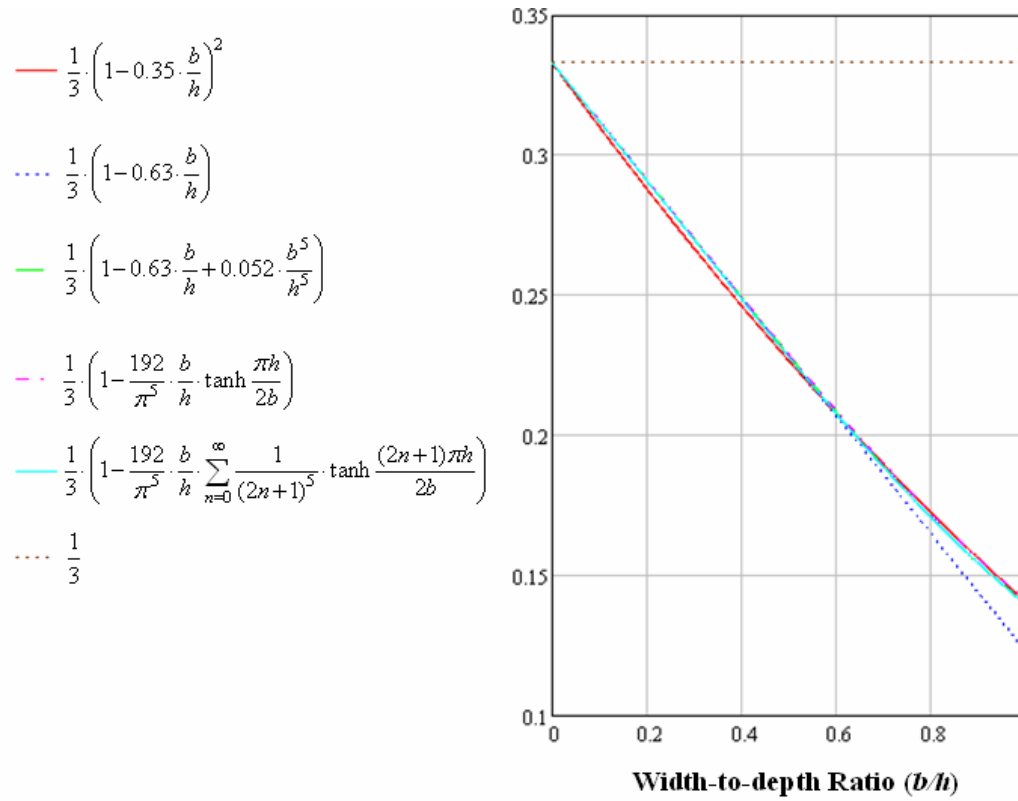


Figure 5.3 – Comparison of the coefficients  $\beta_c$  calculated from different equations

the diagonal tension cracks. The outer skin concrete is assumed to form a thin-walled tube including the closed stirrups and the longitudinal corner bars.

The post-cracking torsional rigidity expressions developed by previous researchers are based on a 3-D model, denoted as the thin-walled tube space truss model, which is based on Rausch's (1929) space truss analogy. According to the model, a solid beam turns into a thin-walled tube after formation of the diagonal cracks. The thin-walled tube, providing the post-cracking torsional rigidity, is a space truss, which is composed of three different types of members (Figure 5.4). Helical concrete strips between the diagonal tension cracks form the compression struts which are assumed to be connected to the closed stirrups and the longitudinal reinforcing bars at the joints through hinges.

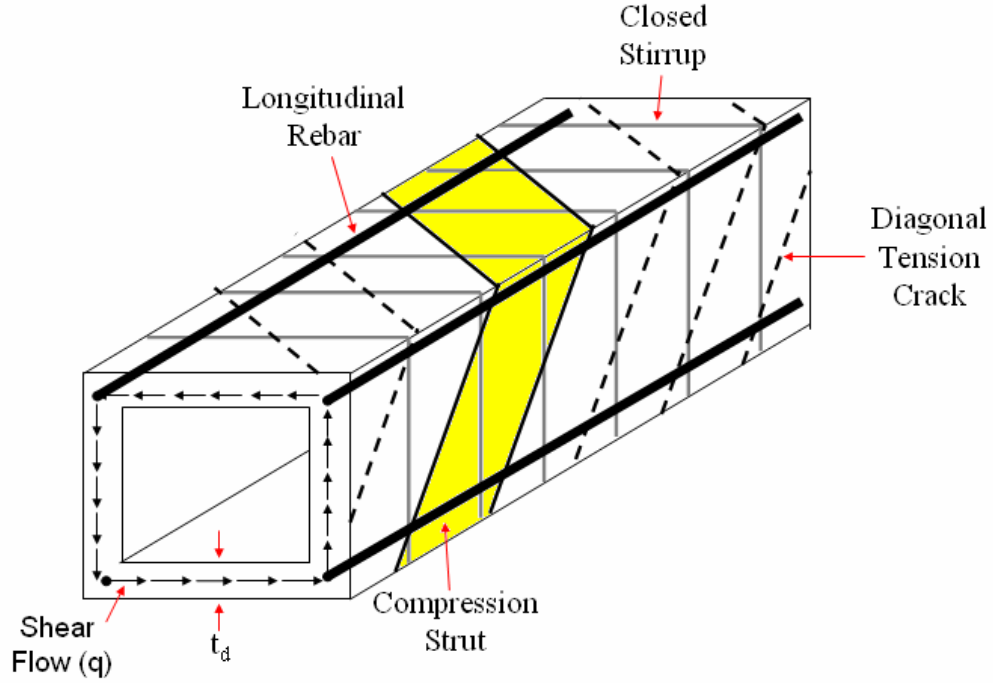


Figure 5.4 –Thin-walled tube space truss model

Compressive stresses in the tube are carried by the compression struts while the tensile stresses are carried by the shear and longitudinal reinforcement. Using the equilibrium of forces and compatibility of strains in the space truss, Lampert (1973) was able to develop a post-cracking torsional rigidity expression (Equation 5.23) for rectangular reinforced concrete beams.

$$G_{cr} \cdot C_{cr} = \frac{4 \cdot E_s \cdot A_2^3}{p_2^2 \cdot \left( \frac{4 \cdot n \cdot \lambda \cdot A_2}{p_2 \cdot t_i} + \frac{1}{\rho_l} + \frac{1}{\rho_s} \right)} \quad (5.23)$$

where  $A_2$  is the area bounded by the lines connecting the centers of the longitudinal corner bars;  $p_2$  is the perimeter of the area bounded by the lines connecting the centers of the corner bars;  $\lambda$  is a multiplier for the concrete strain [ $\lambda=3$  according to Lampert

(1973)];  $n$  is the modular ratio of steel to concrete;  $t_i$  is the wall thickness of the tube.  $t_i$  is the smaller of  $b/6$  and  $b_2/5$ ;  $b$  is the width of the beam and  $b_2$  is the smaller dimension of the rectangle formed by the lines connecting the centers of the longitudinal corner bars.

The three terms in the denominator of Equation (5.23) correspond to the contributions of the concrete struts, the longitudinal reinforcing bars and the closed stirrups, respectively.

Hsu (1973) proposed a similar equation using the thin-walled tube space truss model:

$$G_{cr} \cdot C_{cr} = \frac{4 \cdot E_s \cdot A_e^2 \cdot A_{cp}}{p_e^2 \cdot \left( \frac{4 \cdot n \cdot A_{cp}}{p_e \cdot t_e} + \frac{1}{\rho_l} + \frac{1}{\rho_s} \right)} \quad (5.24)$$

where  $A_e$  is the area bounded by the centerline of the effective wall;  $p_e$  is the perimeter of the area bounded by the centerline of the effective wall;  $A_{cp}$  is the gross area of the section;  $t_e$  is the effective wall thickness. Based on the previous experimental results, Hsu (1973) proposed an empirical equation to obtain  $t_e$ :

$$t_e = 1.4 \cdot (\rho_l + \rho_s) \cdot b \quad (5.25)$$

Later, Hsu (1990) introduced the concept of shear flow zone. According to the concept, thickness of the thin-walled tube, providing the post-cracking torsional rigidity, is the thickness of the shear flow zone ( $t_d$ ) in the post-cracking stage. Thickness of the shear flow zone depends on the applied torque according to the following equation:

$$t_d = \frac{4 \cdot T_a}{A_{cp} \cdot f_c} \quad (5.26)$$

where  $T_a$  is the applied torque. Equation (5.26) was obtained by Hsu (1990) using the softened truss model.

Finally, Tavio and Teng (2004) developed an equation for the torsional rigidity of a reinforced concrete beam at cracking, using the shear flow zone concept:

$$(GC)_{cr} = \frac{4 \cdot \mu \cdot E_s \cdot A_o^2 \cdot A_{cp}}{p_o^2 \cdot \left( \frac{1}{\rho_l} + \frac{1}{\rho_s} \right)} \quad (5.27)$$

where  $A_o$  is the area bounded by the centerline of the shear flow zone;  $p_o$  is the perimeter of the area bounded by the centerline of the shear flow zone and  $\mu$  is a multiplier. Tavio and Teng (2004) stated that a value of  $\mu = 1.5$  matches well with the experimental data in the literature.

Equations (5.23) and (5.24) correspond to the post-cracking torsional rigidity ( $G_{cr}C_{cr}$  in Figure 5.1), which is the slope of the initial linear portion of the post-cracking segment of the torque-twist curve. Equation (5.27), on the other hand, corresponds to torsional cracking at rigidity  $[(GC)_{cr}$  in Figure 5.1], which is the slope of the secant line connecting the end point of the horizontal plateau of the torque-twist curve (Point B in Figure 5.1) to the origin. The lack of the first term in the denominator of Equation (5.27) depicts that Tavio and Teng (2004) neglected the contribution of the concrete compression struts to the torsional rigidity at cracking in order to simplify the expression.

### 5.3 Experimental Torsional Rigidities of the Test Beams

Figures (5.5) & (5.6) illustrate the experimental torque-twist curves of B44-1 and B36L-1 to explain the torsional behavior of a reinforced concrete beam in a lateral-torsional

buckling test. The experimental torque-twist curves of the remaining specimens are presented in Appendix D.

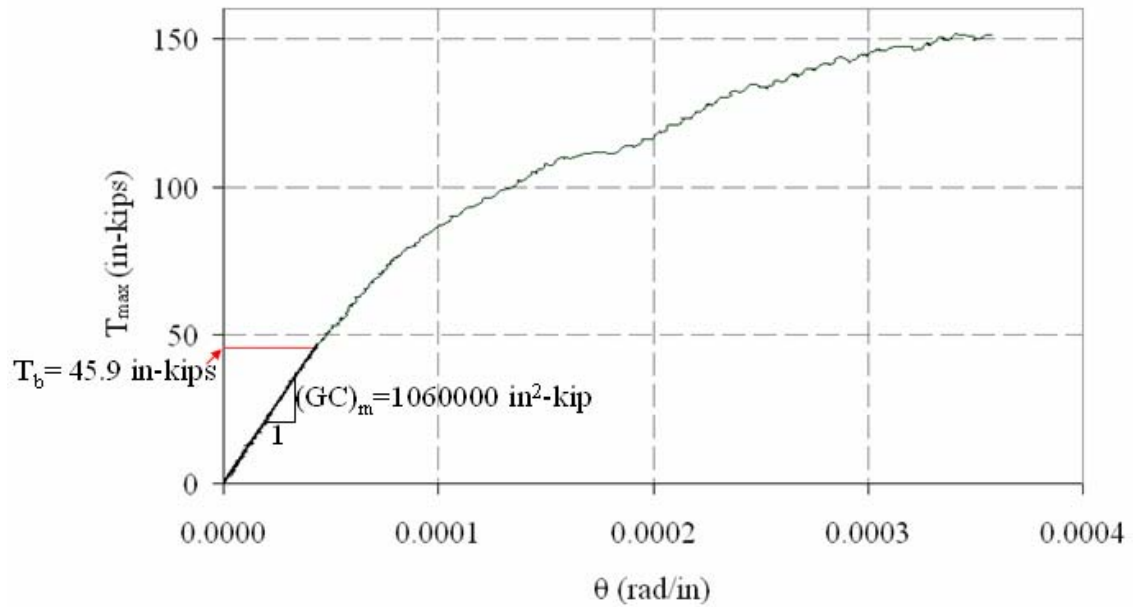


Figure 5.5 –Experimental torque-twist curve of Specimen B44-1

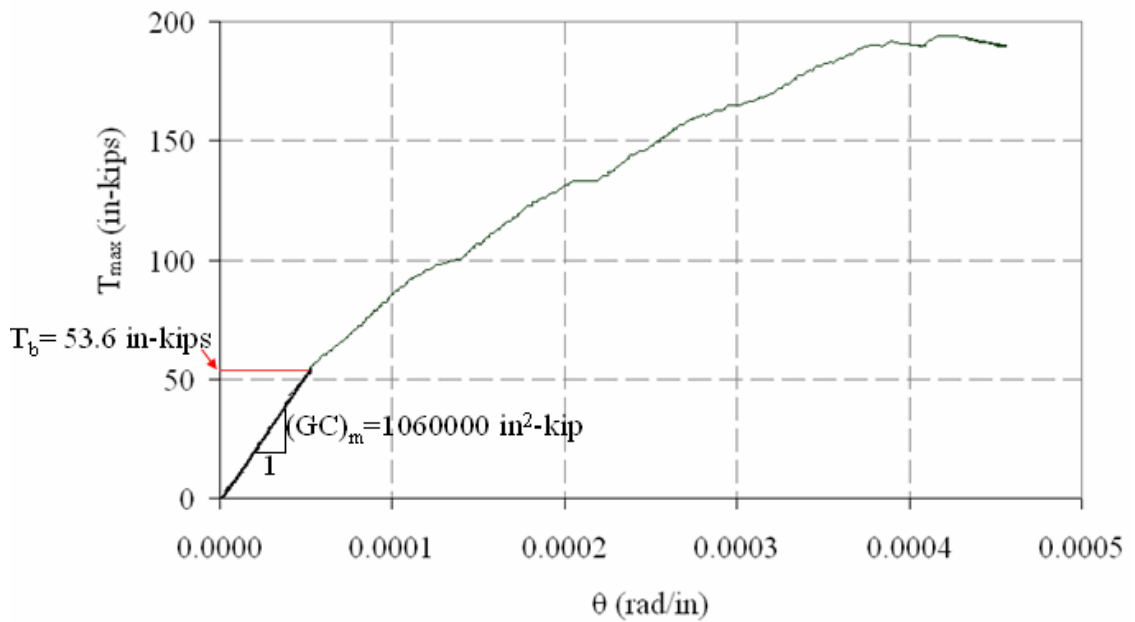


Figure 5.6 – Experimental torque-twist curve of Specimen B36L-1



Application of a single concentrated load at mid-span and simple support conditions in and out of plane at the beam ends resulted in the non-uniform distribution of the torsional moment along the span of each specimen, as previously shown in Figure 3.34(b). Due to the non-uniform moment distribution, the torque-twist curve of a test beam is somewhat different from the typical torque-twist curve of a reinforced concrete beam under uniform torque throughout the span. In Figure 5.1, the horizontal plateau (AB) corresponds to the diagonal cracking throughout the entire span of a beam when the applied torque reaches the cracking torque. In other words, the entire beam is subject to diagonal cracking at the same stage of loading and the redistribution of the strains throughout the whole span creates a noticeable softening in the beam beyond the initial linear portion of the torque-twist curve. According to the experimental results obtained by Hsu (1968), the horizontal plateau is distinct in reinforced concrete beams with closed stirrups up to a total volumetric reinforcement ratio ( $\rho_t$ ) of 0.04-0.05.

In Figures (5.5) & (5.6), on the other hand, the torque-twist curve does not have a pronounced horizontal plateau due to the progressive reduction in the torsional rigidity of the beam. In Figure 5.7, the torque-twist curve of B44-2 is approximated with a series of linear segments with decreasing slopes to illustrate that the overall torsional rigidity of the beam reduces gradually as the diagonal tension cracks, existing in the support zones earlier in the test, spread towards the inner portions of the span in the further stages of loading.

The maximum torsional moment in the beam at the initiation of buckling ( $T_b$ ) is shown with a heavy solid line on Figures (5.5) & (5.6). In the torque-twist curve of each specimen,  $T_b$  falls into the first linear segment of the curve, which has the greatest slope

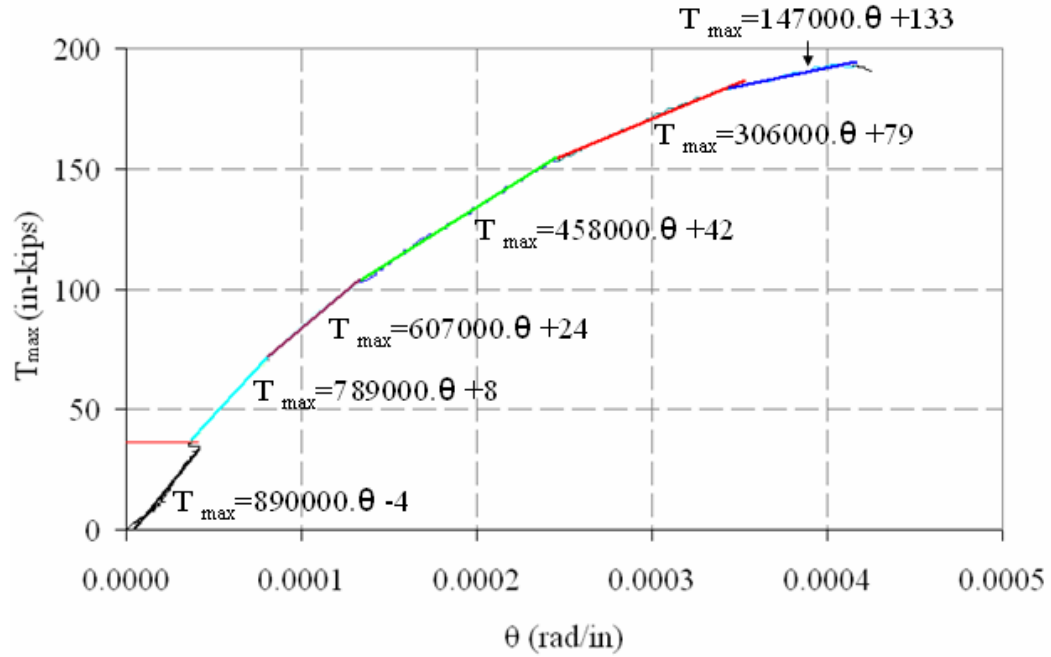


Figure 5.7 – Approximation of the torque-twist curve of B44-2 into a series of line segments

among all segments. The fact that progressive reduction in the slope of the curve starts beyond  $T_b$  manifests the absence of the diagonal tension cracks in the entire beam at the time of buckling. In other words, all of the specimens were diagonally uncracked at the initiation of buckling. The same conclusion can be drawn from Table 5.1, which tabulates cracking torques of the specimens, according to Equations (5.1) and (5.5), together with the maximum torsional moments in the beams at the start of buckling ( $T_b$ ).  $T_b$  of each of the specimens, except B18-2 and B30, is smaller than the cracking torques obtained from both equations.  $T_b$  values of B18-2 and B30, on the other hand, are slightly larger than  $T_{cr}$ , obtained from Equation (5.1). However, B18-2 and B30 are accepted as completely uncracked at the initiation of buckling, since  $T_b$  of each specimen is smaller than  $T_{cr}$

according to Equation (5.5), which is developed based on the results of several tests, carried out by Hsu (1968).

Table 5.1 – Maximum torsional moments at the initiation of buckling and the cracking torques of the specimens

Specimen	$T_b^*$ (in-kips)	$T_{cr}$ (in-kips)	
		Equation (5.1)	Equation (5.5)
B18-1	12.6	8.5	34.9
B30	48.5	41.1	78.3
B36	27.6	50.8	95.9
B44-1	45.9	70.4	114.1
B44-2	36.2	70.6	114.5
B44-3	30.7	71.1	114.9
B36L-1	53.6	60.0	96.7
B36L-2	49.8	60.0	97.0

\* Maximum Measured Torsional Moment in the Beam at the Initiation of Buckling

Table 5.2 tabulates the torsional rigidities of the beams, calculated from Equations (5.9), (5.18), (5.20), (5.24) and (5.27). The table also includes the slopes of the initial linear segments of the experimental torque-twist curves of the specimens, for the sake of comparison. The slope of the experimental torque-twist curve of a beam under the loading and support conditions of the present study cannot be directly compared to the torsional rigidity values calculated from the aforementioned equations, due to the non-uniform torsional moment distribution along the beam span. The experimental torque-twist curves were obtained by plotting twist per unit length of the beam ( $\theta$ ) against the maximum torsional moment along the span ( $T_{max}$ ). The torsional moment in the beam decreases from maximum at the ends to minimum at mid-span. Therefore,  $T_{max}$  corresponds to the laterally-supported beam ends only. The slope of a torque-twist curve is the torsional rigidity of a beam if the torsional moment is constant through the entire

Table 5.2 – Torsional rigidities of the specimens

Specimen	Torsional Rigidity ( $\times 10^6$ in <sup>2</sup> -kips)					
	(GC) <sub>m</sub> Fig. 5.4	(GC) <sub>u</sub> Eq. 5.9	(CG) <sub>hw</sub> Eq. 5.18	(GC) <sub>sb</sub> Eq. 5.20	G <sub>cr</sub> C <sub>cr</sub> Eq. 5.24	(GC) <sub>cr</sub> Eq. 5.27
B44-1	1.067	0.751	0.284	0.669	0.045	0.115
B44-2	0.890	0.768	0.289	0.685	0.046	0.115
B44-3	1.166	0.798	0.297	0.712	0.047	0.116
B36L-1	1.059	0.685	0.273	0.614	0.043	0.101
B36L-2	0.988	0.720	0.282	0.646	0.044	0.101
B36	0.859	0.500	0.192	0.453	0.032	0.069
B30	0.612	0.410	0.151	0.369	0.026	0.056
B22-1	0.178	0.059	0.023	0.051	0.005	0.010
B22-2	0.198	0.048	0.019	0.042	0.004	0.008
B18-2	0.181	0.041	-	0.034	0.003	0.007

span. In the case of the test specimens, the slope of the experimental torque-twist curve, plotting  $T_{max}$  vs.  $\theta$ , is greater than the actual torsional rigidity of the beam, since only the support zones resist large torsional moments in the order of  $T_{max}$ . However, the slopes of the experimental curves are shown in Figures (5.5) & (5.6) and tabulated in Table 5.2 to compare the order of magnitude of the experimental torsional rigidities of the beams with the analytical values calculated from the uncracked and post-cracking rigidity expressions.

To conclude, the experimental torque-twist curves of the specimens reveal that the torsional behavior of a reinforced concrete beam, buckling elastically, is closely predicted by St. Venant's theory, and thus, the torsional rigidity of a concrete beam at the buckling instant can be obtained from Equation (5.9). The profound difference between the slopes of the initial linear portions of the experimental torque-twist curves  $[(GC)_m]$  and the post-

cracking torsional rigidities of the beams (last two columns in Table 5.2) clearly indicates that concrete beams, buckling elastically, do not undergo diagonal cracking. In the next section, some modifications to Equation (5.9) are proposed to account for the case of inelastic lateral-torsional buckling in reinforced concrete beams.

#### 5.4 Proposed Torsional Rigidity Expression

As explained in the previous section, the torsional constant ( $C$ ) of a reinforced concrete beam is closely estimated by St. Venant's theory prior to the formation of diagonal tension cracks. The material rigidity term in Equation (5.9) is the shear modulus of rigidity of concrete ( $G_c$ ), which is obtained from the elastic modulus ( $E_c$ ) through Equation (5.10).

The use of  $E_c$  in the critical moment calculations is appropriate only if the beam buckles elastically. To account for both elastic and inelastic lateral torsional buckling of concrete beams, another modulus of elasticity, termed as the overall modulus of elasticity [Equation (4.16)], was proposed. Using a simplified form of St. Venant's torsional constant, presented in Section 5.2.1, and accounting for the possible inelastic material behavior of concrete at the instant of buckling, the following torsional rigidity expression is proposed for the rectangular reinforced concrete beams:

$$(GC)_o = G_o \cdot \left[ \frac{b^3 \cdot h}{3} \cdot \left( 1 - 0.63 \cdot \frac{b}{h} \right) \right] \quad (5.28)$$

where  $G_o$  is the overall modulus of rigidity of concrete, calculated from Equation (5.29):

$$G_o = \frac{E_o}{2 \cdot (1 + \nu)} \quad (5.29)$$

where  $E_o$  is the overall modulus of elasticity of concrete, obtained from Equation (5.30):

$$E_o = \left( \frac{E_{\text{sec}} + E_c}{2} \right) \quad (5.30)$$

## CHAPTER VI

### CRITICAL MOMENT CALCULATIONS AND INFLUENCES OF THE INITIAL GEOMETRIC IMPERFECTIONS ON THE LATERAL STABILITY OF REINFORCED CONCRETE BEAMS

#### 6.1 Introduction

A geometrically perfect beam buckles when the applied moment reaches a critical value, denoted as the critical moment ( $M_{cr}$ ). In the presence of initial geometric imperfections, on the other hand, the ultimate moment-carrying capacity, also termed as the limit moment ( $M_L$ ), of a beam is smaller than the critical moment ( $M_{cr}$ ) corresponding to the perfect initial configuration of the beam.

In Section 6.2, the critical moment calculations of beams are presented. Determination of the critical moment of a beam includes the evaluation of its torsional and lateral bending rigidities. Therefore, Section 6.2 is linked to Chapters IV and V.

In Section 6.3, the influences of the initial geometric imperfections on the lateral stability of reinforced concrete beams are explained. Section 6.3 also presents an equation to calculate the limit moment ( $M_L$ ) of a concrete beam with initial lateral imperfections (sweep) and initial twisting angle from the critical moment ( $M_{cr}$ ) corresponding to the initially perfect configuration of the beam.

#### 6.2 Critical Moment Calculations

Timoshenko and Gere (1963) developed critical moment expressions for beams with different cross-sectional shapes, loading and support conditions. Equation (6.1) is a very general form of the critical moment expression, developed by Vacharajittiphan et al.

(1974) considering the influence of the in-plane (vertical) deformations of a beam prior to buckling on the lateral stability:

$$M_{cr} = \frac{C_1}{C_2 \cdot L} \cdot \frac{\sqrt{EI_y \cdot GJ \cdot \left(1 + \frac{\pi^2 EC_w}{GJL^2}\right)}}{\sqrt{\left(1 - \frac{EI_y}{EI_x}\right) \cdot \left[1 - \frac{GJ}{EI_x} \cdot \left(1 + \frac{\pi^2 EC_w}{GJL^2}\right)\right]}} \quad (6.1)$$

where  $C_1$  is a constant corresponding to the loading conditions of a beam;  $C_2$  is a constant corresponding to the support conditions;  $M_{cr}$  is the critical moment;  $L$  is the unbraced length;  $EI_x$ ,  $EI_y$ ,  $GJ$ ,  $EC_w$  are the in-plane, out-of-plane, torsional and warping rigidities of a beam, respectively.

Smitses and Hodges (2006) stated that the effect of warping rigidity ( $EC_w$ ) is considerable in thin-walled open cross-sections only. According to Timoshenko and Gere (1963),  $C_w$  can be taken zero in a beam with narrow rectangular cross-section. Hence, Equation (6.1) simplifies to Equation (6.2):

$$M_{cr} = \frac{C_1}{C_2 \cdot L} \cdot \frac{\sqrt{EI_y \cdot GJ}}{\sqrt{\left(1 - \frac{EI_y}{EI_x}\right) \cdot \left(1 - \frac{GJ}{EI_x}\right)}} \quad (6.2)$$

The expression in the square root in the denominator of Equation (6.2) corresponds to the in-plane (vertical) deformations of a beam prior to buckling. In deep beams, the in-plane flexural rigidity ( $EI_x$ ) is significantly greater than the out-of-plane flexural rigidity ( $EI_y$ ) and the torsional rigidity ( $GJ$ ). Therefore, the square root term in the denominator is very close to unity in deep beams. Ignoring this term does not change



the calculated values to a major extent. For instance, Beams B44 of the present study had a  $EI_y / EI_x$  ratio of 0.0048 and a  $GJ / EI_x$  ratio of 0.0080. Using these values, the square root term in the denominator becomes 0.994, which corresponds to a 0.6% change in the critical moment. When the square root term in the denominator is ignored, Equation (6.2) reduces to Equation (6.3):

$$M_{cr} = \frac{C_1}{C_2 \cdot L} \cdot \sqrt{EI_y \cdot GJ} \quad (6.3)$$

According to Allen and Bulson (1980), the constant  $C_1$  has a value of 4.23 for a single concentrated load at midspan. The effective length ratio  $C_2$  has a value of 1.00 when a beam is simply-supported in and out of plane.

The applied load has an additional destabilizing effect on the beam when it is applied above the centroid of the section (Figure 1.22 of Chapter I). On the contrary, the load has a stabilizing effect on the beam when it is applied below the centroid. Equations (1.21) – (1.23), proposed by Stiglat (1991), account for the influence of the location of the load application point with respect to the centroid of the section. Timoshenko and Gere (1963) developed a critical load expression considering the influence of the location of the point of application of load with respect to the centroid of the midspan cross-section. Accordingly, Equation (6.3) can be modified to Equation (6.4) to account for this effect:

$$M_{cr} = \frac{4.23}{L} \cdot \left( 1 - 1.74 \cdot \frac{e}{L} \cdot \sqrt{\frac{EI_y}{GJ}} \right) \cdot \sqrt{EI_y \cdot GJ} \quad (6.4)$$

where  $e$  is the initial vertical distance of the load from the shear center of the beam section.

$EI_y$  and  $GJ$  are the rigidities of a homogeneous and elastic beam. The lateral bending rigidity ( $B_o$ ) and the torsional rigidity  $[(GC)_o]$  of a reinforced concrete beam are different from  $EI_y$  and  $GJ$  due to the differences in behavior between a reinforced concrete beam and a homogeneous and elastic beam, such as cracking of concrete, elastic-inelastic material behaviors of concrete and reinforcing steel, etc. In the present study, Equation (4.17) and Equation (5.28) are proposed for calculating the lateral bending rigidity and the torsional rigidity of a reinforced concrete beam, respectively.

Considering all the aforementioned changes, Equation (6.5) is proposed:

$$M_{cr} = \frac{4.23}{L} \cdot \left( 1 - 1.74 \cdot \frac{e}{L} \cdot \sqrt{\frac{B_o}{(GC)_o}} \right) \cdot \sqrt{B_o \cdot (GC)_o} \quad (6.5)$$

### 6.3 Influences of Sweep and Initial Twisting Angle on the Lateral Stability of Reinforced Concrete Beams

Initial geometric imperfections play a crucial role in the stability of beams. Concrete girders possess three different types of geometric imperfections: camber (initial in-plane deformation), sweep (initial out-of-plane deformation) and initial twisting angle.

Influence of sweep on the lateral stability of reinforced concrete beams is two-fold. First, the out-of-plane deformations of a beam are affected by the sweep. A geometrically perfect beam does not experience lateral deformations and twisting rotations until bifurcation buckling takes place. When the buckling moment is reached, a

beam free from sweep undergoes very large lateral deformations and rotations at a constant moment level. Nevertheless, the load-deflection behavior of a beam is different in the presence of sweep, which causes the beam to undergo lateral deformations in the pre-buckling stage of loading. Lateral deformations start with the initiation of loading and grow at a relatively low rate in the pre-buckling stage. Once the beam buckles, the lateral deformations and twisting rotations grow at much higher rates while the moment carried by the beam is maintained at an approximately constant level.

Similarly, the initial twisting angle in a beam causes the beam to experience twisting rotations even prior to buckling. The twisting rotations, growing slowly in the pre-buckling stage, become very large after buckling takes place.

The second effect of sweep is the reduction in the ultimate load carried by a concrete beam. A geometrically perfect beam buckles when the maximum moment carried by the beam reaches the critical moment. Nonetheless, the moment carrying capacity of a beam with sweep is smaller than the critical moment ( $M_{cr}$ ). The maximum moment on the load-deflection curve of an imperfect beam is termed as the limit moment ( $M_L$ ) of the beam, which should be distinguished from the critical moment.

To clarify the above discussion, the experimental load-lateral deflection curves of the beams in specimen groups B44 and B36L are illustrated in Figures 6.1 and 6.2, respectively. The load-deflection curves do not start from the origin. The sweep of each beam at the centroid of midspan section was taken as the initial lateral deflection (deflection at zero load). The load-lateral deflection curves of the other specimens are presented in Appendix D.

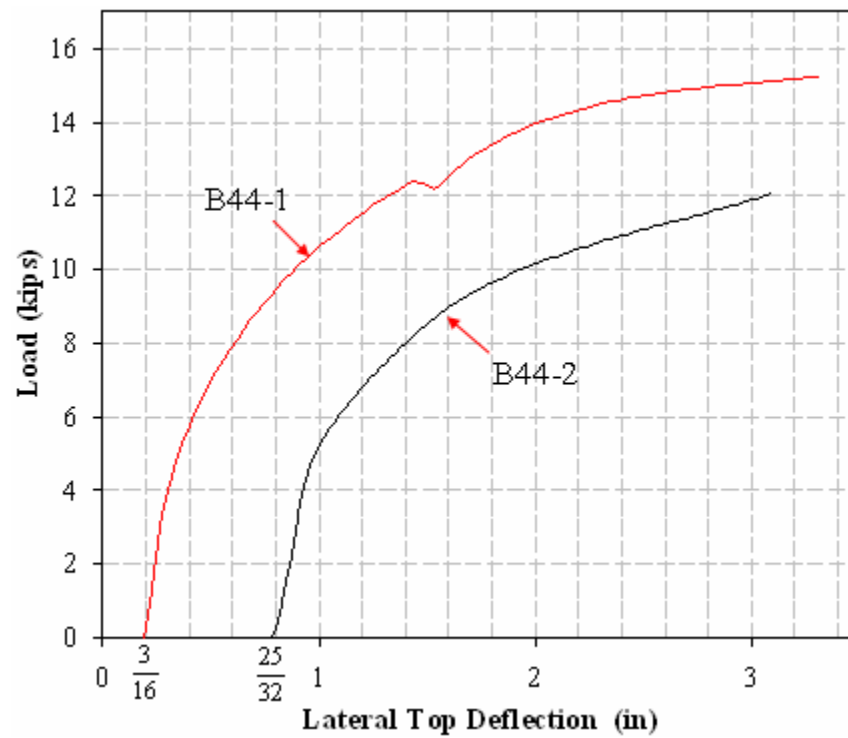


Figure 6.1 – Lateral top deflections of B44-1 and B44-2 at midspan

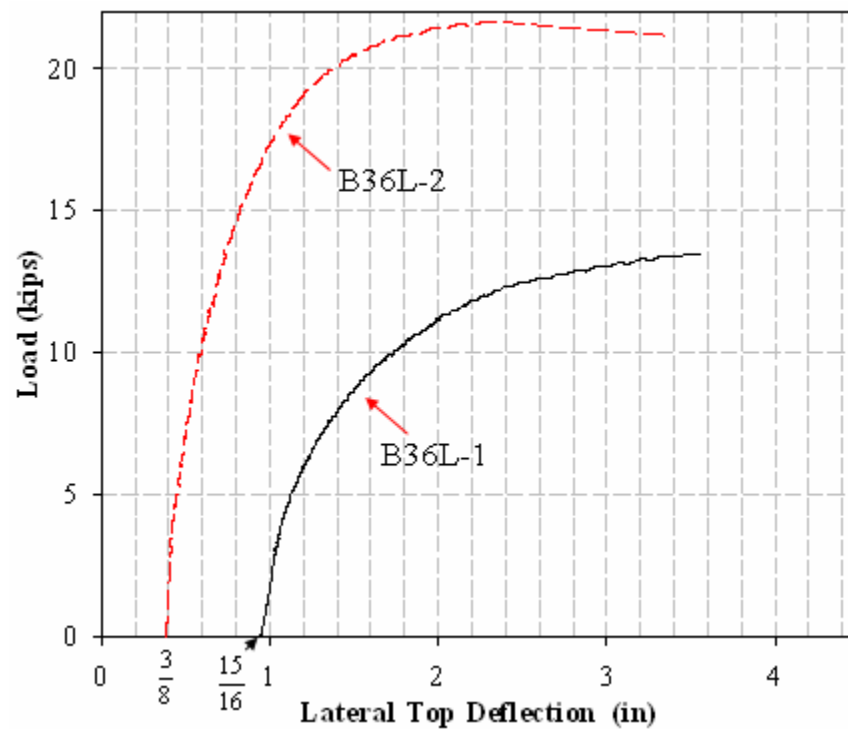


Figure 6.2 – Lateral top deflections of B36L-1 and B36L-2 at midspan

According to Figures 6.1 and 6.2, the load-lateral deflection curve of a reinforced concrete beam has an initial linear portion and a curved portion. The curved portion turns into an approximately horizontal line beyond the limit load, meaning that the lateral deflections in the beam increase excessively at a constant load level when the beam buckles. The two-fold influence of sweep on the lateral stability of reinforced concrete beams can be observed in Figures 6.1 and 6.2. The beam with the greatest sweep experiences larger out-of-plane deformations than its companion before reaching the ultimate moment. Furthermore, the ultimate moment carried by the beam having the largest sweep is smaller than the ultimate moment carried by its companion.

The influences of sweep on the limit moment and the load-deflection behavior of a concrete beam can be understood by considering the differences between the load-lateral deflection curves corresponding to the identical beams. First, the load-deflection curves of the companion beams differ in the slope of the initial linear portion of the curve, which increases as the girder sweep decreases. Secondly, sweep affects the sharpness of the curved portion of the load-deflection curve. When the girder sweep increases, the linear portion of the curve ends at lower load levels and the slope of the curve decreases from a maximum to zero along a greater portion of the curve, creating a smoother curved portion.

The differences between the load-lateral deflection curves of identical beams with different sweeps can be clearly observed in Figure 6.2. B36L-1 and B36L-2 were identical in nominal dimensions, cross-sectional details and nominal material strengths, and they only differed in initial geometric imperfections (Table B.4 in Appendix B). The initial lateral deformations of B36L-1 and B36L-2 were measured as 15/16 and 3/8

inches, respectively, at the top of the beams at midspan. The initial linear portion of the load-deflection curve of Specimen B36L-2 is steeper than the linear portion of the curve of Specimen B36L-1. Furthermore, the load-deflection behavior of the beam with greater sweep (B36L-1) ceased to be linear at earlier stages of loading than the beam with smaller sweep (B36L-2). B36L-1, which buckled at a load of 13.5 kips, has a linear load-deflection behavior up to 5 kips. On the other hand, the load-deflection curve of B36L-2, with a buckling load of 21.6 kips, remains linear up to 15 kips. Since the linear portion of the curve of B36L-1 ends at smaller loads and the slope of the curve gradually decreases up to the buckling load, the load-deflection curve of B36L-1 has a smoother curve beyond the linear portion. B36L-2, on the contrary, has a sharp curve beyond the linear portion due to the rapid decrease in the slope of the curve beyond the longer linear portion.

The reduction in the limit moment ( $M_L$ ) of a reinforced concrete beam due to sweep has not been studied extensively in the literature. Burgoyne and Stratford (2001) stated that the additional stresses associated with the initial minor-axis curvature created by sweep are responsible for the reduction in the ultimate moment of a concrete beam. Longitudinal strains in a beam with an initial lateral curvature originate from in-plane and out-of-plane bending moments. Figure 6.3 illustrates the longitudinal strain distributions in the cross-section of a beam caused by the major-axis and minor-axis bending moments. In a geometrically perfect beam, strains from minor-axis bending [Figure 6.3(a)] are not present up to buckling. In a beam with initial lateral deformations, nevertheless, the minor-axis curvature created by the sweep produces longitudinal strains even prior to the application of load. Since the beam undergoes lateral deformations as

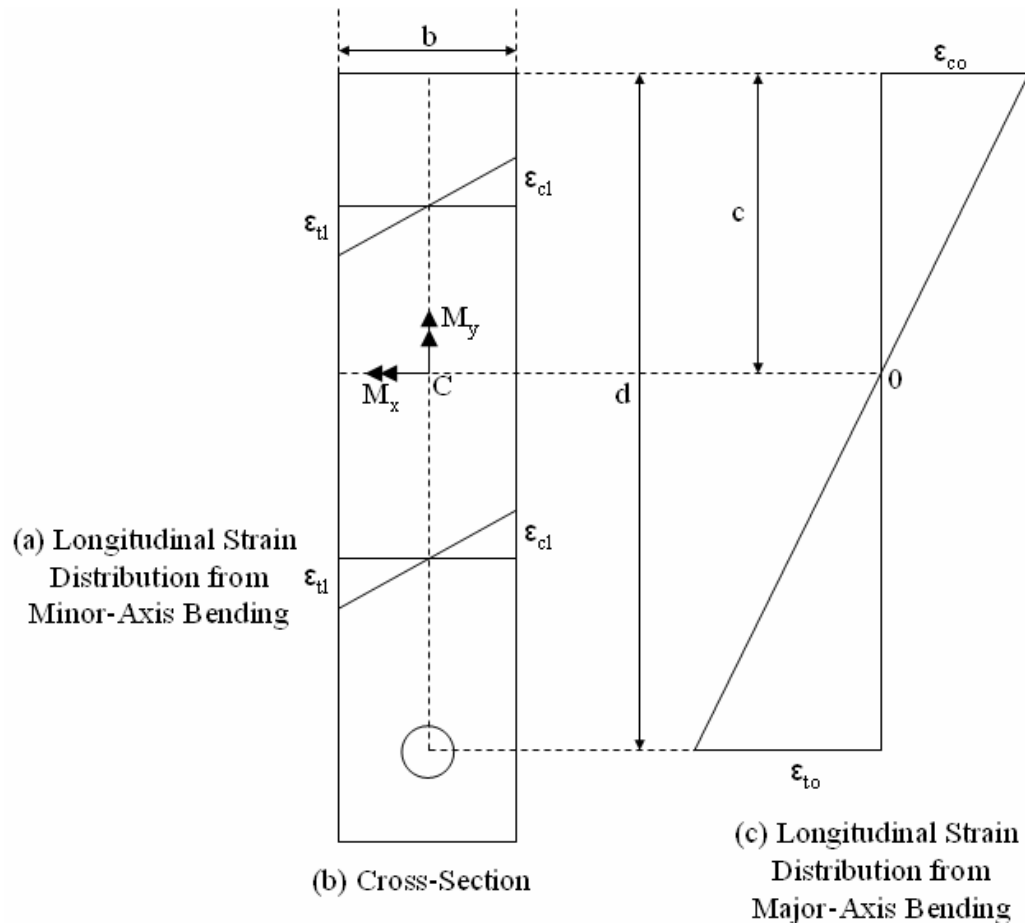


Figure 6.3 – Longitudinal strain distributions in a cross-section from major-axis and minor-axis bending moments

loading progresses, the additional stresses associated with the minor-axis curvature increase. According to Burgoyne and Stratford (2001), cracking of concrete led by the longitudinal stresses from the minor-axis bending moments results in the reduction of the lateral bending rigidity of the beam, which decreases the limit moment ( $M_L$ ). As the sweep of a concrete beam increases, the initial longitudinal strains related to the minor-axis curvature increase and the reduction in the buckling resistance of a beam due to cracking takes place earlier in the loading history. Hence, the limit moment of a concrete beam decreases with the increasing sweep.

To inspect the correctness of the above statements, the strain data obtained in the second set of experiments was examined. As previously explained in Section 3.1.3, longitudinal strains were measured on the lateral faces of each beam at midspan. Assuming that minor axis of the cross-section is coincident with the vertical centroidal axis, the compressive strain on the concave face of a beam ( $\epsilon_{cl}$  in Figure 6.3) resulting solely from the lateral bending moment is equal to the tensile strain on the convex face ( $\epsilon_{tl}$ ) originating from lateral bending. Therefore, the longitudinal strain from major-axis bending at a particular depth can be obtained by averaging the two strains measured on the convex and concave faces of the beam at that depth. The difference between the strain measured on the concave face and the average of the two strains is the compressive strain ( $\epsilon_{cl}$ ) created by the minor-axis bending only while the difference between the strain measured on the convex face and the average of the two strains is the tensile strain ( $\epsilon_{tl}$ ) from lateral bending.

Figures 6.4 and 6.5 illustrate the extreme compression fiber strains of Beams B44 and B36L at midspan resulting from the in-plane bending moments only. The extreme compression fibers at midspan are the most stressed compression fibers of a beam. The load-strain curves in Figures 6.4 and 6.5 are linear up to the limit load ( $P_L$ ). The linear relationships in the figures imply that the in-plane bending moments created elastic material response in the beams. The load-strain curves in Figures 6.4 and 6.5 show a different character from the load-lateral deflection curves of the beams, shown in Figures 6.1 and 6.2. The load-deflection curves do not remain linear up to the limit load. Beyond a certain limit, the slope of the load-deflection curve starts decreasing until vanishing at



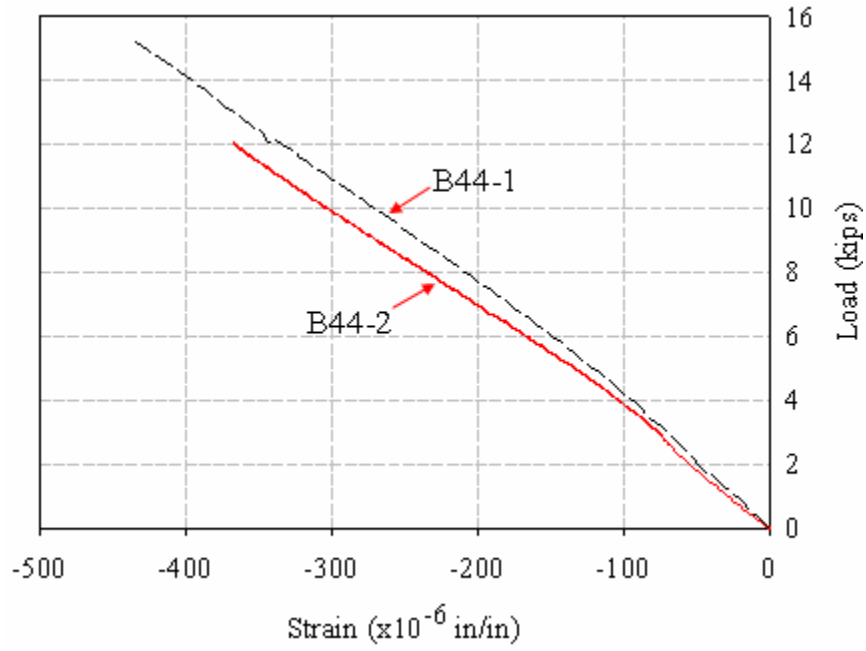


Figure 6.4 – Extreme compression fiber strains of B44-1 and B44-2 from major-axis bending

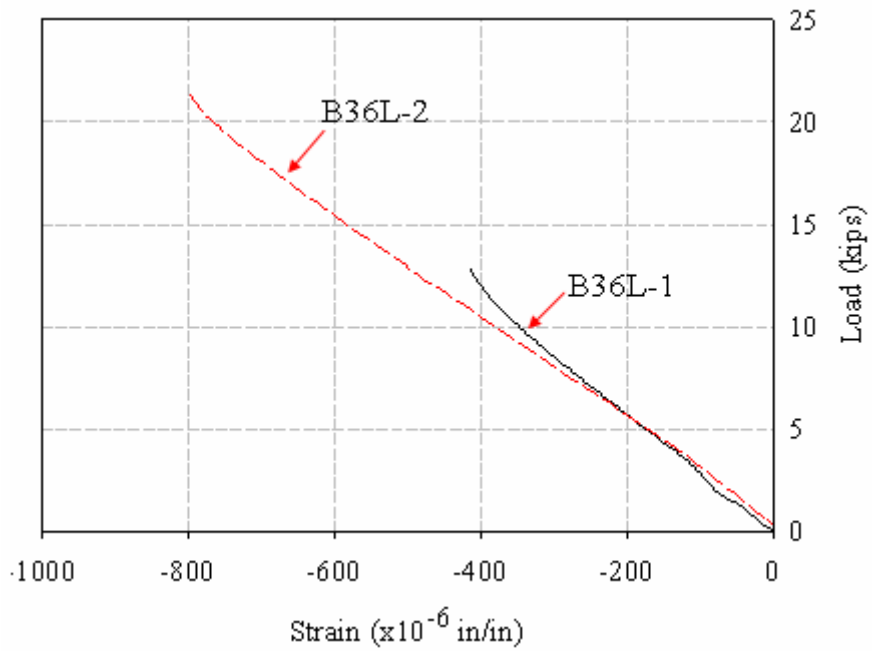


Figure 6.5 – Extreme compression fiber strains of B36L-1 and B36L-2 from major-axis bending

the ultimate load. The continuous decrease in the slope of the load-deflection curve refers to the reduction in the lateral bending rigidity of the beam. This reduction is not related to the increase in major-axis bending strains since the linear load-strain relationship of each beam is preserved up to buckling, unlike the load-lateral deflection relationship.

Figures 6.6 and 6.7 depict the minor-axis bending strains on the convex, tension, faces of the specimens at the top. The load-strain curves in the figures do not start from the origin. The strain at zero load corresponds to the initial strain created by the minor-axis curvature associated with the sweep. Each curve ends at the point corresponding to the limit load carried by the specimen prior to buckling. Both figures indicate that the minor axis bending strains of the companion beams at the limit load were approximately equal to each other. Furthermore, a comparison of Figures 6.6 and 6.7 with Figures 6.1 and 6.2 indicates that the load-minor axis bending strain curve of each beam has the same character as the load-lateral deflection curve of the beam. The same character of the two curves implies that the reduction in the lateral bending rigidity of a beam, which leads to instability, is related to the increase in the strains from the minor-axis bending moments. Moreover, the approximately equal values of the in-plane bending strains of the companion beams at limit load imply that a concrete beam loses its stability when the minor-axis bending strains in the beam reach certain levels. Therefore, the experimental results of the present study agree with the statements of Burgoyne and Stratford (2001), who associated the instability failure of an imperfect concrete beam with the reduction in its lateral bending rigidity due to the cracking of concrete caused by the increase in the strains from minor-axis curvature as the load increases.

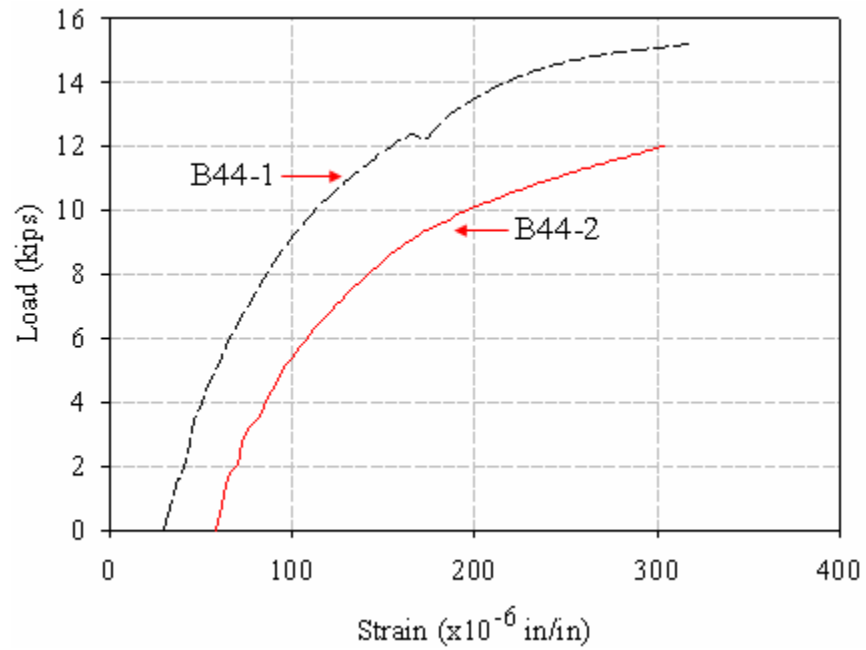


Figure 6.6 –Extreme top strains on the convex faces of B44 caused by minor-axis bending

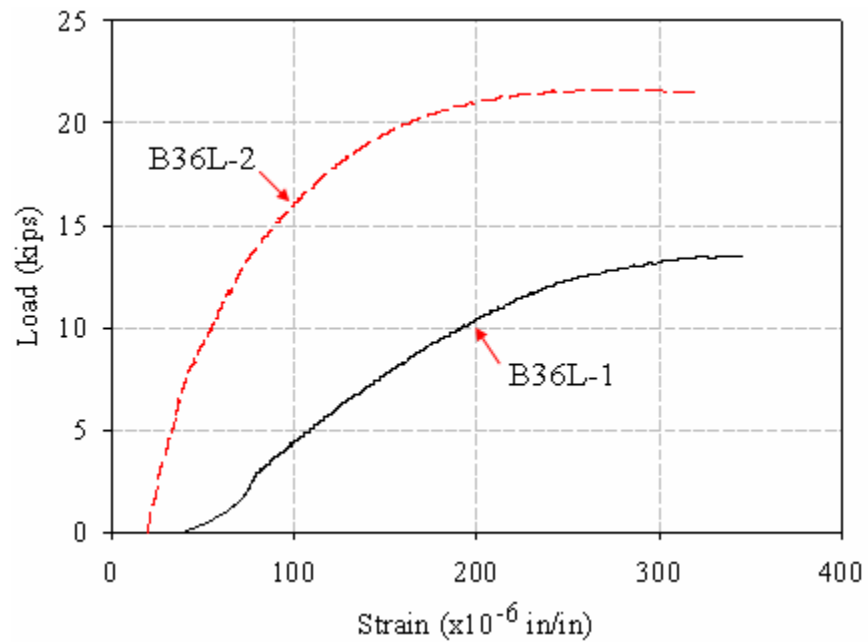


Figure 6.7 –Extreme top strains on the convex faces of B36L caused by minor-axis bending

In the present study, an equation was developed to calculate the ultimate load-carrying capacity of a reinforced concrete beam with initial out-of-plane deformations. The limit load of an imperfect beam is obtained by reducing the critical load of a perfect beam in an amount equal to the influence of sweep to the load-carrying capacity of the beam. A similar approach was previously used by Burgoyne and Stratford (2001) to obtain the minor-axis curvature of a beam under a certain load.

To understand the following discussion, twisting angles in a beam accompanying the lateral deformations should be taken into consideration. A geometrically imperfect beam experiences twisting rotations and lateral deformations prior to buckling when loaded. Owing to the twisting rotations, the major and minor axes of a beam rotate about the longitudinal axis passing through the centroid of the cross-section (Figure 6.8).  $v$ , which will be used in the following equations, is the lateral deflection of the centroid of the midspan section in the direction of the major axis of the twisted configuration of the section ( $x''x''$  in Figure 6.8).  $v$  is measured from a longitudinal axis passing through the centroids of the end sections of a beam. In other words,  $v$  measured with respect to the perfect configuration of a beam.

Burgoyne and Stratford (2001) expressed the load-deflection behavior of a beam under its self-weight as follows, when the initial lateral imperfection and the critical self-weight of the beam are known:

$$v = \frac{v_o}{1 - \frac{w}{w_{cr}}} \quad (6.6)$$

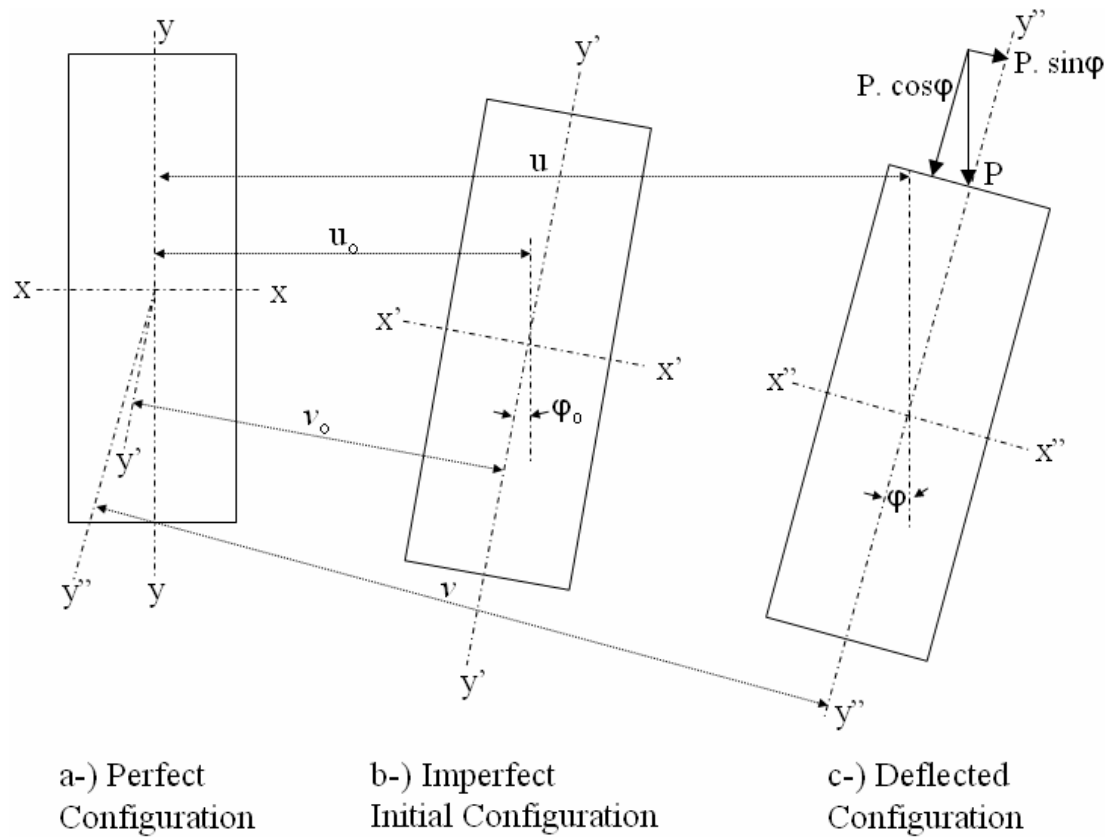


Figure 6.8 – Rotation of the major and minor axes of a section due to twist

where  $w$  is the self-weight per unit length of the beam;  $w_{cr}$  is the critical self-weight per unit length, which causes buckling of the beam;  $v_o$  is the initial imperfection at the center of the beam in the direction of the major axis of the initial configuration of midspan section (Figure 6.8).

Equation (6.6) is modified to account for the concentrated midspan loading used in the present study:

$$\nu = \frac{\nu_o}{1 - \frac{P}{P_{cr}}} \quad (6.7)$$

where  $P$  is the applied load and  $P_{cr}$  is the critical load corresponding to the beam free from initial geometric imperfections.

Equations (6.6) and (6.7) are based on a method developed by Southwell (1932). Southwell's (1932) method is used for obtaining the buckling load and the initial imperfections of a beam by examining the experimental load and deflection measurements of the beam under loads much lower than the critical load. Figure 6.9(a) is the Southwell plot for the lateral deflection data of Specimen B44-1. The inverse slope of the plot gives the buckling load of the specimen, while the absolute value of the x-intercept of the plot is the initial lateral centroidal deflection of the beam at midspan. In Appendix H, Southwell's (1932) method and the modified versions of the method proposed by Meck (1977) and Massey (1963) are discussed in more detail and the application of the three methods to the data obtained in the present experimental program are described.

Figure 6.9(b) compares the experimental load-lateral deflection curve of Specimen B44-1 to the analytical curve obtained by using Equation (6.7). Due to the close agreement between the experimental and analytical curves, Equation (6.7) was used for expressing the load-deflection behavior of a reinforced concrete beam with initial geometric imperfections in closed form when developing the limit load ( $P_L$ ) formula.

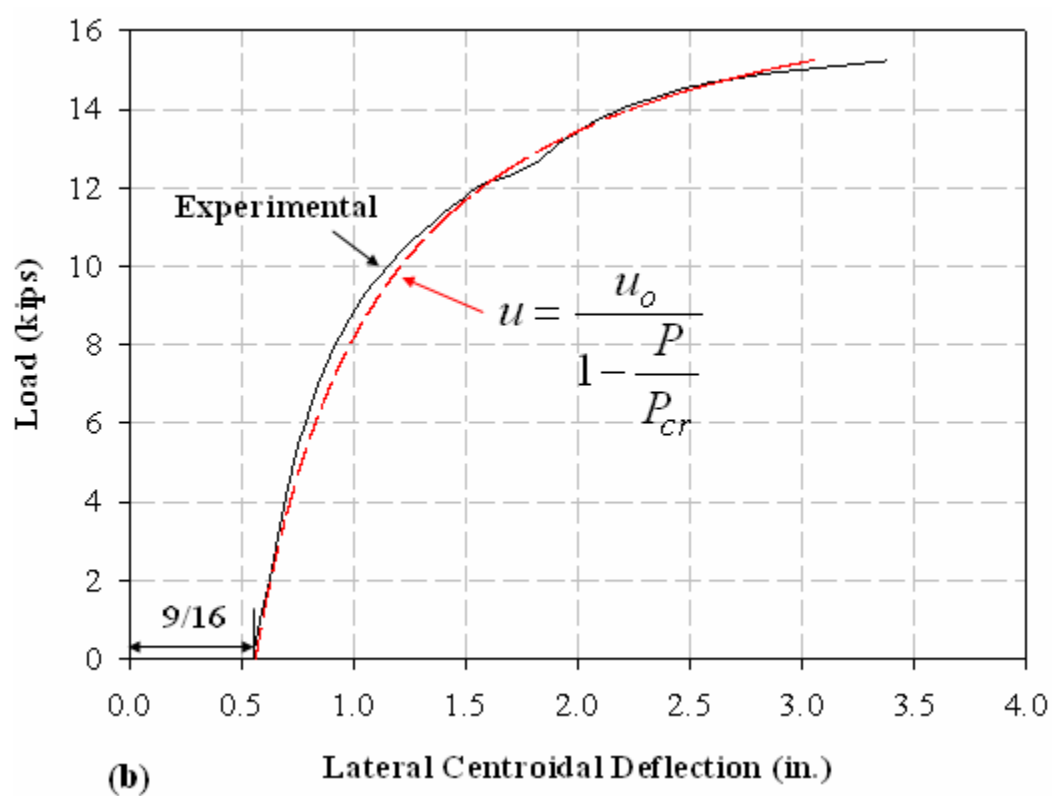
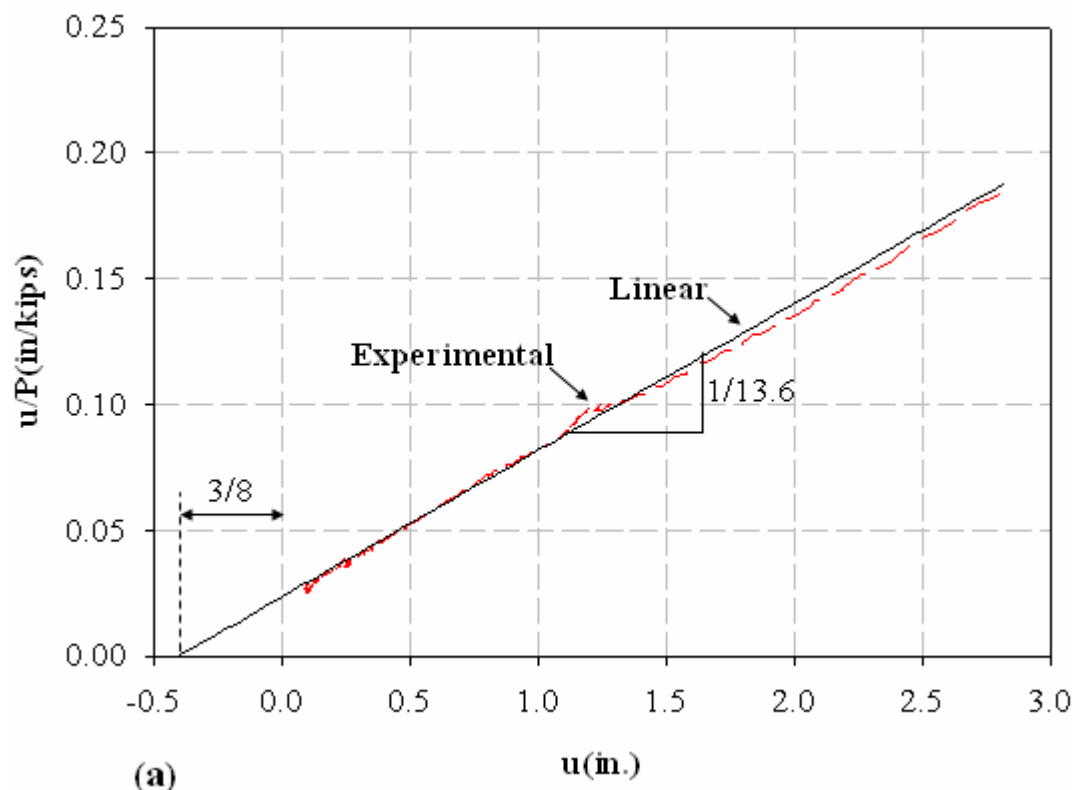


Figure 6.9 - (a) Southwell (1932) Plot; (b) Load-Deflection Plot for Specimen B44-1

It is to be noted that  $P$  is applied at the top of the beam. The deflection of the point of application of load (midwidth of the top face) in the direction of the major axis of the twisted configuration ( $v_t$ ) is related to the deflection of the centroid ( $v$ ) according to Equation (6.8):

$$v_t = v + \frac{h}{2} \cdot \tan(\phi) \quad (6.8)$$

where  $\phi$  is the angle of twist of the beam at midspan corresponding to the load  $P$ . Similarly, the initial deflection of the load application point in the major-axis direction ( $v_{to}$ ) is related to the initial centroidal deflection according to Equation (6.9):

$$v_{to} = v_o + \frac{h}{2} \cdot \tan(\phi_o) \quad (6.9)$$

where  $\phi_o$  is the initial angle of twist of the beam.

Using Southwell's (1932) method, a relation between  $\phi$  and  $\phi_o$  similar to Equation (6.7) is obtained:

$$\phi = \frac{\phi_o}{1 - \frac{P}{P_{cr}}} \quad (6.10)$$

Secondly, the relation between the vertical applied load and the lateral deflection should be assessed. The additional lateral deflection of the point of application of load ( $v_t - v_{to}$ ) is created by the component of the vertical applied load ( $P$ ) in the direction of the major axis of the twisted section ( $P \cdot \sin\phi$ ):



$$\left( \nu + \tan(\phi) \cdot \frac{h}{2} \right) - \left( \nu_o + \tan(\phi_o) \cdot \frac{h}{2} \right) = \frac{P \cdot \sin(\phi) \cdot L^3}{48 \cdot E_c \cdot I_y} \quad (6.11)$$

where  $L$  is the unbraced length of the beam;  $E_c$  is the elastic modulus of concrete and  $I_y$  is the second moment of area about the vertical centroidal axis of the beam section.

Although the minor-axis bending rigidity of a concrete beam can be much lower than  $E_c I_y$  right before buckling, the use of  $E_c I_y$  in Equation (6.11) was found out to agree much better with the experimental results of the present study.

Combining Equations (6.7), (6.10) and (6.11) and using the small angle assumption, the limit load  $P_L$  is related to the critical load of a beam according to Equation (6.12):

$$P_L = P_{cr} - \frac{(\nu_o + \phi_o \cdot h/2) \cdot (48 \cdot E_c \cdot I_y)}{\phi_{ult} \cdot L^3} \quad (6.12)$$

where  $\phi_{ult}$  is the angle of twist of the beam at midspan corresponding to  $P_L$ . The sweep of the centroid ( $u_o$  in Figure 6.8) is related to  $\nu_o$  according to Equation (6.13):

$$u_o = \nu_o \cdot \cos(\phi_o) \quad (6.13)$$

Using Equation (6.13) and the small angle assumption, Equation (6.12) is modified to Equation (6.14):

$$P_L = P_{cr} - \frac{(u_o + \phi_o \cdot h/2) \cdot (48 \cdot E_c \cdot I_y)}{\phi_{ult} \cdot L^3} \quad (6.14)$$

In Chapter VII, analytical load estimates from Equation (6.14) are compared to the experimental results and the analytical estimates from other methods in the literature. Furthermore, simplifications to Equation (6.14) for design codes are presented in Chapter VIII.

## **CHAPTER VII**

### **EXPERIMENTAL RESULTS AND OBSERVATIONS AND CORRELATION OF THE ANALYTICAL AND EXPERIMENTAL RESULTS**

Section 7.1 presents the crack patterns of the specimens after buckling and some of the experimental results. Section 7.2 compares the analytical estimates from different formulations to the experimental limit loads of the specimens measured in the tests.

#### **7.1 Experimental Results and Observations**

##### **7.1.1 Cracks Patterns of the Specimens**

Restrained shrinkage cracks of the specimens were marked prior to the tests to distinguish the initial cracks from the cracks formed after the application of load. Vertical flexural cracks extending through the entire depth of the beam at midspan and diagonal tension cracks outside the midspan region constituted the typical crack pattern on the convex faces of the specimens (Figure 7.1) after buckling. Few diagonal cracks in the vicinity of the end supports and vertical flexural cracks only in the bottom portion of the beam at and around midspan were observed on the concave faces of the beams after lateral torsional buckling (Figure 7.2).

All specimens of the experimental program were failed by lateral torsional buckling. Therefore, similar crack patterns were observed in all specimens. At the initial stages of loading, flexural cracks initiated and propagated in the tension zone of each beam around midspan. These vertical cracks were visible both on convex and concave faces of the beam (Figure 7.3). As the applied load was increased, approaching to the



Figure 7.1 –Typical crack pattern on the convex faces of the specimens after buckling

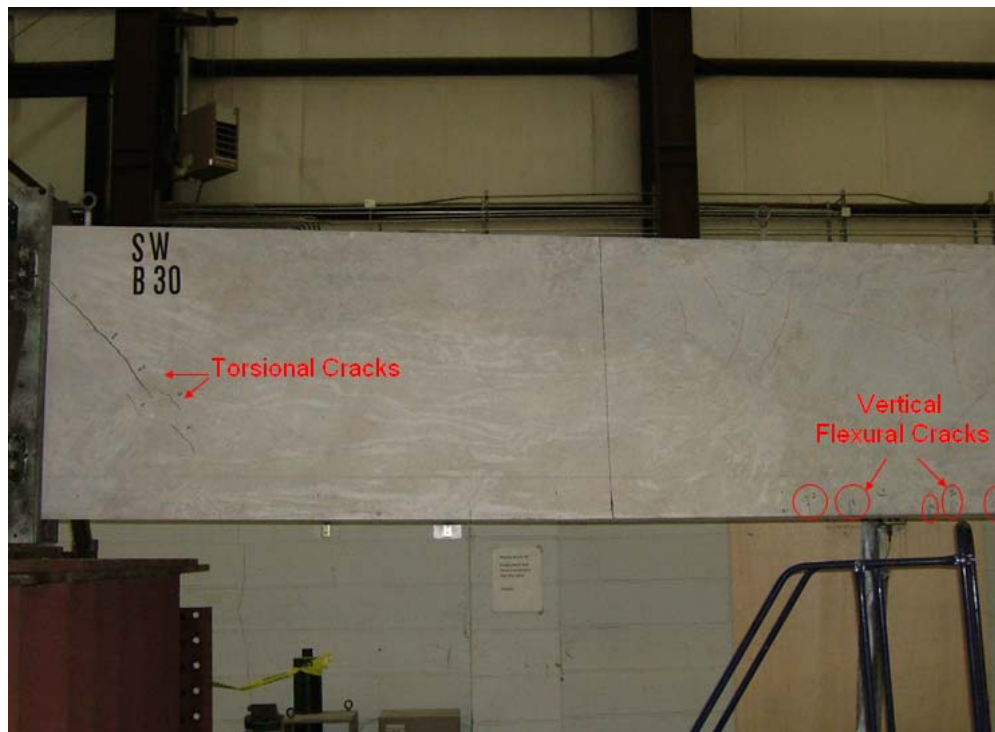


Figure 7.2 –Typical crack pattern on the concave faces of the specimens after buckling



Figure 7.3 – Flexural cracks on the concave face of B44-3 at midspan before buckling

critical load value, lateral deflections and rotations in the beam increased and lateral bending and torsion became more dominant on the crack patterns of the beams. The flexural tension cracks in the outermost fibers of the tension zone, initiated by the in-plane flexural moments, extended upwards on the convex side of the beam (Figure 7.4) due to the tensile strains introduced by lateral bending. On the contrary, the flexural cracks stopped propagating and closed up to a certain extent on the concave side as a result of the compressive strains originating from the lateral bending moments (Figure 7.3). Since the lateral bending moment reached its maximum value at midspan, the vertical flexural cracks extending through the entire depth of the beam were encountered around midspan on the convex faces of the beams.



Figure 7.4 –Vertical cracks on the convex face of B44-2 at midspan after buckling

Cracking outside the midspan region in the test beams was in the form of diagonal tension cracks resulting from the torsional moments and shear forces due to the large lateral displacements after buckling. Figures 7.5 and 7.6 illustrate the directions of the shear and principal stresses in the beams due to the shear forces and torsional moments, respectively. Direct shear stresses (shear stresses due to the shear forces) coincided with the shear stresses from torsion on the convex sides of the beams while the direct shear stresses opposed the shear stresses from torsion on the concave sides. Since the shear stresses from both sources added up on the convex side, the diagonal tension cracks were pronounced on the convex faces of the beams (Figure 7.7). Nevertheless, few or no diagonal cracks could be spotted on the concaves face of the beams (Figure 7.8).

Figure 7.6(b) shows the typical torsional moment diagram of the beams tested in the present study. Ignoring the location of the point of application of load with respect to the shear center of the midspan section, the torque induced by the lateral deflections in each beam increased from zero at midspan to a maximum value at the beam ends. Accordingly, the torsional moments were greater in the vicinity of the laterally-supported beam ends. The greater shear stresses from torsion around the supports overcame the direct shear stresses and few diagonal tension cracks became visible on the concave faces of the beam at and around the supports (Figure 7.8). The diagonal tension cracks on the concave side in the vicinity of the end supports were in perpendicular direction (reversed) to the diagonal tension cracks on the convex side due to torsional restraint at the beam ends. The diagonal cracks on the convex and concave sides were connected to each other at the top of the beam, where the extensions of the diagonal tension cracks were visible (Figure 7.9).

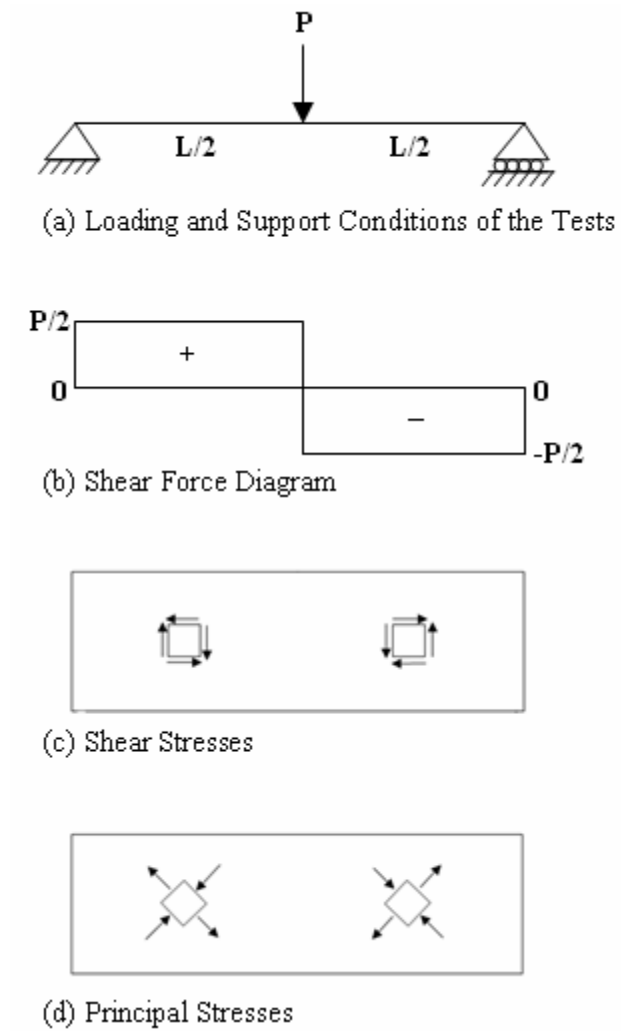
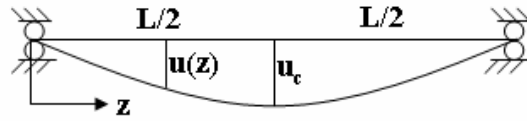
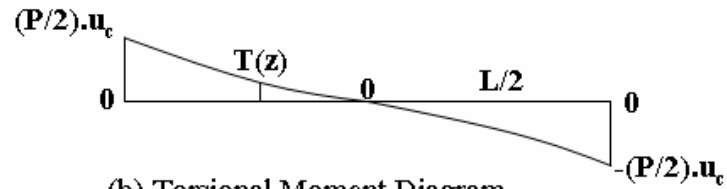


Figure 7.5 –Directions of the shear and principal stresses due to the shear forces





(a) Typical Lateral Deformations of the Test Beams  
(Top View)



(b) Torsional Moment Diagram



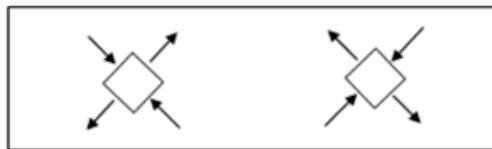
(c) Shear Stresses on the Convex Face



(d) Principal Stresses on the Convex Face



(e) Shear Stresses on the Concave Face



(g) Principal Stresses on the Concave Face

Figure 7.6 –Directions of the shear and principal stresses due to the torsional moments



Figure 7.7 –Diagonal tension cracks on the convex face of B36L-1 after buckling



Figure 7.8 –Diagonal tension cracks on the concave face of B18-2 after buckling



Figure 7.9 –Diagonal tension cracks continuing on the top surface of B44-2 after buckling

### 7.1.2 Experimental Results

The experimental load-lateral (out-of-plane) deflection, load-vertical (in-plane) deflection and torque-twist curves of the specimens are presented in Appendix D. The midspan strain distributions of the beams throughout the test are presented in Appendix C.

All specimens of the present study experienced elastic lateral-torsional buckling. Figures 7.10 to 7.12 illustrate the measured greatest compressive strains of the specimens at the initiation of buckling on the experimental stress-strain curve of concrete. The point corresponding to each of the specimens is on the initial portion of the stress-strain curve of concrete, implying that concrete in each specimen behaved elastically at initiation of

buckling. Similarly, the reinforcing bars in the specimens were measured to be strained within the elastic range of the stress-strain curve of steel (Appendix C).

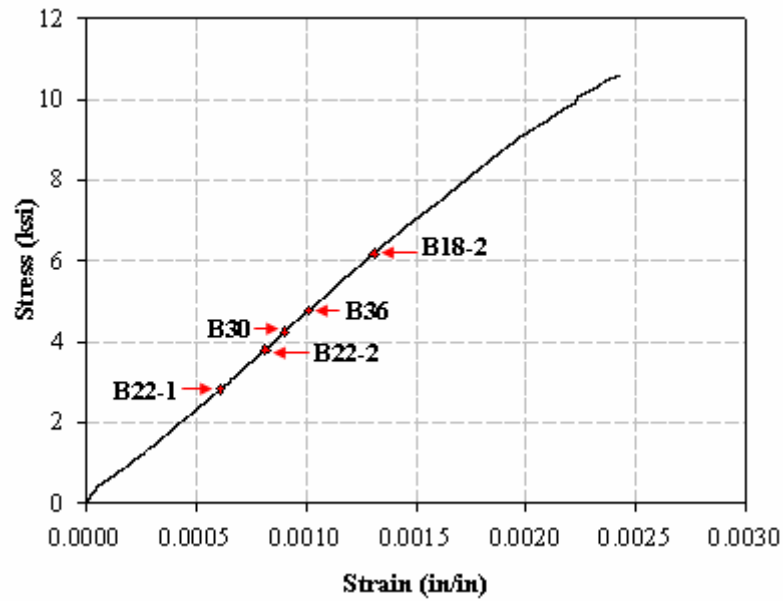


Figure 7.10 – Maximum compressive strains in the first set of beams, illustrated on the stress-strain curve of concrete

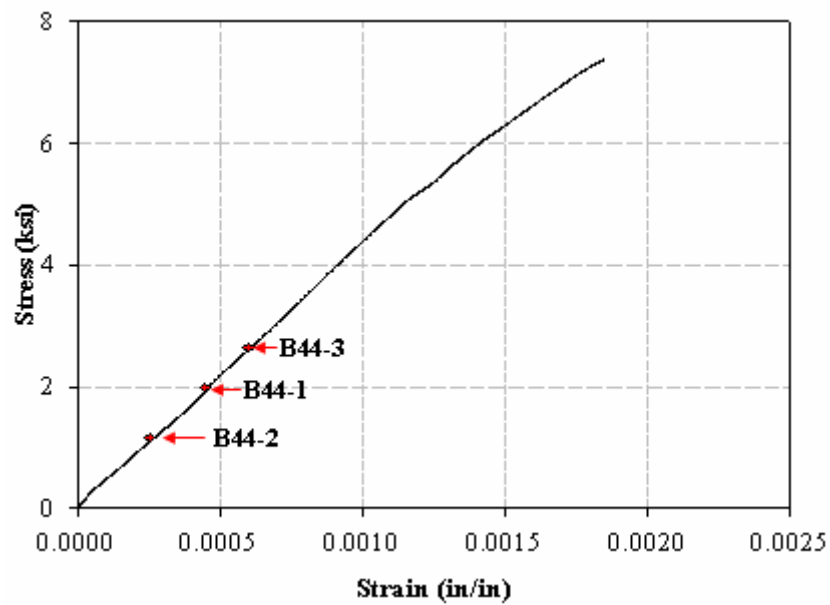


Figure 7.11 – Maximum compressive strains in B44 at the time of buckling

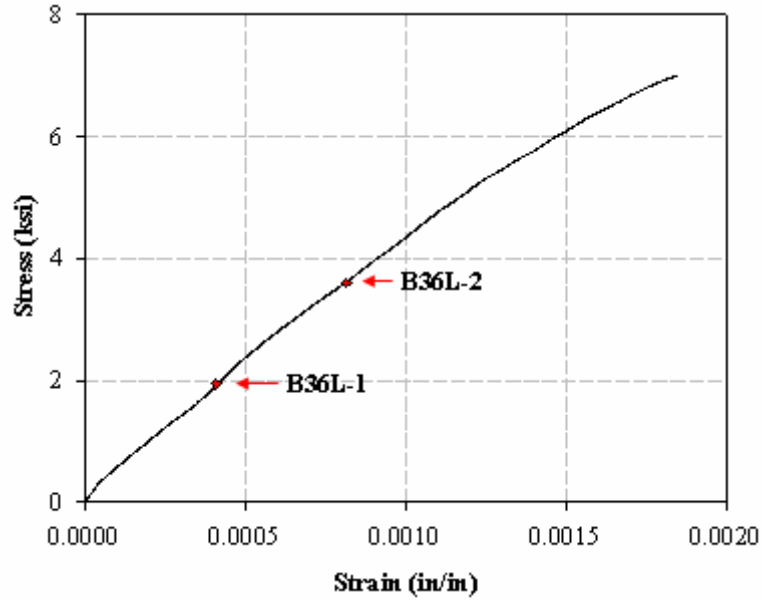


Figure 7.12 – Maximum compressive strains in B36L at the time of buckling

## 7.2 Correlation of the Analytical and Experimental Results

In Table 7.1, analytical estimates according to four different formulae in the literature and the formula proposed in the present study are tabulated together with the experimental limit loads of the specimens. Table 7.2 presents the experimental to analytical load ratios of the specimens according to the formulae used in Table 7.1. The experimental to analytical load ratios corresponding to different analytical formulae are also compared in Figure 7.13 for each specimen. Specimen B44-3 is not included in Tables 7.1 and 7.2 and Figure 7.13, since the experimental data of this beam, which buckled in the opposite direction to its sweep, was not considered reliable to be compared to the analytical estimates from different solutions.

The equations used for obtaining the analytical estimates in Tables 7.1 and 7.2 and Figure 7.13 are presented here. The limit load estimates according to the method

proposed in the present study are obtained from Equation (7.1), which was previously given in Chapter VI [Equation (6.14)]:

$$P_L = \frac{16.92 \cdot \sqrt{B_o \cdot (GC)_o}}{L^2} \cdot \left( 1 - 1.74 \cdot \frac{e}{L} \cdot \sqrt{\frac{B_o}{(GC)_o}} \right) - \frac{u_{to} \cdot (48 \cdot E_c \cdot I_y)}{\sin(\phi_{ult}) \cdot L^3} \quad (7.1)$$

where  $L$  is the unbraced length of the beam;  $B_o$  is the lateral bending rigidity, obtained from Equation (7.2);  $(GC)_o$  is the torsional rigidity, calculated from Equation (7.3);  $e$  is the vertical distance of the load application point from the centroid of the midspan cross section;  $u_{to}$  is the sweep at the top of the beam at midspan;  $E_c$  is the elastic modulus of concrete;  $I_y$  is the second moment of area of the beam section about the minor axis;  $\phi_{ult}$  is the angle of twist of the beam at midspan corresponding to the limit load.

$$B_o = \left[ \left( \frac{b^3 \cdot c}{12} \right) \cdot \frac{1}{1 + \left( \frac{\omega \cdot M_{cra}}{M_{cr}} \right)^2 \cdot \left( \frac{c}{h} - 1 \right)} \right] \cdot \left( \frac{E_{sec} + E_c}{2} \right) \quad (7.2)$$

where  $b$  and  $h$  are the width and height of the beam, respectively;  $c$  is the depth of the neutral axis from the compression face;  $M_{cra}$  is the cracking moment;  $M_{cr}$  is the critical moment;  $E_{sec}$  is the secant modulus of elasticity of concrete corresponding to the extreme compression fiber strain at midspan at the instant when  $P_{cr}$  is reached;  $\omega$  is a constant, which has a value of 1 in the absence of restrained shrinkage cracks in concrete and a value of 2/3 in the presence of restrained shrinkage cracks.

$$(GC)_o = \frac{E_{sec} + E_c}{4 \cdot (1 + \nu)} \cdot \left[ \frac{b^3 \cdot h}{3} \cdot \left( 1 - 0.63 \cdot \frac{b}{h} \right) \right] \quad (7.3)$$

where  $\nu$  is Poisson's ratio of concrete.

First, the torsional and lateral bending rigidities of a beam should be calculated from Equations (7.3) and (7.2), respectively. Next, the limit load ( $P_{ult}$ ) can be calculated from Equation (7.1), using the calculated values of  $B_o$  and  $(GC)_o$ . Equations (7.2) and (7.3) correspond to the bending and torsional rigidities of a rectangular reinforced concrete beam when the beam is subjected to an applied load of  $P_{cr}$ . For example,  $E_{sec}$  in the equations is the secant modulus of elasticity of concrete corresponding to extreme compression fiber strain at midspan when the maximum in-plane bending moment in the beam is equal to  $M_{cr}$ . Furthermore,  $c$  in Equation (7.2) is the neutral axis depth of the beam section resisting a moment of  $M_{cr}$ . Considering the terms  $E_{sec}$ ,  $c$  and  $M_{cr}$  in the rigidity expressions, Equations (7.2) and (7.3) also depend on Equation (7.1). Due to this interdependence, an iterative procedure is needed to calculate the limit load of a beam. In Appendix F, the critical moment calculations of one of the specimens are shown as an example.

The limit load of a beam depends on the girder sweep and the angle of twist at the instant when the limit load is reached. Table 7.3 tabulates  $u_{to}$  and  $\phi_{ult}$  values, which were used in Equation (7.1) to calculate the limit loads of the specimens.  $u_{to}$  values in the table are the sweep values measured at the top of each specimen at midspan. The initial lateral imperfections of the specimens measured at different points along the length of each beam are presented in Appendix B.  $\phi_{ult}$  values in Table 7.3 on the other hand, are the twisting angles calculated according to the method described in Section 3.1.3 of Chapter III from the lateral deflection measurements taken in the tests.

Table 7.1 – Experimental and analytical critical load values of the specimens

Specimen	Experimental Load, $P_{ex}$ (kips)	Analytical Load, $P_{an}$ (kips)				
		Elastic & Homog. Material, $P_{el}$ , Eq. (7.4)	Hansell & Winter (1959), $P_{hw}$ , Eq. (7.7)	Sant & Bletzacker (1961), $P_{sb}$ , Eq. (7.10)	Massey (1967), $P_m$ , Eq. (7.14)	Present Study, $P_{ult}$ , Eq. (7.1)
<b>B18-1</b>	12.4	26.7	10.2	19.8	17.7	9.0
<b>B18-2</b>	12.0	23.7	9.4	17.6	15.6	8.9
<b>B22-1</b>	8.7	33.2	12.8	25.4	21.4	8.0
<b>B22-2</b>	11.0	27.5	10.7	21.0	18.7	*
<b>B30</b>	22.0	86.6	31.9	69.1	51.9	17.0
<b>B36</b>	39.2	101.5	39.1	80.6	67.3	40.6
<b>B44-1</b>	15.2	38.8	13.2	31.2	24.1	15.6
<b>B44-2**</b>	12.0	40.1	13.7	32.6	24.2	7.2
<b>B36L-1</b>	13.5	36.7	13.4	30.0	22.9	11.4
<b>B36L-2</b>	21.7	38.7	14.0	31.7	24.5	18.2

\* Sweep of Specimen B22-2 is not known.

\*\* Specimen B44-3 buckled in opposite direction to its sweep. Due to this unusual situation, the experimental data of B44-3 was not considered reliable to compare to the analytical estimates.



Table 7.2 – Experimental-to-analytical critical load ratios of the specimens

Specimen	Elastic & Homog. Material, $P_{ex}/P_{el}$	Hansell& Winter (1959), $P_{ex}/P_{hw}$	Sant & Bletzacker (1961), $P_{ex}/P_{sb}$	Massey (1967), $P_{ex}/P_m$	Present Study, $P_{ex}/P_{ult}$
<b>B18-1</b>	0.46	1.22	0.63	0.70	1.38
<b>B18-2</b>	0.51	1.28	0.68	0.77	1.35
<b>B22-1</b>	0.26	0.68	0.34	0.41	1.09
<b>B22-2</b>	0.40	1.03	0.52	0.59	*
<b>B30</b>	0.25	0.69	0.32	0.42	1.29
<b>B36</b>	0.39	1.00	0.49	0.58	0.97
<b>B44-1</b>	0.39	1.15	0.49	0.64	0.97
<b>B44-2**</b>	0.30	0.88	0.37	0.50	1.67
<b>B36L-1</b>	0.37	1.01	0.45	0.59	1.18
<b>B36L-2</b>	0.56	1.54	0.68	0.88	1.19
<b>Mean</b>	0.39	1.05	0.50	0.61	1.23
<b>S.D.</b>	0.10	0.26	0.13	0.15	0.22
<b>COV%</b>	26	25	27	24	18

\* Sweep of Specimen B22-2 is not known.

\*\* Specimen B44-3 buckled in opposite direction to its sweep. Due to this unusual situation, the experimental data of B44-3 was not considered reliable to compare to the analytical estimates.

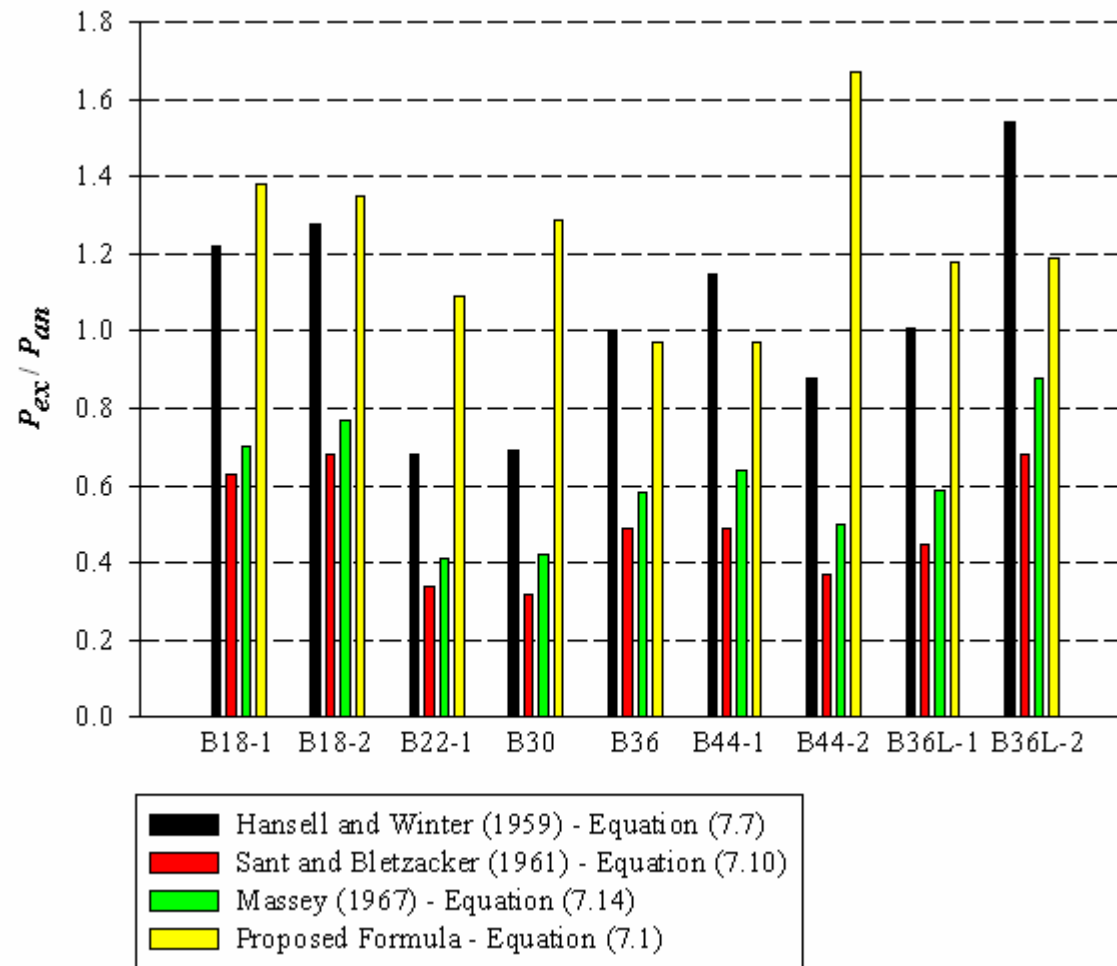


Figure 7.13 – Experimental-to-analytical critical load ratios of the specimens according to different formulae

Table 7.3 – Measured sweeps and angles of twist at limit load of the specimens at midspan

Specimen	Sweep, $u_{to}$ (in)	Angle of Twist at Limit Load $\phi_{ult}$ (deg)
<b>B18-1</b>	7/16	1.17
<b>B18-2</b>	1/8	0.45
<b>B22-1</b>	11/16	1.66
<b>B30</b>	5/8	0.86
<b>B36</b>	7/32	0.52
<b>B44-1</b>	9/16	0.77
<b>B44-2</b>	25/32	0.55
<b>B36L-1</b>	3/4	0.70
<b>B36L-2</b>	11/32	0.65

The column denoted as the elastic and homogeneous material in Table 7.1 gives the analytical values calculated by assuming that a reinforced concrete beam is a homogeneous and elastic body, not subjected to cracking under loads. Regarding these assumptions, the ultimate load ( $P_{el}$ ) of a concrete beam can be calculated from Equation (7.4):

$$P_{el} = \frac{16.92 \cdot \sqrt{B_{el} \cdot (GC)_u}}{L^2} \cdot \left( 1 - 1.74 \cdot \frac{e}{L} \cdot \sqrt{\frac{B_{el}}{(GC)_u}} \right) \quad (7.4)$$

where  $B_{el}$  is the lateral flexural rigidity of an elastic and homogeneous beam with a solid rectangular cross section;  $(GC)_u$  is the uncracked torsional rigidity of a reinforced concrete beam (Equation 5.9 in Chapter V).  $B_{el}$  and  $(GC)_u$  are calculated from Equations (7.5) and (7.6), respectively:

$$B_{el} = E_c \cdot \frac{b^3 \cdot h}{12} \quad (7.5)$$

$$(GC)_u = \frac{E_c}{2 \cdot (1 + \nu)} \cdot \beta_c \cdot b^3 \cdot h \quad (7.6)$$

where  $\beta_c$  is the coefficient for St. Venant's torsional constant, obtained from Equation (5.11).

Although Equations (7.4) - (7.6) do not reflect the true behavior of a reinforced concrete beam, the results obtained from Equation (7.4) are included in Table 7.1 to compare the limit load of each specimen to the limit load of a homogeneous and elastic beam with the same dimensions as the specimen.

The analytical ultimate load estimates according to Hansell and Winter (1959) were obtained from Equations (7.7):

$$P_{hw} = \frac{16.92 \cdot \sqrt{B_{hw} \cdot (GC)_{hw}}}{L^2} \cdot \left( 1 - 1.74 \cdot \frac{e}{L} \cdot \sqrt{\frac{B_{hw}}{(GC)_{hw}}} \right) \quad (7.7)$$

where  $B_{hw}$  and  $(GC)_{hw}$  are the lateral flexural and torsional rigidities according to the expressions proposed by Hansell and Winter (1959), given as

$$B_{hw} = E_{sec} \cdot \frac{b^3 \cdot c}{12} \quad (7.8)$$

$$(GC)_{hw} = \frac{E_{sec}}{2 \cdot (1 + \nu)} \cdot \left[ \frac{b^3 \cdot c}{3} \cdot \left( 1 - 0.35 \cdot \frac{b}{d} \right)^2 \right] \quad (7.9)$$

where  $d$  is the effective depth of the beam from the compression face.

The ultimate load values according to Sant and Bletzacker (1961) are obtained from the following equation:

$$P_{sb} = \frac{16.92 \cdot \sqrt{B_{sb} \cdot (GC)_{sb}}}{L^2} \cdot \left( 1 - 3.48 \cdot \frac{e}{L} \cdot \sqrt{\frac{B_{sb}}{(GC)_{sb}}} \right) \quad (7.10)$$

where  $B_{sb}$  and  $(GC)_{sb}$  are the lateral flexural and torsional rigidities according to the expressions proposed by Sant and Bletzacker (1961), given as

$$B_{sb} = E_r \cdot \frac{b^3 \cdot d}{12} \quad (7.11)$$

$$(GC)_{sb} = \frac{E_r}{2 \cdot (1 + \nu)} \cdot \left( \frac{b^3 \cdot d}{3} \right) \quad (7.12)$$

where  $E_r$  is the reduced modulus of elasticity of concrete corresponding to the extreme compression fiber strain at midspan at the instant when the applied load is equal to  $P_{sb}$ .  $E_r$  is calculated from

$$E_r = \frac{4 \cdot E_c \cdot E_{tan}}{\left( \sqrt{E_c} + \sqrt{E_{tan}} \right)^2} \quad (7.13)$$

where  $E_{tan}$  is the tangent modulus of elasticity of concrete corresponding to the extreme compression fiber strain at midspan at the instant when the applied load is equal to  $P_{sb}$ .

The expression in parenthesis in Equation (7.10), which corresponds to the destabilizing or stabilizing effect of the load applied above or below the centroid of the midspan section, is different from the respective expression in Equations (7.1) and (7.7). In their study, Sant and Bletzacker (1961) considered the influence of the distance of the

load application point from the centroid of the section and included the expression in parenthesis in Equation (7.10) to account for this influence. In the present study, the original critical moment expression [Equation (7.10)] proposed by Sant and Bletzacker (1961) was used together with the torsional and lateral bending rigidity expressions developed by Sant and Bletzacker (1961).

Finally, the ultimate load values according to Massey's (1967) formulation were obtained from the following equation:

$$P_m = \frac{16.92 \cdot \sqrt{B_m \cdot (GC)_m}}{L^2} \cdot \left( 1 - 1.74 \cdot \frac{e}{L} \cdot \sqrt{\frac{B_m}{(GC)_m}} \right) \quad (7.14)$$

where  $B_m$  and  $(GC)_m$  are the lateral flexural and torsional rigidities according the expressions proposed by Massey (1967), given as

$$B_m = E_{\text{sec}} \cdot \frac{b^3 \cdot c}{12} + E_s \cdot \Sigma I_{sy} \quad (7.15)$$

$$(GC)_m = G'_c \cdot \beta_c \cdot b^3 \cdot h + \frac{1}{3} \cdot (G_s - G'_c) \cdot \Sigma b_s^3 \cdot t_s + \frac{\gamma \cdot b_l^2 \cdot d_l \cdot A_o \cdot E_s}{2 \cdot \sqrt{2} \cdot s} \quad (7.16)$$

where  $\Sigma I_{sy}$  is the moment of inertia of the longitudinal steel about the minor axis of the section;  $b_s$  and  $t_s$  are the width and thickness of the longitudinal reinforcement layer, respectively (illustrated in Figure 1.18 in Chapter I);  $\gamma$  is a constant defined by Cowan (1953);  $b_l$  and  $d_l$  are the breadth and depth of the cross-sectional area enclosed by the closed stirrup, respectively (Figure 1.18);  $s$  is the spacing of the stirrups;  $A_o$  is the cross-sectional area of one leg of the stirrup;  $E_s$  and  $G_s$  are the modulus of elasticity and

modulus of rigidity of steel, respectively;  $G'_c$  is the reduced modulus of rigidity of concrete, calculated according to the following equation:

$$G'_c = \frac{E_{sec}}{2 \cdot (1 + \nu)} \quad (7.17)$$

Tables 7.1 and 7.2, and Figure 7.13 indicate that the analytical estimates produced by the proposed method are in good agreement with the experimental results. Furthermore, the analytical estimates from the proposed method never exceeded the experimental ultimate loads, with the exception of Specimens B36 and B44-1, for which the analytical estimates are only 3-4% greater than the experimental values. The experimental to analytical load ratios corresponding to the proposed method were in the range of 0.97-1.67 with a mean value of 1.23 and coefficient of variation of 0.18 (Table 7.2).

Among the formulae proposed by the previous researchers, the equation given by Hansell and Winter (1959) closely estimated the limit loads of the specimens with the experimental to analytical load ratios in the range of 0.68-1.54 (a mean value of 1.05 and coefficient of variation of 0.25). The formulae proposed by Sant and Bletzacker (1961) and Massey (1967) constantly overestimated the limit loads of the specimens. The analytical estimates from Sant and Bletzacker's (1961) formula sometimes reached 2.5-3 times the limit loads measured in the tests.

As mentioned before,  $u_o$  and  $\varphi_{ult}$  are needed to calculate the limit load of a beam according to Equation (7.1).  $\varphi_{ult}$ , in particular, is a quantity which is determined by testing a beam to failure. Since testing a beam to failure is not always possible, particularly in a real construction, a value for  $\varphi_{ult}$  should be assumed in the limit load

calculations. In Chapter VIII, Equation (7.1) is modified by assuming constant values for  $\varphi_{ult}$  to simplify the equation.



## CHAPTER VIII

### SUMMARY AND CONCLUSIONS

#### 8.1 Summary

The present study investigated the lateral stability of rectangular reinforced concrete beams both analytically and experimentally. The experimental part of the study provided the experimental results of reinforced concrete beams, whose initial geometric imperfections, shrinkage cracking conditions and material properties are completely known. In the analytical part of the study, the following formula was developed for estimating the limit loads ( $P_L$ ) of simply-supported rectangular reinforced concrete beams with initial geometric imperfections, subjected to a concentrated load at midspan:

$$P_L = \frac{4 \cdot M_{cr}}{L} - \frac{u_{to} \cdot (48 \cdot E_c \cdot I_y)}{\sin(\phi_{ult}) \cdot L^3} \quad (8.1)$$

where  $P_L$  is the limit load;  $L$  is the unbraced length of the beam;  $u_{to}$  is the sweep at the top of the beam at midspan;  $E_c$  is the elastic modulus of concrete;  $I_y$  is the second moment of area of the beam section about the minor axis;  $\phi_{ult}$  is the angle of twist of the beam at midspan corresponding to the limit load ( $P_L$ ).  $M_{cr}$  is the critical moment corresponding to the geometrically perfect configuration of the beam, obtained from Equation (8.2):

$$M_{cr} = \frac{4.23}{L} \cdot \left( 1 - 1.74 \cdot \frac{e}{L} \cdot \sqrt{\frac{B_o}{(GC)_o}} \right) \cdot \sqrt{B_o \cdot (GC)_o} \quad (8.2)$$

where  $B_o$  is the lateral bending rigidity, obtained from Equation (8.3);  $(GC)_o$  is the torsional rigidity, calculated from Equation (8.4);  $e$  is the vertical distance of the load application point from the centroid of the midspan cross section.

$$B_o = \left[ \left( \frac{b^3 \cdot c}{12} \right) \cdot \frac{1}{1 + \left( \frac{\omega \cdot M_{cra}}{M_{cr}} \right)^2 \cdot \left( \frac{c}{h} - 1 \right)} \right] \cdot \left( \frac{E_{sec} + E_c}{2} \right) \quad (8.3)$$

$$(GC)_o = \frac{E_{sec} + E_c}{4 \cdot (1 + \nu)} \cdot \left[ \frac{b^3 \cdot h}{3} \cdot \left( 1 - 0.63 \cdot \frac{b}{h} \right) \right] \quad (8.4)$$

where  $b$  and  $h$  are the width and height of the beam, respectively;  $c$  is the depth of the neutral axis from the compression face;  $M_{cra}$  is the cracking moment, obtained from Equation (8.5);  $\omega$  is a constant, which has a value of 1 in the absence of restrained shrinkage cracks in concrete and a value of 2/3 in the presence of restrained shrinkage cracks and  $\nu$  is Poisson's ratio of concrete.  $E_{sec}$  is the secant modulus of elasticity of concrete corresponding to the extreme compression fiber strain at midspan at the instant when  $M_{cr}$  is reached.  $E_{sec}$  is calculated from Equation (8.6).

$$M_{cra} = \frac{I_{ucr} \cdot (7.5 \cdot \sqrt{f'_c})}{h - \bar{y}} \quad (8.5)$$

where  $7.5 \cdot \sqrt{f'_c}$  is the modulus of rupture of normal-weight concrete, given in ACI 318-05 (2005) Section 9.5.2.3;  $\bar{y}$  is the depth of the center of gravity of the transformed

section from the top surface of the beam;  $I_{ucr}$  is the moment of inertia of the transformed section about the major axis, obtained from Equation (8.7).

$$E_{\text{sec}} = \frac{f_c}{\varepsilon_c} \quad (8.6)$$

where  $f_c$  and  $\varepsilon_c$  are the extreme compression fiber stress and extreme compression fiber strain at midspan corresponding to the critical moment  $M_{cr}$ .

$$I_{ucr} = \frac{1}{12} \cdot b \cdot h^3 + b \cdot h \cdot \left( \bar{y} - \frac{h}{2} \right)^2 + (n-1) \cdot A_s \cdot (d - \bar{y})^2 \quad (8.7)$$

where  $A_s$  is the cross-sectional area of the flexural reinforcement;  $n$  is the modular ratio of steel to concrete;  $d$  is the effective depth of the centroid of tension reinforcement from compression face. When calculating the uncracked moment of inertia,  $I_{ucr}$ , the flexural reinforcement is transformed into an equivalent concrete area in accordance with the modular ratio of steel to concrete,  $n$ .

Due to the interdependence of  $M_{cr}$ ,  $B_o$  and  $(GC)_o$ , an iterative process is needed when calculating the limit load of a beam. This interdependence is also present in the methods proposed by Hansell and Winter (1959), Sant and Bletzacker (1961) and Massey (1967). The primary reason for the interdependence of the critical moment and the lateral bending and torsional rigidities is that the modulus of elasticity and modulus of rigidity terms in the rigidity expressions depend on the maximum compressive strain in the beam corresponding to the critical moment, as explained in Appendix F in more detail.

The experimental stage of the study consisted of testing eleven reinforced concrete beams with  $d/b$  ratios between 10.20 and 12.45 and  $L/b$  ratios between 96 and

156. Beam thickness, depth and unbraced length were 1.5 to 3.0 in., 18 to 44 in., and 12 to 39.75 ft, respectively. The test beams were simply-supported in and out of plane and subjected to a single concentrated load at midspan. The end supports allowed warping deformations in the beams while restraining the torsional rotations at the beam ends. The loading mechanism used in the tests provided lateral translational and rotational freedom at the load application point and ensured that the vertical orientation of the applied load was maintained throughout the entire test. The in-plane (vertical) and out-of-plane (lateral) deformations, the torsional rotations and the strain distributions in the beams were measured at midspan, continuously along the tests.

There are several factors influencing the lateral stability of reinforced concrete beams. Initial geometric imperfections, shrinkage cracking, contribution of the longitudinal and shear reinforcement to the torsional and lateral bending rigidities, creep, inelastic stress-strain properties of concrete and reinforcing steel, loading and support conditions are some of the major factors affecting the lateral stability. Investigating the influences of several factors in the same experiments renders the analysis and interpretation of the experimental data cumbersome. In the present experimental program, the main factor whose effects were investigated is the initial lateral imperfections (sweep) of a beam. To detect the effects of sweep, the influences of some of the other factors were minimized or eliminated through the following ways:

- The specimens of the present experimental program were designed in such a way that both concrete and reinforcing steel in the beams remained in the elastic ranges of their stress-strain curves throughout the loading process. By eliminating the inelastic stress-strain properties of concrete and steel, pure elastic material behavior was

attained and the effects of inelasticity on the lateral stability of the specimens were eliminated. Nevertheless, the lateral and torsional rigidity expressions proposed in the present study account for both elastic and inelastic material behaviors of concrete and reinforcing steel to be applicable for all reinforced concrete beams with different dimensions, reinforcement details and material properties.

- Restrained shrinkage cracking of concrete was tried to be prevented through the measures described in Section 4.4. Addition of Shrinkage Reducing Admixtures (SRA) to concrete and early removal of the beams from the forms minimized the amount and extent of shrinkage cracking in the second set of specimens.
- The specimens were designed in a way that the contributions of the longitudinal and shear reinforcement to the lateral stability of the beams were negligible. The longitudinal reinforcing bars were located along the vertical centroidal axis of the beam section. Presuming that the minor axis of the beam is coincident with the vertical centroidal axis throughout the test, the longitudinal reinforcement did not contribute to the lateral bending rigidities of the beams since the second moment of area of the longitudinal reinforcement ( $\Sigma I_{sy}$ ) is equal to zero in this design. Furthermore, the specimens did not experience diagonal tension cracking up to buckling. Prior to the formation of diagonal tension cracks, a reinforced concrete beam behaves as a solid and homogeneous body, whose torsional rigidity is provided by the entire cross-section. In the pre-cracking stage, contributions of the flexural and shear reinforcement to the torsional rigidity are negligible. Due to the absence of torsional cracks in the beams up to buckling, contribution of the reinforcement to the resistance of torsional moments was disregarded.

- All specimens of the experimental program were tested under identical loading and support conditions. Consequently, the effects of the loading and support conditions on the test results of companion beams (beams with identical nominal dimensions, reinforcement details and material properties) were eliminated.
- Concrete from the same batch and reinforcing steel from the same batch were used in the companion beams to keep the material properties constant so that the experimental results of the companion beams were not affected from the differences between the mechanical properties of the beams.
- To eliminate the influence of creep on the lateral stability, the test beams were loaded continuously up to the ultimate load without interruption.

Although the experimental program aimed at eliminating the influences of the aforementioned factors on the lateral stability of the specimens, all factors affecting the lateral stability of a reinforced concrete beam were taken into consideration in the development of the proposed analytical method. For instance, Equation (4.18) in Chapter IV gives the lateral bending rigidity of a reinforced concrete beam, considering the influence restrained shrinkage cracking. For the possible contribution of the longitudinal reinforcing bars, on the other hand, Equation (4.16) was developed. Furthermore, both torsional and lateral bending rigidity expressions developed in the present study are applicable to the cases of elastic and inelastic lateral-torsional buckling.

## 8.2 Conclusions

Some of the conclusions drawn from the present study for the lateral stability of rectangular reinforced concrete beams follow:

- The load predictions from the proposed analytical method showed good correlation with the experimental results. The analytical to experimental limit load ratios of the specimens ranged from 0.97 to 1.67 for the proposed analytical method. The analytical method developed in the present study is superior to the analytical methods proposed by Hansell and Winter (1959), Sant and Bletzacker (1961) and Massey (1967) in incorporating the effects of sweep, shrinkage cracking and inelastic stress-strain properties of concrete into the buckling formula.
- Among the former methods considered in the present study, the analytical method proposed by Hansell and Winter (1959) produced better correlation with the experimental results than the methods proposed by Sant and Bletzacker (1961) and Massey (1967), which constantly overestimated the ultimate loads of the beams.
- In contrast to the methods in the literature, the load estimates produced by the proposed method were smaller or slightly larger than the experimental buckling loads of the specimens (Table 7.2), which makes the proposed method more conservative than the methods proposed by Hansell and Winter (1959), Sant and Bletzacker (1961) and Massey (1967). Even some of the load estimates from the method proposed by Hansell and Winter (1959), which was in closer agreement with the experimental results than the methods proposed by Sant and Bletzacker (1961) and Massey (1967), were greater than the experimental buckling loads of the specimens.
- In the case of elastic lateral torsional buckling, reinforced concrete beams do not undergo diagonal tension cracking before buckling. Therefore, the uncracked torsional rigidity closely reflects the torsional resistance of a reinforced concrete beam at the instant of buckling, if the beam buckles elastically. Moreover,

contributions of the longitudinal and shear reinforcement to the torsional rigidity of a reinforced concrete beam is negligible in elastic buckling since the reinforcement of a concrete beam has a major influence on the torsional behavior of a concrete beam only after diagonal cracking.

- The influence of the longitudinal reinforcement on the lateral stability of a concrete beam originates from its contribution to the lateral bending rigidity. Similarly, restrained shrinkage cracking of concrete affects the lateral stability of a beam by reducing its lateral bending rigidity. Lateral bending rigidity expression given in Equation (4.17) considers the increase in the lateral bending rigidity of a reinforced concrete beam due to the contribution of the flexural reinforcement while the rigidity expression given in Equation (4.16) was developed regarding the negative influence of shrinkage cracking of concrete on the lateral bending rigidity.
- A geometrically imperfect concrete beam does not reach the critical moment corresponding to the geometrically perfect configuration of the beam. The additional stresses originating from the initial minor-axis curvature from sweep cause the imperfect beam to crack earlier in the loading process (at smaller load levels). Cracking on the convex side of the beam greatly reduces the lateral bending rigidity and the load-carrying capacity of the beam starts decreasing before reaching the critical load. The maximum load on the load-lateral deflection curve of an imperfect beam is denoted as the limit load, which should be distinguished from the critical load. The limit load formula proposed in the present study is based on reducing the critical load by an amount equal to the destabilizing effect of the sweep on the beam.



- Results of the present experimental program indicated that an increase in the sweep can greatly reduce the ultimate load resisted by a reinforced concrete beam before losing its stability. The significant differences between the ultimate loads of the companion beams mainly originated from the different initial lateral imperfections of the beams. For instance, the experimental ultimate load of Specimen B36L-2 (11/32 in sweep) was 38% greater than the experimental ultimate load of Specimen B36L-1 (3/4 in sweep).
- To calculate the limit load of an imperfect reinforced concrete beam from Equation (7.1), the angle of twist ( $\varphi_{ult}$ ) of the beam needs to be known.  $\varphi_{ult}$  is a parameter indicating the torsional rotations in a beam till buckling and it is determined by testing a beam to failure. In the design of a concrete beam, a value for  $\varphi_{ult}$  should be assumed. The  $\varphi_{ult}$  values of the test specimens ranged from 0.45 degrees to 1.66 degrees. However, most of the specimens had a midspan angle of twist between 0.55 degrees to 0.75 degrees at the limit load level. As  $\varphi_{ult}$  decreases, the reduction in the limit load of a beam increases. Therefore, assuming a value between 0.55 and 0.60 degrees for  $\varphi_{ult}$  seems reasonable and safe according to the available experimental data. However, more experimental data is needed to make more accurate assumptions.

### 8.3 Future Research

The analytical method, proposed in the present study, incorporates several factors influencing the lateral stability of reinforced concrete beams. The factors with considerable influence were restated in Section 8.1. The experimental stage of the study, nonetheless, aimed at investigating the effects of the initial lateral imperfections on the

buckling behavior of reinforced concrete beams. To achieve this goal, the effects of the other influential factors were tried to be minimized, if not eliminated. Hence, further experiments are needed to investigate the effects of the factors, which were disregarded in the present experimental program. For example, all specimens of the experimental program were failed by elastic lateral torsional buckling. Further experiments on reinforced concrete beams subject to inelastic lateral torsional buckling are needed to investigate the degree of agreement between the experimental ultimate loads of the beams and the estimates produced by the proposed analytical method in the case of inelastic lateral torsional buckling. Similarly, the accuracy of the analytical estimates needs to be explored experimentally when the longitudinal reinforcement of a concrete beam contributes to the lateral stability to a major extent. As stated before, the contribution of a longitudinal rebar to the lateral bending rigidity of a beam increases as the lateral distance of the bar from the minor axis increases. Further experiments on reinforced concrete beams with longitudinal reinforcing bars distributed along the sides of the beams can be useful to examine the accuracy of the estimates from the proposed analytical method when the reinforcement plays an important role in resisting the lateral bending moments.

Finally, more experimental data is needed to determine the common values of the twisting angle at limit load ( $\phi_{ult}$ ) of reinforced concrete beams, which is used in Equation (8.1) for calculating the limit load of a reinforced concrete beam with initial geometric imperfections. Based on a statistical analysis on the results of a large number of lateral torsional buckling tests of reinforced concrete beams, the appropriate values of  $\phi_{ult}$  can be determined and recommended in the structural concrete codes for using in Equation (8.1).

## APPENDIX A

### NOMINAL AND MEASURED DIMENSIONS OF THE SPECIMENS

The actual dimensions of a concrete beam can be significantly different than the nominal dimensions. For a more precise analytical study, the actual dimensions of a beam, determined from several measurements throughout the beam, should be used when calculating the analytical critical loads. In this concern, the dimensions of the specimens were measured at several locations throughout each beam. The tables of the present appendix tabulate the nominal and measured dimensions of the specimens together with the means ( $\mu$ ), standard deviations ( $\sigma$ ) and the percent coefficients of variation ( $c_v$  %) of the measurements. Standard deviations and coefficients of variation of the measurements are included in the tables to reflect the degree of variation in the measurements of a dimension.

Table A.1 and A.2 present the heights of the specimens, measured at several locations along the lengths of the beams. The locations of the measurements are shown in Figure A.1.

Tables A.3 and A.5, on the other hand, present the widths of the specimens, measured at several locations along the depth and length of each beam. The locations of the measurement points are shown in Figure A.2.

Each of the first set of beams was cut at mid-length after the test to determine the actual locations of the longitudinal reinforcing bars in the beams. The widths of the beams measured along the cuts are tabulated in Table A.4.

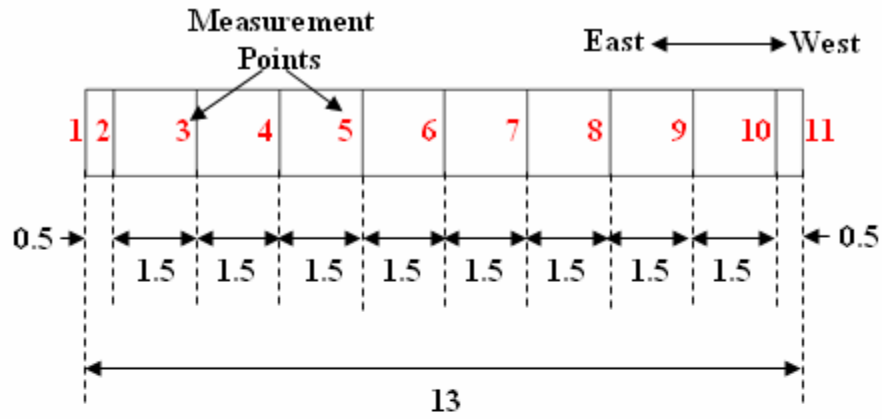
Table A.6 presents the unbraced lengths of the first set of beams. Table A.7, on the other hand, presents the total lengths of the second set of beams, measured at five different depths, as shown in Figure A.3. The unbraced span lengths of B44 and B36L were measured as 39.33 ft.

Table A.1 – Nominal and measured heights of the first set of specimens

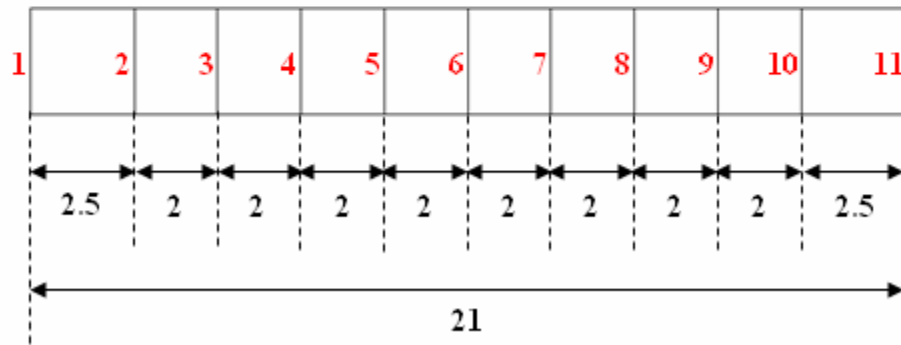
Specimen		B 36	B 30	B 22-1	B 22-2	B 18-1	B 18-2
Nominal Height (in)		36.000	30.000	22.000	22.000	18.000	18.000
	Measurement Point (Fig.A.1a&b)						
Measured Height (in)	1	35.906	30.000	22.000	22.063	18.000	18.000
	2	35.969	30.063	22.031	22.125	18.094	18.094
	3	36.063	30.063	22.031	22.094	18.156	18.125
	4	36.094	30.031	22.000	22.063	18.125	18.094
	5	36.063	29.969	21.969	22.063	18.125	18.063
	6	36.031	29.875	22.000	22.094	18.063	18.094
	7	36.031	29.938	22.000	22.094	18.125	18.094
	8	36.000	29.875	22.031	22.000	18.063	18.000
	9	36.031	29.938	22.000	22.000	18.125	18.000
	10	36.094	30.000	22.000	22.000	18.156	18.000
	11	35.875	29.969	21.938	22.188	18.000	18.188
	$\mu$	36.014	29.975	22.000	22.071	18.094	18.068
	$\sigma$	0.068	0.063	0.026	0.055	0.053	0.059
	$c_v\%$	0.19	0.21	0.12	0.25	0.29	0.33

Table A.2 – Nominal and measured heights of the second set of beams

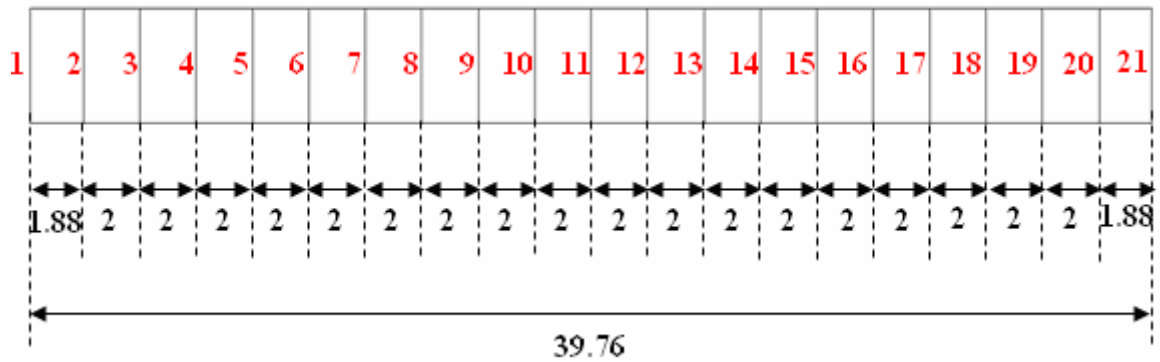
Specimen		B44-1	B44-2	B44-3	B36L-1	B36L-2
Nominal Height (in)		44	44	44	36	36
	Measurement Point (Figure A.1c)					
Measured Height (in)	1	44	44	44 1/16	36 5/32	36 1/16
	2	44	43 31/32	44 1/16	36	36
	3	44 1/8	44	43 15/16	36 3/32	36 1/8
	4	44 1/16	44 1/32	44 3/32	36 1/32	36 1/32
	5	44 3/32	44	44	36	36
	6	44 1/8	44 1/32	44 1/16	36 1/32	36
	7	44 3/16	44	44 1/8	36	36 1/16
	8	44 1/16	44	44 5/32	35 7/8	36
	9	44 1/8	43 29/32	44 3/32	36	35 7/8
	10	44 1/8	43 29/32	44 3/32	36	36 1/16
	11	44	43 31/32	44 3/32	36 1/16	36
	12	43 15/16	44 1/32	44 1/8	36	36
	13	43 7/8	44 1/32	44 3/32	36 1/8	36 1/16
	14	43 27/32	44 1/32	44 3/16	36	36 1/32
	15	43 13/16	44 1/16	43 7/8	36 1/8	36 1/16
	16	43 13/16	44	44	36 1/8	36 1/16
	17	43 13/16	43 29/32	44 3/32	36 3/32	36
	18	43 25/32	44 1/64	44 1/16	36 1/8	36 1/32
	19	43 13/16	44 3/32	44	36 3/32	36
	20	43 27/32	44 1/8	44 1/32	36 1/16	36 1/16
	21	43 15/16	44 1/8	44 1/32	36 1/32	36
	$\mu$	43 31/32	44 1/64	44 1/16	36 3/64	36 1/32
	$\sigma$	1/8	1/16	5/64	1/16	3/64
	% $c_v$	0.30	0.17	0.16	0.18	0.13



(a) B18 and B22



(b) B30 and B36



(c) B36L and B44

Figure A.1—Height measurement points along the lengths of the beams  
(All dimensions are in feet)

Table A.3 – Nominal and measured widths of the first set of specimens along the span

Specimen		B 36	B 30	B 22-1	B 22-2	B 18-1	B 18-2
Nominal Width (in)		2.500	2.500	1.500	1.500	1.500	1.500
	Meas. Point (Fig. A.2a&b)						
Measured Width (in)	1	2.438	2.563	1.578	1.563	1.563	1.484
	2	2.500	2.500	1.578	1.563	1.578	1.500
	3	2.438	2.438	1.563	1.563	1.578	1.453
	4	2.438	2.500	1.594	1.547	1.516	1.500
	5	2.469	2.531	1.625	1.563	1.547	1.547
	6	2.469	2.438	1.531	1.469	1.547	1.609
	7	2.531	2.469	1.578	1.500	1.594	1.594
	8	2.469	2.500	1.547	1.500	1.516	1.516
	9	2.438	2.500	1.609	1.531	1.516	1.516
	10	2.438	2.531	1.500	1.531	1.516	1.516
	11	2.469	2.500	1.453	1.516	1.516	1.594
	12	2.406	2.500	1.547	1.484	1.516	1.578
	$\mu$	2.458	2.498	1.559	1.527	1.542	1.534
	$\sigma$	0.032	0.035	0.046	0.032	0.029	0.045
	$c_v\%$	1.301	1.401	2.951	2.096	1.881	2.934

Table A.4 – Widths of the first set of specimens along the depth of midspan section

Specimen		B 36	B 30	B 22-1	B 22-2	B 18-1	B 18-2
Nominal Width		2.500	2.500	1.500	1.500	1.500	1.500
Measured Height (in)	1	2.575	2.586	1.576	1.447	1.567	1.632
	2	2.595	2.540	1.630	1.469	1.557	1.647
	3	2.617	2.537	1.590	1.474	1.550	1.643
	4	2.655	2.557	1.583	1.495	1.529	1.592
	5	2.652	2.583	1.588	1.497	1.539	1.611
	6	2.617	2.567	1.565	1.512	1.535	1.605
	7	2.643	2.614	1.549	1.524	1.547	1.612
	8	2.616	2.622	1.540	1.494		1.587
	9	2.641	2.639		1.517		
	10	2.643	2.660		1.527		
	11	2.613	2.637				
	12	2.605	2.619				
	13	2.602					
	14	2.552					
	15	2.550					
	16	2.496					
	17	2.496					
	18	2.498					
	19	2.490					
	$\mu$	2.587	2.597	1.578	1.496	1.546	1.616
	$\sigma$	0.056	0.039	0.026	0.025	0.012	0.016
	$c_v\%$	2.147	1.508	1.652	1.646	0.788	0.990

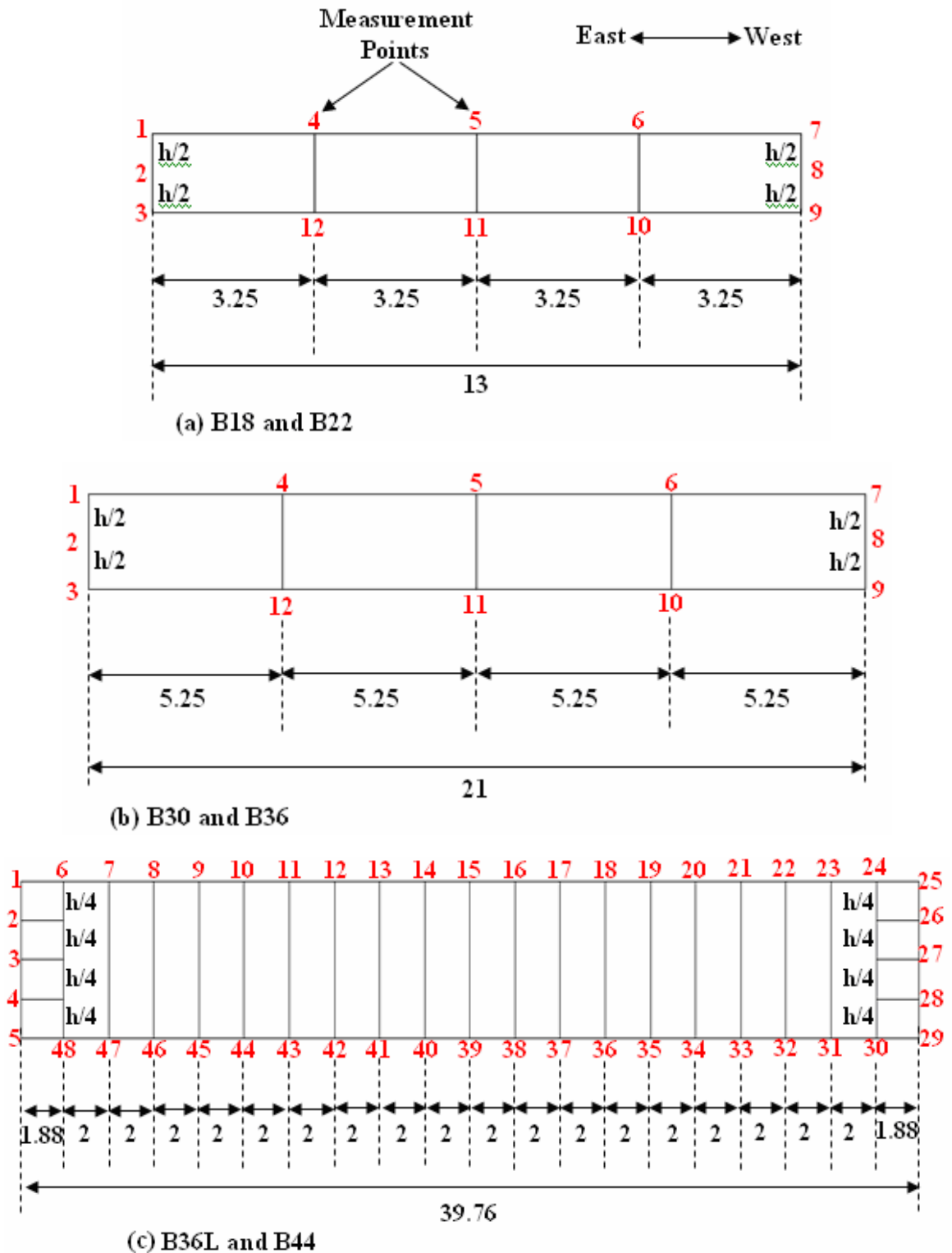


Figure A.2—Width measurement points along the lengths of the specimens  
(All dimensions are in feet)



Table A.5 – Nominal and measured widths of the second set of beams

Specimen		B44-1	B44-2	B44-3	B36L-1	B36L-2
Nominal Width (in)		3.000	3.000	3.000	3.000	3.000
	Measurement Point (Figure A.2c)					
Measured Width (in)	1	3.015	3.000	3.028	3.111	3.030
	2	3.038	3.000	3.049	3.080	3.037
	3	3.070	3.063	3.100	3.116	3.068
	4	3.028	3.031	3.077	3.102	3.162
	5	3.094	3.000	3.070	3.070	3.060
	6	3.043	3.012	3.074	3.287	3.150
	7	3.000	3.003	3.042	3.283	3.280
	8	3.051	2.999	3.105	3.159	3.189
	9	3.063	3.043	3.017	3.125	3.346
	10	3.038	3.002	3.011	3.206	3.336
	11	3.067	2.996	3.084	3.325	3.165
	12	3.032	3.031	3.144	3.265	3.268
	13	2.997	3.054	3.005	3.150	3.303
	14	2.963	3.039	3.009	3.172	3.297
	15	3.033	2.960	2.909	3.159	3.238
	16	3.012	3.055	3.054	3.170	3.244
	17	3.031	3.028	3.086	3.130	3.333
	18	3.103	3.037	3.122	3.144	3.179
	19	3.149	3.009	3.042	3.143	3.218
	20	3.019	3.015	3.016	3.270	3.164
	21	3.042	2.982	3.027	3.163	3.214
	22	3.063	2.992	3.127	3.093	3.298
	23	3.055	3.072	3.034	3.245	3.273
	24	3.067	3.036	3.040	3.219	3.337
	25	3.107	3.122	3.061	3.160	3.147
	26	3.109	3.122	2.973	3.283	3.266
	27	3.064	3.042	2.859	3.284	3.296
	28	3.051	3.050	2.892	3.205	3.186
	29	3.036	3.120	2.982	3.281	3.103
	30	3.106	3.094	3.031	3.258	3.365
	31	3.070	3.074	3.096	3.142	3.125
	32	3.022	3.121	3.115	3.121	3.111
	33	3.033	3.022	3.090	3.245	3.066
	34	3.053	3.056	3.100	3.216	3.195
	35	3.095	3.026	3.101	3.239	3.105
	36	3.076	3.100	3.137	3.171	3.065
	37	3.065	3.006	3.111	3.280	3.070
	38	3.085	3.012	3.020	3.123	3.107
	39	3.025	3.084	3.089	3.207	3.062
	40	3.073	2.982	2.993	3.161	3.162
	41	3.082	3.096	3.048	3.061	3.166
	42	2.998	3.083	3.115	3.068	3.197
	43	3.054	3.037	2.988	3.192	3.109
	44	3.128	3.031	3.001	3.310	3.243
	45	2.944	3.063	3.072	3.190	3.145
	46	3.047	3.156	3.128	3.149	3.208
	47	3.046	3.156	3.180	3.160	3.226
	48	3.017	3.188	3.147	3.143	3.185
	$\mu$	3.051	3.048	3.054	3.184	3.190
	$\sigma$	0.039	0.050	0.068	0.070	0.091
	% C <sub>v</sub>	1.3	1.6	2.2	2.2	2.8

Table A.6 – Nominal and measured span lengths of first set of specimens

Specimen		B 36	B 30	B 22-1	B 22-2	B 18-1	B 18-2
Beam Length (in)		252.000	252.000	156.000	156.000	156.000	156.000
Span (in)		240.000	240.000	144.000	144.000	144.000	144.000
	Measurement Depth (Figure A.3)						
Measured Span (in)	1	239.500	239.875	143.750	143.750	143.750	143.719
	2	239.375	239.813	143.750	143.781	143.781	143.688
	3	239.375	239.750	143.750	143.750	143.750	143.688
	4	239.375	239.688	143.750	143.813	143.781	143.688
	5	239.500	239.688	143.750	143.813	143.750	143.688
	$\mu$	239.425	239.763	143.750	143.781	143.763	143.694
	$\sigma$	0.061	0.073	0.000	0.028	0.015	0.012
	$c_v\%$	0.025	0.030	0.000	0.019	0.010	0.008

Table A.7 – Nominal and measured total lengths of the second set of specimens

Specimen		B44-1	B44-2	B44-3	B36L-1	B36L-2
Nominal Length (ft)		39.75	39.75	39.75	39.75	39.75
	Measurement Depth (Figure A.3)					
Measured Length (ft)	1	39.76	39.75	39.75	39.78	39.78
	2	39.77	39.74	39.76	39.79	39.77
	3	39.78	39.74	39.76	39.79	39.77
	4	39.77	39.75	39.77	39.80	39.78
	5	39.77	39.75	39.77	39.79	39.78
	$\mu$	39.77	39.75	39.76	39.79	39.78
	$\sigma$	0.01	0.01	0.01	0.01	0.01
	$\% c_v$	0.02	0.01	0.02	0.02	0.01

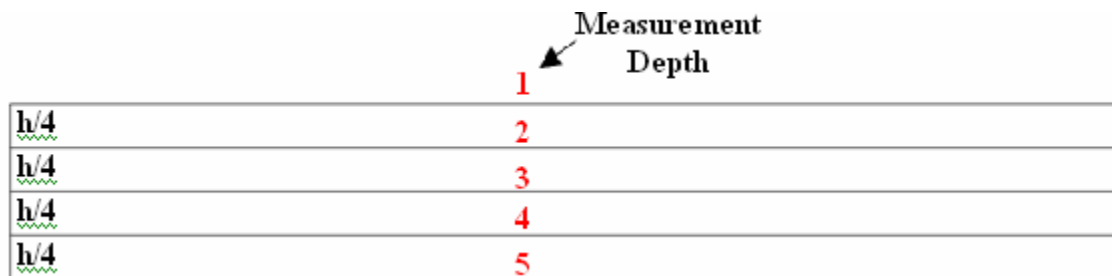


Figure A.3–Length measurement depths of the specimens

## **APPENDIX B**

### **MEASURED INITIAL GEOMETRIC IMPERFECTIONS AND PERMANENT DEFORMATIONS OF THE SPECIMENS**

The initial lateral deformations, sweeps, of the test beams are tabulated in Tables B.1-B.4. The tables present the lateral deformations at the extreme top, mid-height and extreme bottom of each beam. Sweep was measured at three different levels along the depth of each beam to obtain the initial angles of twist of the specimens. Furthermore, the initial lateral deflections of the beams were measured at several points along the length of each beam to determine the exact curved shapes of the specimens out of plane. Knowledge of the lateral bows of the test beams prior to loading was essential in the analytical stage of the present study. The number and locations of the measurement points along the lengths of the beams are illustrated in Figure B.1. Southward deflections in Tables B.1-B.4 are positive while the northward ones are negative according to the sign convention shown in Figure B.1.

Table B.1 – Measured sweeps of Specimens B18

Measurement Point along the Span (Figure B.1a)	Sweep (in)				
	B18-1		B18-2		
	Top	Bottom	Top	Midheight	Bottom
1	-1/8	-3/16	-1/32	-1/32	-1/32
2	-5/16	-5/16	-1/16	-1/16	-1/16
3	-7/16	-7/16	-1/8	-1/8	-1/8
4	-7/16	-7/16	-1/8	-1/8	-1/8
5	-7/16	-7/16	-1/8	-1/8	-1/8
6	-7/16	-7/16	-3/32	-3/32	-3/32
7	-1/4	-5/16	-1/16	-1/16	-1/16

Table B.2 – Measured sweeps of Specimens B30 and B36

Measurement Point along the Span (Figure B.1b)	Sweep (in)					
	B30			B36		
	Top	Midheight	Bottom	Top	Midheight	Bottom
1	-1/4	-3/16	-3/16	1/32	1/64	1/32
2	-7/16	-3/8	-1/4	1/8	5/32	1/8
3	-5/8	-9/16	-1/2	1/8	5/32	1/8
4	-5/8	-9/16	-1/2	7/32	3/16	7/32
5	-5/8	-9/16	-1/2	7/32	3/16	7/32
6	-1/2	-7/16	-3/8	7/32	3/16	7/32
7	-1/4	-3/16	-1/8	1/8	3/32	1/8

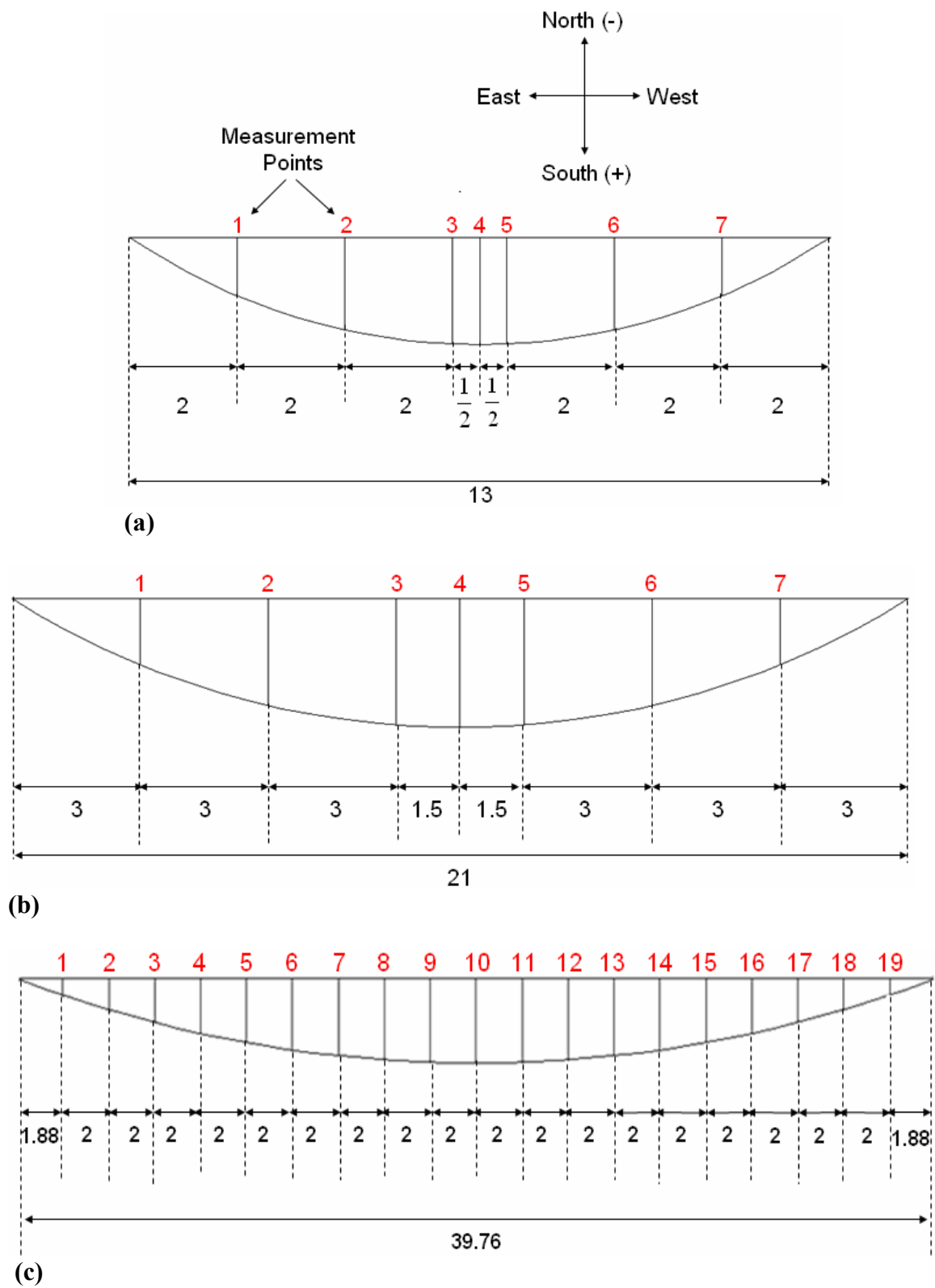


Figure B.1 – Imperfection measurement points on beams (a) B18; (b) B30 and B36; (c) B44 and B36L (All dimensions are in feet.)

Table B.3 – Measured sweeps of Specimens B44

Measurement Point along the Span (Figure B.1c)	Sweep (in)								
	B44-1			B44-2			B44-3		
	Top	Midheight	Bottom	Top	Midheight	Bottom	Top	Midheight	Bottom
<b>1</b>	1/16	1/8	1/8	1/32	1/8	5/32	-11/32	-3/16	-1/4
<b>2</b>	3/16	1/8	1/8	1/16	5/32	1/8	-9/16	-3/8	-5/16
<b>3</b>	3/16	3/16	3/16	3/16	3/16	3/16	-5/8	-9/16	-1/2
<b>4</b>	1/8	1/8	1/8	9/32	7/32	7/32	-29/32	-13/16	-3/4
<b>5</b>	3/16	3/16	3/16	13/32	11/32	3/8	-1 1/8	-7/8	-1
<b>6</b>	1/4	1/4	3/16	17/32	1/2	9/16	-1 7/32	-1 5/32	-1 3/16
<b>7</b>	3/8	3/16	3/16	21/32	11/16	5/8	-1 3/8	-1 5/32	-1 1/4
<b>8</b>	1/4	3/16	1/4	23/32	5/8	19/32	-1 1/2	-1 9/32	-1 7/16
<b>9</b>	3/8	3/16	1/8	3/4	11/16	5/8	-1 9/16	-1 3/8	-1 1/2
<b>10</b>	9/16	3/8	1/4	25/32	23/32	13/16	-1 3/8	-1 3/8	-1 1/2
<b>11</b>	5/16	5/16	5/16	3/4	13/16	27/32	-1 5/16	-1 5/16	-1 1/2
<b>12</b>	5/16	1/4	5/16	25/32	27/32	7/8	-1 3/8	-1 5/16	-1 1/2
<b>13</b>	1/4	1/4	5/16	27/32	27/32	29/32	-1 9/32	-1 1/4	-1 7/16
<b>14</b>	1/4	3/16	1/4	7/8	13/16	27/32	-1 1/4	-1 5/32	-1 3/8
<b>15</b>	1/4	3/16	1/4	3/4	11/16	3/4	-1 1/8	-1 1/8	-1 1/4
<b>16</b>	3/16	3/16	3/16	19/32	9/16	5/8	-7/8	-13/16	-1 1/16
<b>17</b>	3/16	1/8	3/16	17/32	17/32	17/32	-5/8	-9/16	-3/4
<b>18</b>	1/4	1/8	1/4	3/8	7/16	3/8	-7/16	-3/8	-3/8
<b>19</b>	1/4	1/8	1/4	1/4	1/4	1/4	-1/4	-3/16	-1/4

Table B.4 – Measured sweeps of Specimens B36L

Measurement Point along the Span (Figure B.1c)	Sweep (in)					
	B36L-1			B36L-2		
	Top	Midheight	Bottom	Top	Midheight	Bottom
1	-3/16	-3/16	-3/16	-1/8	-1/4	-1/16
2	-3/8	-7/16	-3/16	-3/16	-1/8	-1/4
3	-9/16	-5/8	-5/16	-1/4	-1/8	-9/32
4	-5/8	-5/8	-1/4	-1/8	-3/16	-5/16
5	-11/16	-7/8	-5/16	-5/32	-3/16	-11/32
6	-7/8	-3/4	-5/16	-3/8	-3/8	-7/16
7	-7/8	-5/8	-7/16	-9/32	-1/2	-1/2
8	-3/4	-7/8	-9/16	-11/32	-1/2	-3/8
9	-15/16	-3/4	-19/32	-11/32	-9/16	-3/8
10	-15/16	-7/8	-11/16	-3/8	-9/16	-5/16
11	-1	-13/16	-5/8	-1/4	-3/8	-3/8
12	-3/4	-1	-11/16	-13/32	-1/2	-3/8
13	-3/4	-3/4	-1/2	-15/32	-1/2	-11/32
14	-13/16	-5/8	-9/16	-1/2	-1/2	-11/32
15	-11/16	-5/8	-1/2	-1/2	-1/2	-3/8
16	-3/4	-9/16	-3/8	-5/16	-1/4	-3/16
17	-5/8	-9/16	-5/16	-1/4	-5/16	-3/16
18	-1/4	-1/2	-1/4	-3/16	-5/16	-1/8
19	-1/8	-1/4	-1/8	-5/32	-1/4	-1/16

Figures B.2 to B.10 illustrate the sweeps of the specimens at mid-height. Figures B.11-B.15 depict the permanent lateral deformations of the specimens at midheight, measured after the complete removal of the applied load while Figures B.16-B.20 show the permanent angles of twist of the specimens along the beam length. The sinusoidal curves, obtained from Equations B.1 and B.2, are included in Figures B.2-B.20 to compare the initial lateral bow and the permanent deformed shape of the centerline of each beam to the sinusoidal curve.

$$u(z) = u_o \cdot \sin\left(\frac{\pi \cdot z}{L}\right) \quad (\text{B.1})$$

$$\phi(z) = \phi_o \cdot \sin\left(\frac{\pi \cdot z}{L}\right) \quad (\text{B.2})$$

where  $z$  = the longitudinal distance from the end of a beam,  $L$  = the total length of the beam;  $u(z)$  and  $u_o$  = sweep of the beam at mid-height, at a distance  $z$  from the end and at mid-span respectively;  $\phi(z)$  and  $\phi_o$  = the angles of twist at a distance  $z$  and at mid-span, respectively. Figures B.11-B.20 reveal that the permanent deformations of a buckled beam are in close agreement with the sinusoidal curve which implies that the buckled shape of a beam can be best approximated by the sinus function.



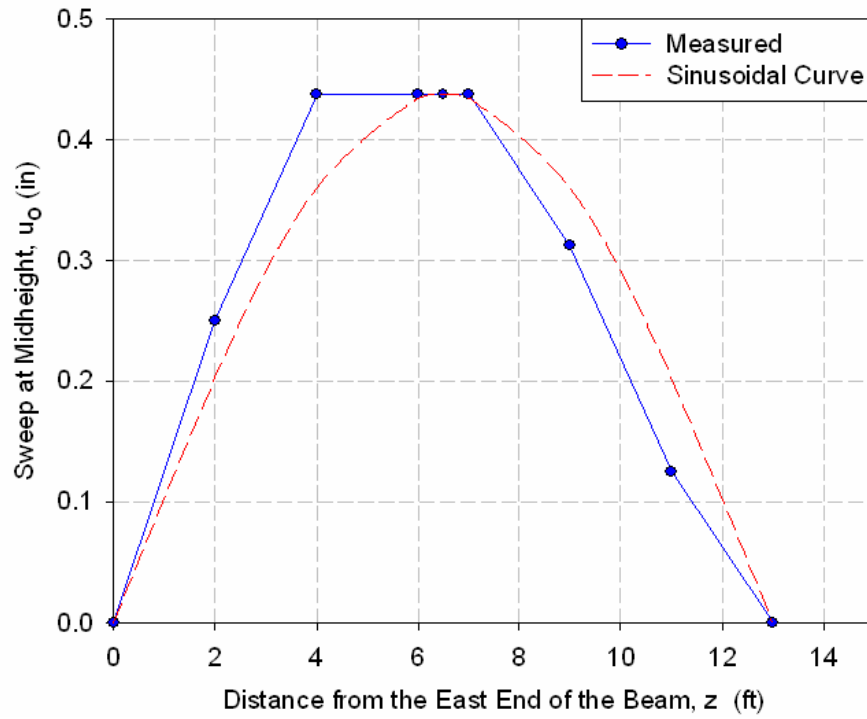


Figure B.2 - Sweep at midheight of B18-1

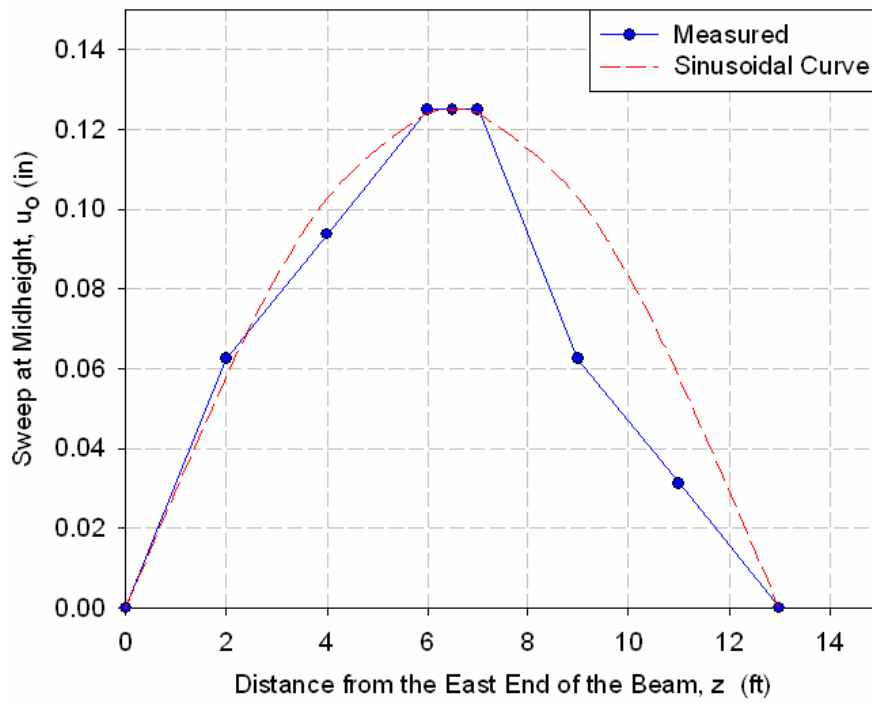


Figure B.3 - Sweep at midheight of B18-2

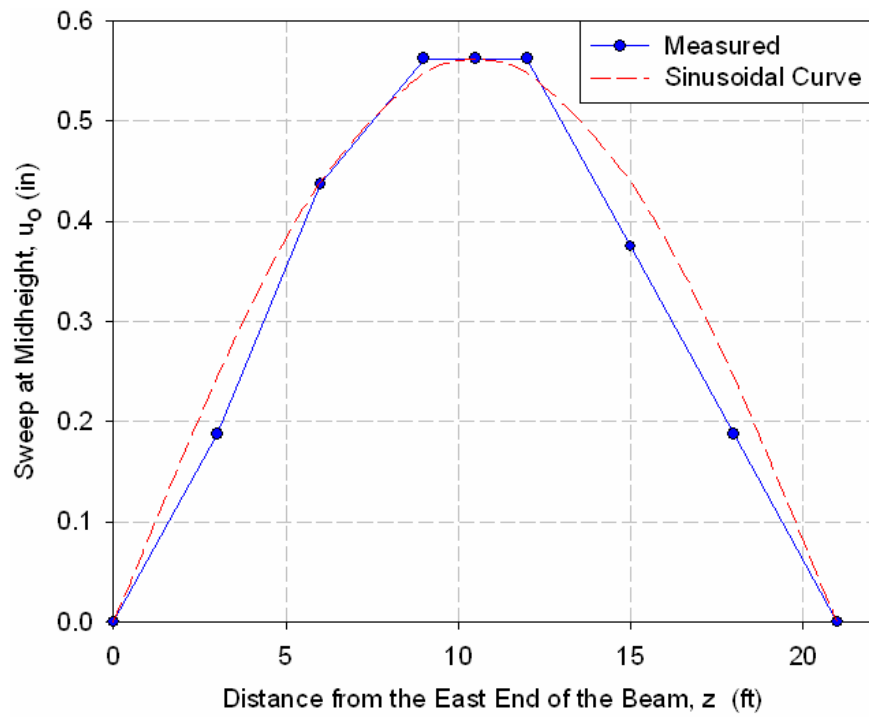


Figure B.4 – Sweep at midheight of B30

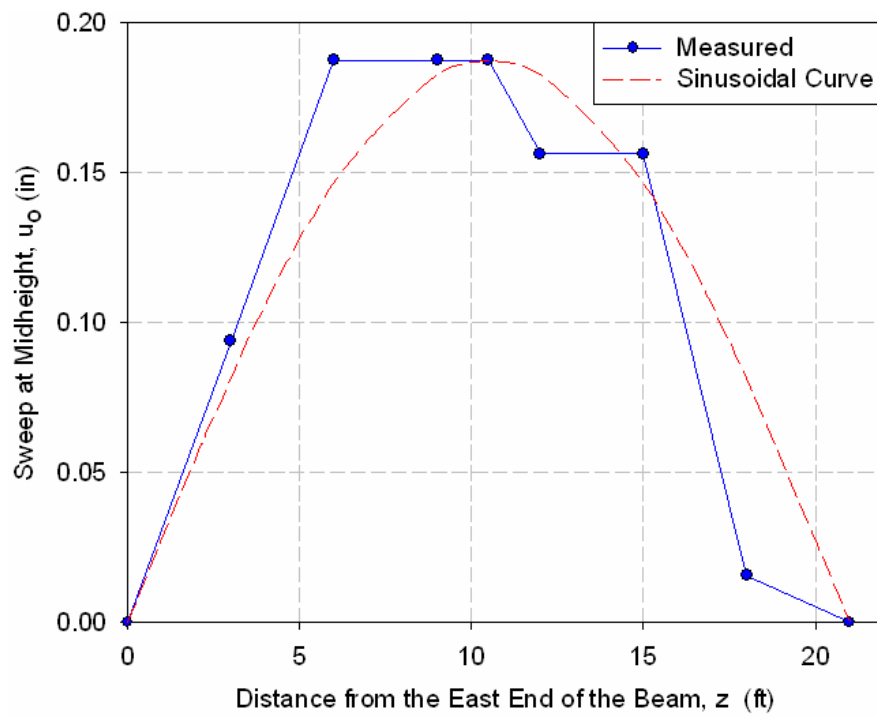


Figure B.5 - Sweep at midheight of B36

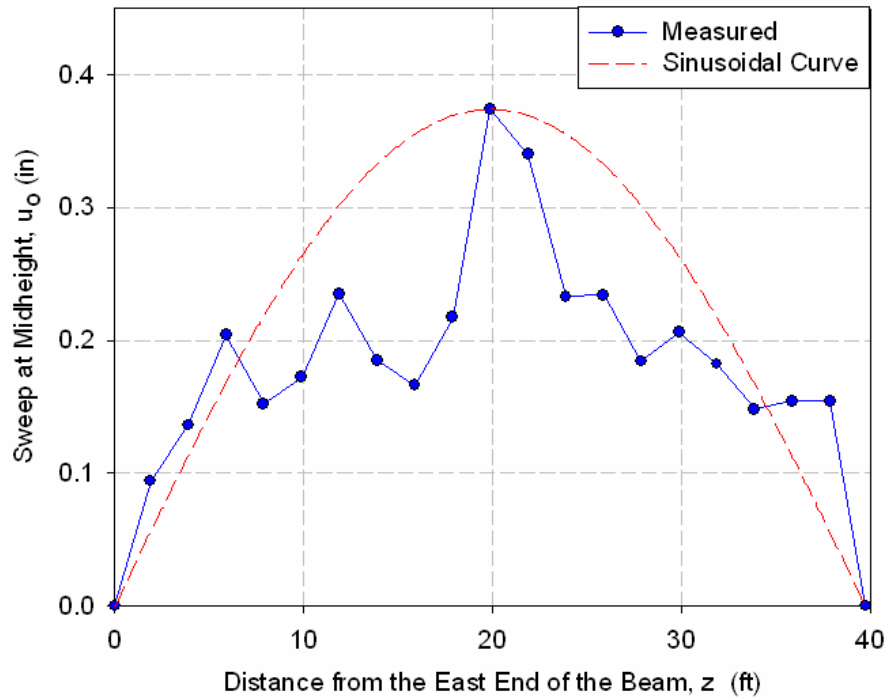


Figure B.6 - Sweep at midheight of B44-1

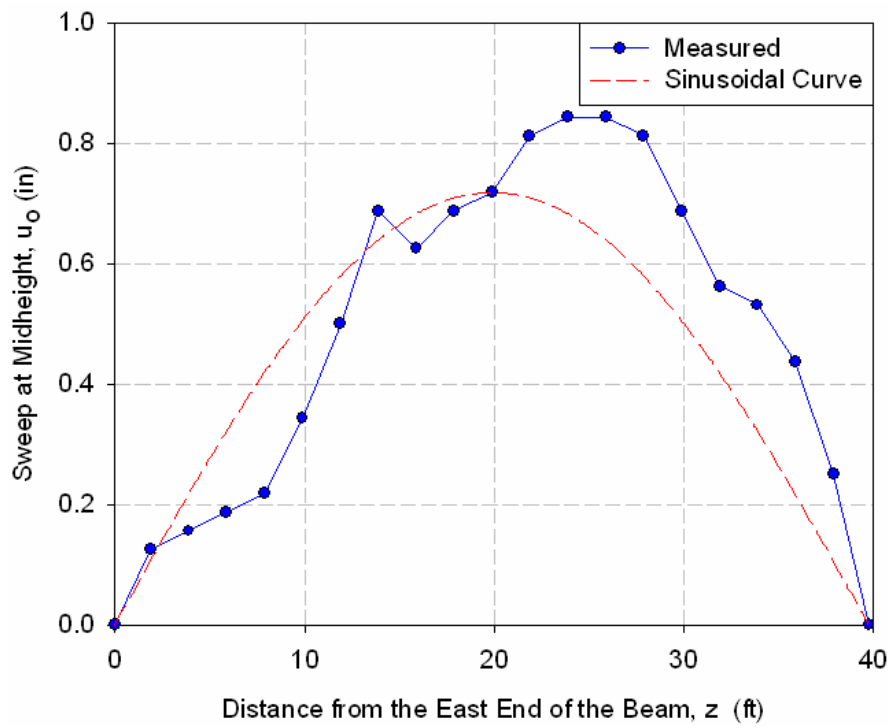


Figure B.7 - Sweep at midheight of B44-2

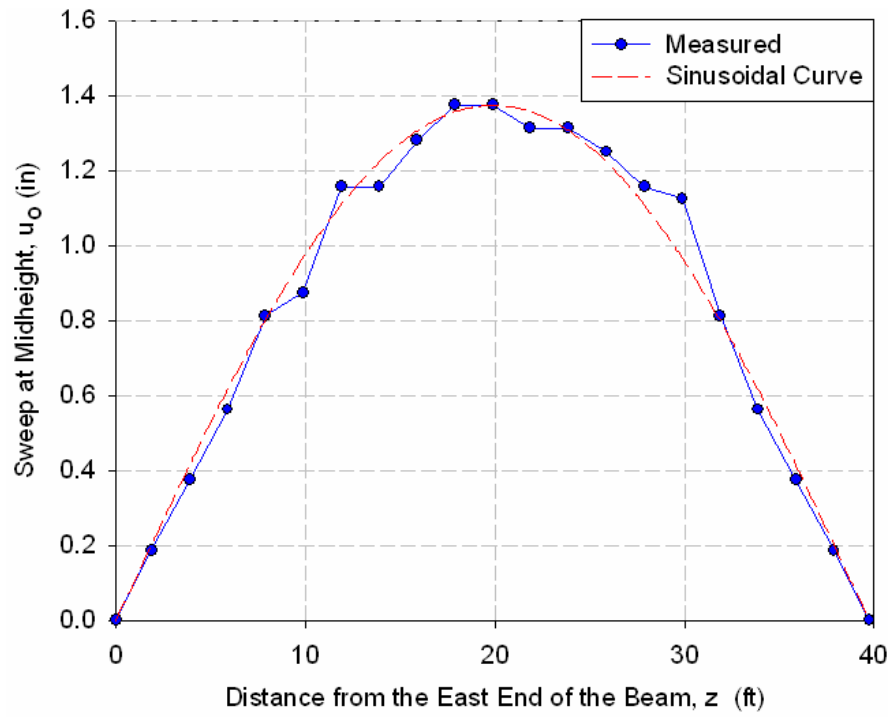


Figure B.8 - Sweep at midheight of B44-3

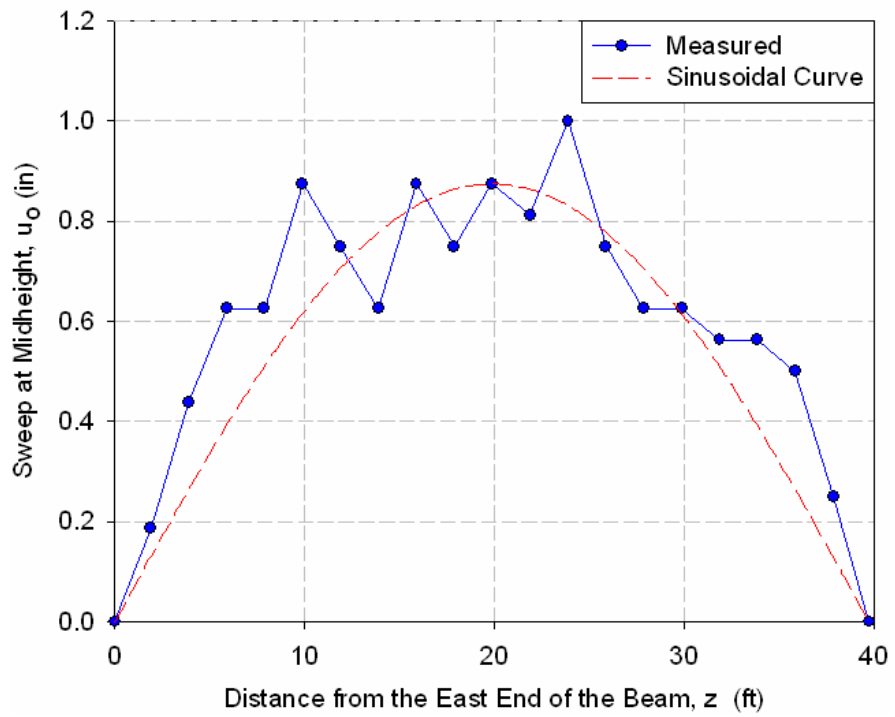


Figure B.9 - Sweep at midheight of B36L-1

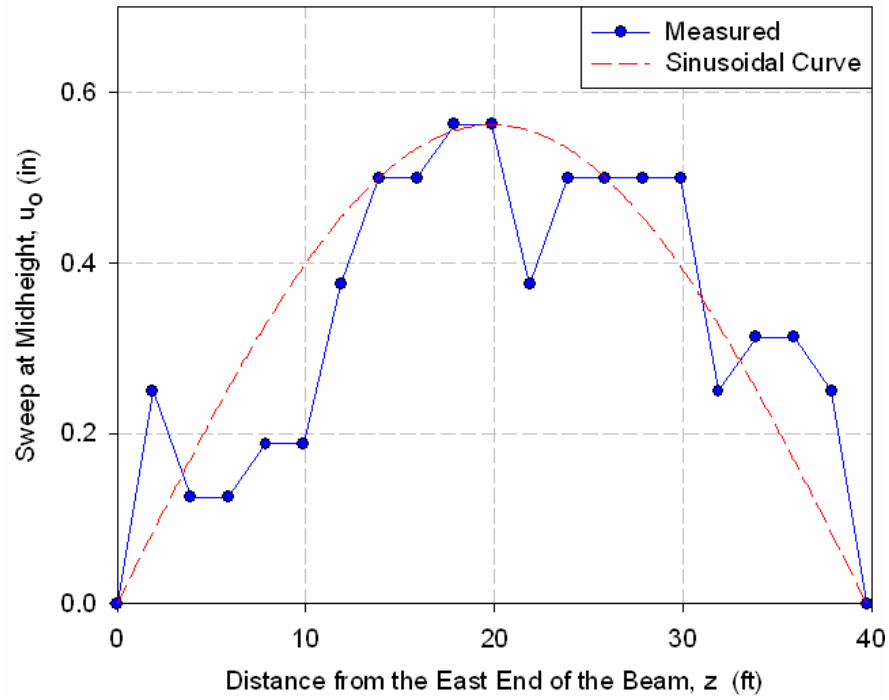


Figure B.10 - Sweep at midheight of B36L-2

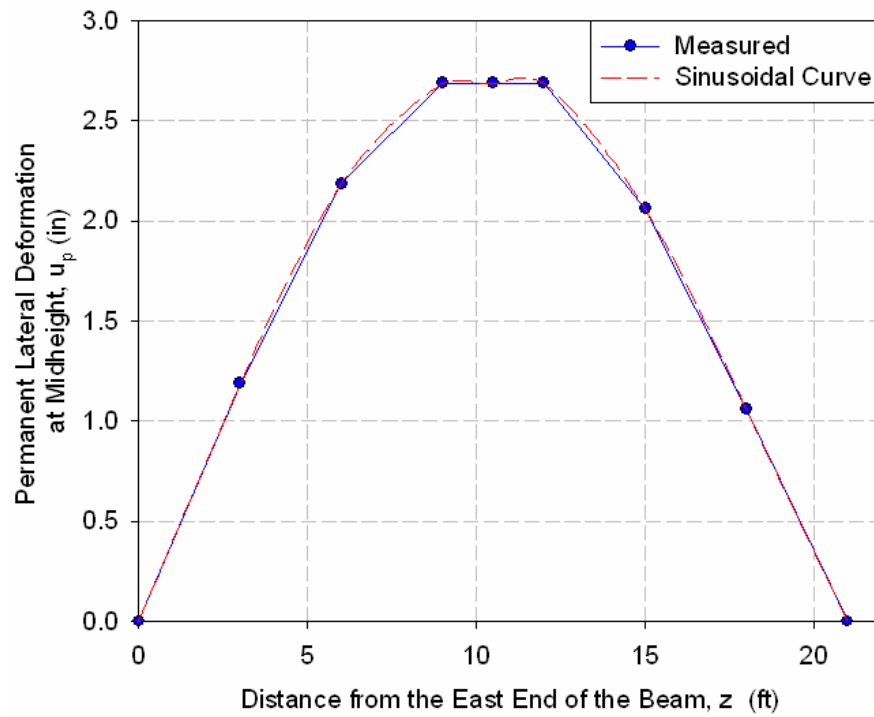


Figure B.11 – Permanent lateral deformation at midheight of B30

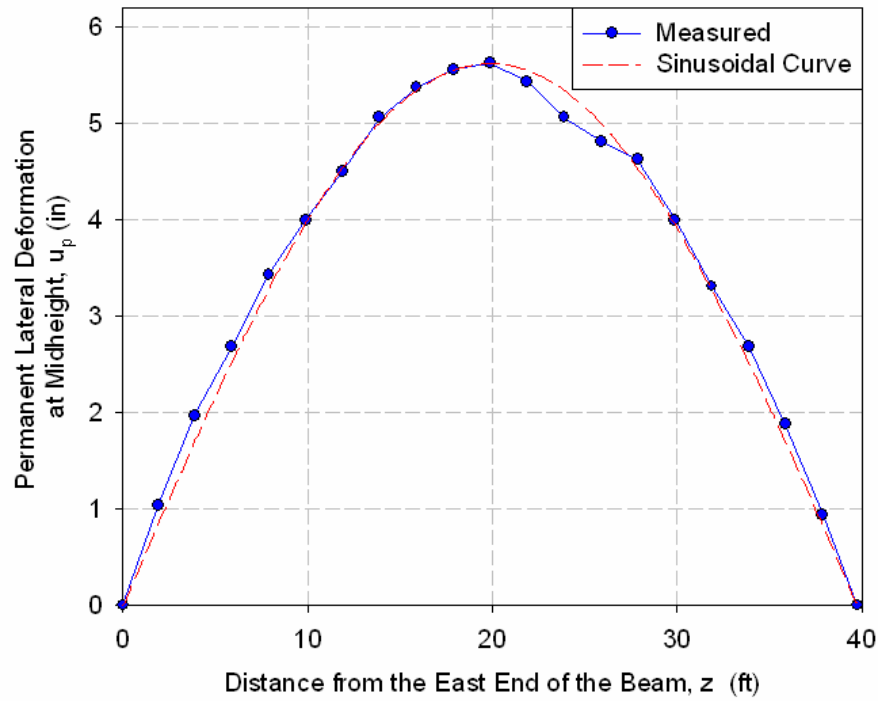


Figure B.12 – Permanent lateral deformation at midheight of B44-1

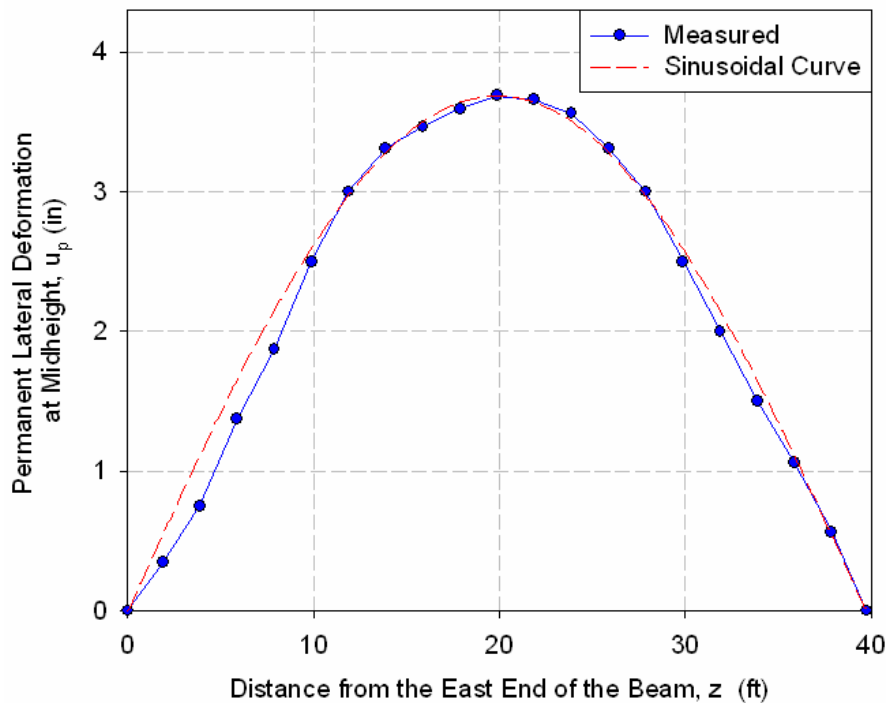


Figure B.13 – Permanent lateral deformation at midheight of B44-2

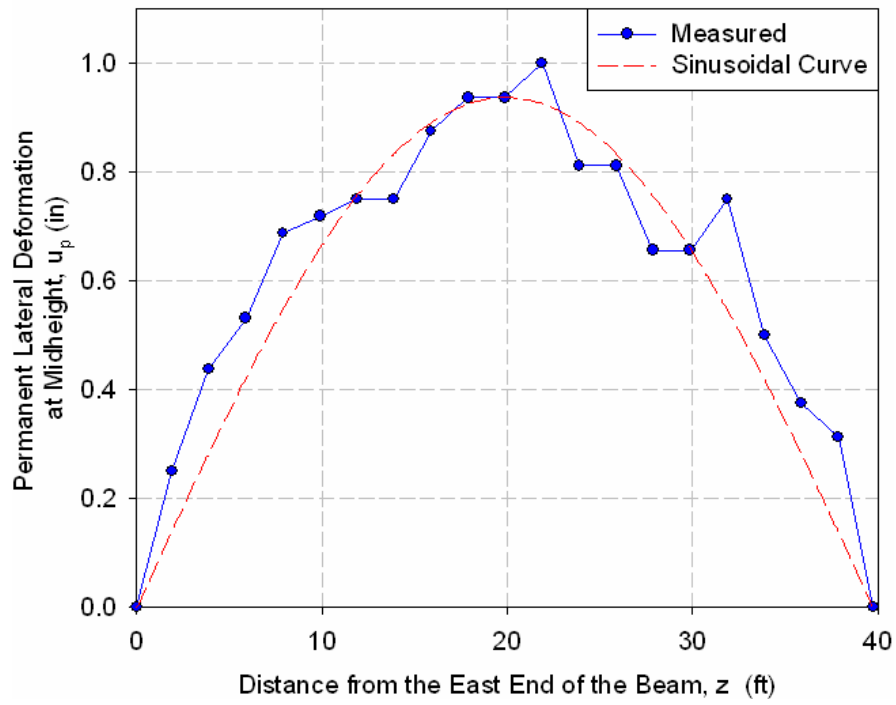


Figure B.14 - Permanent lateral deformation at midheight of B44-3

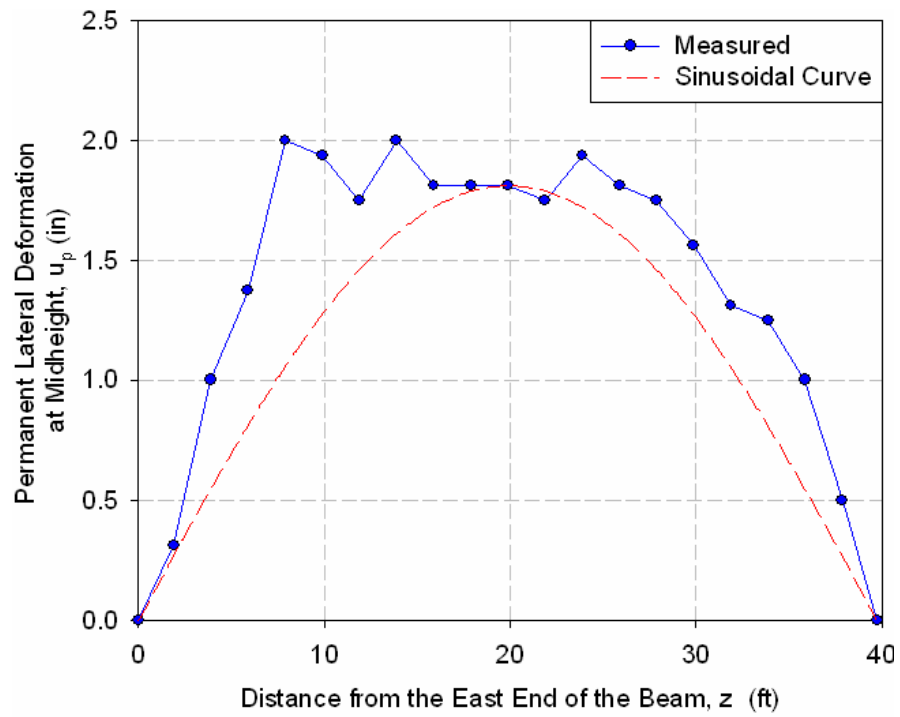


Figure B.15 - Permanent lateral deformation at midheight of B36L-1

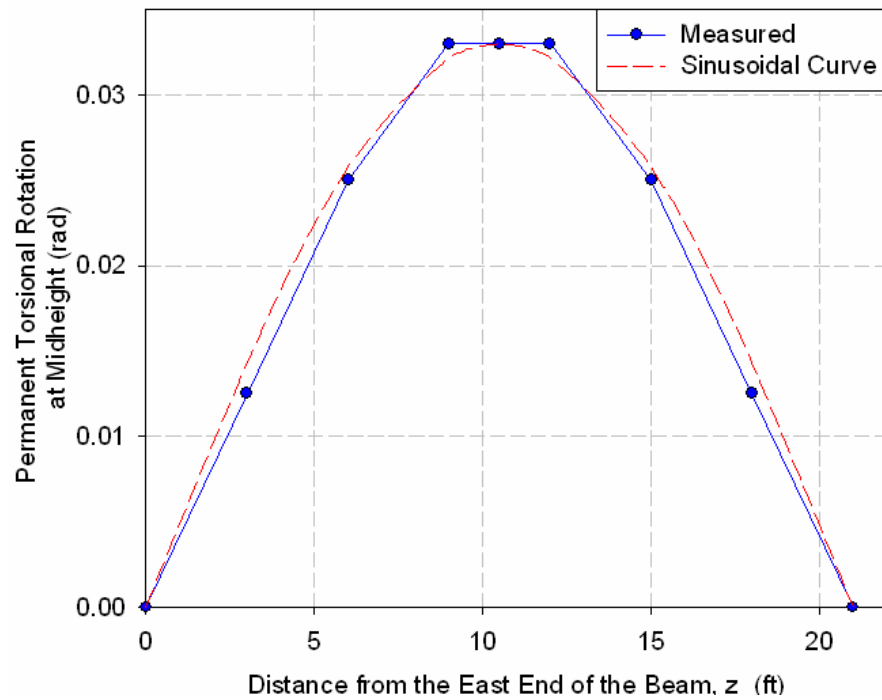


Figure B.16 – Permanent torsional rotations of B30

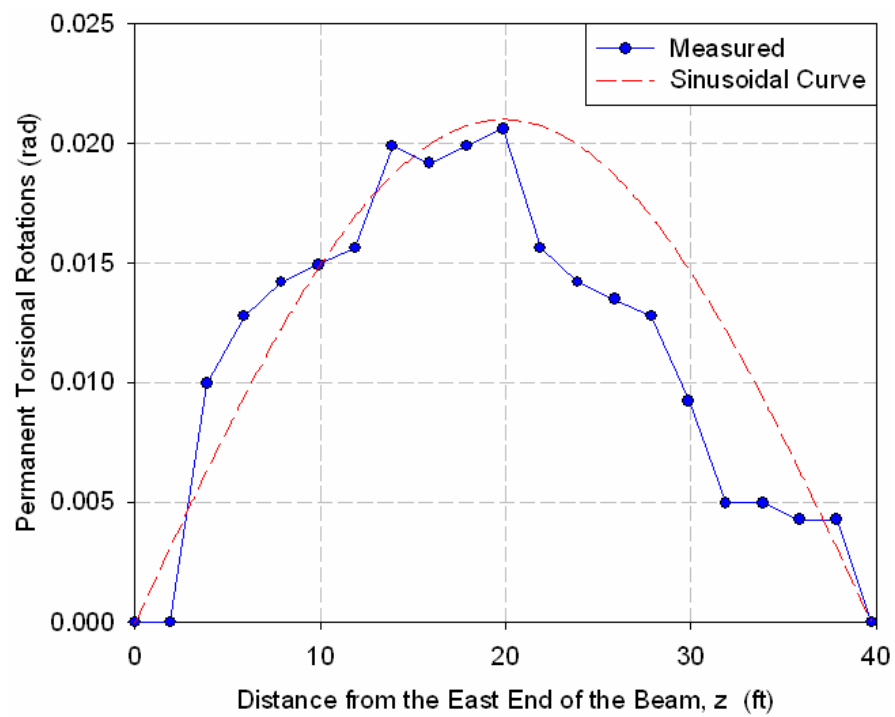


Figure B.17 – Permanent torsional rotations of B44-1



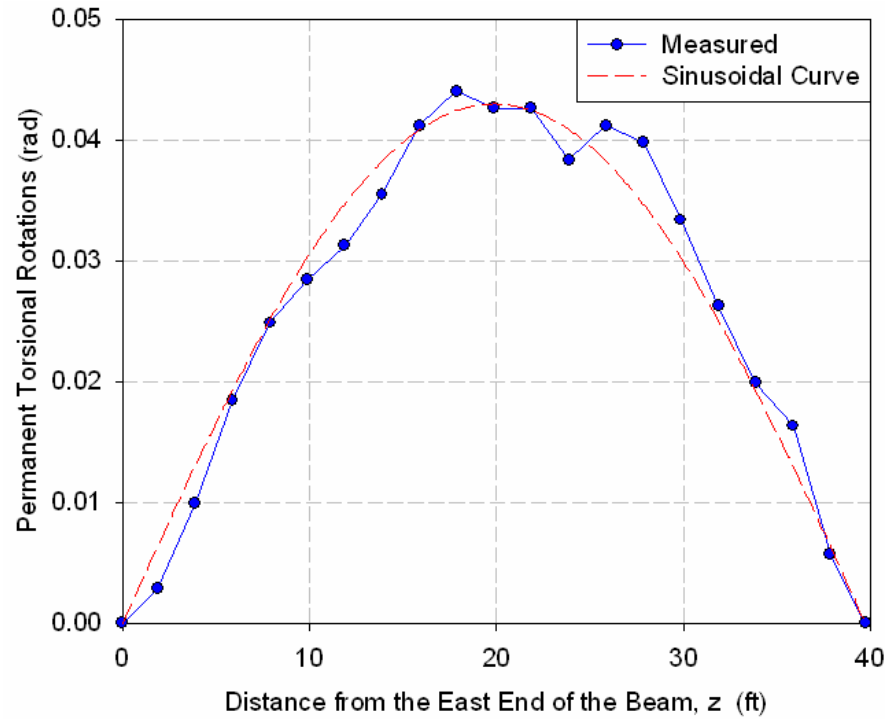


Figure B.18 – Permanent torsional rotations of B44-2

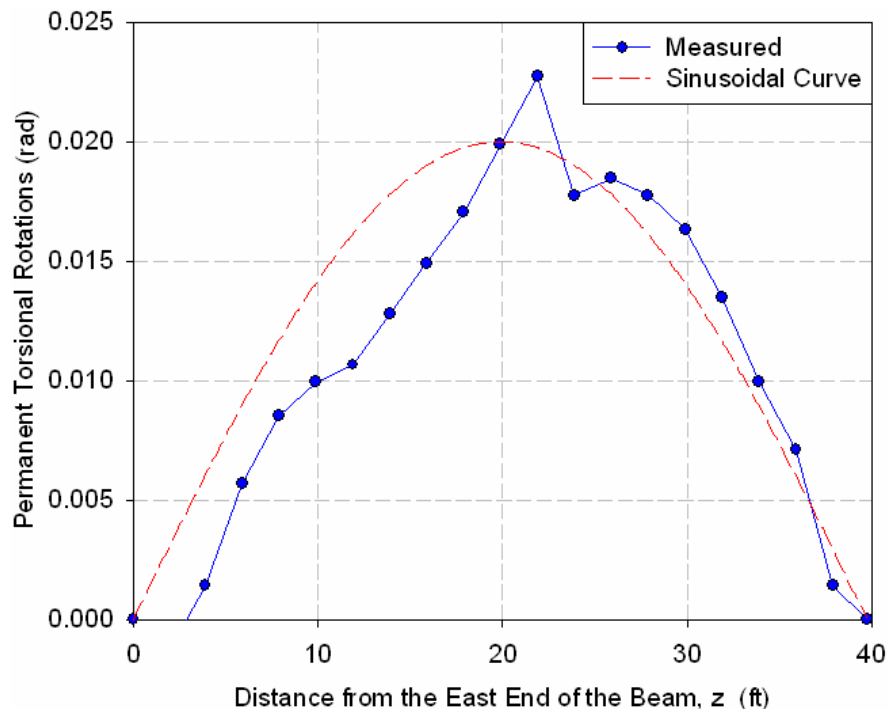


Figure B.19 – Permanent torsional rotations of B44-3

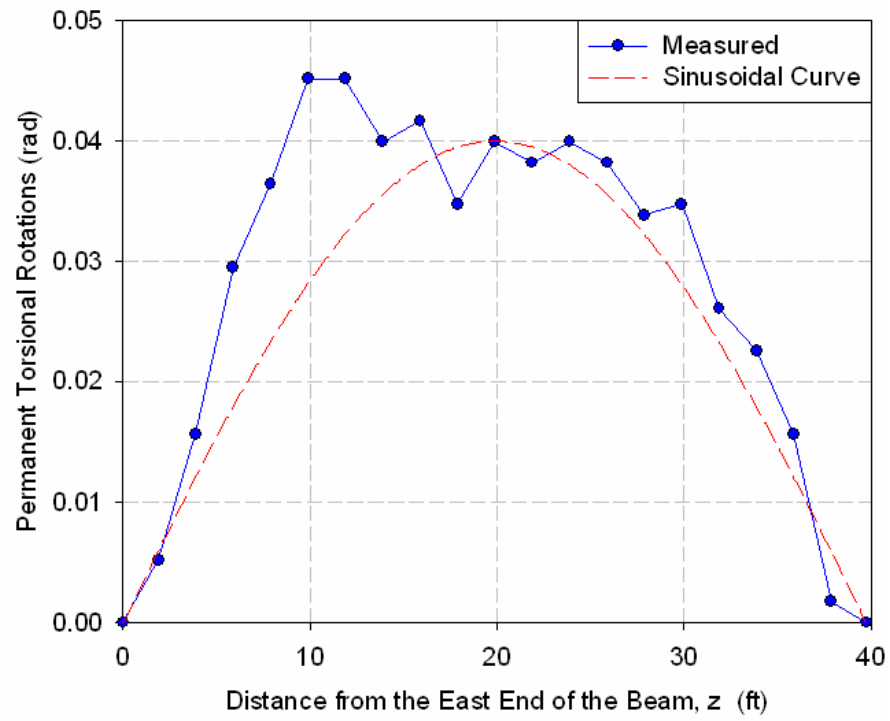


Figure B.20 – Permanent torsional rotations of B36L-1

## **APPENDIX C**

### **MIDSPAN STRAIN DISTRIBUTIONS OF THE BEAMS AT DIFFERENT LOAD LEVELS**

The present appendix presents the longitudinal strain distributions along the depth of the midspan section of each of the second set of specimens. As explained in Chapter III, in the second set of tests longitudinal strains were measured continuously throughout the tests, through strain gages attached on the convex and concave faces of the beams at mid-span. Convex and concave faces of a beam are at equal distances from the mid-width of the beam. The minor axis of the cross section of a beam coincides with the vertical centroidal axis, if the beam section is symmetric about the midwidth. Longitudinal strains originating from out-of-plane bending increase from zero at the minor axis to a maximum at the outermost fibers of the section. In other words, the minor axis of a section is only strained by major-axis bending because the lateral bending stresses vanish at minor axis.

The specimens of the present study were designed symmetrically about the midwidth. Therefore, the minor axis of each specimen was coincident with the vertical centroidal axis, and thus, the concave and convex faces of the beam were at equal distances from the minor axis, assuming that the beams were perfectly symmetric about the vertical centroidal axes, as designed. Accordingly, the compressive strains from lateral bending on the concave faces were equal to the tensile strains from lateral bending on the convex faces of the beams at mid-span. The longitudinal strain distributions along the minor axes of the specimens, which originate solely from in-plane bending, were obtained by averaging the longitudinal strains measured on the convex and concave faces

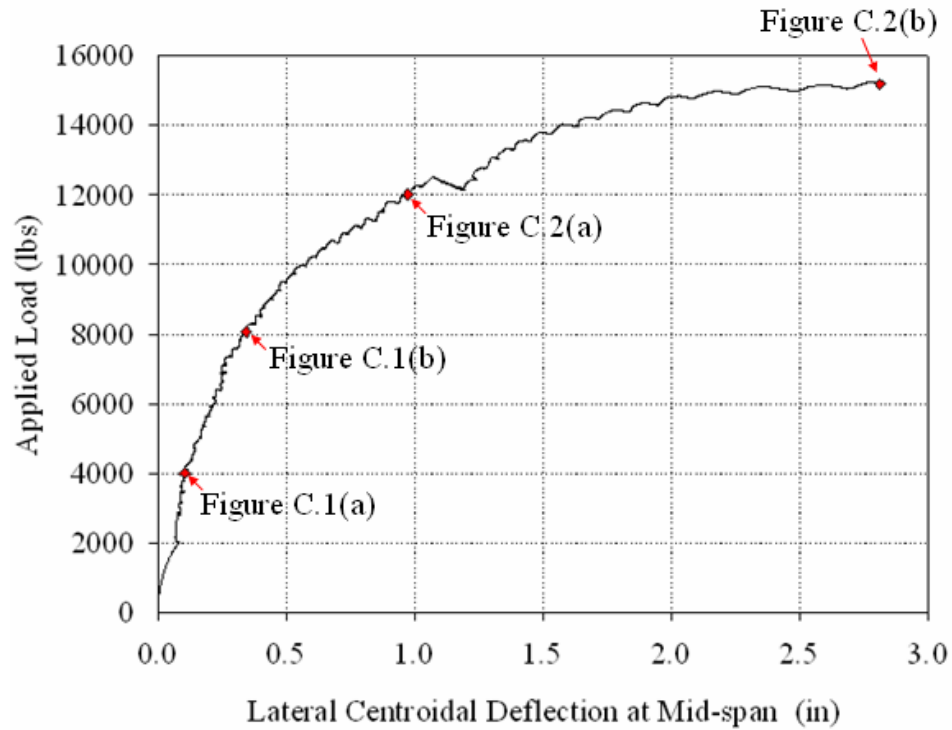
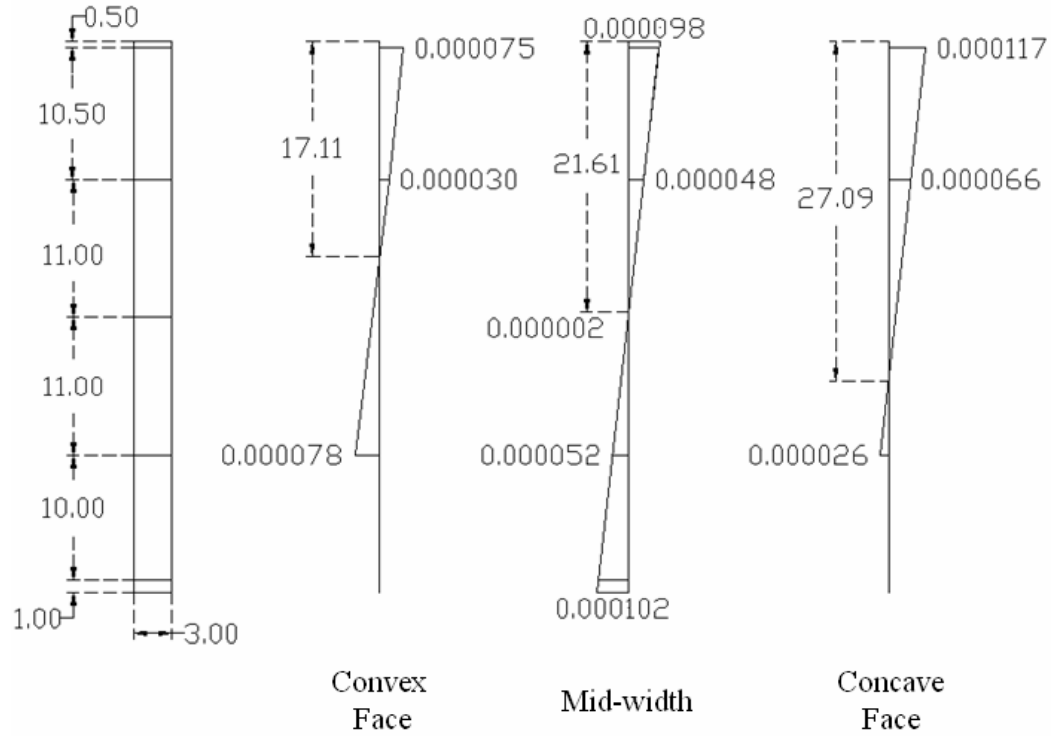
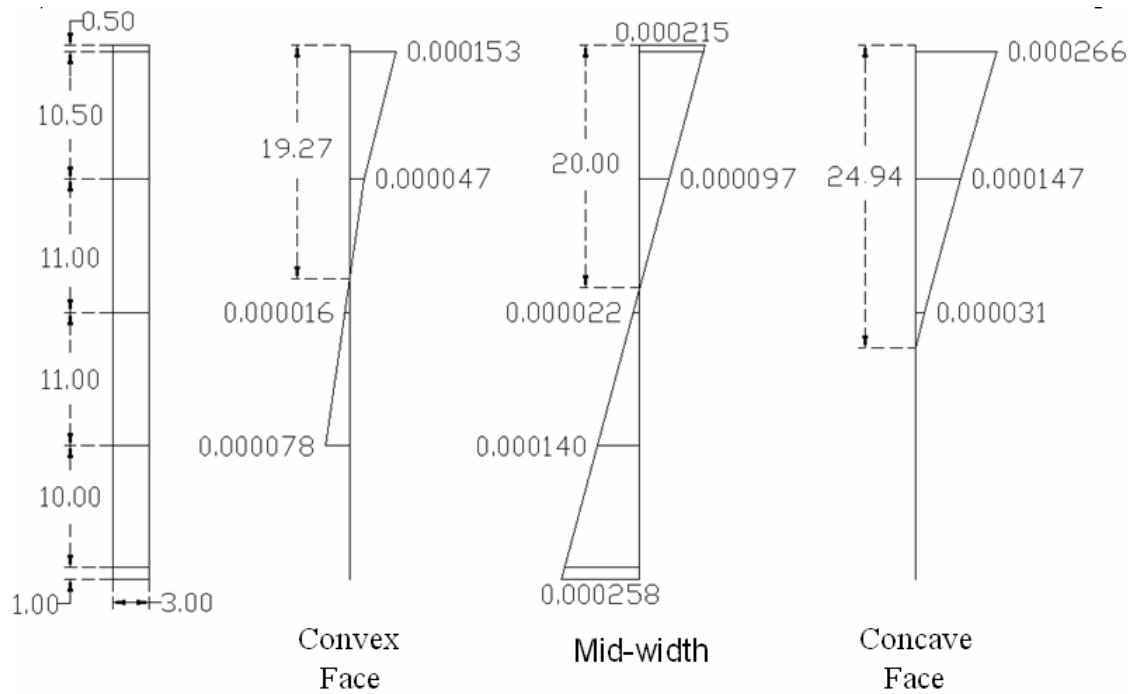


Figure C.1 – Loads and lateral deflections corresponding to the strain distributions in Figures C.2 to C.4

of the beams. The longitudinal strains distributions on the convex and concave faces and along the minor axes of the beams were illustrated in the following figures for different load levels along the tests. The applied loads and lateral centroidal deflections corresponding to the strain distributions in the figures are shown on the load-lateral deflection curves of the specimens (Figures C.1, C.5, C.8, C.12 and C.15).

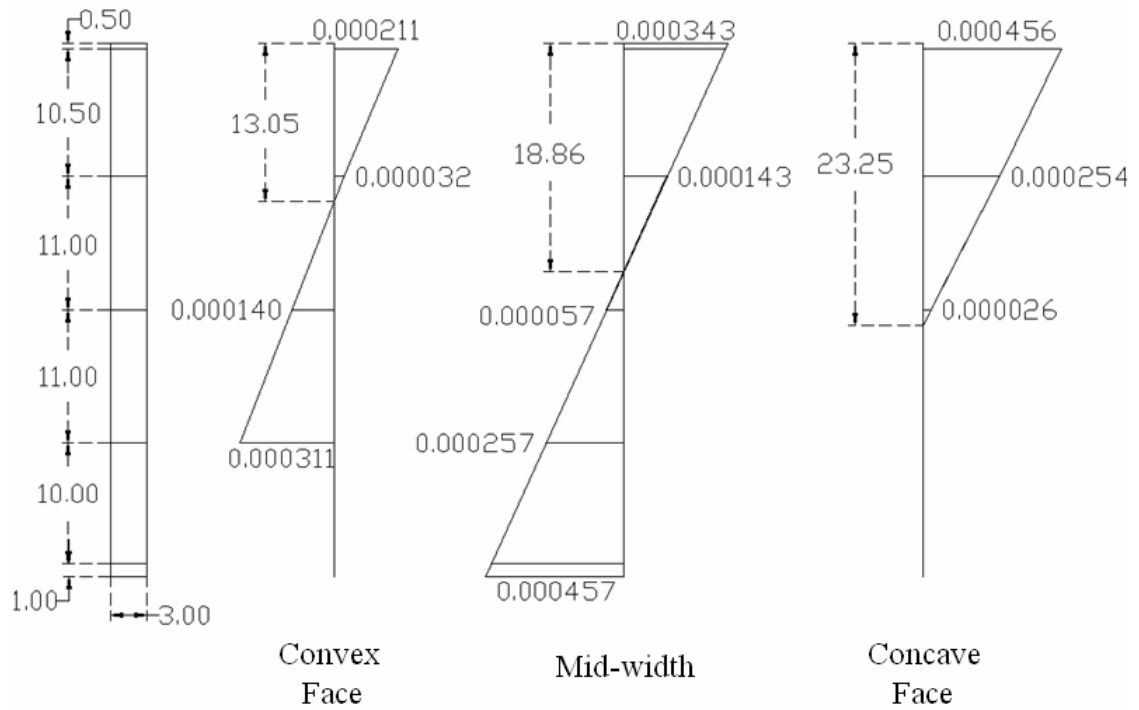


(a)  $P=4000$  lbs

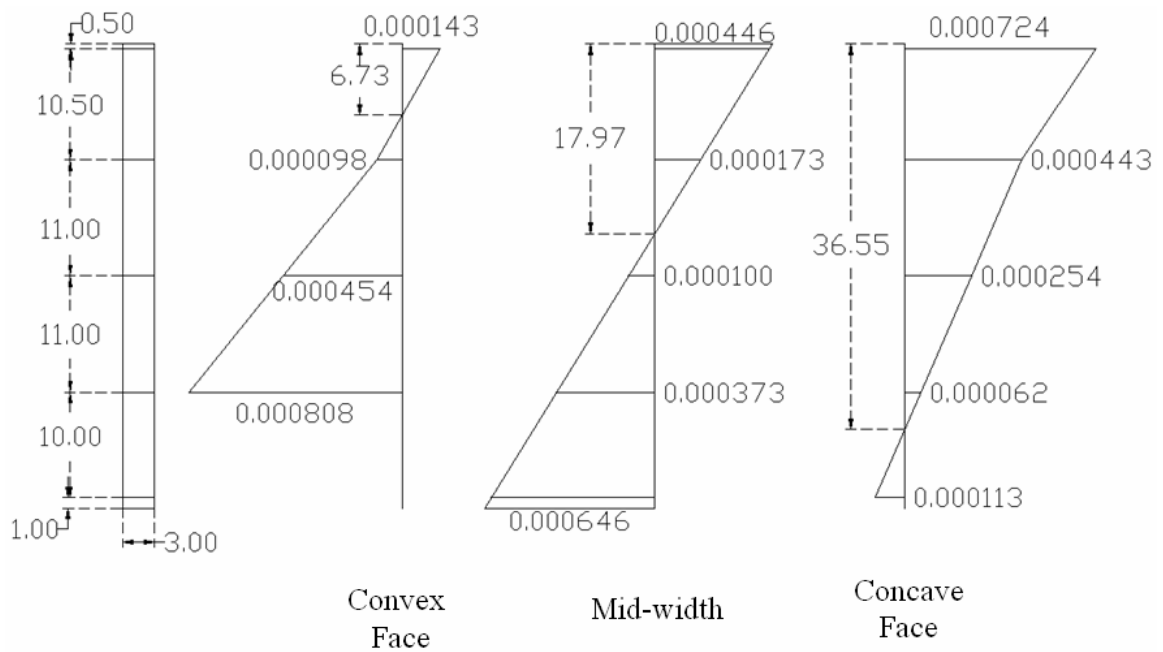


(b)  $P=8050$  lbs

Figure C.2 – Midspan strain distributions of B44-1 at the initial stages of loading

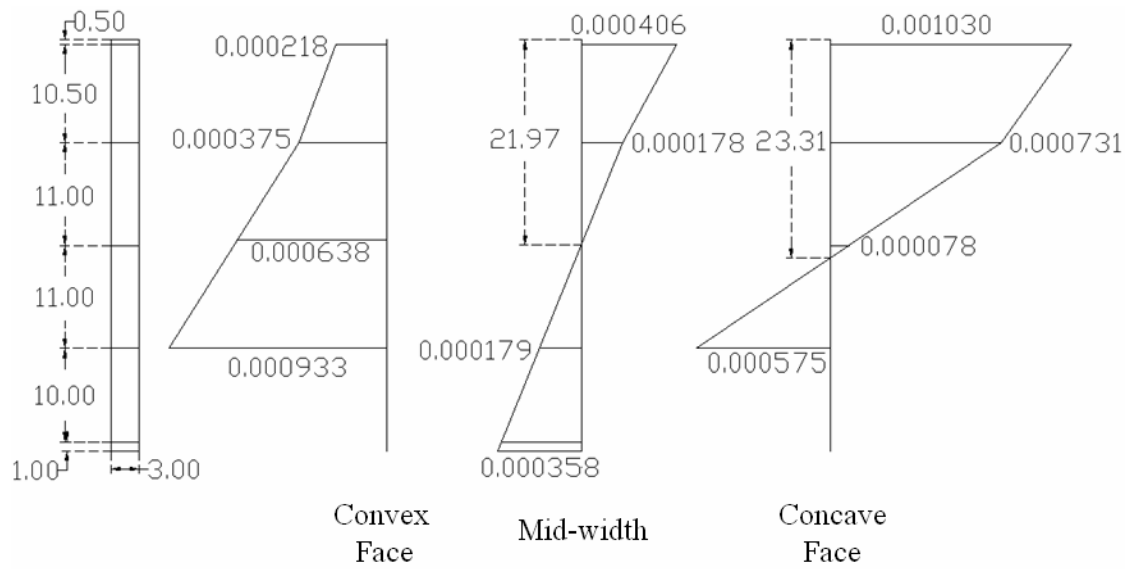


(a)  $P=12000$  lbs



(b)  $P=15150$  lbs (Buckling Load)

Figure C.3 – Midspan strain distributions of B44-1 close to buckling



P=15000 lbs

Figure C.4 – Midspan strain distributions of B44-1 after buckling

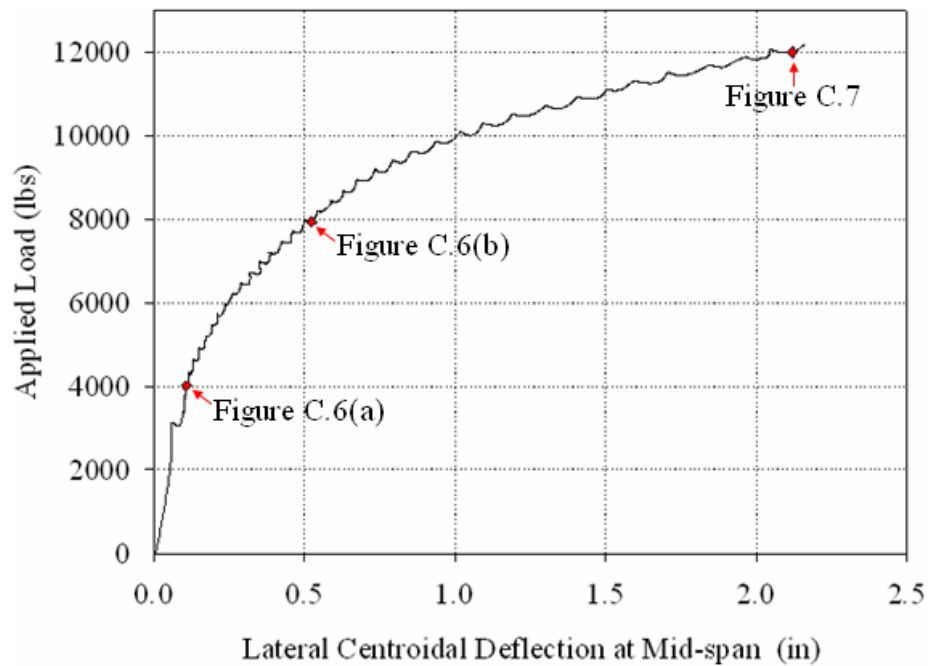
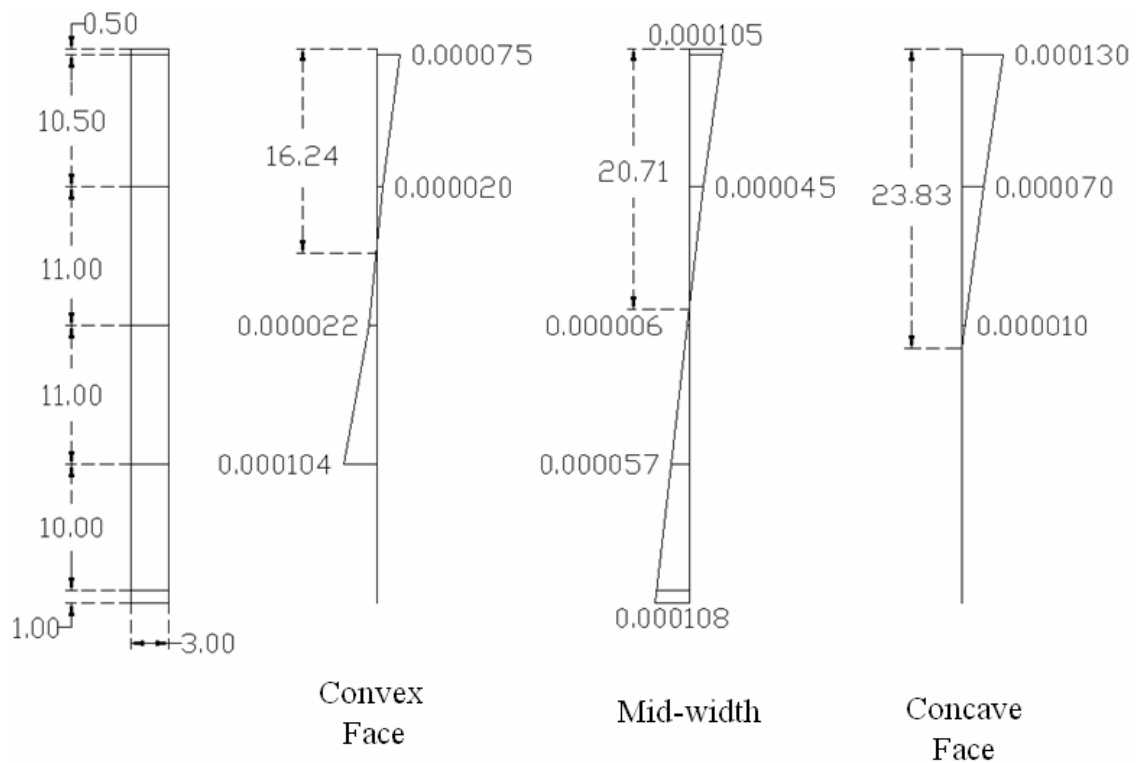
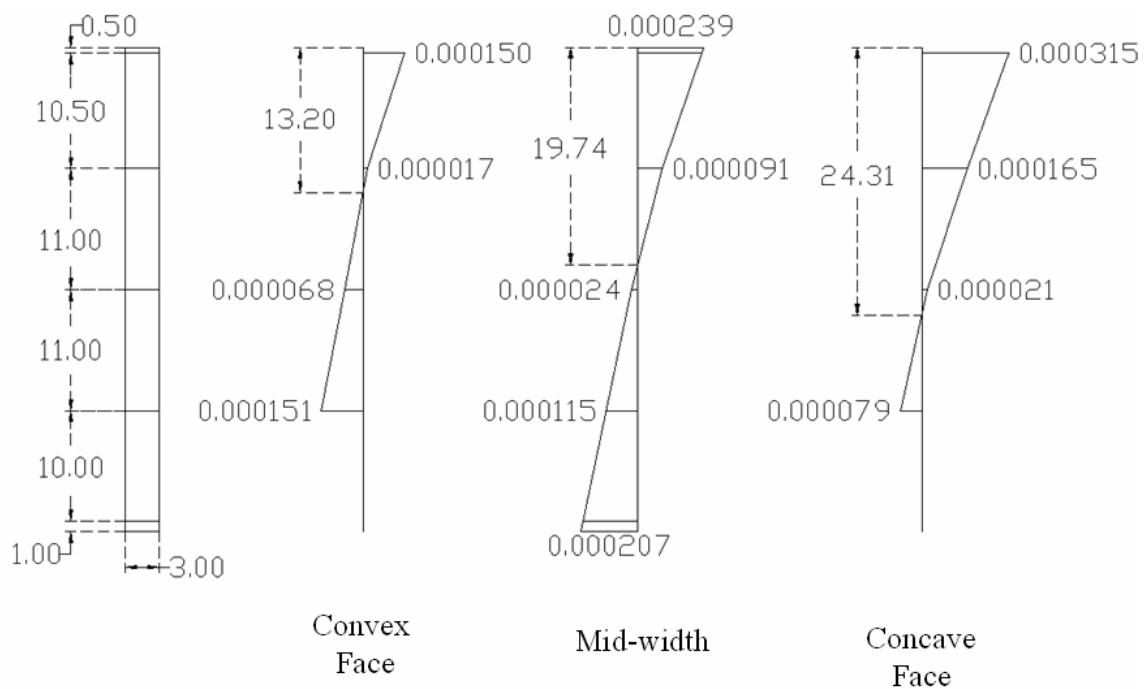


Figure C.5 – The Loads and lateral deflections corresponding to the strain distributions in Figures C.6 and C.7



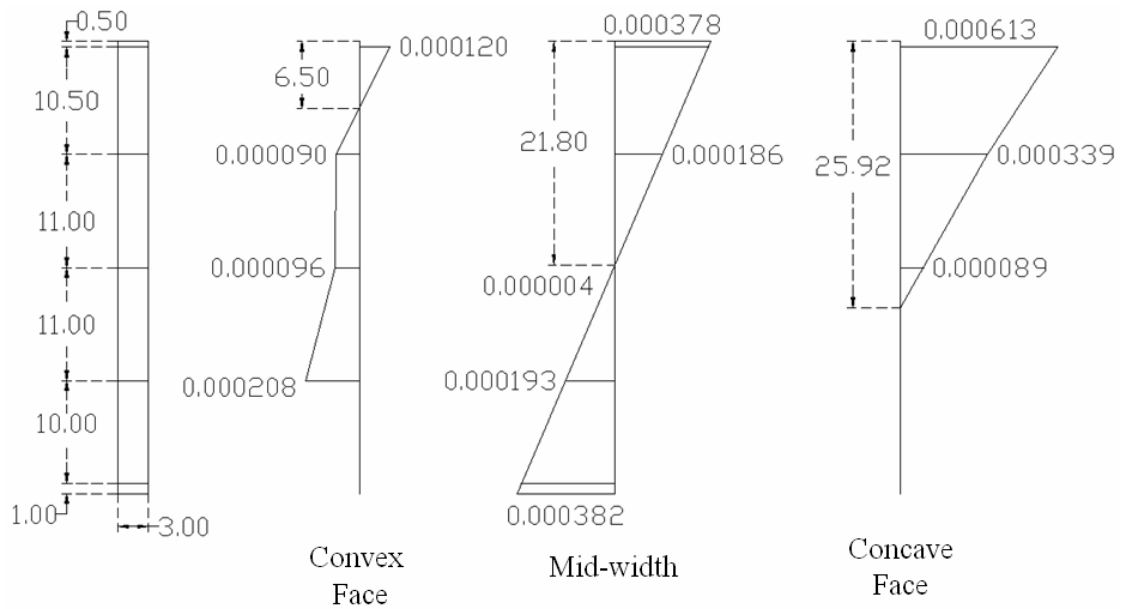
(a)  $P=4000$  lbs



(b)  $P=7950$  lbs

Figure C.6 – Midspan strain distributions of B44-2 at the initial stages of loading





P=12000 lbs (Buckling Load)

Figure C.7 – Midspan strain distributions of B44-2 at the initiation of buckling

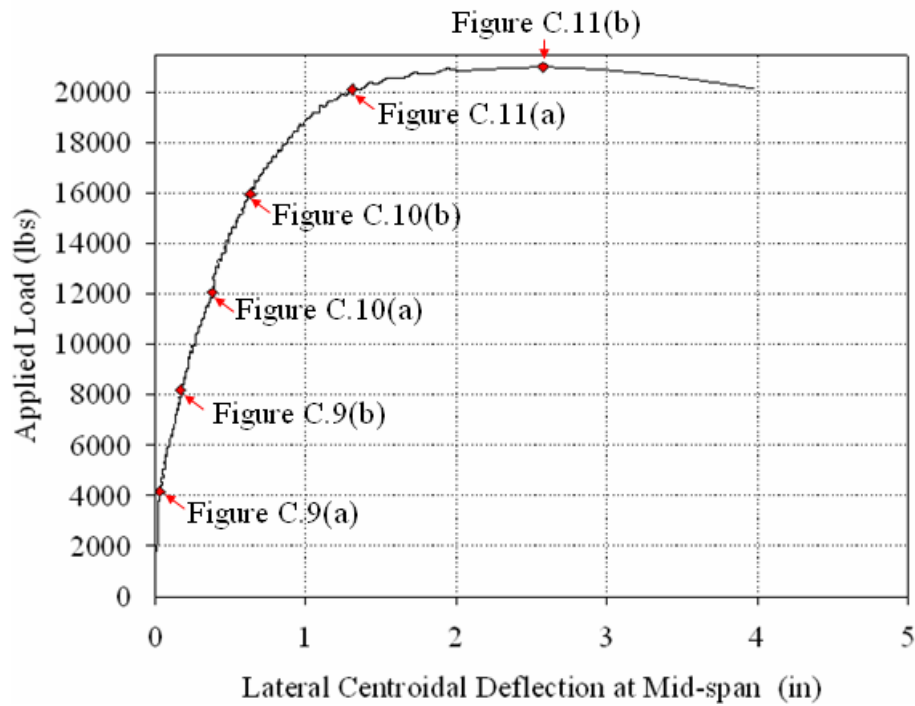
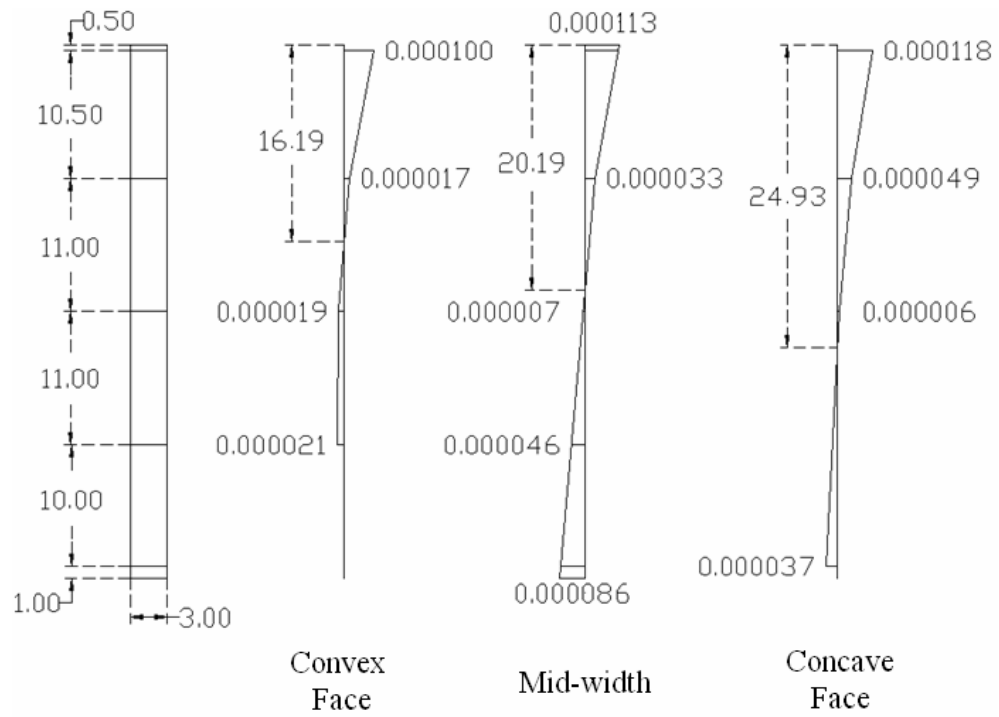
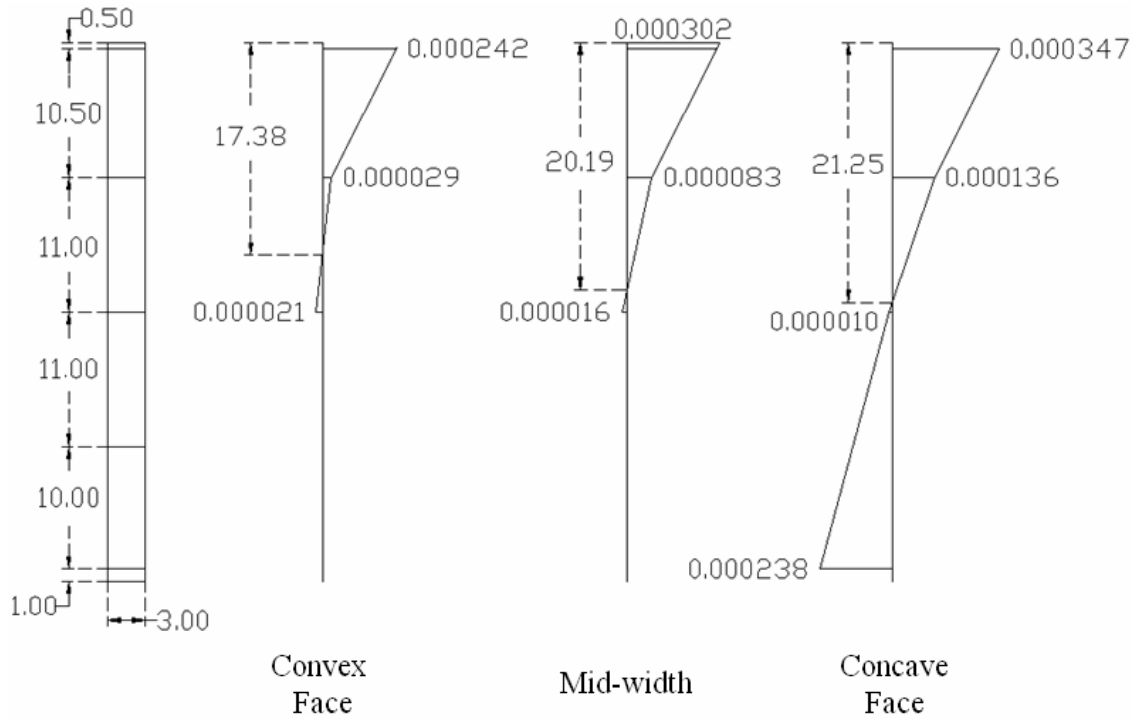


Figure C.8 – The Loads and lateral deflections corresponding to the strain distributions in Figures C.9 to C.11

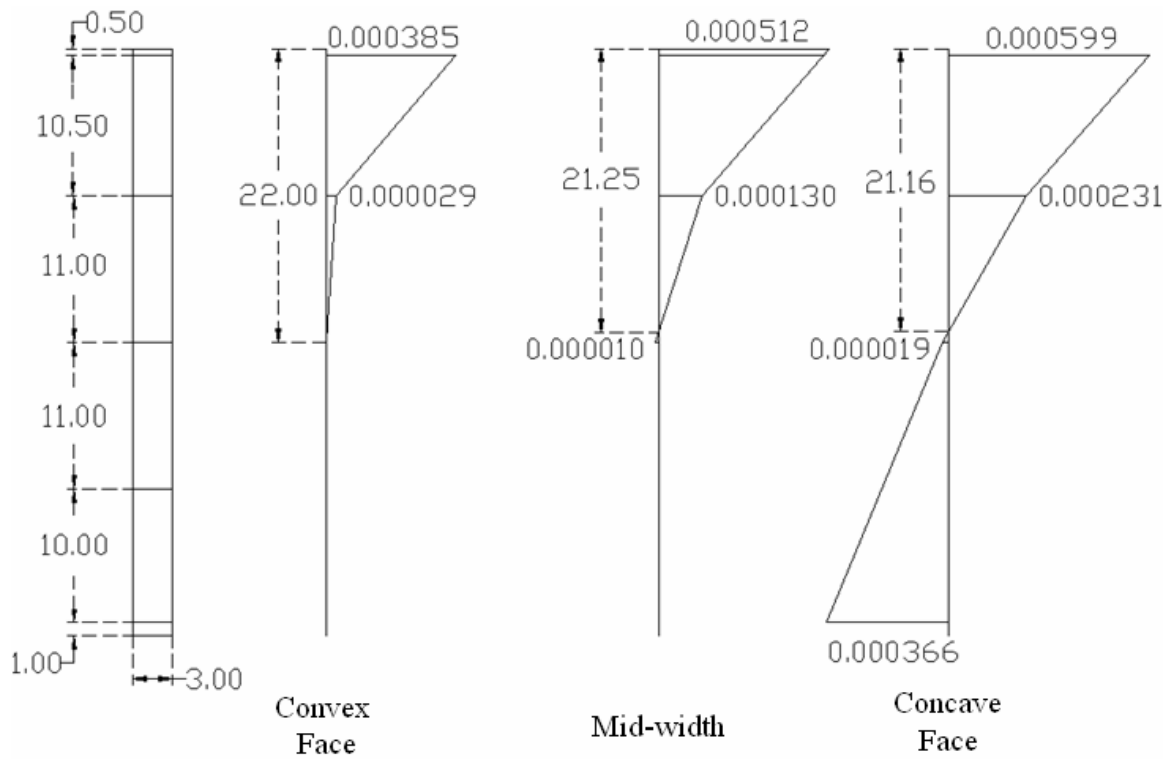


(a)  $P=4150$  lbs

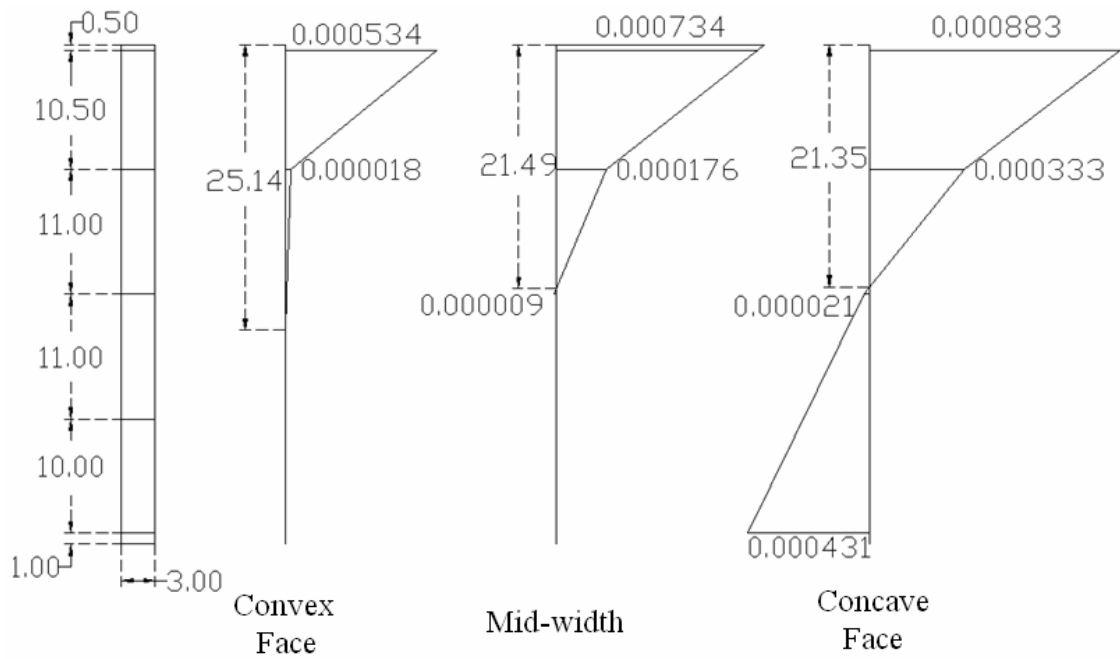


(b)  $P=8200$  lbs

Figure C.9 – Midspan strain distributions of B44-3 at the initial stages of loading

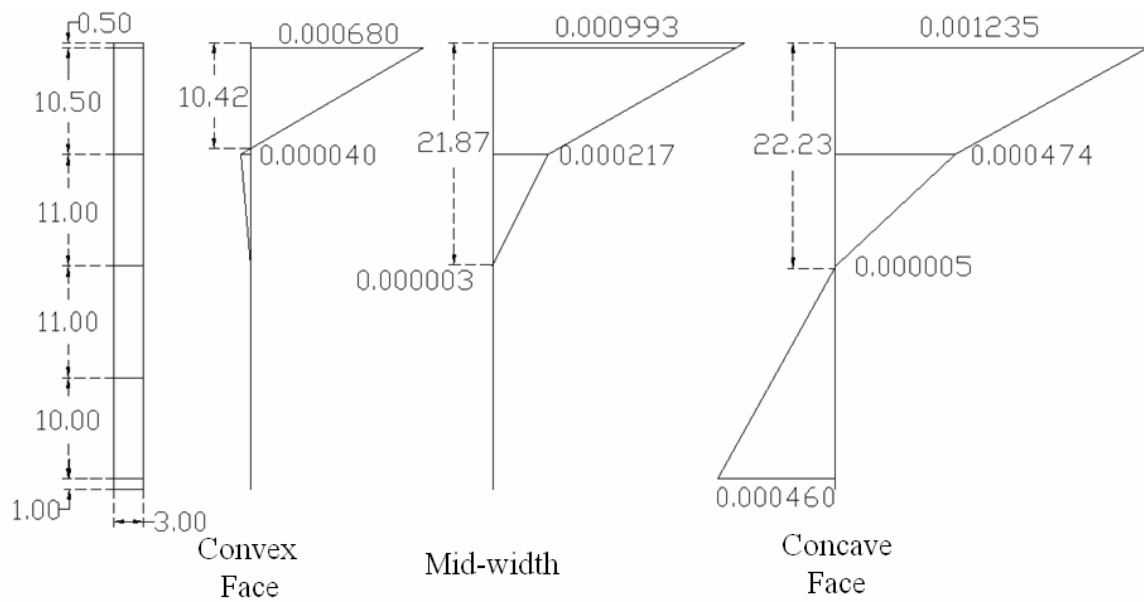


(a)  $P=12050$  lbs

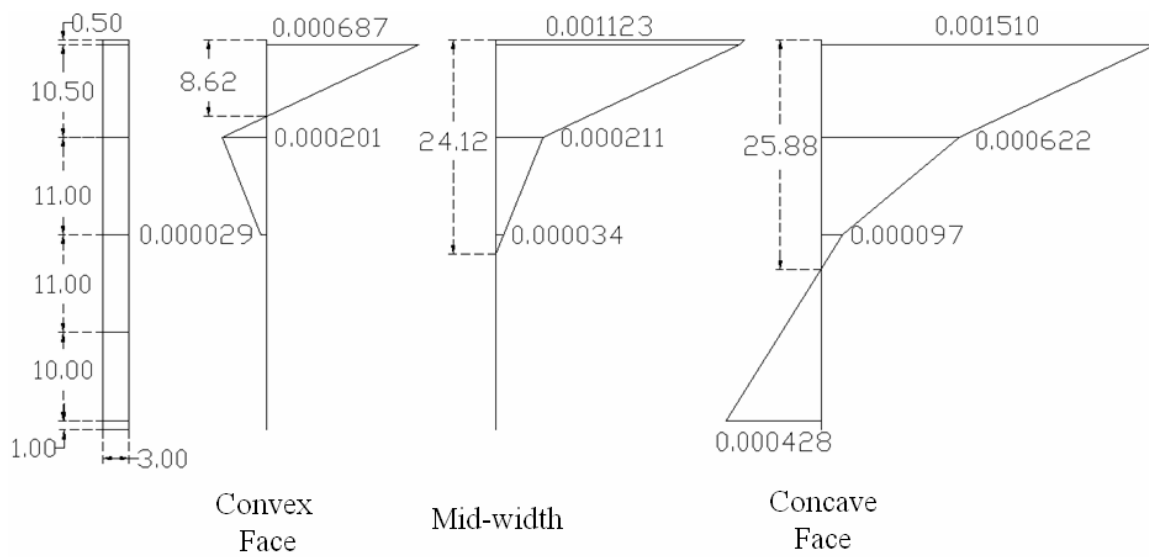


(b)  $P=16000$  lbs

Figure C.10 – Midspan strain distributions of B44-3 at different load levels



(a)  $P=20100$  lbs



(b)  $P=21000$  lbs

Figure C.11 – Midspan strain distributions of B44-3 close to buckling

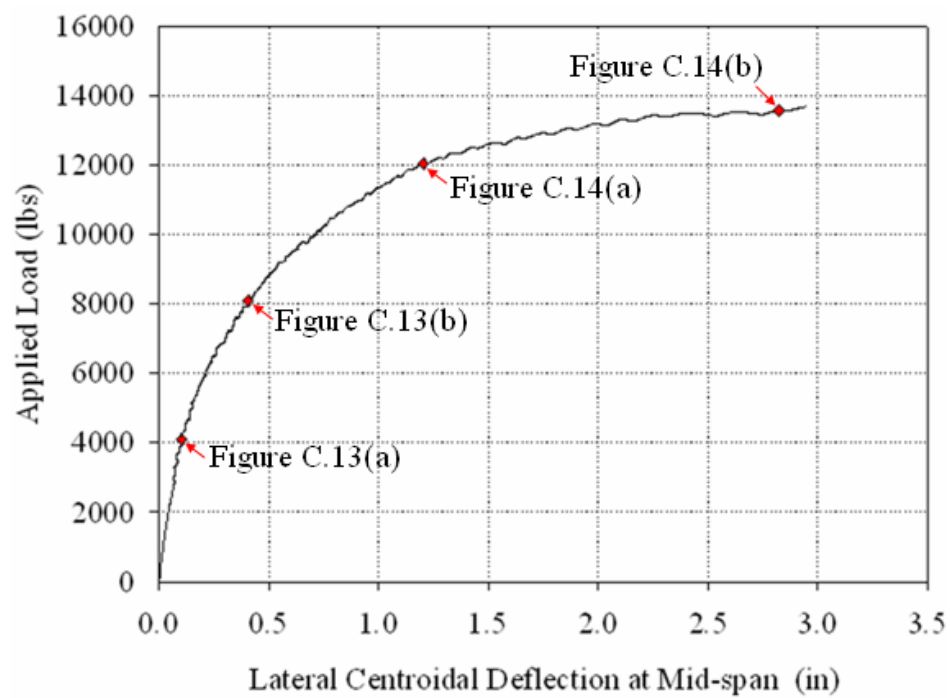
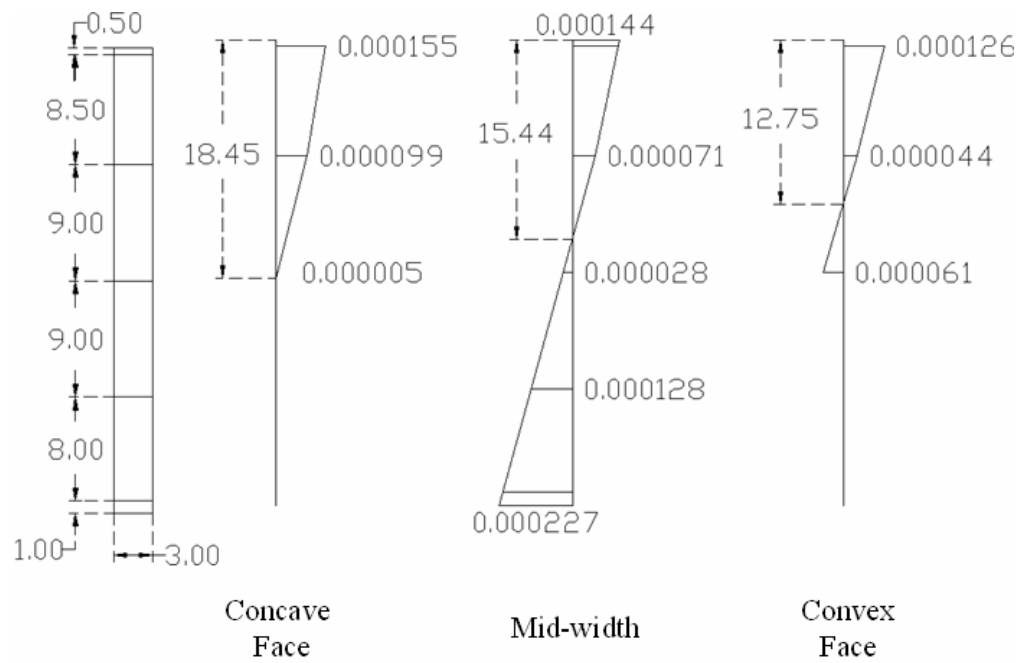
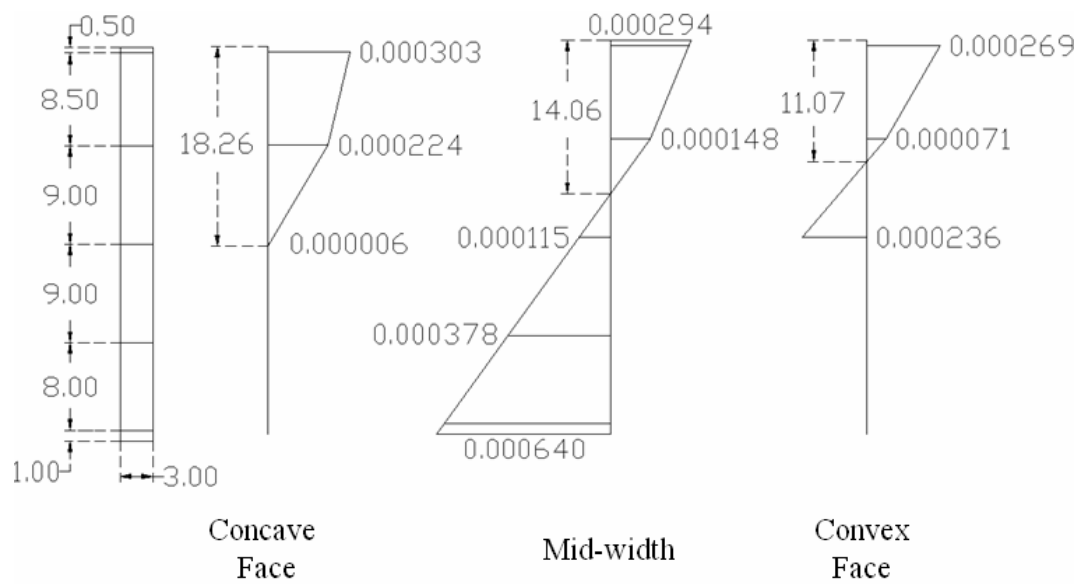


Figure C.12 – The Loads and lateral deflections corresponding to the strain distributions in Figures C.13 and C.14

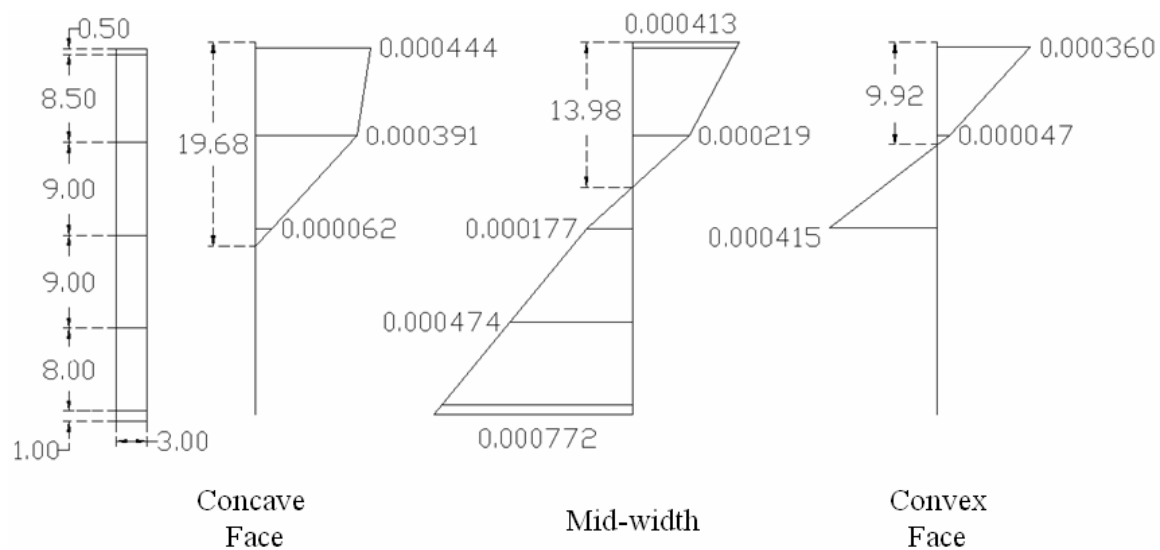


(a)  $P=4050$  lbs

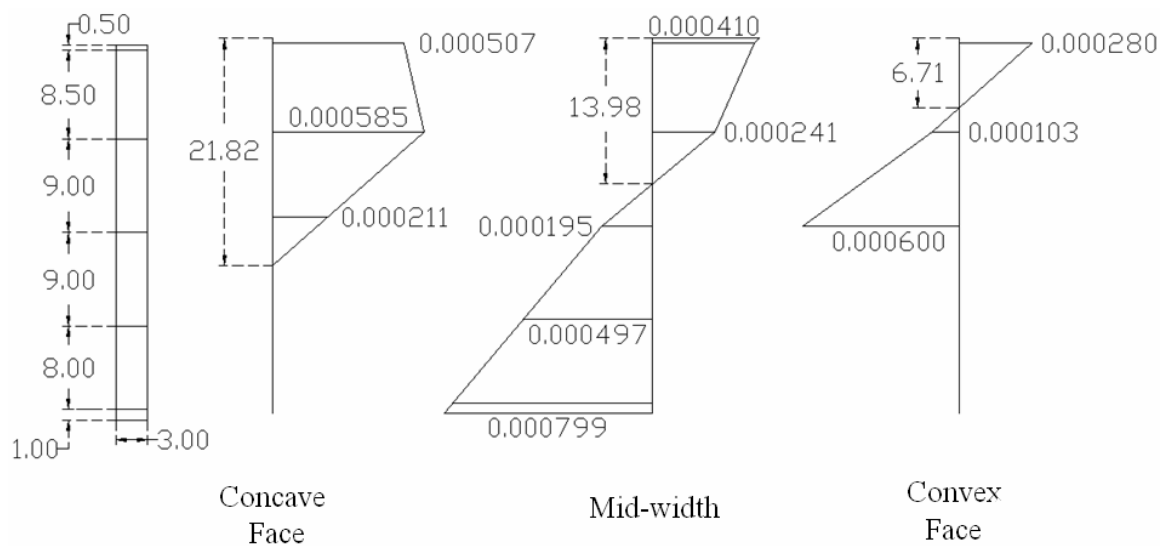


(b)  $P=8050$  lbs

Figure C.13 – Midspan strain distributions of B36L-1 at the initial stages of loading



(a)  $P=12050$  lbs



(b)  $P=13550$  lbs (buckling load)

Figure C.14 – Midspan strain distributions of B36L-1 close to buckling

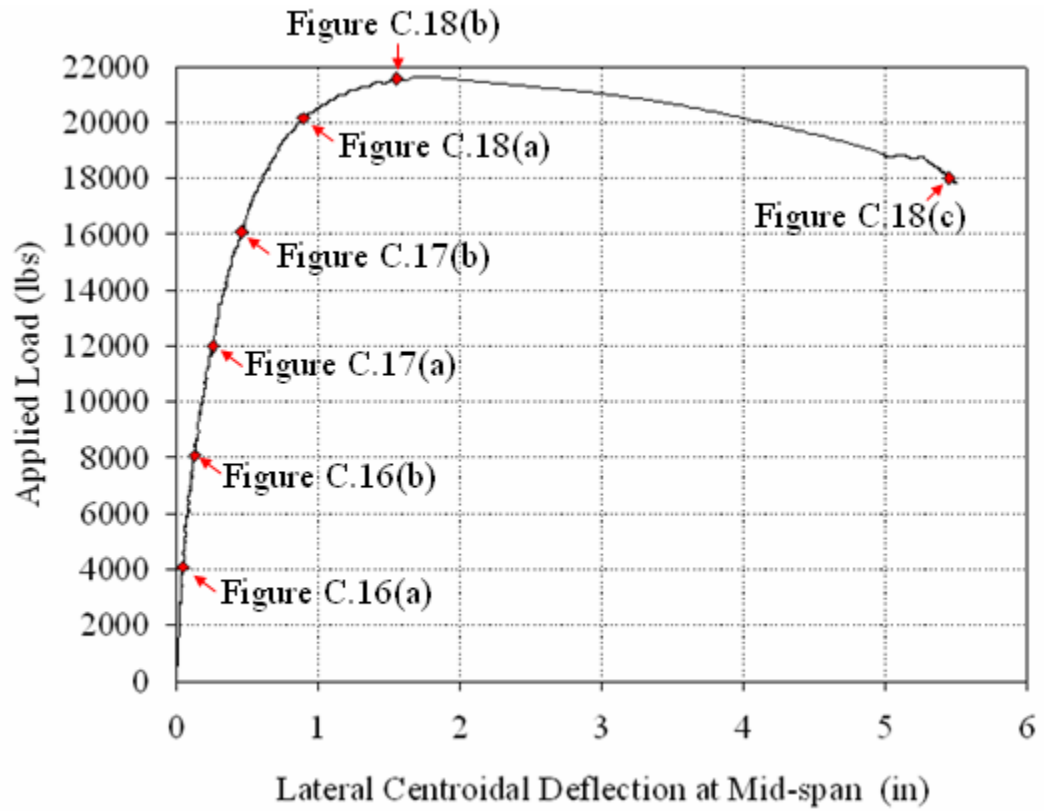


Figure C.15 – The Loads and lateral deflections corresponding to the strain distributions in Figures C.16 to C.18



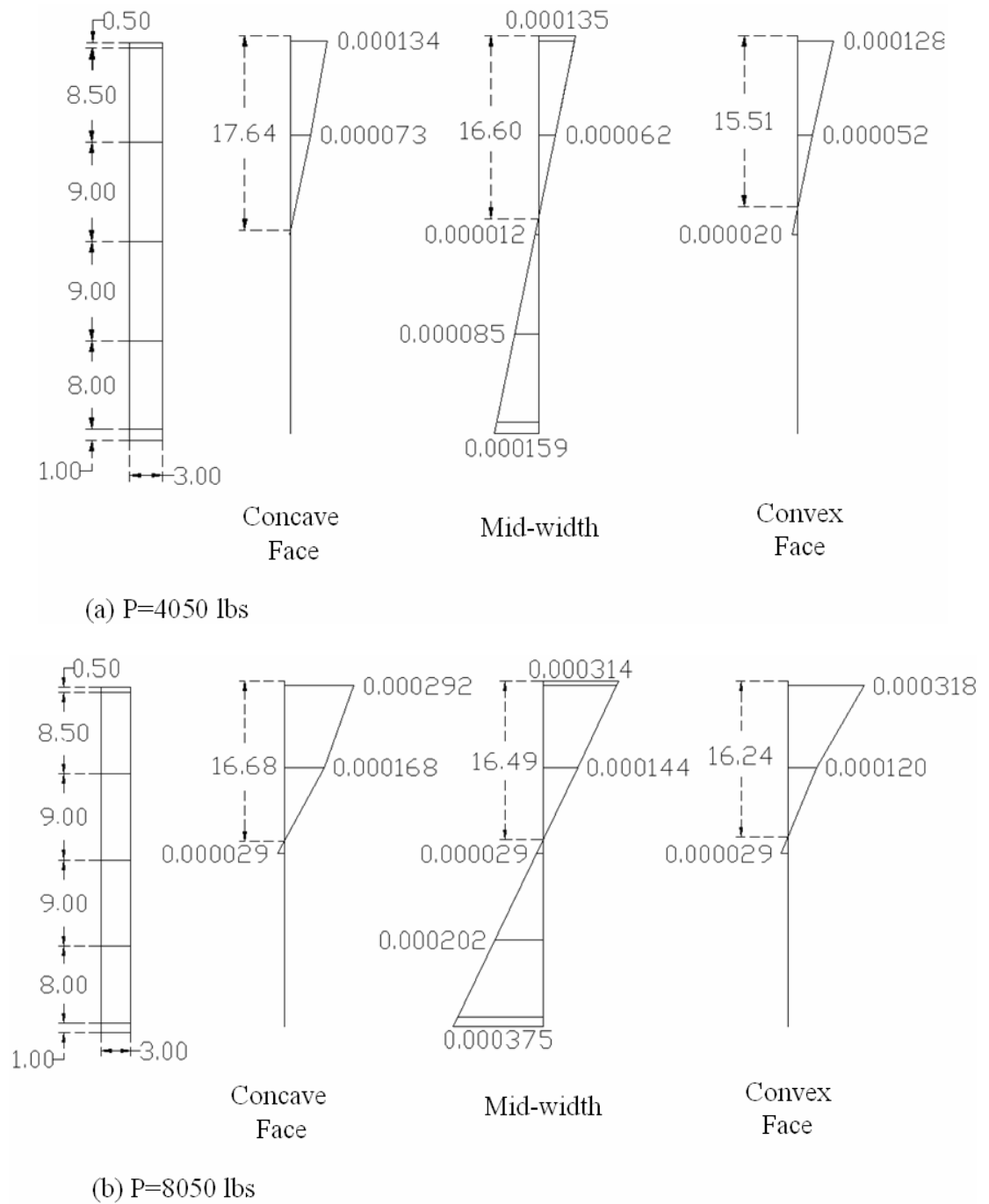


Figure C.16 – Midspan strain distributions of B36L-2 at the initial stages of loading

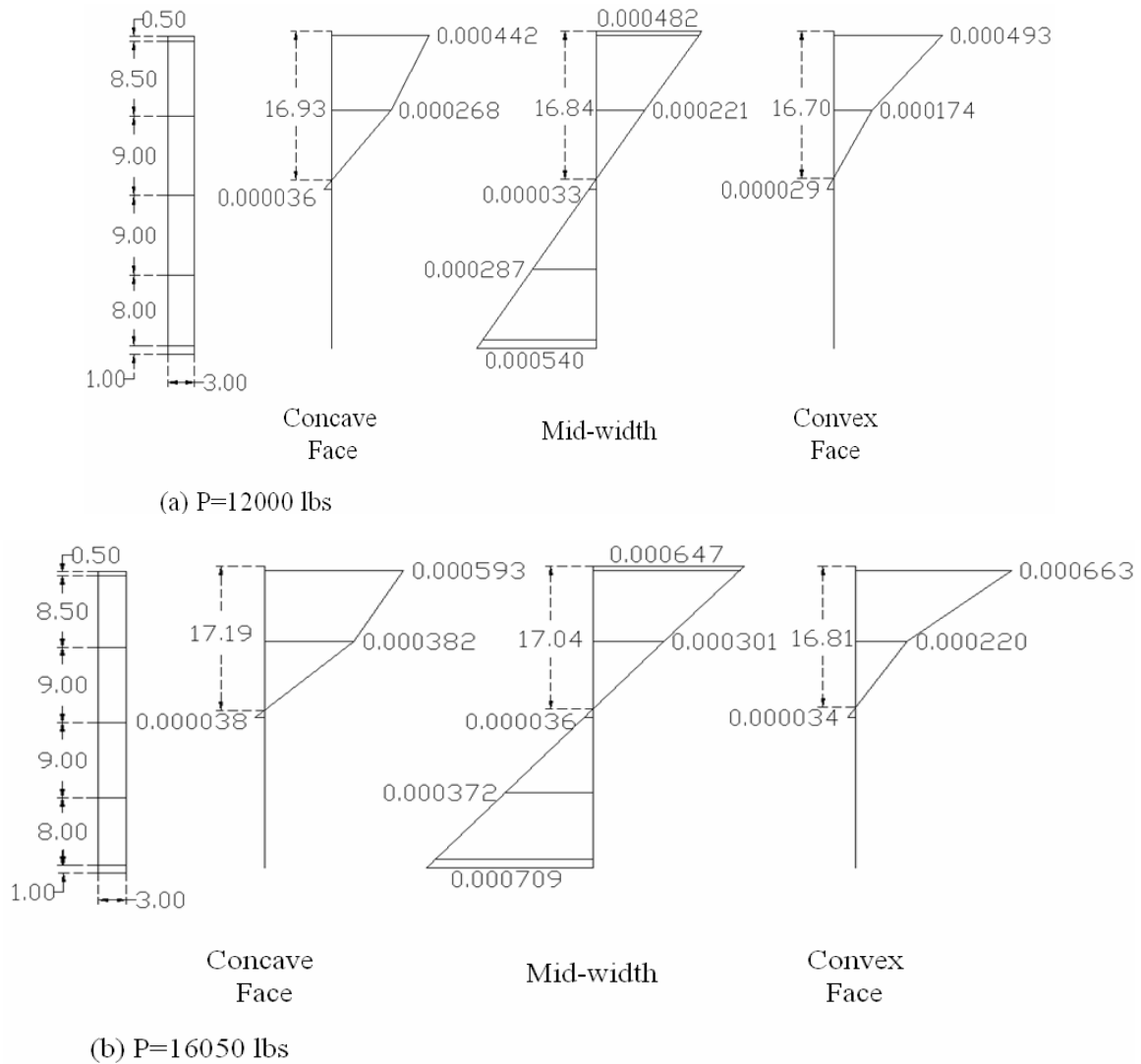
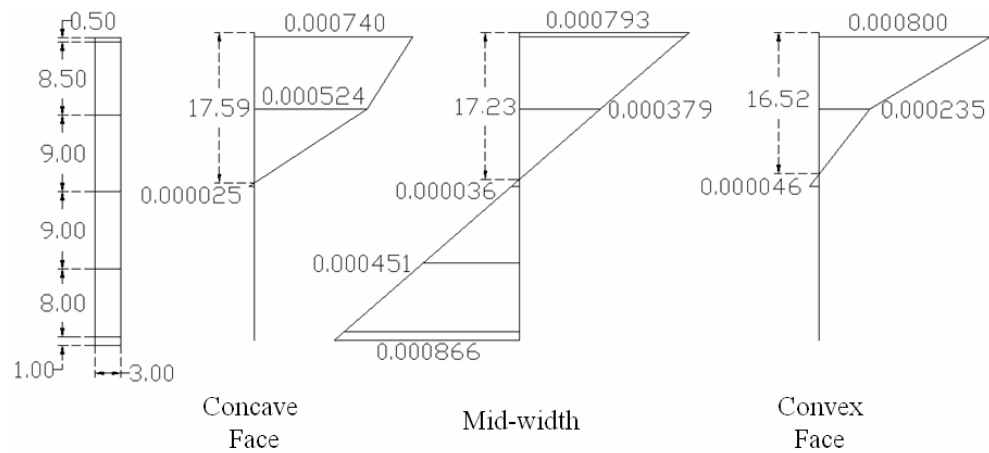
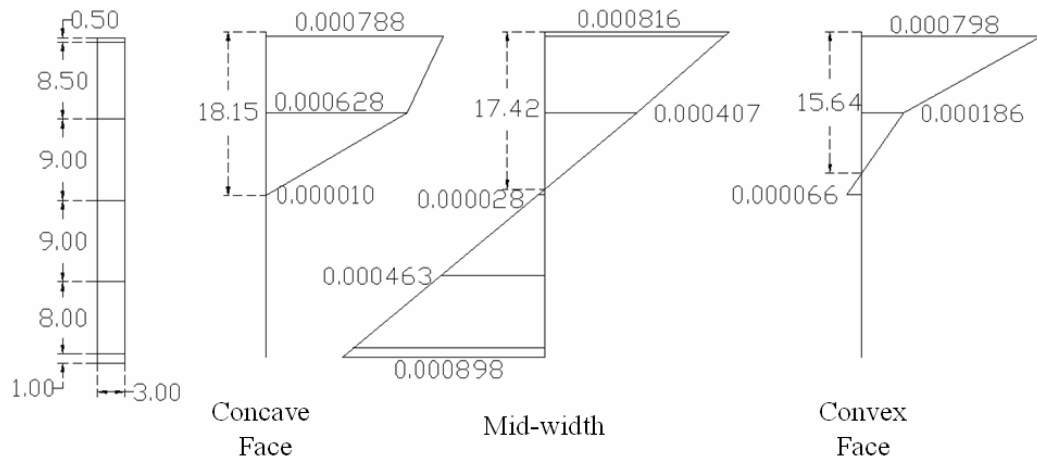


Figure C.17 – Midspan strain distributions of B36L-2 at different load levels

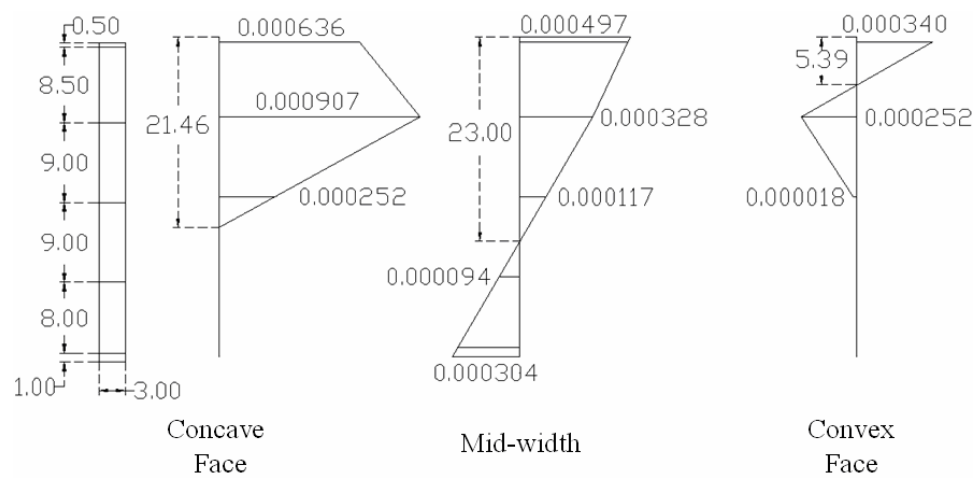
Figure C.19-C.21 illustrate the depthwise strains on the convex and concave faces of Specimen B44-1 at different load levels. The depthwise strains at mid-span of B44-1 were measured to determine the exact state of stress at mid-span and to detect any distortions in the beam during the test. The measured strain values indicate that the depthwise strains did not reach significant levels prior to buckling. The relatively higher values of depthwise strains in the post-buckling stage (Figure C.21) are related to the excessive out-of-plane deformations after buckling.



(a)  $P=20150$  lbs



(b)  $P=21550$  lbs (Buckling Load)



(c)  $P=18000$  lbs

Figure C.18 – Midspan strain distributions of B36L-2 prior to and after buckling

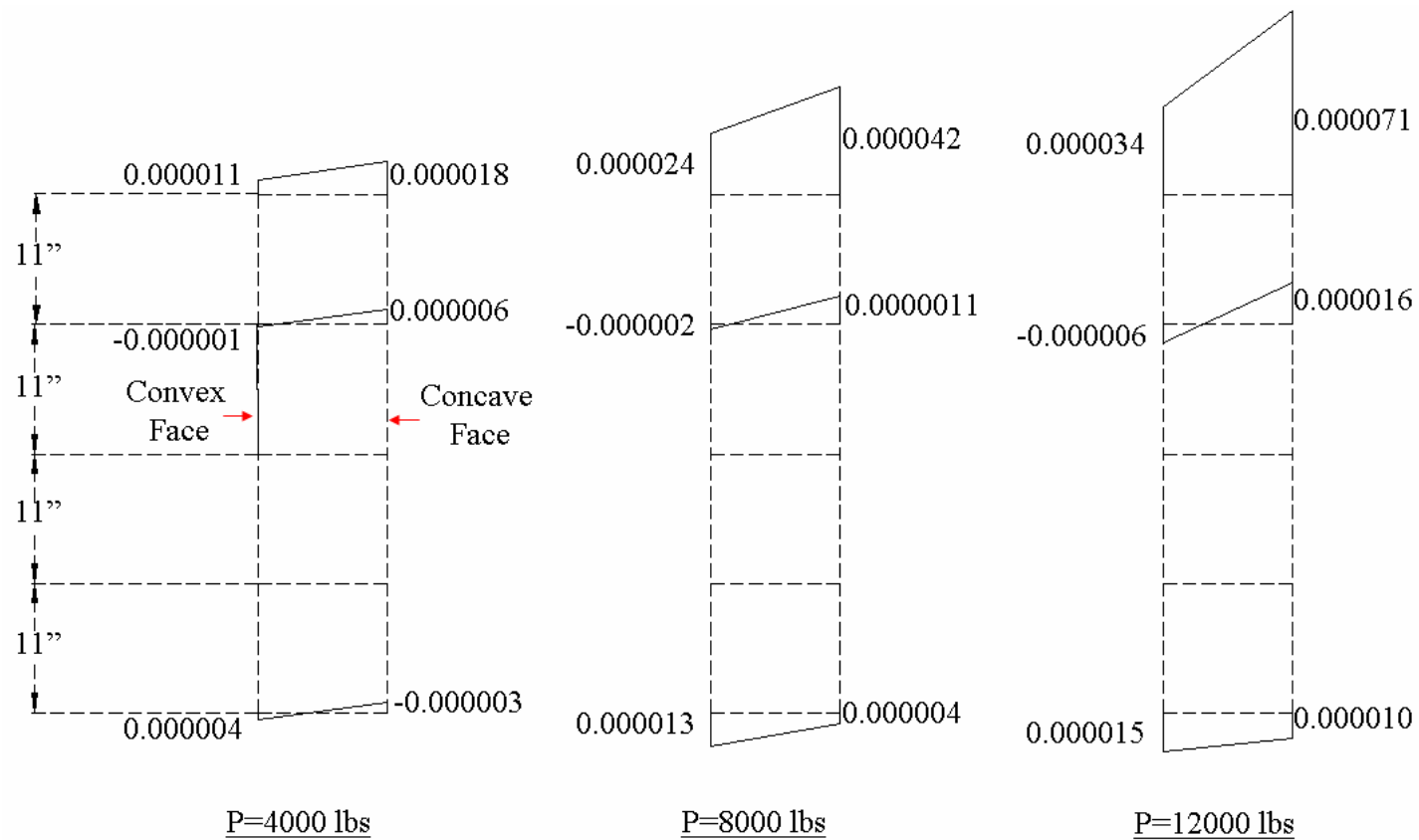


Figure C.19 – Depthwise strains along the midspan section of B44-1 at the initial stages of loading

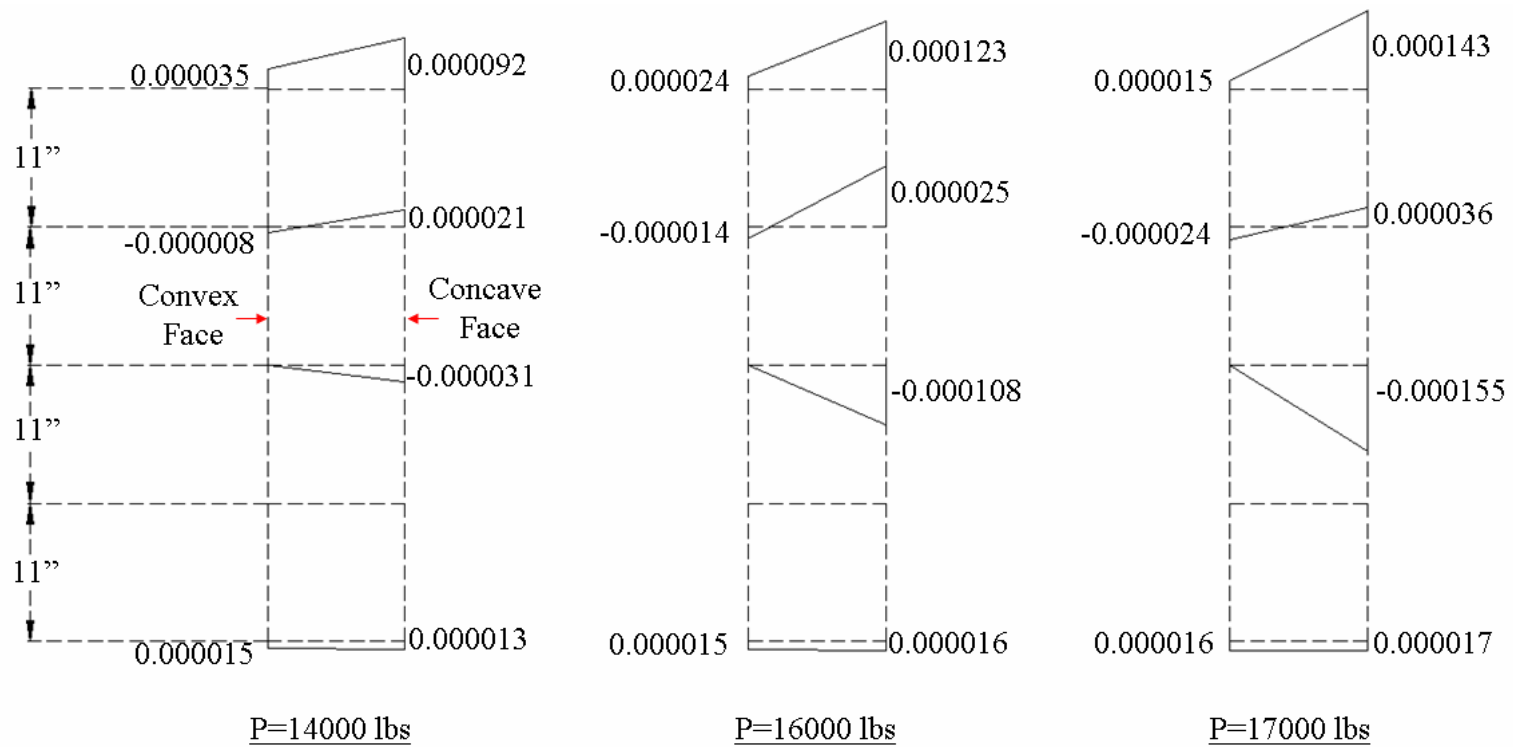


Figure C.20 – Depthwise strains along the midspan section of B44-1 at the final stages of loading

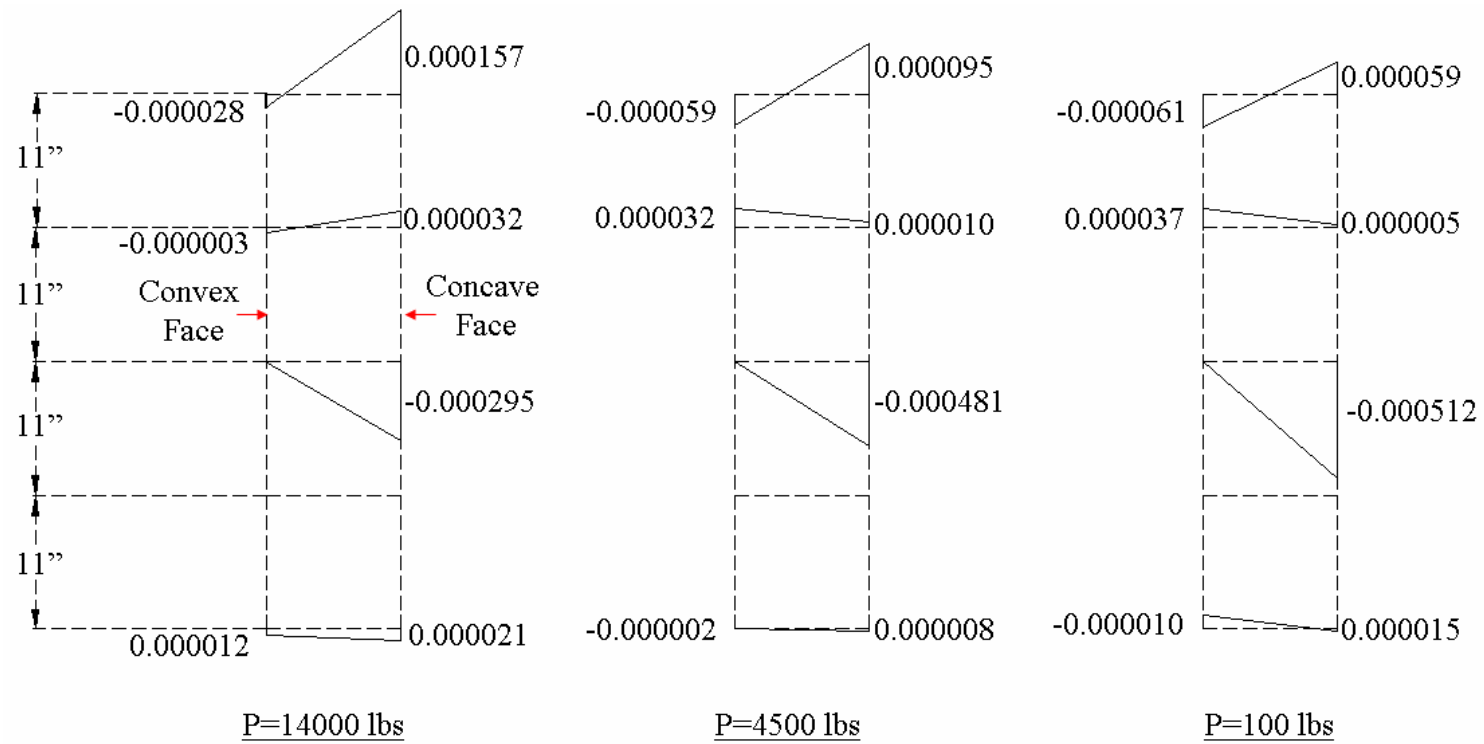


Figure C.21 – Depthwise strains along the midspan section of B44-1 during unloading

## **APPENDIX D**

### **EXPERIMENTAL LOAD-DEFLECTION PLOTS OF THE SPECIMENS**

This appendix is a collection of the experimental load-deflection plots of the specimens. The load-lateral (out-of-plane) deflection, load-vertical (in-plane) deflection and the torque-twist plots of the specimens are presented in the appendix.

Each of Figures D.1 to D.10 shows the lateral deflections of a specimen, measured at different points along the depth of the beam at mid-span. The depths of the measurement points are also shown on the figures for the sake of comparison. As previously explained in Section 3.1.3 of this dissertation, the goal of measuring the lateral deflections of the beams at different depths was to evaluate the torsional rotations and distortions in the beams.

In Figures D.11 and D.12, the load-lateral centroidal deflection curves of the companion beams are compared for the Specimen Groups B44 and B36L, respectively. The load-lateral deflection behavior of a reinforced concrete beam is greatly influenced by its initial lateral imperfections. Due to the significant influence of sweep on the stability, the centroidal sweep of each beam at midspan is illustrated on the respective load-lateral deflection curve.

Each of the load-deflection curves in Figures D.1 to D.12 does not start from the origin. The initial deflection value of each curve (the deflection at zero load) corresponds to the initial lateral deformation of the beam at the particular depth. Including the initial lateral imperfections in the plots was important particularly in Figures D.11 and D.12 to illustrate the influence of sweep on the buckling behaviors of the companion beams. In

Section 6.3 of this dissertation, the effects of sweep on the load-lateral deflection behaviors of the companion beams in Specimen Groups B44 and B36L were explained.

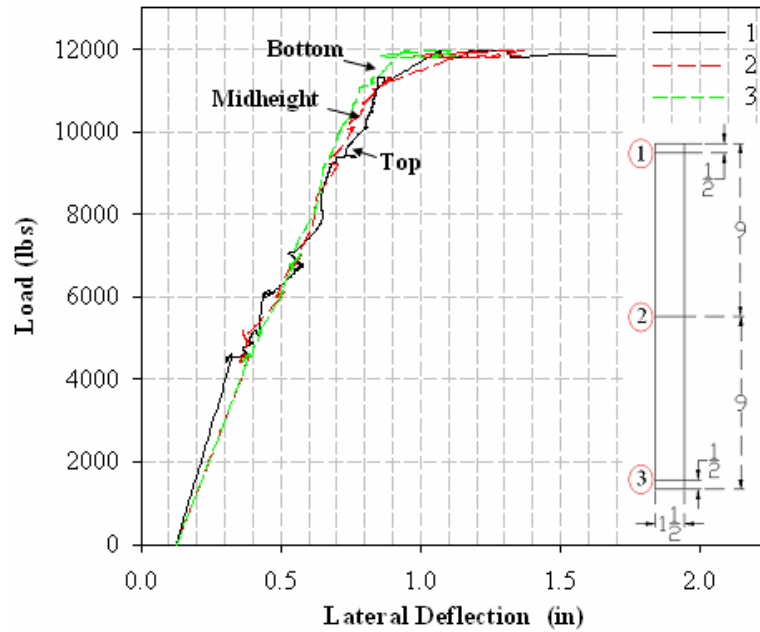


Figure D.1 – Out-of-plane deflections of B18-2 at midspan

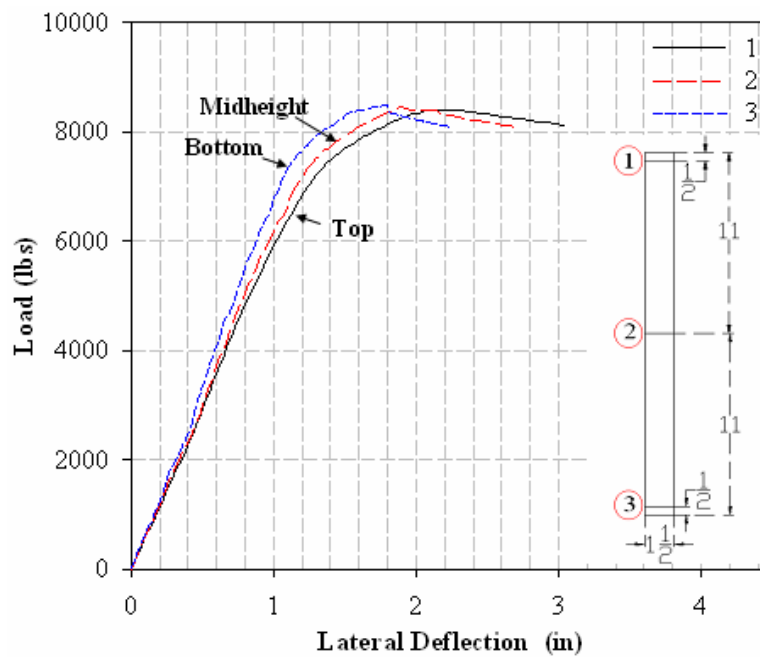


Figure D.2 – Out-of-plane deflections of B22-1 at midspan



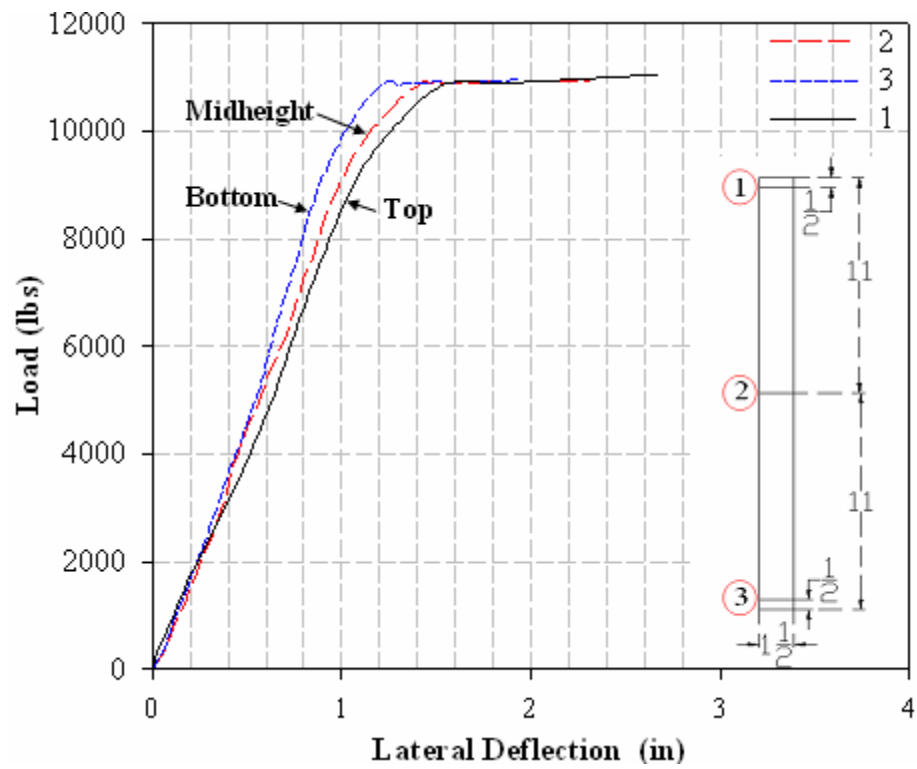


Figure D.3 – Out-of-plane deflections of B22-2 at midspan

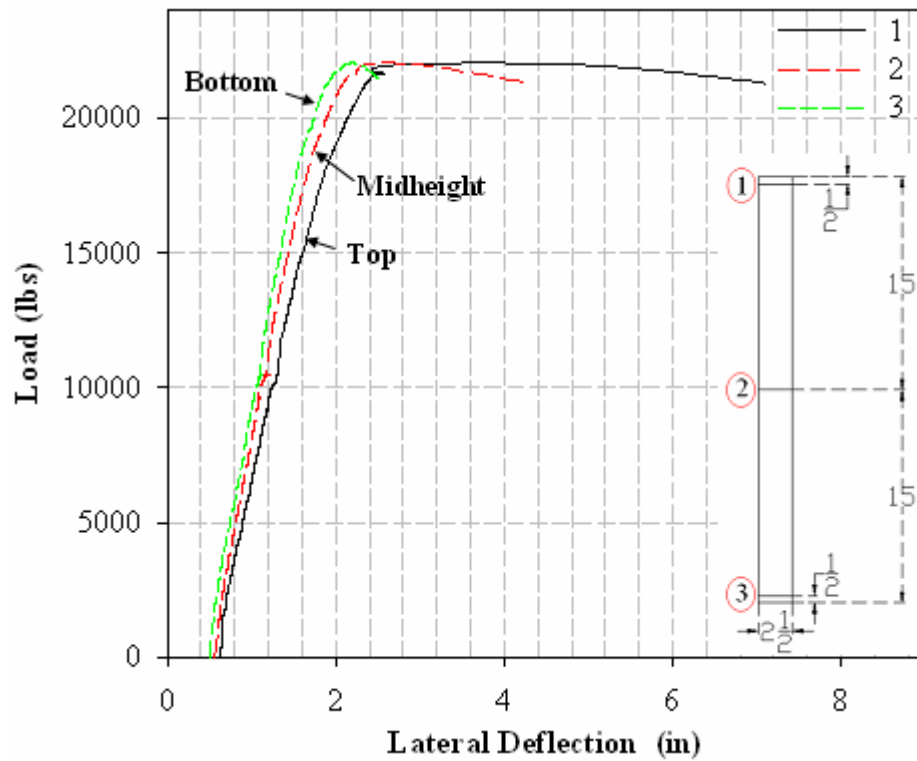


Figure D.4 – Out-of-plane deflections of B30 at midspan

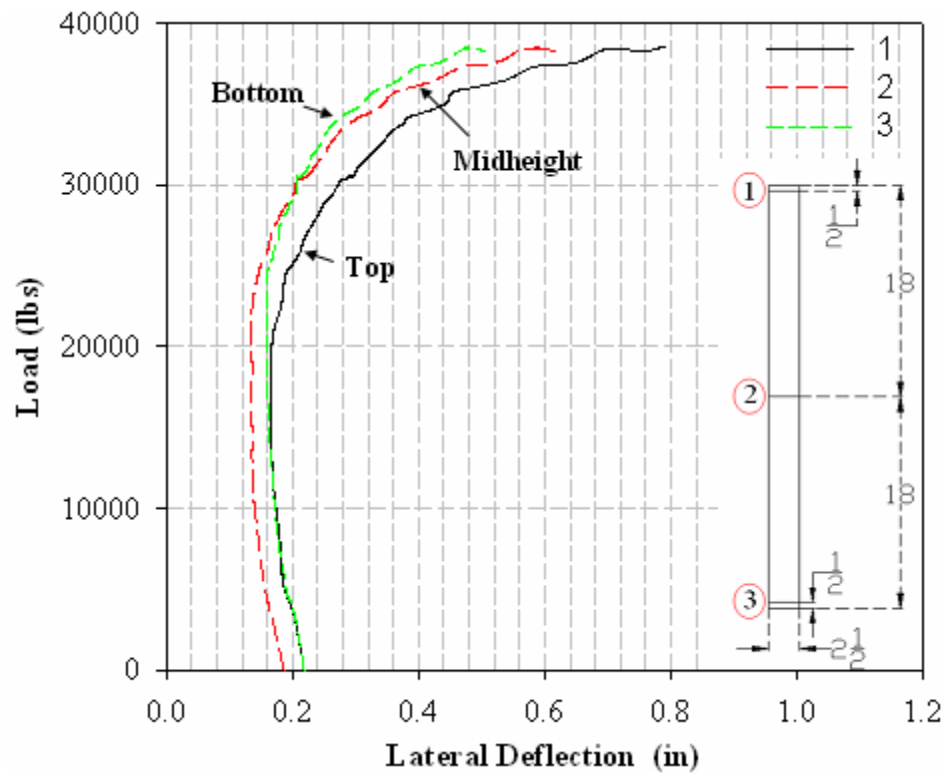


Figure D.5 – Out-of-plane deflections of B36 at midspan

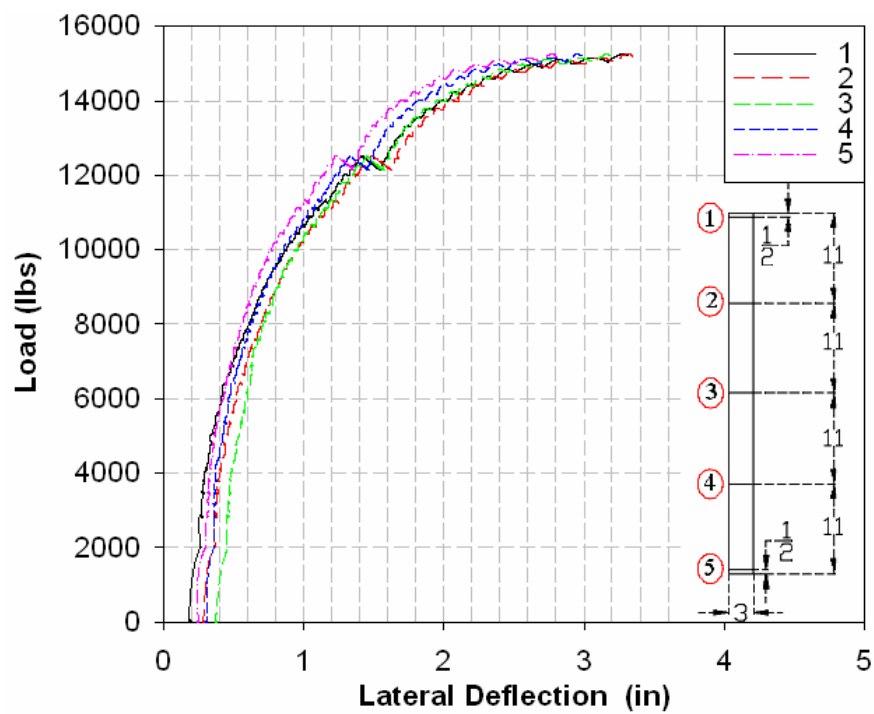


Figure D.6 – Out-of-plane deflections of B44-1 at midspan

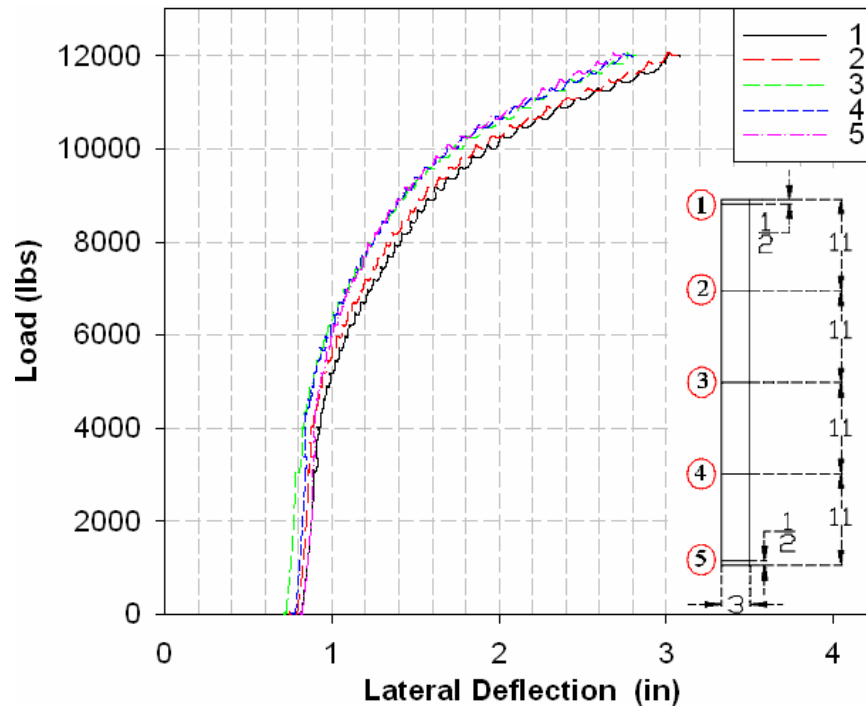


Figure D.7 – Out-of-plane deflections of B44-2 at midspan

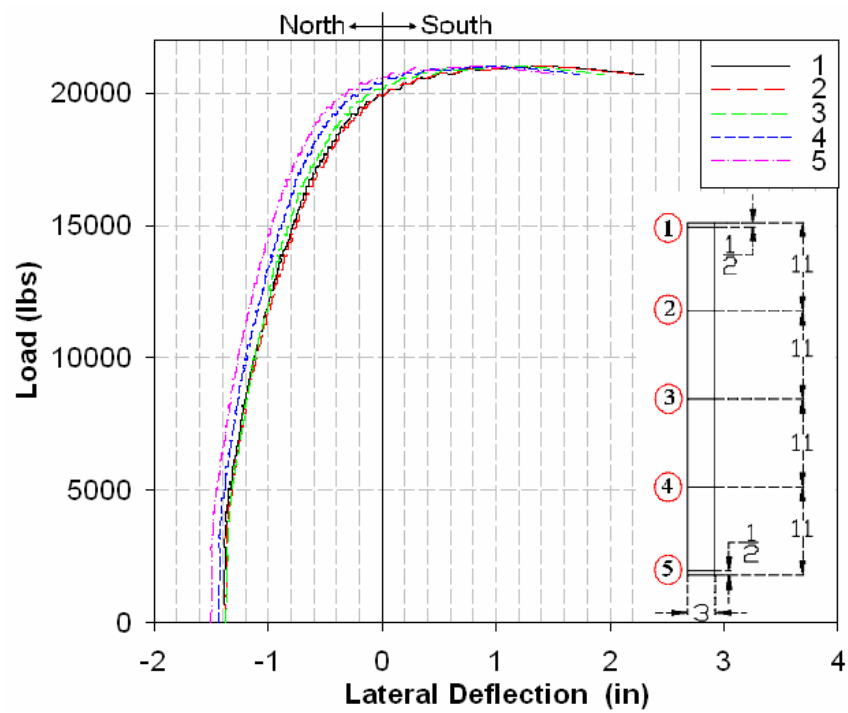


Figure D.8 – Out-of-plane deflections of B44-3 at midspan

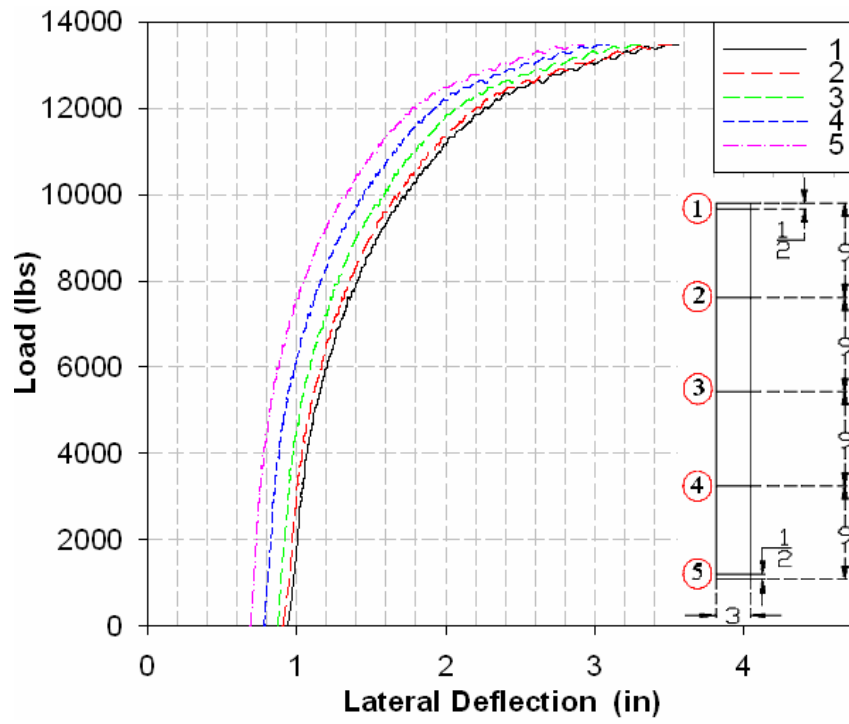


Figure D.9 – Out-of-plane deflections of B36L-1 at midspan

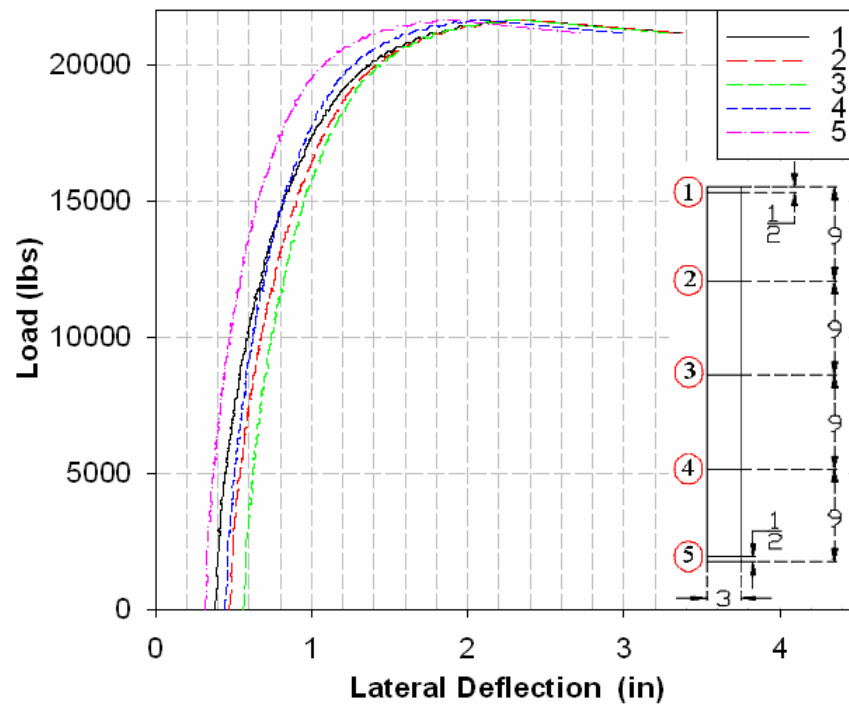


Figure D.10 – Out-of-plane deflections of B36L-2 at midspan

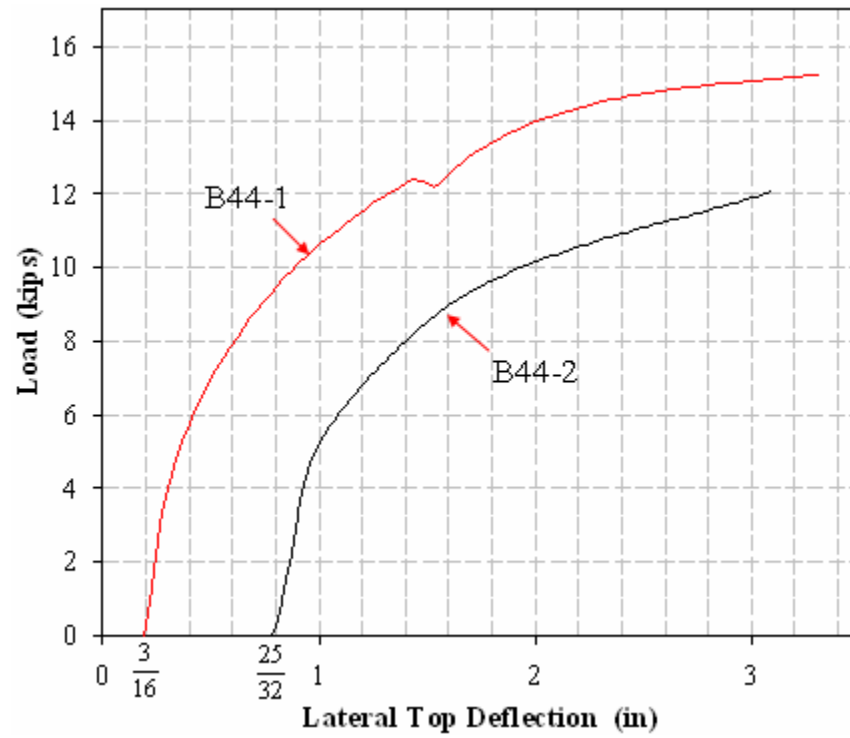


Figure D.11 – Lateral centroidal deflections of Beams B44 at midspan

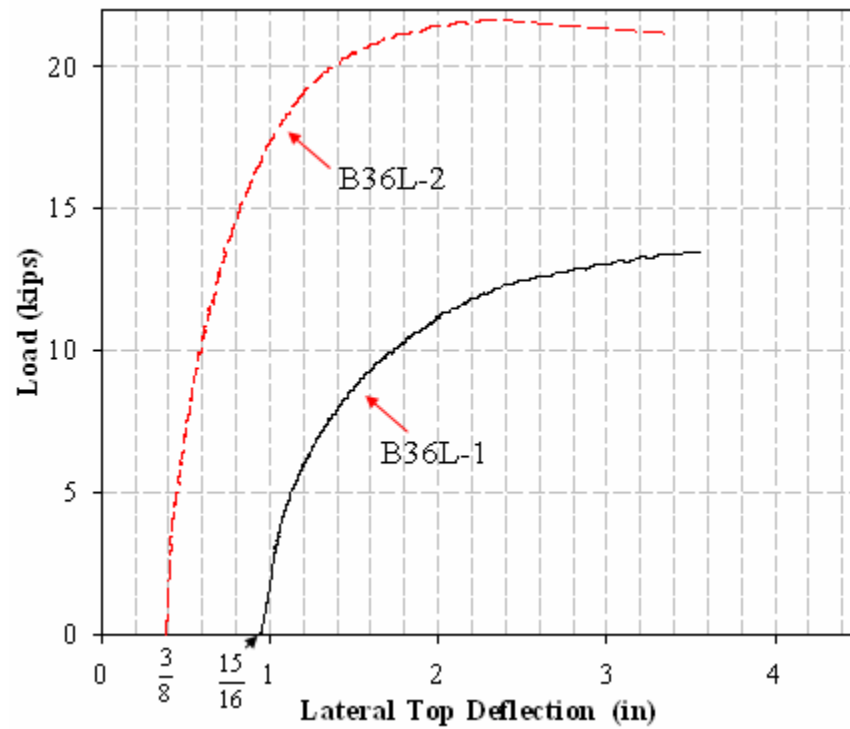


Figure D.12 – Lateral centroidal deflections of Beams B36L at midspan

Figures D.13 to D.21 illustrate the load-vertical deflection curves of the specimens. The plots also include analytical load-deflection curves, obtained by using the cracked moment of inertia and two different effective moment of inertia expressions in Equation (D.1), which gives the in-plane deflections at midspan of a simply-supported beam, subjected to a concentrated load at midspan.

$$v_c = \frac{P \cdot L^3}{48 \cdot EI_x} \quad (D.1)$$

where  $P$  is the applied load;  $L$  is the span length;  $EI_x$  is the in-plane flexural rigidity.

Two of the analytical curves in each figure correspond to the effective moment of inertia expressions proposed by Branson (1963) and Bischoff (2005). The third analytical curve, on the other hand, corresponds to the cracked moment of inertia, which is the moment of inertia of a beam section when the entire tension zone of the section is rendered ineffective in resisting bending moments due to flexural cracking. The effective moments of inertia according to Branson (1963) and Bischoff (2005) and the cracked moment of inertia are calculated from Equations (D.2), (D.3) and (D.4), respectively.

$$I_{eb} = \left( \frac{M_{cra}}{M_a} \right)^3 \cdot I_g + \left[ 1 - \left( \frac{M_{cra}}{M_a} \right)^3 \right] \cdot I_{cr} \quad (D.2)$$

$$\frac{1}{I_{ebi}} = \left( \frac{M_{cra}}{M_a} \right)^2 \cdot \frac{1}{I_g} + \left[ 1 - \left( \frac{M_{cra}}{M_a} \right)^2 \right] \cdot \frac{1}{I_{cr}} \quad (D.3)$$

$$I_{cr} = \frac{1}{12} \cdot b \cdot c^3 + n \cdot A_s \cdot (d - c)^2 \quad (D.4)$$

where  $I_g$  is the gross moment of inertia (Equation D.5);  $M_a$  is the maximum in-plane

bending moment in the beam;  $M_{cra}$  is the cracking moment of the beam;  $c$  is the neutral axis depth from the compression face when all fibers in the compression zone are stressed below the elastic limit of concrete;  $b$  is the width of the beam;  $A_s$  is the total cross-sectional area of the longitudinal reinforcement;  $n$  is modular ratio of steel to concrete.

$$I_g = \frac{1}{12} \cdot b \cdot h^3 \quad (D.5)$$

where  $h$  is the height of the beam.

In Specimens B22 and B30, restrained shrinkage cracking was detected. Based on the studies of Scanlon and Bischoff (2008), the term  $M_{cra}$  in Equations (D.2) and (D.3) was replaced with  $2M_{cra}/3$  to account for the reduction in the effective moments of inertia of B22 and B30 due to the presence of shrinkage cracks in concrete.

The experimental load-deflection curves of Beams B18-2, B36, B44 and B36L are in close agreement with the analytical curves corresponding to the effective moments of inertia proposed by Branson (1963) and Bischoff (2005). The load-deflection behaviors of Beams B22 and B30, nonetheless, are not closely estimated by Equation (D.1) when effective moment of inertia is used in the equation. Figures D.14 and D.15 indicate that the initial linear portions of the experimental load-vertical deflection curves of Specimens B22 and B30 are coincident with the analytical line corresponding to the cracked moment of inertia ( $I_{cr}$ ), most probably due to shrinkage cracking of concrete.

Figures D.22 to D.26 illustrate the torque-twist curves of the test specimens. The ordinate axes represent the maximum torsional moment in a beam ( $T_{max}$ ), meaning the torque at the beam ends, while the x-axes represent the twist at mid-span ( $\theta$ ), calculated by dividing the angle of twist of the beam at midspan to the longitudinal distance from

support to mid-span. The red line in each figure indicates the maximum torsional moment ( $T_b$ ) in the beam at the instant of buckling.

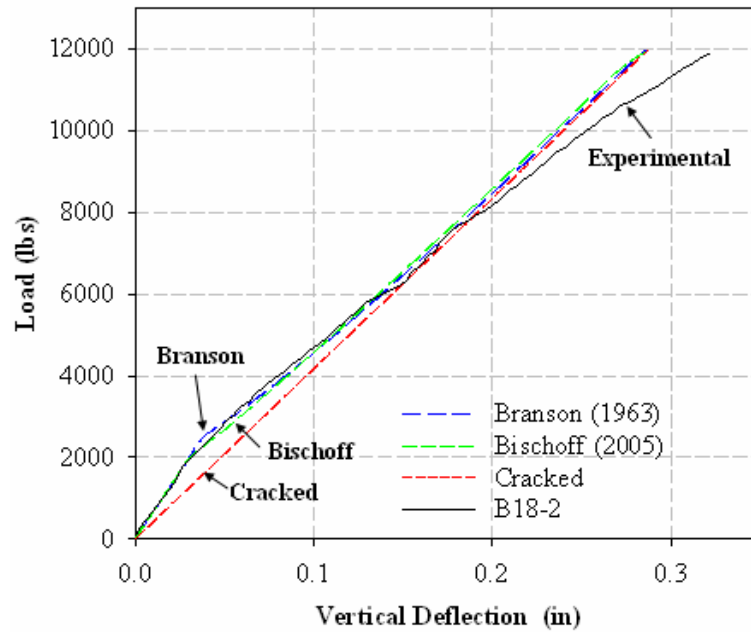


Figure D.13 - In-plane deflections of Beam B18-2 at midspan

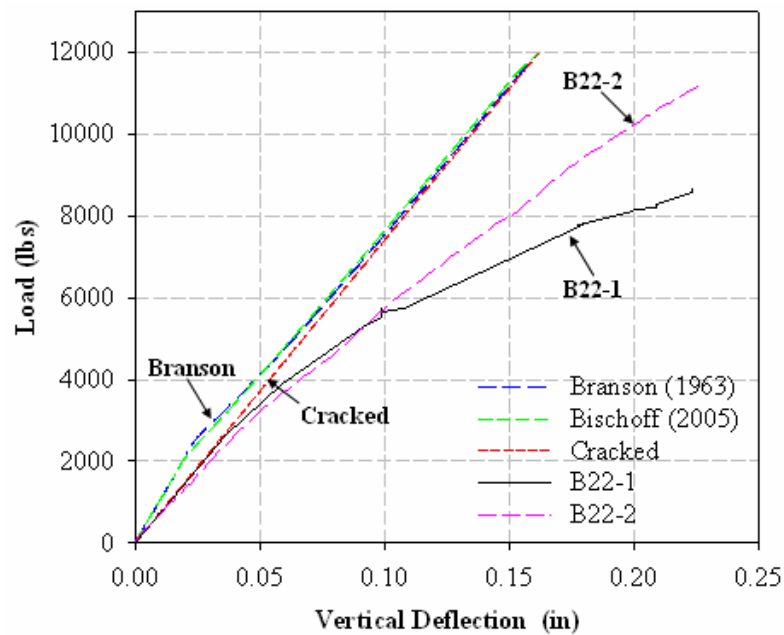


Figure D.14 - In-plane deflections of Beams B22 at midspan



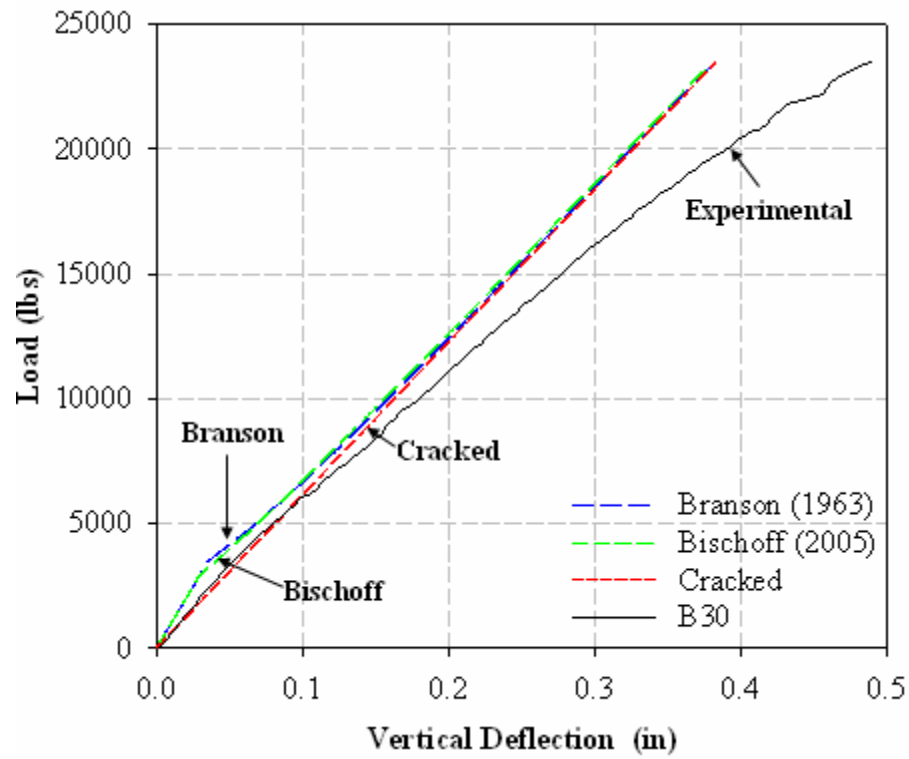


Figure D.15 - In-plane deflections of Beam B30 at midspan

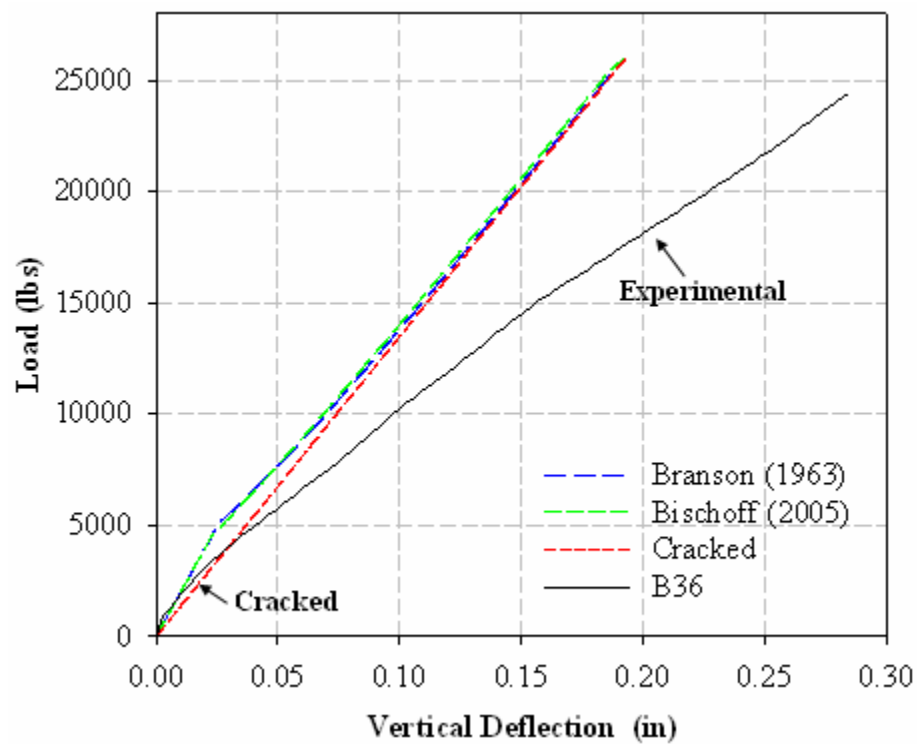


Figure D.16 - In-plane deflections of Beam B36 at midspan

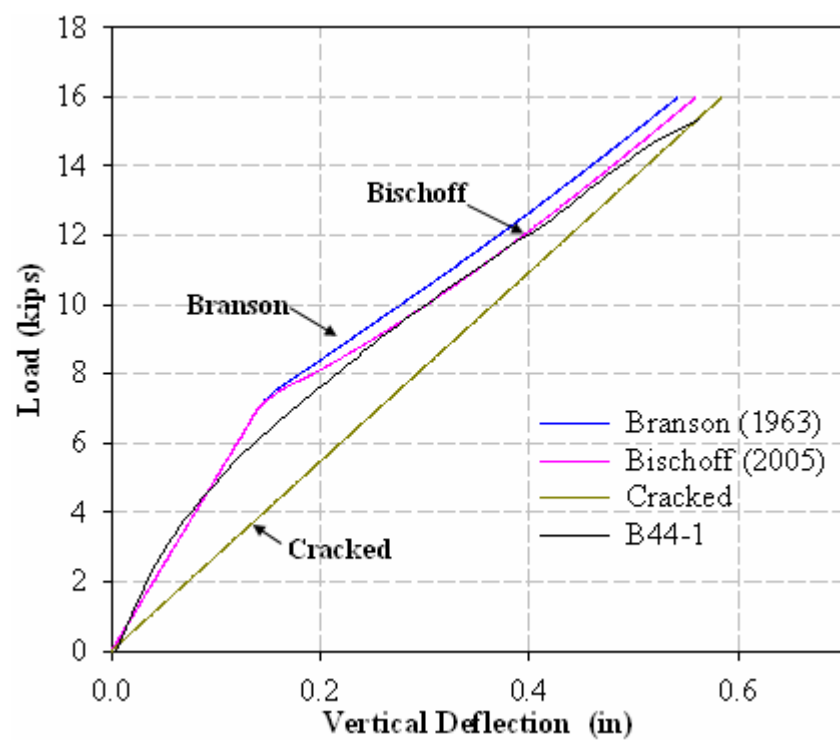


Figure D.17 – In-plane deflections of B44-1 at midspan

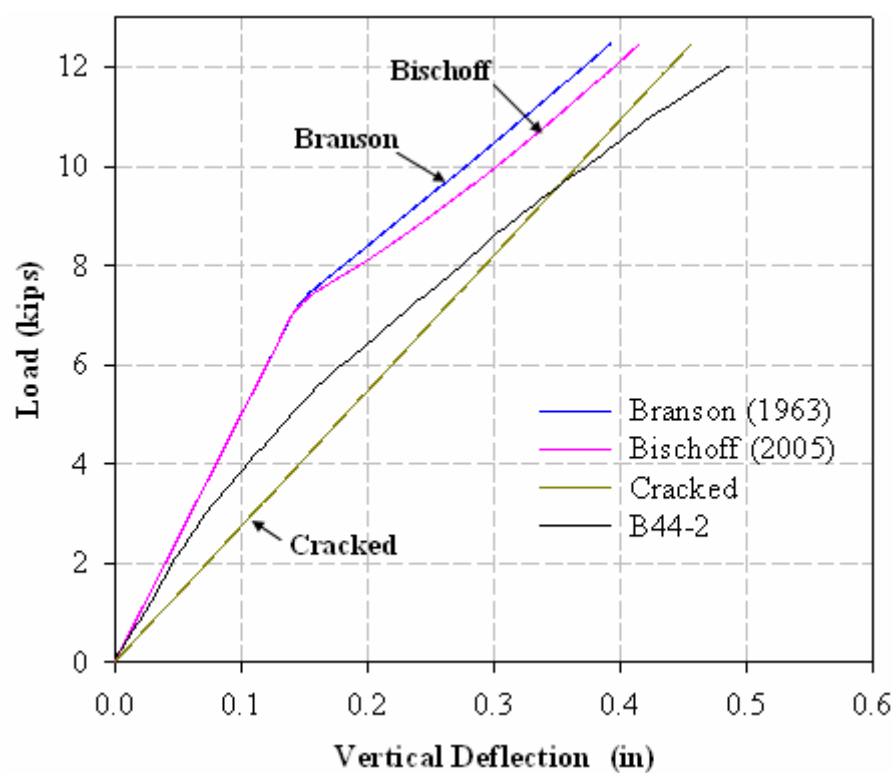


Figure D.18 – In-plane deflections of B44-2 at midspan

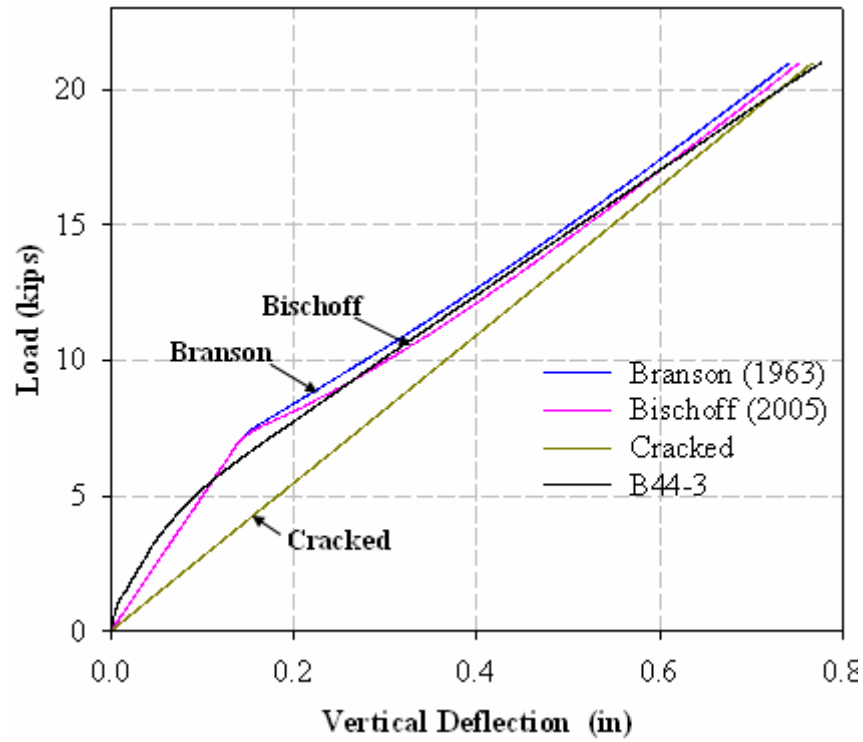


Figure D.19 – In-plane deflections of B44-3 at midspan

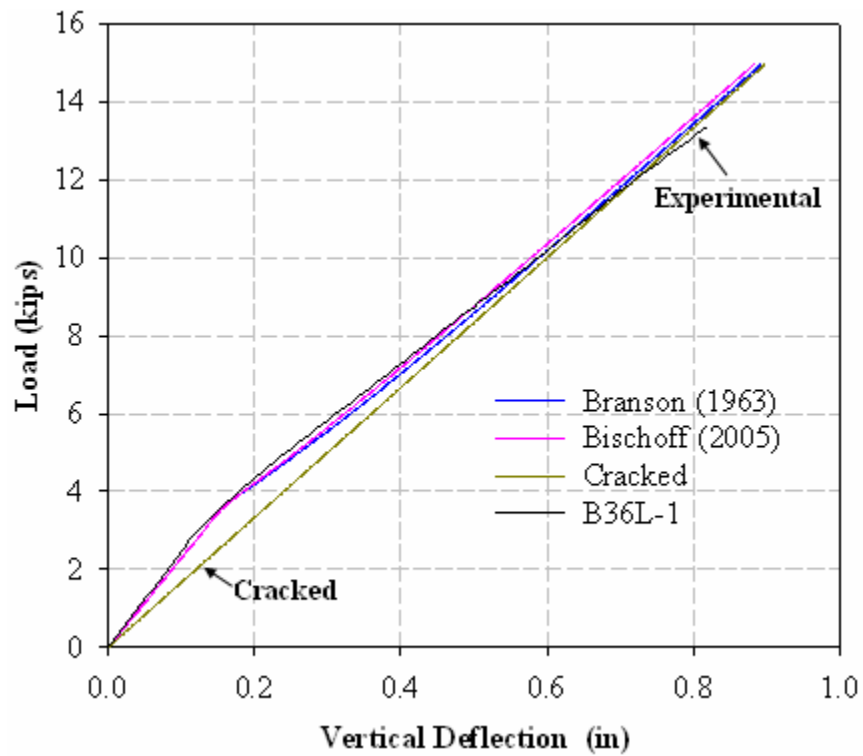


Figure D.20 – In-plane deflections of B36L-1 at midspan

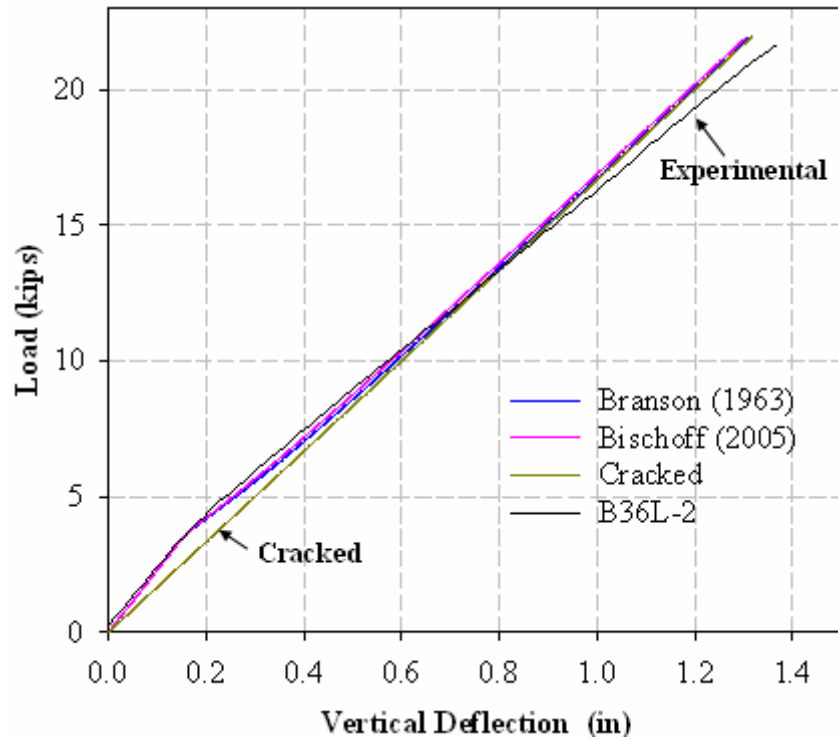


Figure D.21 – In-plane deflections of B36L-2 at midspan

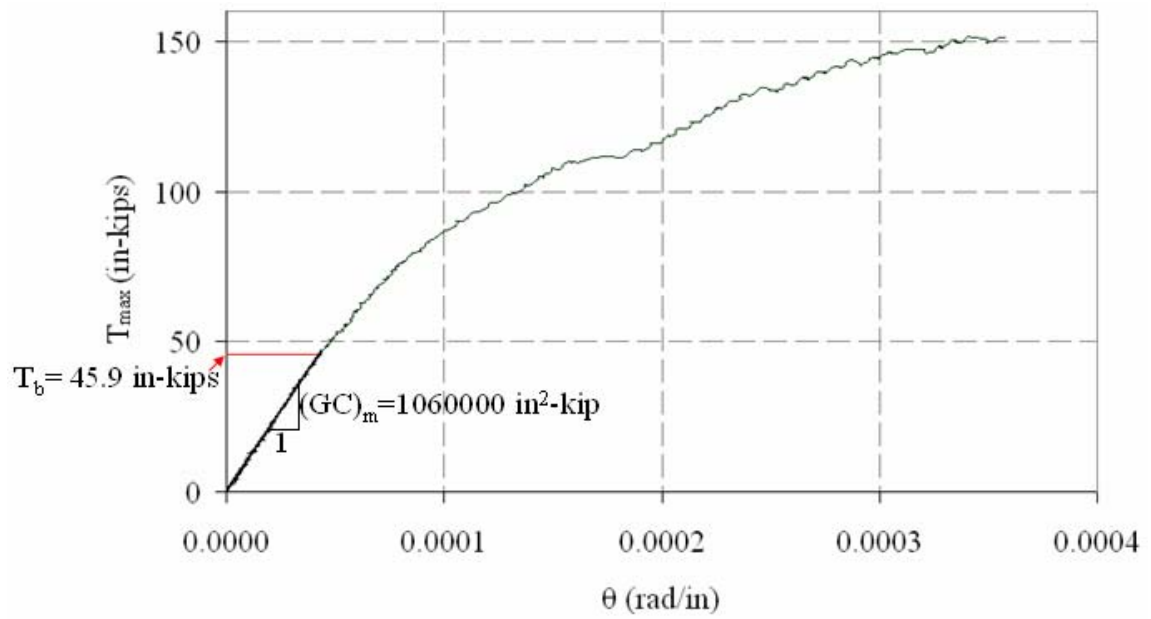


Figure D.22 –Experimental torque-twist curve of Specimen B44-1

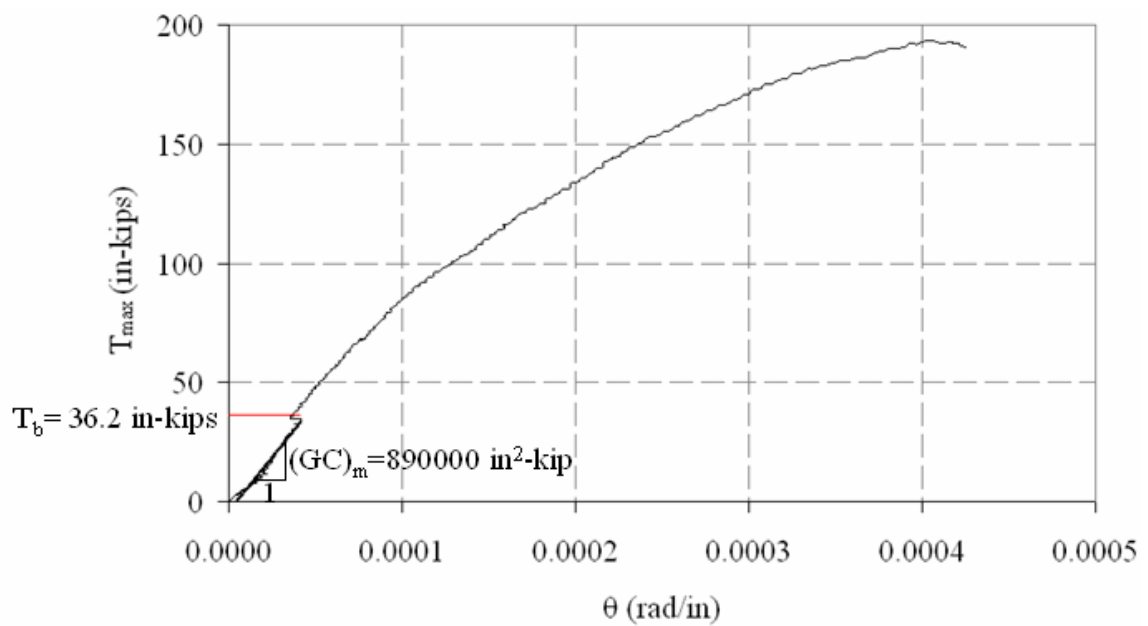


Figure D.23 –Experimental torque-twist curve of Specimen B44-2

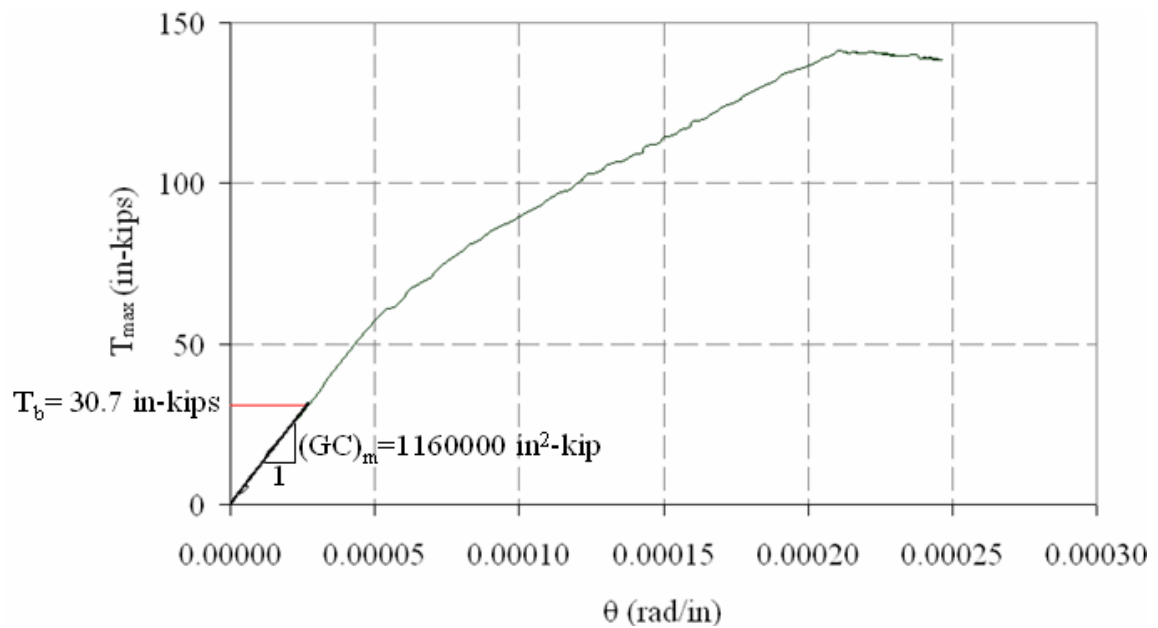


Figure D.24 –Experimental torque-twist curve of Specimen B44-3

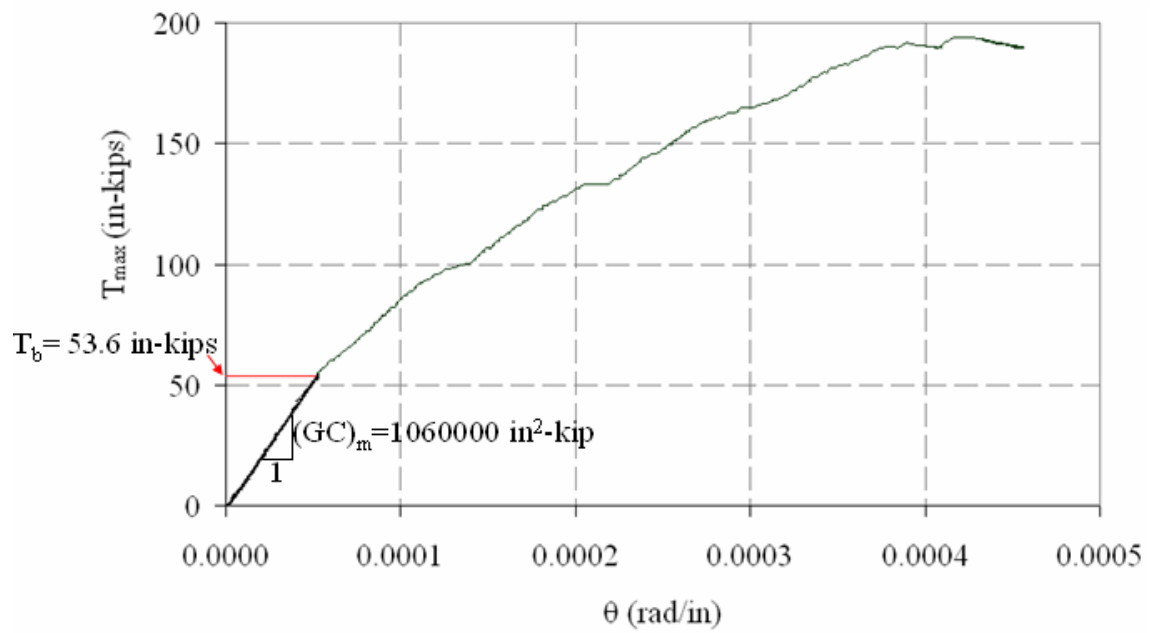


Figure D.25– Experimental torque-twist Curve of Specimen B36L-1

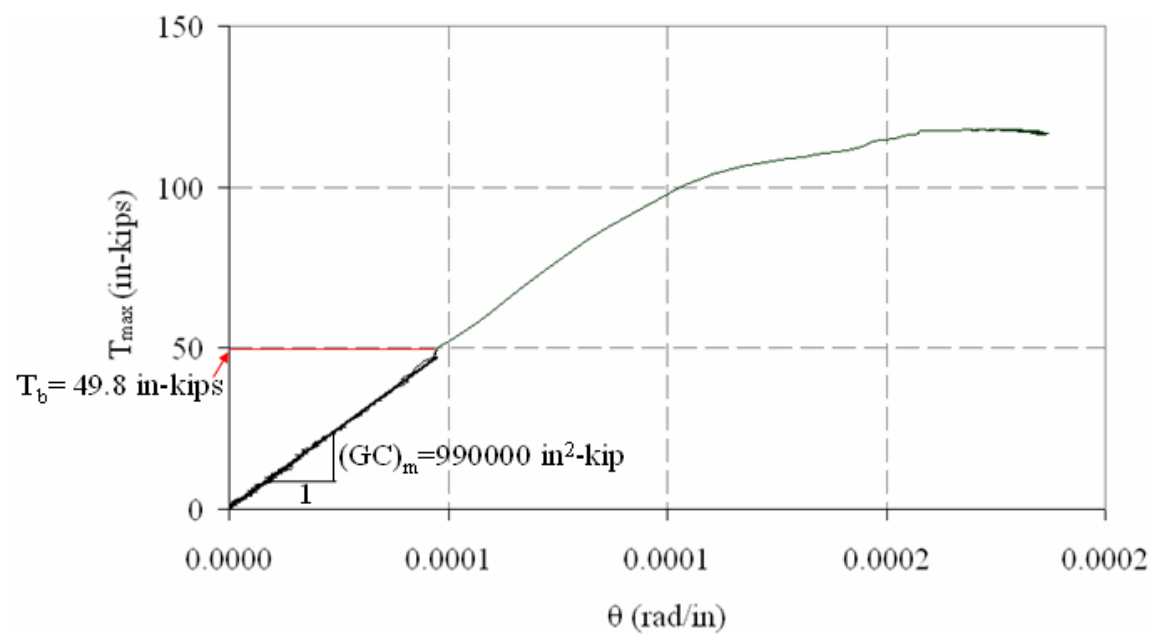


Figure D.26– Experimental torque-twist curve of Specimen B36L-2

## APPENDIX E

### METHOD FOR THE EVALUATION OF THE CENTROIDAL DEFLECTIONS AND ROTATION OF A BEAM

This appendix presents the approach presented by Zhao (1994) and extended by Stoddard (1997), which was used in the present study to convert the coupled deflection measurements from the potentiometers into in-plane and out-of-plane deflections and rotations at the shear center (centroid in rectangular sections).

The direction at which the beam buckles changes the geometric relations. Therefore, the equations given by Stoddard (1997) were modified to account for the direction of buckling. In the present study, a beam experiencing out-of-plane deformations towards the lateral potentiometers is assumed to buckle in positive direction (Figure E.1). Conversely, buckling away from the lateral potentiometers is defined as buckling in negative direction. Equations corresponding to the both directions of buckling are presented here.

At the beginning of the test, two potentiometers, T and B (denoting the top and bottom potentiometers, respectively) were positioned horizontally while a third potentiometer, V (denoting the vertical potentiometer) was positioned vertically as shown in Figure E.1.

$u_c$ ,  $v_c$  and  $\varphi_c$  are the out-of-plane and in-plane deflections and the angle of twist at shear center, respectively.  $T_o$ ,  $B_o$  and  $V_o$  are the initial string lengths while  $T_f$ ,  $B_f$  and  $V_f$  are the final string lengths of potentiometers T, B and V, respectively. The lateral and vertical deflections of the point  $B_p$  are denoted as  $B_x$  and  $B_y$ , respectively. Using the

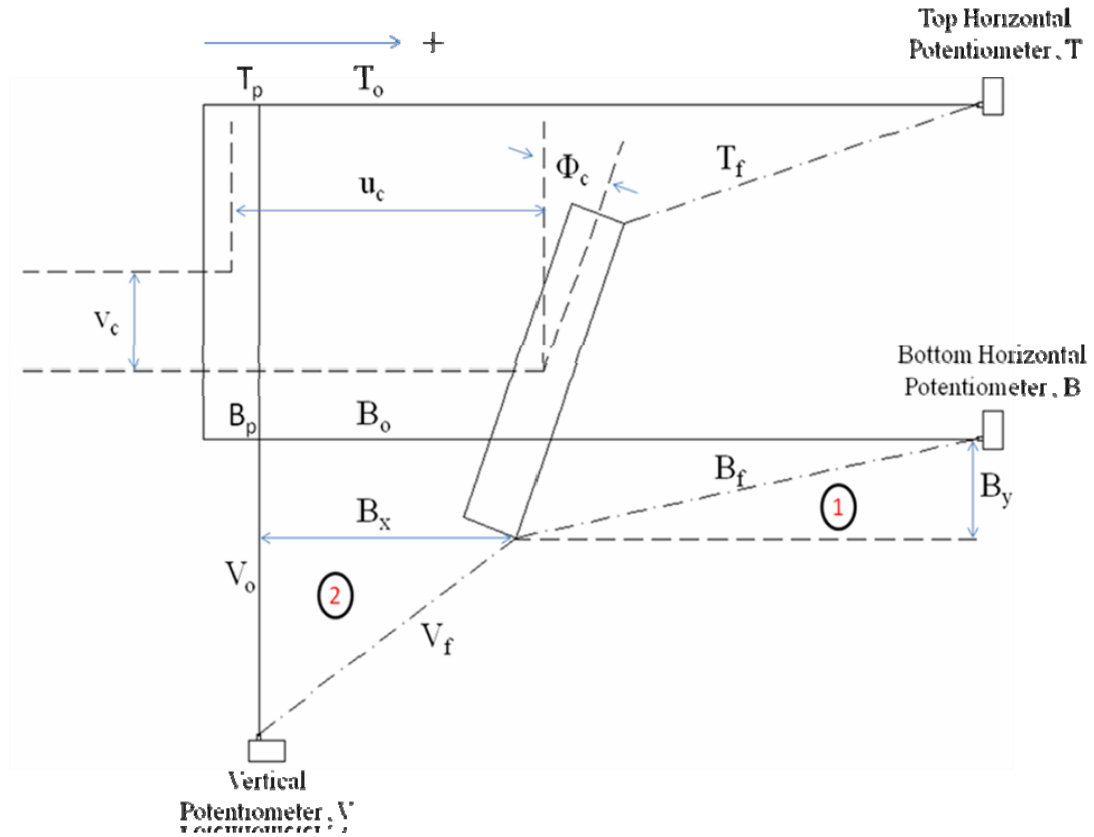


Figure E.1 – Potentiometer configuration in the test

Pythagorean theorem for triangles 1 and 2 (Figure E.1), Equations (E.1) and (E.2) are obtained.

$$(B_o - B_x)^2 + B_y^2 = B_f^2 \quad (E.1)$$

$$(V_o - B_y)^2 + B_x^2 = V_f^2 \quad (E.2)$$

When the beam buckles in negative direction, Equation (E.3) should be used instead of Equation (E.1) while Equation (E.2) remains unchanged.

$$(B_o + B_x)^2 + B_y^2 = B_f^2 \quad (E.3)$$



The solution of Equations (E.1) and (E.2) yields two sets of solution,  $(B_{x1}, B_{y1})$  and  $(B_{x2}, B_{y2})$ .

$$B_{x1} = \frac{B_o \cdot A_1 - V_o \cdot A_2}{A_3} \quad (\text{E.4})$$

$$B_{y1} = \frac{V_o \cdot A_1 - B_o \cdot A_2}{A_3} \quad (\text{E.5})$$

$$B_{x2} = \frac{B_o \cdot A_1 + V_o \cdot A_2}{A_3} \quad (\text{E.6})$$

$$B_{y2} = \frac{V_o \cdot A_1 + B_o \cdot A_2}{A_3} \quad (\text{E.7})$$

where,

$$A_1 = B_o^2 + V_o^2 - B_f^2 + V_f^2 \quad (\text{E.8})$$

$$A_2 = \sqrt{\frac{-B_o^4 - B_f^4 - V_o^4 - V_f^4 + 2 \cdot B_o^2 \cdot (B_f^2 - V_o^2 + V_f^2) + 2 \cdot B_f^2 \cdot (V_o^2 + V_f^2)}{+2 \cdot V_o^2 \cdot V_f^2}} \quad (\text{E.9})$$

$$A_3 = 2 \cdot (B_o^2 + V_o^2) \quad (\text{E.10})$$

$$A_4 = B_o^2 + V_o^2 + B_f^2 - V_f^2 \quad (\text{E.11})$$

Similarly, the solution of Equations (E.2) and (E.3) yields,

$$B_{x3} = \frac{-B_o \cdot A_1 - V_o \cdot A_2}{A_3} \quad (\text{E.12})$$

$$B_{y3} = \frac{V_o \cdot A_1 + B_o \cdot A_2}{A_3} \quad (\text{E.13})$$

$$B_{x4} = \frac{-B_o \cdot A_1 + V_o \cdot A_2}{A_3} \quad (\text{E.14})$$

$$B_{y4} = \frac{V_o \cdot A_4 - B_o \cdot A_2}{A_3} \quad (\text{E.15})$$

After calculating  $B_x$  and  $B_y$ , the angle of twist in the beam can be obtained from the unbuckled and buckled configurations of the beam. In Figure E.2, edges of triangle 1 are determined from geometry. Using the Pythagorean theorem for the triangle, Equation (E.16) is developed.

$$\begin{aligned} & \left[ B_o - \left( B_x - \left( \frac{b}{2} \right) \cdot \cos \phi_c \right) - \left( h \cdot \sin \phi_c + \left( \frac{b}{2} \right) \cdot \cos \phi_c \right) \right]^2 \\ & + \left[ \left( B_y - \left( \frac{b}{2} \right) \cdot \sin \phi_c \right) + h \cdot (1 - \cos \phi_c) + \left( \frac{b}{2} \right) \cdot \sin \phi_c \right]^2 = T_f^2 \end{aligned} \quad (\text{E.16})$$

Equation (E.16) can be simplified to become

$$\left[ B_o - B_x - h \cdot \sin \phi_c \right]^2 + \left[ B_y + h \cdot (1 - \cos \phi_c) \right]^2 = T_f^2 \quad (\text{E.17})$$

When the beam buckles in the negative direction, Equation (E.17) changes to Equation (E.18).

$$\left[ B_o + B_x + h \cdot \sin \phi_c \right]^2 + \left[ B_y + h \cdot (1 - \cos \phi_c) \right]^2 = T_f^2 \quad (\text{E.18})$$

The solution of Equation (E.17) yields

$$\phi_{c1} = a \tan 2 \left[ \frac{1}{2} \cdot \frac{C_a + \sqrt{D_a \cdot E_a}}{F_a}, \frac{1}{2} \cdot \frac{G_a - (h + B_y) \cdot \sqrt{D_a \cdot E_a}}{F_a \cdot \sqrt{D_a}} \right] \quad (\text{E.19})$$

Figure E.2 – Angle of twist calculations

$$E_a = \begin{pmatrix} -B_x^4 + 4 \cdot B_o \cdot B_x^3 - 6 \cdot B_o^2 \cdot B_x^2 - 2 \cdot B_x^2 \cdot B_y^2 + 2 \cdot B_x^2 \cdot T_f^2 \\ -4 \cdot h \cdot B_x^2 \cdot B_y + 4 \cdot B_o \cdot B_x \cdot B_y^2 - 4 \cdot B_o \cdot B_x \cdot T_f^2 \\ + 8 \cdot h \cdot B_o \cdot B_x \cdot B_y + 4 \cdot B_o^3 \cdot B_x + 4 \cdot h \cdot B_y \cdot T_f^2 \\ -4 \cdot h \cdot B_o^2 \cdot B_y - 2 \cdot B_o^2 \cdot B_y^2 - 4 \cdot h \cdot B_y^3 + 2 \cdot B_y^2 \cdot T_f^2 \\ + 4 \cdot h^2 \cdot T_f^2 - 4 \cdot h^2 \cdot B_y^2 + 2 \cdot B_o^2 \cdot T_f^2 - B_o^4 - B_y^4 - T_f^4 \end{pmatrix} \quad (\text{E.23})$$

$$F_a = \left( h^2 + B_y^2 + 2 \cdot B_y \cdot h + B_o^2 + B_x^2 - 2 \cdot B_o \cdot B_x \right) \cdot h \quad (\text{E.24})$$

$$G_a = \begin{pmatrix} -4 \cdot h^2 \cdot B_o \cdot B_x + 2 \cdot h^2 \cdot B_o^2 + 2 \cdot h^2 \cdot B_x^2 + B_o^4 \\ + B_x^4 - 4 \cdot B_o^3 \cdot B_x + 6 \cdot B_o^2 \cdot B_x^2 + B_o^2 \cdot B_y^2 \\ + 2 \cdot h \cdot B_o^2 \cdot B_y - B_o^2 \cdot T_f^2 - 4 \cdot B_o \cdot B_x^3 + B_x^2 \cdot B_y^2 \\ + 2 \cdot h \cdot B_x^2 \cdot B_y - B_x^2 \cdot T_f^2 - 2 \cdot B_o \cdot B_x \cdot B_y^2 \\ - 4 \cdot h \cdot B_o \cdot B_x \cdot B_y + 2 \cdot B_o \cdot B_x \cdot T_f^2 \end{pmatrix} \quad (\text{E.25})$$

It is to be noted that the roots of Equation (E.18) can be obtained by changing the signs of the terms containing  $B_x$  in Equations (E.21) to (E.25).

Finally, the lateral and vertical displacements of the shear center ( $u_c$  and  $v_c$ ) are determined from the following geometric relations in terms of the angle of twist at the shear center ( $\phi_c$ ) and the lateral and vertical displacements of point  $B_p$  ( $B_x$  and  $B_y$ ):

$$u_c = B_x + \frac{h}{2} \cdot \sin \phi_c + \frac{b}{2} (1 - \cos \phi_c) \quad (\text{E.26})$$

$$v_c = B_y + \frac{h}{2} \cdot (1 - \cos \phi_c) - \frac{b}{2} \sin \phi_c \quad (\text{E.27})$$

$$u_c = B_x + \frac{h}{2} \cdot \sin \phi_c + \frac{b}{2} (1 + \cos \phi_c) \quad (\text{E.28})$$

$$v_c = B_y + \frac{h}{2} \cdot (1 - \cos \phi_c) + \frac{b}{2} \sin \phi_c \quad (\text{E.29})$$

Equations (E.26) and (E.27) are valid when the beam buckles in the positive direction (Figure E.3) while Equations (E.28) and (E.29) are used when the beam buckles in the negative direction.

For each set of  $(B_x, B_y)$ , two different twist angles are obtained according to Equations (E.19) and (E.20). Similarly, two different sets of out-of-plane and in-plane centroidal deflections are calculated using Equations (E.26) to (E.29) for each set of  $(B_x, B_y)$ . Since two different sets of roots are obtained by solving Equations (E.1) and (E.2), there are four different sets of deflection and rotation values of the centroid. To choose the correct solution set, each set was compared to the deflection measurements taken by the string potentiometers. The solution set in closest agreement with the experimental data was chosen.



## APPENDIX F

### CRITICAL MOMENT CALCULATIONS OF THE SPECIMENS

This appendix presents the procedures used in the critical moment calculations of the specimens. Each section presents the critical load calculations according to one of the methods described in Chapter VII. The equations used in the calculations are shown on the left halves of the following pages. On the right halves of the pages, on the other hand, the equations and the meaning of the terms used in the equations are explained.

The critical and ultimate load calculations presented in Sections F.2 to F.5 require an iterative procedure because of the interdependence of the variables. The iterative procedure was carried out through the programming tools of Mathcad 14.0 (2005). The programs used in the iterative procedure are given in Section F.2.

In this appendix,  $\varepsilon_c$  denotes the extreme compression fiber strain of a beam at midspan.

#### F.1 Critical Load Calculations Assuming that a Reinforced Concrete Beam is an Elastic and Homogeneous Body, Free from Cracking

$$B_{eh} = E_c \cdot \left( \frac{1}{12} \cdot b^3 \cdot h \right)$$

Lateral flexural rigidity of the entire beam section with elastic material behavior

$$E_c$$

Elastic modulus of concrete obtained from cylinder tests

$$b, h, L$$

Width, depth and span length of the beam, respectively

$$\beta_c = \frac{1}{3} \cdot \left( 1 - \frac{192}{\pi^5} \cdot \frac{b}{h} \cdot \sum_{n=0}^{\infty} \frac{1}{(2n+1)^5} \cdot \tanh \frac{(2n+1)\pi h}{2b} \right)$$

Coefficient for St. Venant's torsional constant

$$G_c = \frac{E_c}{2 \cdot (1 + \nu)}$$

Modulus of rigidity of concrete

$\nu$

Poisson's ratio of concrete from material tests

$$(GC)_u = \beta_c \cdot b^3 \cdot h \cdot G_c$$

Uncracked torsional rigidity of the beam according to St. Venant's theory

$$M_{el} = \frac{C_1}{C_2 \cdot L} \cdot \left( 1 - 1.74 \cdot \frac{e}{L} \sqrt{\frac{B_{eh}}{(GC)_u}} \right) \cdot \sqrt{B_{eh} \cdot (GC)_u}$$

Critical moment of a beam

$$C_1 = 4.23$$

The loading factor for a beam loaded with a single concentrated load at midspan

$$C_2 = 1.00$$

The effective length factor accounting for the simple support conditions in and out of plane

$$\left( 1 - 1.74 \cdot \frac{e}{L} \sqrt{\frac{B_{eh}}{(GC)_u}} \right)$$

The expression accounting for the destabilizing effect of the load, applied above the centroid of the beam section

$$P_{el} = \frac{4}{L} \cdot (M_{el} - M_s)$$

The critical load of a beam by also taking into account the self-weight of the beam

$$M_s$$

Bending Moment at Midspan Originating from the Self-Weight of the Beam

## F.2 Critical Load Calculations according to Hansell and Winter's (1959) Formulation

The critical moment calculations according to Hansell and Winter (1959) require an iterative procedure. Using an analogy with the tangent modulus theory in inelastic buckling of columns, Hansell and Winter (1959) stated that the secant modulus of elasticity of concrete corresponding to the strain at the extreme compression fibers is the modulus of the compression zone of a beam section in bending. Since the secant modulus



( $E_{sec}$ ) depends on the extreme compression fiber strain ( $\epsilon_c$ ),  $E_{sec}$  was denoted as a function of  $\epsilon_c$  in the calculations,  $E_{sec}(\epsilon_c)$ .

According to Hansell and Winter (1959), the lateral bending rigidity ( $B_{hw}$ ) and the torsional rigidity ( $C_{hw}$ ) of a reinforced concrete beam is provided by the compression zone only. Ignoring the rotations in the neutral axis of a section due to the twisting rotations in the beam, the compression zone is a rectangular area ( $b \times c$ ).

The neutral axis depth ( $c$ ) of the beam section and the strain at the extreme compression fibers ( $\epsilon_c$ ) depend on the critical moment ( $M_{hw}$ ). To calculate  $M_{hw}$ , the lateral bending rigidity ( $B_{hw}$ ) and the torsional rigidity ( $C_{hw}$ ) of a beam are needed. Since  $B_{hw}$  and  $C_{hw}$  are functions of  $c$  and  $\epsilon_c$ , there is interdependence between  $M_{hw}$  and  $c$ ,  $\epsilon_c$ . To calculate  $M_{hw}$ ,  $c$  and  $\epsilon_c$ , programming tools of Mathcad 13.0 (2005) were used.  $c$  and  $\epsilon_c$  were obtained from the following programs:

```

c := | for  $\epsilon_c \in 0.0001, 0.0002 \dots 0.0035$ 
      |
      | c ← 0.002in
      | while  $\left| c - \frac{A_s \cdot E_s \cdot \epsilon_s(c, \epsilon_c)}{0.5 f_c(\epsilon_c) \cdot b} \right| > 10^{-5} \text{in} \wedge (c < 100 \text{in})$  if  $\epsilon_s(c, \epsilon_c) > \epsilon_y$ 
      |   c ← c + 0.0001in
      |    $\frac{A_s \cdot f_y}{0.5 f_c(\epsilon_c) \cdot b}$  otherwise
      | break if  $M_{hw}(\epsilon_c, c) - A_s \cdot E_s \cdot \epsilon_s(c, \epsilon_c) \cdot \left( d - \frac{c}{3} \right) < 10 \text{lb} \cdot \text{in}$  if  $\epsilon_s(c, \epsilon_c) < \epsilon_y$ 
      | break if  $M_{hw}(\epsilon_c, c) - A_s \cdot f_y \cdot \left( d - \frac{c}{3} \right) < 10 \text{lb} \cdot \text{in}$  if  $\epsilon_s(c, \epsilon_c) > \epsilon_y$ 
      | return c

```

■

```

 $\varepsilon_c :=$ 
  for  $\varepsilon_c \in 0.0001, 0.0002 \dots 0.0035$ 
     $c \leftarrow$ 
       $c \leftarrow 0.002\text{in}$ 
      while  $\left| c - \frac{A_s \cdot E_s \cdot \varepsilon_s(c, \varepsilon_c)}{0.5 f_c(\varepsilon_c) \cdot b} \right| > 10^{-5}\text{in} \wedge (c < 100\text{in})$  if  $\varepsilon_s(c, \varepsilon_c) > \varepsilon_y$ 
         $c \leftarrow c + 0.0001\text{in}$ 
         $\frac{A_s \cdot f_y}{0.5 f_c(\varepsilon_c) \cdot b}$  otherwise
      break if  $M_{hw}(\varepsilon_c, c) - A_s \cdot E_s \cdot \varepsilon_s(c, \varepsilon_c) \cdot \left(d - \frac{c}{3}\right) < 10\text{lb}\cdot\text{in}$  if  $\varepsilon_s(c, \varepsilon_c) < \varepsilon_y$ 
      break if  $M_{hw}(\varepsilon_c, c) - A_s \cdot f_y \cdot \left(d - \frac{c}{3}\right) < 10\text{lb}\cdot\text{in}$  if  $\varepsilon_s(c, \varepsilon_c) > \varepsilon_y$ 
    return  $\varepsilon_c$ 

```

The expressions used in the programs are explained as follows:

$\varepsilon_s(c, \varepsilon_c)$

Strain in the centroid of the tension reinforcement, which is a function of  $c$  and  $\varepsilon_c$

$$f_c(\varepsilon_c) = \frac{f'_c \cdot \beta \cdot \left(\frac{\varepsilon_c}{\varepsilon_o}\right)}{\beta - 1 + \left(\frac{\varepsilon_c}{\varepsilon_o}\right)^{k \cdot \beta}}$$

Stress at the extreme compression fibers

$$\beta = \frac{1}{1 - \frac{f'_c}{\varepsilon_o \cdot E_c}} \quad \text{and} \quad k = \frac{0.00689 \cdot f'_c}{20}$$

The factor '0.00689' is used to convert the compressive strength in psi to MPa, since the stress-strain equation is given in terms of MPa.

The above stress-strain relationship is the stress-strain model proposed by Carreira and Chu (1985) for high-strength concrete. In Section 2.2 of this dissertation, Carreira and Chu's (1985) model was shown to be in perfect agreement with the experimental stress-strain curves of concrete used in the specimens. Therefore, the above equation was used in the critical moment calculations to link the strains in concrete to the stresses.

$\epsilon_y, f_y$

Yield strain and yield stress of the reinforcing steel, determined from material tests

$E_s$

Modulus of elasticity of the reinforcing steel, determined from material tests

$$M_{hw}(\epsilon_c, c) = \left( \frac{4.23}{L} \cdot \sqrt{B_{hw}(\epsilon_c, c) \cdot (GC)_{hw}(\epsilon_c, c)} \right) \left( 1 - 0.74 \cdot \frac{e}{L} \cdot \sqrt{\frac{B_{hw}(\epsilon_c, c)}{(GC)_{hw}(\epsilon_c, c)}} \right)$$

Critical moment, which is a function of  $c$  and  $\epsilon_c$

$$B_{hw}(\epsilon_c, c) = E_{sec}(\epsilon_c) \cdot \frac{b^3 \cdot c}{12}$$

The lateral bending rigidity expression proposed by Hansell and Winter (1959)

$$(GC)_{hw}(\epsilon_c, c) = \frac{E_{sec}(\epsilon_c)}{2 \cdot (1 + \nu)} \cdot \left[ \frac{b^3 \cdot c}{3} \cdot \left( 1 - 0.35 \cdot \frac{b}{d} \right)^2 \right]$$

The torsional rigidity expression according to Hansell and Winter (1959)

$$E_{sec}(\epsilon_c) = \frac{f_c(\epsilon_c)}{\epsilon_c}$$

The secant modulus is the slope of the line connecting the point  $(\epsilon_c, f_c)$  on the stress-strain curve to the origin

$$P_{hw} = \frac{4}{L} \cdot (M_{hw} - M_s)$$

The critical load of the beam

The programs run until there is a negligible difference between the bending moment obtained from the critical moment expression  $[M_{hw}(\epsilon_c, c)]$  and the bending moment obtained from the stress distribution in the cross-section. The strain measurements in the experiments indicated that all compression fibers in the specimens were stressed within the elastic limit of concrete (elastic lateral torsional buckling). Therefore, bending moment resistance of the beam section was calculated based on a triangular stress distribution in the compression zone of the section.

### F.3 Critical Load Calculations according to Sant and Bletzacker's (1961) Formulation

When calculating the critical load of a beam from the formula proposed by Sant and Bletzacker (1961), an iterative procedure is needed. Therefore, the programs for  $c$  and  $\epsilon_c$ , shown in Section F.2, are used in the critical moment calculations based on Sant and Bletzacker's (1961) formulation.

Sant and Bletzacker (1961) suggested that the reduced modulus of elasticity ( $E_r$ ) corresponding to the extreme compression fiber strain ( $\epsilon_c$ ) is the modulus of a beam section at the instant of buckling. The reduced modulus theory assumes that a portion of the beam (the convex side) undergoes unloading while the remaining portion of the beam (the concave side) is further loaded when the beam buckles. The lateral bending rigidity ( $B_{sb}$ ) and the torsional rigidity ( $C_{sb}$ ) expressions proposed by Sant and Bletzacker (1961) include the reduced modulus of elasticity ( $E_r$ ) as the material term.

The following discussion presents the equations proposed by Sant and Bletzacker (1961) and important details from the calculation procedure:

$$M_{sb}(\epsilon_c, c) = \left( \frac{\frac{4.23}{L} \cdot \sqrt{B_{sb}(\epsilon_c, c) \cdot (GC)_{sb}(\epsilon_c, c)}}{\left( 1 - 3.48 \cdot \frac{e}{L} \cdot \sqrt{\frac{B_{sb}(\epsilon_c, c)}{(GC)_{sb}(\epsilon_c, c)}} \right)} \right) \quad \begin{array}{l} \text{Critical moment expression} \\ \text{proposed by Sant and Bletzacker} \\ \text{(1961)} \end{array}$$

$$\left( 1 - 3.48 \cdot \frac{e}{L} \cdot \sqrt{\frac{B_{sb}(\epsilon_c, c)}{(GC)_{sb}(\epsilon_c, c)}} \right)$$

The expression accounting for the location of the load application point with respect to the centroid of the beam section, given by Sant and Bletzacker (1961)

$$B_{sb}(\epsilon_c) = E_r(\epsilon_c) \cdot \frac{b^3 \cdot d}{12}$$

The lateral bending rigidity expression proposed by Sant and Bletzacker (1961)

$$(GC)_{sb}(\epsilon_c) = \frac{E_r(\epsilon_c)}{2 \cdot (1 + \nu)} \cdot \frac{b^3 \cdot d}{3}$$

$$E_r(\epsilon_c) = \frac{4 \cdot E_c \cdot E_{\tan}(\epsilon_c)}{\left(\sqrt{E_c} + \sqrt{E_{\tan}(\epsilon_c)}\right)^2}$$

$$E_{\tan}(\epsilon_c) = \frac{d}{d\epsilon_c} [f_c(\epsilon_c)]$$

The torsional rigidity expression proposed by Sant and Bletzacker (1961)

Reduced modulus of elasticity of concrete which is a geometric average of the elastic modulus ( $E_c$ ) and the tangent modulus of elasticity [ $E_{tan}(\epsilon_c)$ ] corresponding to the extreme compression fiber strain

Tangent modulus of elasticity is the slope of the line tangent to the stress-strain curve at the point corresponding to the extreme compression fibers.

#### F.4 Critical Load Calculations according to Massey's (1967) Formulation

The iterative procedure explained in Section F.2 is used in the critical moment calculations based on the formula proposed by Massey (1967). Similar to Hansell and Winter (1959), Massey (1967) used the secant modulus theory. However, Massey (1967) also included the contributions of the longitudinal and shear reinforcement of a beam to the lateral bending and torsional rigidity expressions. The following discussion presents the equations proposed by Massey (1967) and important details from the calculation procedure:

$$M_m(\epsilon_c, c) = \left( \frac{4.23}{L} \cdot \sqrt{B_m(\epsilon_c, c) \cdot (GC)_m(\epsilon_c, c)} \right) \left( 1 - 1.74 \cdot \frac{e}{L} \cdot \sqrt{\frac{B_m(\epsilon_c, c)}{(GC)_m(\epsilon_c, c)}} \right)$$

Critical moment, which is a function of  $c$  and  $\epsilon_c$

$$B_m(\epsilon_c, c) = E_{\text{sec}}(\epsilon_c) \cdot \frac{b^3 \cdot c}{12} + E_s \cdot \Sigma I_{sy}$$

The lateral bending rigidity expression proposed by Massey (1967)

$$E_s \cdot \Sigma I_{sy}$$

The contribution of the longitudinal reinforcement to the lateral bending rigidity. When steel yields,  $E_s = 0$ .

$$(GC)_m(\varepsilon_c) = \left( \begin{aligned} &\beta_c \cdot b^3 \cdot h \cdot G'_c(\varepsilon_c) + \\ &\frac{1}{3} \cdot [G_s - G'_c(\varepsilon_c)] \cdot \Sigma b_s^3 \cdot t_s + \\ &\frac{\gamma \cdot b_1^2 \cdot d_1 \cdot A_o \cdot E_s}{2 \cdot \sqrt{2} \cdot s} \end{aligned} \right)$$

The torsional rigidity expression proposed by Massey (1967)

$$G'_c(\varepsilon_c) = \frac{E_{sec}(\varepsilon_c)}{2 \cdot (1 + \nu)}$$

The reduced modulus of rigidity of concrete

$$\frac{1}{3} \cdot [G_s - G'_c(\varepsilon_c)] \cdot \Sigma b_s^3 \cdot t_s$$

Contribution of the Longitudinal Reinforcement to the Torsional Rigidity

$$\frac{\gamma \cdot b_1^2 \cdot d_1 \cdot A_o \cdot E_s}{2 \cdot \sqrt{2} \cdot s}$$

Contribution of the Shear Reinforcement to the Torsional Rigidity

$$b_s, t_s$$

Width and thickness of the longitudinal reinforcement layer, respectively, as illustrated in Figure 1.18

$$b_1, t_1$$

Width and depth of the cross-sectional area enclosed by a closed stirrup, respectively (Figure 1.18)

$$A_o, s$$

Cross-sectional area of one leg of a stirrup and spacing of the stirrups, respectively

$$\gamma$$

a constant defined by Cowan (1953)

## F.5 Ultimate Load Calculations according to the Proposed Method

Different from the other methods, the method proposed in the present study accounts for the reduction in the ultimate load of a beam due to sweep. First, the critical moment of a reinforced concrete beam is calculated using the lateral bending and torsional rigidity expressions proposed in the present study. The critical load corresponds to the

geometrically perfect configuration of the beam. Next, the limit load of the imperfect beam is calculated by reducing the critical load an amount equal to the influence of the sweep on the load-carrying capacity. The equations used in the proposed method are as follows:

$$M_p(\varepsilon_c, c) = \left( \frac{4.23}{L} \cdot \sqrt{B_o(\varepsilon_c, c) \cdot (GC)_o(\varepsilon_c)} \right) \left( 1 - 1.74 \cdot \frac{e}{L} \cdot \sqrt{\frac{B_p(\varepsilon_c, c)}{(GC)_o(\varepsilon_c)}} \right)$$

Critical moment, which is a function of  $c$  and  $\varepsilon_c$

$$B_o(\varepsilon_c, c) = \left[ \frac{b^3 \cdot c}{12} \cdot \frac{1}{1 + \left( \frac{\omega \cdot M_{cra}}{M_p} \right)^2 \cdot \left( \frac{c}{h} - 1 \right)} \right] \cdot \left[ \frac{E_{sec}(\varepsilon_c) + E_c}{2} \right]$$

The lateral bending rigidity expression proposed in the present study

$$(GC)_o(\varepsilon_c) = \left[ \frac{E_{sec}(\varepsilon_c) + E_c}{4 \cdot (1 + \nu)} \right] \cdot \left[ \frac{b^3 \cdot h}{3} \cdot \left( 1 - 0.63 \cdot \frac{b}{h} \right) \right]$$

The torsional rigidity expression proposed in the present study

$$M_{cra}$$

Cracking moment of the beam

$$\omega = \begin{cases} 2/3 & \text{in the presence of shrinkage cracks} \\ 1 & \text{in the absence of shrinkage cracks} \end{cases}$$

The factor accounting for the reduction in the lateral bending rigidity in the presence of shrinkage cracks

$$P_p = (M_p - M_s) \cdot \frac{4}{L}$$

Critical load corresponding to the geometrically perfect configuration of the beam

$$P_{ult} = P_p - \frac{u_{to} \cdot (48 \cdot E_c \cdot I_y)}{\sin(\phi_{ult}) \cdot L^3}$$

Limit load of the beam with a sweep of  $u_{to}$  at the top of the beam at midspan

$$\frac{u_{to} \cdot (48 \cdot E_c \cdot I_y)}{\sin(\phi_{ult}) \cdot L^3}$$

Reduction in the buckling load due to sweep

$$I_y = \frac{1}{12} \cdot b^3 \cdot h$$

Second moment of area of the beam section about the minor axis

$$\phi_{ult}$$

The angle of twist of the beam at midspan at the instant when  $P_{ult}$  is reached. A value of 0.60 degrees was found to be appropriate for most of the beams.

The above equations indicate that the rigidity expressions [ $B_p$  and  $(GC)_p$ ] and the critical moment ( $M_p$ ) are interdependent. Therefore, the iterative approach, summarized in Section F.2, is used to calculate the neutral axis depth ( $c$ ) and the extreme compression fiber strain ( $\epsilon_c$ ) at midspan at the instant when buckling initiates. Then, the critical moment ( $M_p$ ) and the limit load ( $P_{ult}$ ) are obtained.



## **APPENDIX G**

### **CONSTRUCTION DETAILS OF THE SPECIMENS**

This appendix presents some specific details about the specimens of the experimental program.

#### **G.1 Compression Reinforcement**

Lateral torsional buckling arises from the differential behaviors of the tension and compression sides of a beam. The compression side of a beam is subjected to compressive stresses from in-plane bending. When the compressive stresses reach critical levels, the compression side of the beam buckles out of plane. The tension side of the beam, on the other hand, tends to remain stable. The out-of-plane deformations of the compression side cause the tension side to deform out of plane due to the integrity of the beam. However, the out-of-plane deformations of the tension side are much smaller than the deformations of the compression side as a result of the stabilizing effect of the tensile stresses from in-plane bending. The differential out-of-plane deformations along the depth of the beam result in the rotation of the beam about its longitudinal axis. Hence, lateral torsional buckling creates out-of-plane deformations and torsional rotations in a beam.

The stresses in the compression side of a beam are the main cause for lateral torsional buckling. Increasing the out-of-plane bending rigidity of the compression side can restrain the excessive lateral deformations of the compression side, which can indeed prevent lateral torsional buckling. Compression reinforcement contributes to the lateral

bending rigidity of the compression side. Konig and Pauli (1990) indicated experimentally that the compression reinforcement significantly increases the buckling load of a reinforced concrete beam and decreases the out-of-plane deflections of the compression side at buckling. Considering the stabilizing effect of the compression reinforcement, the specimens of the present experimental program did not contain compression reinforcement to ensure that the beams failed in lateral torsional buckling.

The shear reinforcement of the specimens was composed of two layers of welded wire reinforcement (WWR), separated by the longitudinal reinforcing bars (Figure G.1). Due to the lack of compression reinforcement in the beams, spacers were needed to maintain the distance between the WWR sheets in the compression side. For this purpose, spacers cut from reinforcing bars were placed between the WWR sheets (Figure G.1). The lengths of the spacers were smaller than the development lengths of the reinforcing bars, from which the spacers were cut.

## **G.2 Tilt-up and Lifting Mechanisms of the Specimens**

The concrete beams of the present experimental program were cast on their sides to facilitate the mechanical vibration of concrete and to ensure the spread of concrete into the entire form, flowing around the congested reinforcement. A mechanism was needed to tilt up the beams, leaning on their sides, and move them to the test setup using the crane.

Two different lifting systems were used in the two stages of the experimental program. Each of the lifting points in the first set of beams consisted of a headed cast-in-place anchor embedded 7 inches into concrete (Figure G.2). Two lifting points in Beams



Figure G.1 – Reinforcement in Specimen B36

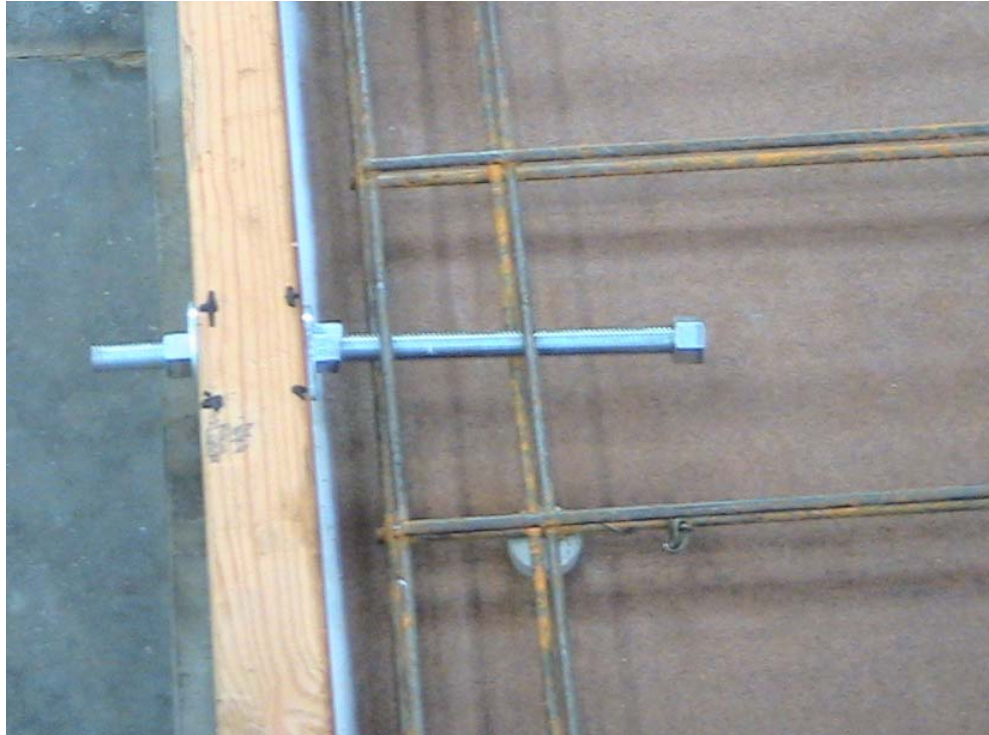


Figure G.2 – The Lifting mechanism in the first set of beams

B18 and B22 and four lifting points in Beams B30 and B36 provided adequate shear capacity to tilt up the beams and adequate tensile capacity to lift the beams.

The beams were lifted through cables attached to the beams at the lifting points. An important consideration for a beam hanging from cables is the angle of inclination of the cables lifting the beam. Stratford and Burgoyne (1999) found out that the buckling load of a concrete beam increases as the angle of inclination of the cables increase and the cables approach to the vertical orientation. Accordingly, the test beams were lifted with vertically-oriented cables when moving to the test setup. As shown in Figure G.3, the specimen was connected to a steel spreader beam with vertical ropes and the spreader beam was connected to the hook of the crane with inclined ropes.

Beams in Specimen Groups B44 and B36L were heavier than the first set of beams (B22, B18, B30 and B36). The lifting points used in the first set of beams were not able to provide adequate shear and tension capacity to tilt up and lift the second set of beams. Therefore, a new lifting point was designed and used in the second stage of the experiments.

The lifting points in the second set of beams were composed of a steel channel and two reinforcing bars welded to the channel. The channel section was included in the mechanism to resist the shear forces at the lifting points during the tilt-up process. The reinforcing bars, on the other hand, provided adequate tensile capacity for the lifting mechanisms while lifting the beams in the vertical position. A nut was welded to the inside of the channel, so that a bolt can be fixed to the lifting mechanism when connecting the lifting points to the crane.

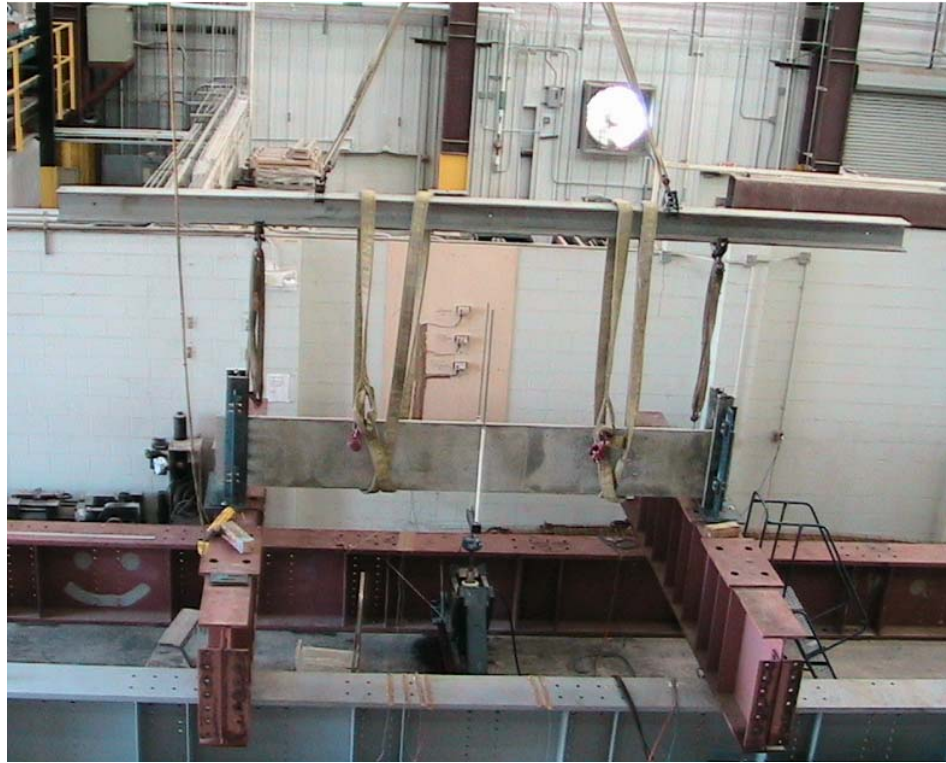


Figure G.3 – Use of spreader beams for lifting the beams

To tilt up and lift the specimens, swift lifting eyes (also known as hoist rings) were attached to the steel channels of the lifting mechanisms by means of high-strength steel bolts (Figure G.4). The bail of a swift lifting eye can pivot about the base of the eye in order to compensate for the direction of lifting. The ability of the bail to pivot about the base made it possible to tilt up and lift the beams continuously without the need for rearranging the lifting system between the tilt-up and lifting processes. The lifting mechanisms used in the specimens were designed according to ACI 318-05 (2005) Appendix D. Different failure mechanisms in the appendix were considered in the design of the lifting points to prevent any possible damage to the beams during the tilt-up and lifting processes.



Figure G.4 – The Lifting point in the second set of beams connected to the spreader beam



## APPENDIX H

### DETERMINATION OF THE EXPERIMENTAL BUCKLING LOADS OF THE SPECIMENS

This appendix introduces the techniques developed by Southwell (1932), Meck (1977) and Massey (1963) for determining the critical loads (limit loads in the case of geometrically imperfect beams) of beams by analyzing their experimental load-deflection data.

In elastic flexural buckling, Southwell plot is a common technique used to obtain the buckling load of a member from its experimental data. In an axially loaded column, for example, there is a linear relationship between  $u_c/P$  and  $u_c$ , where  $P$  is the axial load on the column and  $u_c$  is the lateral deflection at midlength of the column. The slope of the  $u_c/P$  vs.  $u_c$  plot is equal to  $1/P_{cr}$ , where  $P_{cr}$  is the critical load of the column.

Lateral torsional buckling, nevertheless, is more complicated than flexural buckling of columns. A beam subjected to lateral torsional buckling undergoes out-of-plane deformations and torsional rotations at the same time. Cheng and Yura (1988) used two different types of Southwell (1932) plots to analyze the data of their lateral buckling experiments on coped steel beams. Accordingly,  $u_c/P$  was plotted against  $u_c$  and  $\phi_c/P$  was plotted against  $\phi_c$ .  $u_c$  and  $\phi_c$  are the lateral centroidal deflection and the angle of twist at midspan, respectively and  $P$  is the concentrated load applied at midspan of the beam. Cheng and Yura (1988) found out that the critical loads obtained from both plots were almost the same for each specimen. However, the critical loads obtained from the  $u_c/P$  vs.  $u_c$  plots were used, since Cheng and Yura (1988) considered the lateral deflection data in

the tests more reliable than the twist data due to the localized distortions in the test beams.

Meck (1977) proposed the use of a “skewed” version of Southwell plot for lateral torsional buckling of beams. Accordingly,  $u_c/P$  should be plotted against  $\varphi_c$  and  $\varphi_c/P$  should be plotted against  $u_c$ . The geometric mean of the inverse slopes of the two plots gives the critical load ( $P_{cr}$ ).

Massey (1963) proposed a modification to the original Southwell (1932) plot to be applicable to lateral torsional buckling experiments. According to Massey (1963), the term  $P$  in the ordinates of the original Southwell (1932) plots should be replaced with  $P^2$  for the case of lateral torsional buckling. Similarly, Stratford and Burgoyne (1999) stated that a deflection/(load)<sup>2</sup> vs. deflection plot is more appropriate for a beam subject to lateral torsional buckling, based on the studies of Allen and Bulson (1980).

Mandal and Calladine (2002) investigated the use of classical Southwell (1932) plot and the modified versions of Southwell (1932) plot proposed by Meck (1977) and Massey (1963) in lateral torsional buckling experiments and reached several important conclusions. In their study, Mandal and Calladine (2002) analytically showed that the lateral deflection ( $u$ ) and the twist ( $\varphi$ ) of a beam are proportional to each other after the initial stages of loading in a lateral torsional buckling experiment. The direct coupling between  $u$  and  $\varphi$  becomes more pronounced as the load is increased. Consequently, the critical loads obtained from original Southwell (1932) plot and Meck’s (1977) “skewed” version of the Southwell (1932) plot should not be different to a major extent.

In a Southwell (1932) plot, the data points corresponding to the initial stages of loading do not lie on the straight line, which is formed by the majority of the data points.



According to Cheng and Yura (1988), the deviation of the initial points from the ultimate straight line is caused by the initial restraints in the test setup and other experimental errors which are more influential at the initial stages of loading when the applied load is small. Based on the analysis of the experimental data obtained by Cheng and Yura (1988), Mandal and Calladine (2002) found out that the deviation of the initial data points from the eventual straight line is greater in the Massey's (1963) version of the Southwell (1932) plot. This is most probably due to the use of  $P^2$  instead of  $P$  in Massey's (1963) plots.

For the sake of illustration, Figures H.1 to H.3 illustrate the standard Southwell (1932) plots and Meck's (1977) and Massey's (1963) versions of the Southwell plots, respectively, for Specimen B44-2.

Figures H.1 and H.2 agree with the observations of Cheng and Yura (1988), who considered the lateral deflection data in their tests more reliable. Almost all the data points in the first plot of Figure H.1 lie on a straight line. In the second plot of Figure H.1, nonetheless, the data points are too scattered, causing the determination of a straight line to be more complicated. In the Meck's (1977) version of the plots, the data points in both plots are scattered since the twist data is used in both of the plots. The experimental data of the other specimens showed the same characteristic. The large dispersion of the data points makes the determination of the experimental buckling load more difficult when the twist data is used in any version of the Southwell (1932) plot. Therefore, the use of lateral deflection data in the original Southwell (1932) plot is considered easier and more reliable in the determination of the experimental buckling load of a reinforced

concrete beam. The dispersion in the twist data might have been caused by the distortions in the beams, particularly in the midspan region close to the point of application of load.

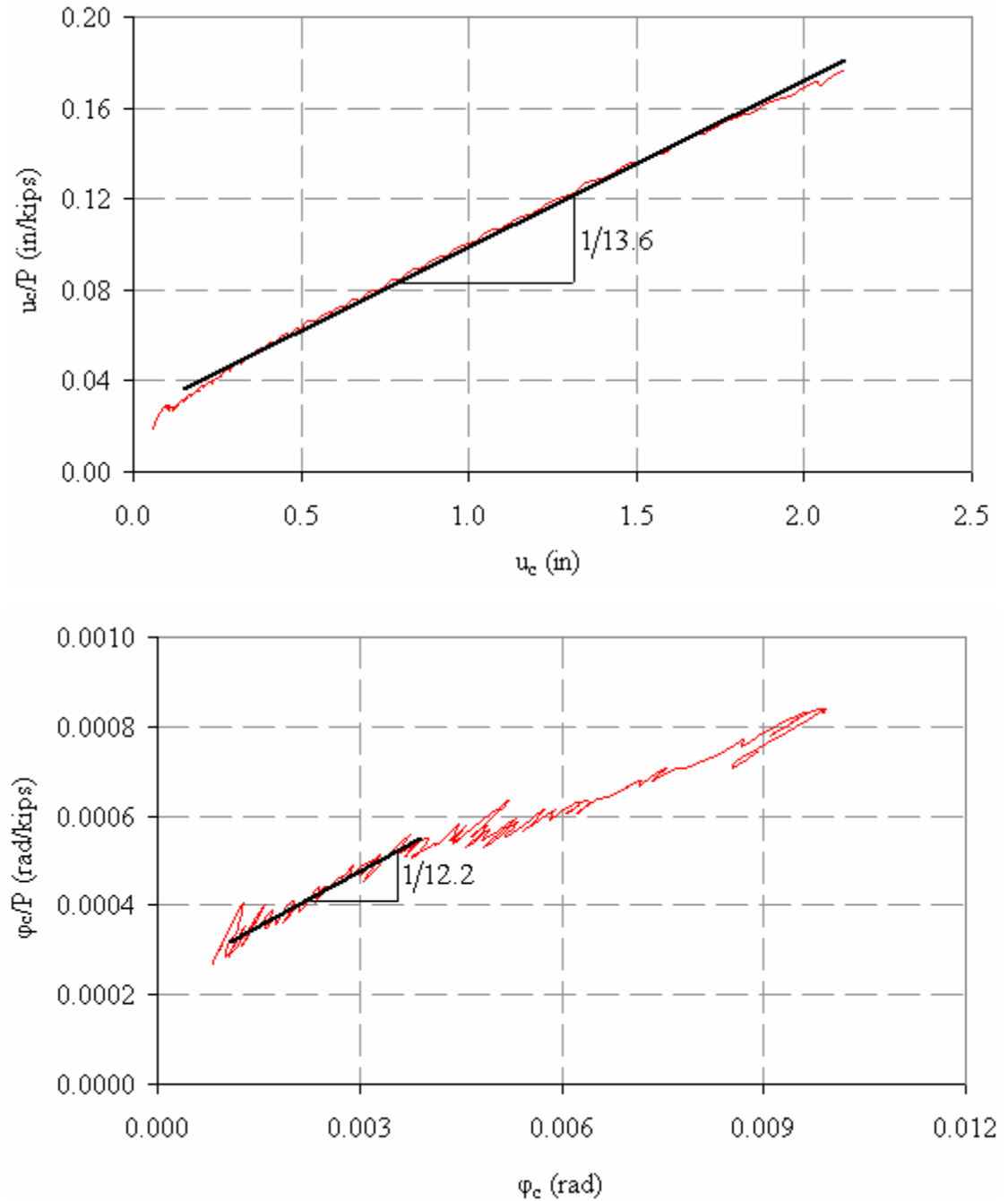


Figure H.1 – Southwell (1932) plots for Specimen B44-2

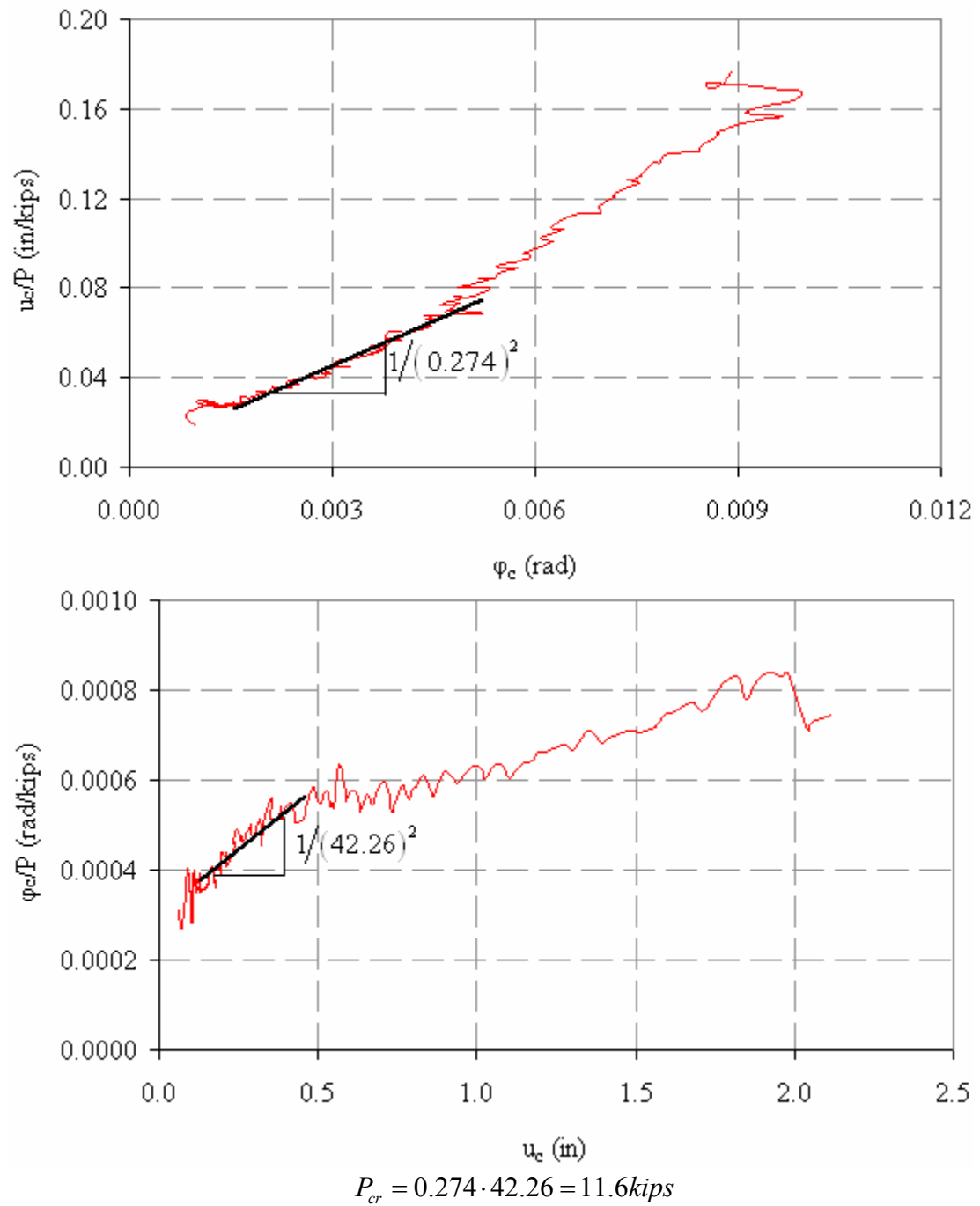


Figure H.2 – Meck’s (1977) version of the Southwell (1932) plots for Specimen B44-2

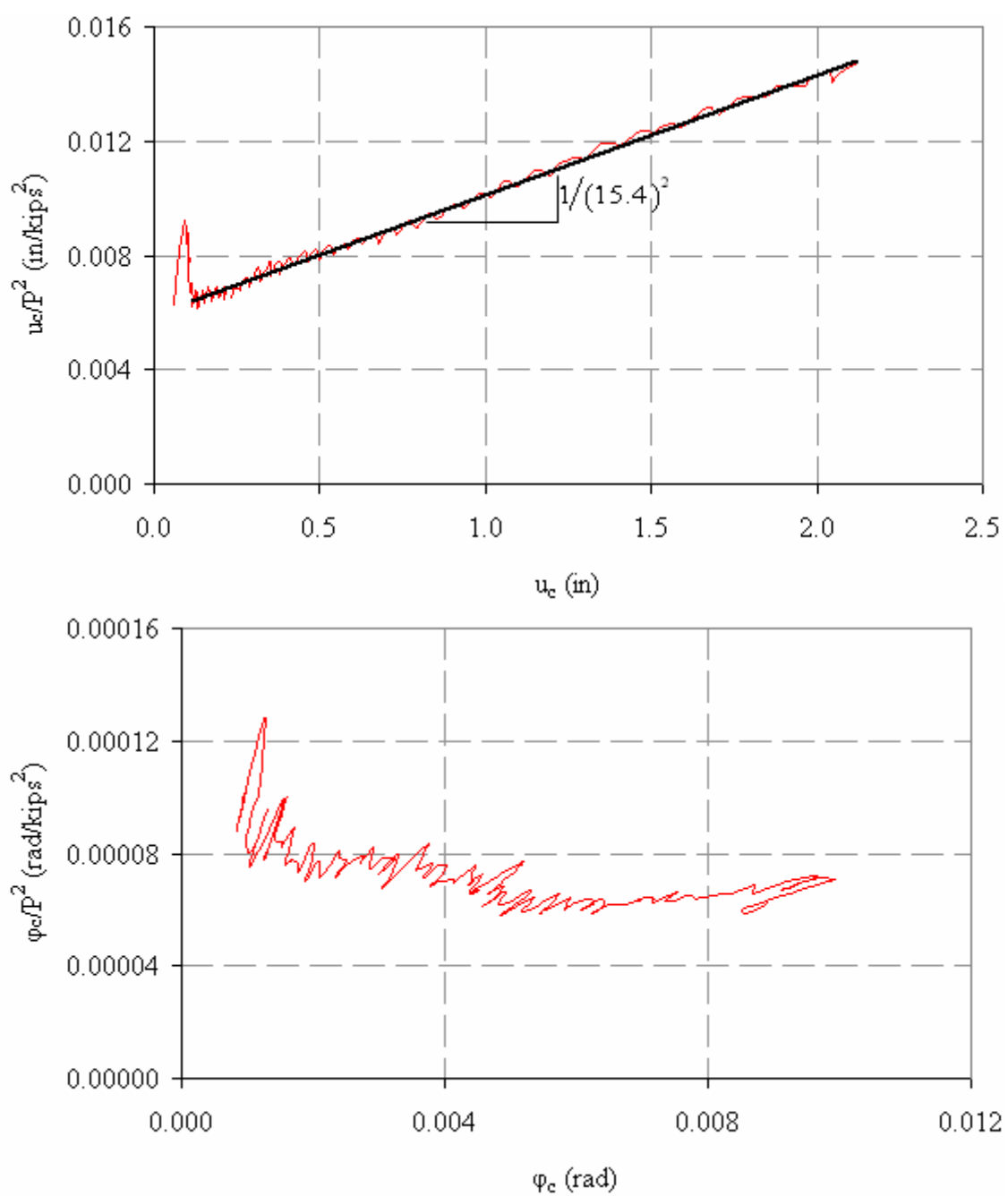


Figure H.3 – Massey's (1963) version of the Southwell (1932) plots for Specimen B44-2

The plots in Figures H.1 to H.3 agree also with the conclusions drawn by Mandal and Calladine (2002). The critical loads obtained from the classical Southwell (1932) plots (Figure H.1) are close to the critical load value obtained from Meck's (1977) version of the plots (Figure H.2). In Table H.1, the critical loads of the second set of specimens, obtained from the classical and Meck's (1977) version of the Southwell (1932) plots are tabulated together with the ultimate loads measured during the tests. The last column in Table H.1 corresponds to the critical load values obtained from the classical Southwell (1932) plot using the lateral deflection data. The tabulated values show that the critical loads according to the classical and Meck's version of the Southwell (1932) plots are in close agreement for all specimens.

Table H.1 – Critical loads from the classical and Meck's (1977) version of the Southwell (1932) plots for the second set of beams

Specimen	Experimental Limit Load (kips)	Critical Load (kips)	
		Meck (1977)	Southwell (1932)
B44-1	15.2	18.7	17.3
B44-2	12.1	11.6	13.6
B44-3	21.0	21.5	20.8
B36L-1	13.5	18.0	17.3
B36L-2	21.6	26.9	26.8

Figure H.3 indicates that the data points in Massey's (1963) version of the plots are more scattered than the classical and Meck's (1977) versions of the plots. Furthermore, the data points corresponding to the initial stages of loading lie further from the eventual straight line in Massey's (1963) version of the plots, as previously established by Mandal and Calladine (2002).

Finally, Table H.1 indicates that both the classical version and the Meck's (1977) version of Southwell (1932) plot overpredict the limit loads of the second set of specimens. Therefore, the limit loads of the specimens measured in the tests were used in the analytical study to be more conservative.

## REFERENCES

- American Concrete Institute (ACI) (2005), “Building Code Requirements for Structural Concrete and Commentary”, *ACI 318-05 and ACI R318-05*, Farmington Hills, Michigan.
- Allen, H. G. and Bulson, P. S. (1980), *Background to Buckling*, McGraw Hill, Maidenhead UK, p. 582
- ASTM A 615/A 615M (2008), “Standard Specification for Deformed and Plain Carbon-Steel Bars for Concrete Reinforcement”, *ASTM International*, West Conshohocken, Pennsylvania.
- ASTM C 39/C 39M (2005), “Standard Test Method for Compressive Strength of Cylindrical Concrete Specimens”, *ASTM International*, West Conshohocken, Pennsylvania.
- ASTM C 157/C 157M (2006), “Standard Test Method for Length Change of Hardened Hydraulic-Cement Mortar and Concrete”, *ASTM International*, West Conshohocken, Pennsylvania.
- ASTM C 192/C 192M (2007), “Standard Practice for Making and Curing Concrete Test Specimens in the Laboratory”, *ASTM International*, West Conshohocken, Pennsylvania.
- ASTM C 469 (2002), “Standard Test Method for Static Modulus of Elasticity and Poisson's Ratio of Concrete in Compression”, *ASTM International*, West Conshohocken, Pennsylvania.
- ASTM C 1611/ C 1611M (2005), “Standard Test Method for Slump Flow of Self-Consolidating Concrete”, *ASTM International*, West Conshohocken, Pennsylvania.
- Bischoff, P. H. (2005), “Reevaluation of Deflection Prediction for Concrete Beams Reinforced with Steel and Fiber Reinforced Polymer Bars”, *Journal of Structural Engineering, ASCE*, Vol. 131, No. 5, pp. 752-762.

- Bischoff, P. H. (2007), "Rational Model for Calculating Deflection of Reinforced Concrete Beams and Slabs", *Canadian Journal of Civil Engineering*, Vol. 34, No. 8, pp. 992-1002.
- Bischoff, P. H. and Scanlon A. (2007), "Effective Moment of Inertia for Calculating Deflections of Concrete Members Containing Steel Reinforcement and Fiber-Reinforced Polymer Reinforcement", *ACI Structural Journal*, Vol. 104, No. 1, pp. 68-75.
- Branson, D. E. (1963), "Instantaneous and Time-Dependent Deflections of Simple and Continuous Reinforced Concrete Beams", *HPR Publication 7*, Part 1, pp. 1-78, Alabama Highway Department, Bureau of Public Roads.
- Burgoyne, C. J. and Stratford, T. J. (2001), "Lateral Instability of Long-Span Prestressed Concrete Beams on Flexible Bearings", *The Structural Engineer*, Vol. 79, No. 6, pp.23-26.
- Carreira, D. J. and Chu K. (1985), "Stress-Strain Relationship for Plain Concrete in Compression", *ACI Journal*, Vol. 82, No. 6, pp. 797-804.
- Cheng, J. J. R. and Yura, A. Y. (1988), "Lateral Buckling Tests on Coped Steel Beams", *Journal of Structural Engineering, ASCE*, Vol. 114, No. 1, pp. 16-30.
- Considère, A. (1891), "Resistance des Pièces Comprimées", *Congrès International de Procèdes de Construction*, Paris, 3:371.
- Cowan, H. J. (1953), "The Theory of Torsion Applied to Reinforced Concrete Design – Part 2", *Civil Engineering and Public Works Review (London)*, Vol. 48, No. 568, pp. 455-480.
- Engesser, F. (1895), "Über Knickfragen", *Schweizerische Bauzeitung*, Vol. 26, pp. 24-26.
- Gilbert, R. I. (2006), "Discussion of "Reevaluation of Deflection Prediction for Concrete Beams Reinforced with Steel and Fiber Reinforced Polymer Bars" by Peter H. Bischoff", *Journal of Structural Engineering, ASCE*, Vol. 132, No. 8, pp. 1328-1330.
- Hansell, W. and Winter G. (1959), "Lateral Stability of Reinforced Concrete Beams", *ACI Journal, Proceedings*, Vol. 56, No. 3, pp. 193-214.



- Hsu, T. T. C. (1968), "Plain Concrete Rectangular Sections ", *Torsion of Structural Concrete*, SP 18, pp. 203-238, American Concrete Institute, Detroit.
- Hsu, T. T. C. (1973), "Post-Cracking Torsional Rigidity of Reinforced Concrete Sections", *ACI Journal*, Proceedings, Vol. 70, No. 5, pp. 352-360.
- Hsu, T. T. C. (1984), *Torsion of Reinforced Concrete*, Van Nostrand Reinhold Company Inc., New York.
- Hsu, T. T. C. (1990), "Shear Flow Zone in Torsion of Reinforced Concrete", *Journal of Structural Engineering*, ASCE, Vol. 116, No. 11, pp. 3206-3226.
- Kollbrunner, C. F. and Bassler, K. (1969), *Torsion in Structures*, Springer-Verlag., New York.
- König, G. and Pauli, W. (1990), "Ergebnisse von Kippversuchen an Schlanken Fertigteilträgern aus Stahlbeton und Spannbeton", *Beton- und Stahlbetonbau*, Vol. 85, No. 10, pp. 253-258.
- Lampert, P. (1973), "Postcracking Rigidity of Reinforced Concrete Beams in Torsion and Bending ", *Analysis of Structural Systems for Torsion*, SP 35, pp. 385-433, American Concrete Institute, Detroit.
- Leemann, A. and Hoffmann, C. (2005), "Properties of Self-Compacting and Conventional Concrete - Differences and Similarities", *Magazine of Concrete Research*, Vol. 57, No. 6, pp. 315-319.
- Loser, R. and Leemann, A. (2009), "Shrinkage and Restrained Shrinkage Cracking of Self-Compacting Concrete Compared to Conventionally Vibrated Concrete", *Materials and Structures*, Vol. 42, No. 1, pp. 71-82.
- Lura, P., Pease, B., Mazzotta, G. B., Rajabipour, F., and Weiss, J. (2007), "Influence of Shrinkage-Reducing Admixtures on Development of Plastic Shrinkage Cracks", *ACI Materials Journal*, Vol. 104, No.2, pp. 187-194.
- Mandal, P. and Calladine, C. R. (2002), "Lateral-Torsional Buckling of Beams and the Southwell Plot", *International Journal of Mechanical Sciences*, Vol. 44, No. 12, pp. 2557-2571.

- Marshall, W. T. (1948), "The Lateral Stability of Reinforced Concrete Beams", *Journal, Institution of Civil Engineers (London)*, Vol. 30, No. 6, pp. 194-196.
- Massey, C. (1963), "Elastic and Inelastic Lateral Instability of I-Beams", *The Engineer*, Vol. 216, No. 5622, pp. 672-674.
- Massey, C. (1967), "Lateral Instability of Reinforced Concrete Beams under Uniform Bending Moments", *ACI Journal, Proceedings*, Vol. 64, No. 3, pp. 164-172.
- Massey, C. and Walter, K. R. (1969), "The Lateral Stability of a Reinforced Concrete Beam Supporting a Concentrated Load", *Building Science*, Vol. 3, No. 1, pp. 183-187.
- Mathcad Student Edition, Version 14.0, Mathsoft, Inc., 2007.
- Mathematica Version 6.0 for Windows, Wolfram Research, Inc., 2007.
- Meck, H. R. (1977), "Experimental Evaluation of Lateral Buckling Loads", *ASCE Journal of Engineering Mechanics Division, Proceedings*, Vol. 103, No. 2, pp. 331-337.
- Mirza, S. A., Hatzinikolas, M., and MacGregor, J. G. (1979), "Statistical Descriptions of Strength of Concrete", *ASCE Journal of Structural Division, Proceedings*, Vol. 105, No. 6, pp. 1021-1037.
- Nawy, E. D. (2005), *Reinforced Concrete: a fundamental approach*, Pearson Prentice Hall, Upper Saddle River, New Jersey, pp. 52-53.
- Revathi, P. and Menon, D. (2006), "Estimation of Critical Buckling Moments in Slender Reinforced Concrete Beams", *ACI Structural Journal*, Vol. 103, No. 2, pp. 296-303.
- Rausch, E. (1929), "Berechnung des Eisenbetons gegen Verdrehung", Ph.D. thesis, Technische Hochschule, Berlin.

- Saint-Venant, B. de (1856). “Mémoire sur la Torsion des Prismes (lu à l’Académie le 13 juin 1853)”, *Mémoires des Savants Etrangers, Mémoires Présentés par Divers Savants à l’Académie des Sciences, de l’Institut Impérial de France et Imprimé par son Ordre*, V. 14, p. 233-560.
- Sant, J. K. and Bletzaker, R. W. (1961), “Experimental Study of Lateral Stability of Reinforced Concrete Beams”, *ACI Journal*, Proceedings Vol. 58, No. 6, pp. 713-736.
- Scanlon, A. and Bischoff, P. H. (2008), “Shrinkage Restraint and Loading History Effects on Deflections of Flexural Members”, *ACI Structural Journal*, Vol. 105, No.4, pp. 498-506.
- Shah, S. P., Karaguler, M. E., and Sarigaphuti, M. (1992), “Effects of Shrinkage Reducing Admixtures on Restrained Shrinkage Cracking of Concrete”, *ACI Materials Journal*, Vol. 89, No.3, pp. 289-295.
- Siev, A. (1960), “The Lateral Buckling of Slender Reinforced Concrete Beams”, *Magazine of Concrete Research (London)*, Vol. 12, No. 36, pp. 155-164.
- Simitses, G. J., and Hodges, D. H. (2006), *Fundamentals of Structural Stability*, Elsevier Inc., Jordan Hill, Oxford, pp. 251-256.
- Southwell, E. V. (1932), “On the Analysis of Experimental Observations in Problems of Elastic Stability”, *Proceedings of Royal Society of London*, Vol. 135, pp. 601-616.
- Stiglat, K. (1971), “Näherungsberechnung der Kritischen Kipplasten von Stahlbetonbalken”, *Die Bautechnik*, Vol. 48, No. 3, pp. 98-100.
- Stiglat, K. (1991), “Zur Näherungsberechnung der Kipplasten von Stahlbeton- und Spannbetonträgern über Vergleichsschlankheiten”, *Beton- und Stahlbetonbau*, Vol. 86, No. 10, pp. 237-240.
- Stoddard, W. P. (1997), “Lateral-Torsional Buckling Behavior of Polymer Composite I-Shaped Members”, Ph.D. thesis, Georgia Institute of Technology, Atlanta, Georgia.

- Stratford, T. J. and Burgoyne, C. J. (1999), "Lateral Stability of Long Precast Concrete Beams", *Proceedings of the Institution of Civil Engineers: Structures and Buildings*, Vol. 134, No. 2, pp.169-180.
- Tavio, and Teng, S. (2004), "Effective Torsional Rigidity of Reinforced Concrete Members", *ACI Structural Journal*, Vol. 101, No. 2, pp. 252-260.
- Timoshenko, S. P. and Gere, J. M. (1963), *Theory of Elastic Stability*, International Edition, McGraw-Hill Book Co., New York, pp. 251-277.
- Timoshenko, S. P. and Goodier, J. N. (1970), *Theory of Elasticity*, International Edition, McGraw-Hill Book Co., New York, pp. 309-313.
- Tomaszewicz, A. (1984), "Betongens Arbeidsoliagram", *FCB/SINTEF Rapport*, STF65 A84065.
- Turcry, P. and Loukili, A. (2006), "Evaluation of Plastic Shrinkage Cracking of Self-Consolidating Concrete", *ACI Materials Journal*, Vol. 103, No. 4, pp. 272-279.
- Turcry, P., Loukili, A., Haidar, K., Pijaudier-Cabot, G., and Belarbi A. (2006), "Cracking Tendency of Self-Compacting Concrete Subjected to Restrained Shrinkage: Experimental Study and Modeling", *Journal of Materials in Civil Engineering, ASCE*, Vol. 18, No. 1, pp. 46-54.
- Vacharajittiphan, P., Woolcock, S. T., and Trahair, N. S. (1974), "Effect of In-plane Deformation on Lateral Buckling." *Journal of Structural Mechanics*, Vol. 3, No. 1, pp. 29-60.
- Von Kármán, T. (1910), *Encyklopädie der Mathematischen Wissenschaften*, Vol. IV4, p. 349.
- Wang, C. (1953), *Applied elasticity*, McGraw-Hill Book Co. Inc., New York, pp. 85-89.
- Wee, T. H., Chin, M. S., and Mansur, M. A. (1996), "Stress-Strain Relationship of High-Strength Concrete in Compression", *Journal of Materials in Civil Engineering, ASCE*, Vol. 8, No. 2, pp. 70-76.

- Weiss, W. J. and Shah, S. P. (2002), “Restrained Shrinkage Cracking: The Role of Shrinkage Reducing Admixtures and Specimen Geometry”, *Materials and Structures*, Vol. 34, No. 246, pp. 85-91.
- Yarimci, E., Yura, J. A., and Lu, L. W. (1967), “Techniques for Testing Structures Permitted to sway”, *Experimental Mechanics*, Vol. 7, No. 8, pp. 321-331.
- Yen, B. T. (1974), “Beams”, *Structural steel design*, editor Lambert Tall, 2<sup>nd</sup> Edition, The Ronald Press Company, New York, p. 196.
- Yura, J. A. and Phillips, B. A. (1992), “Bracing Requirements for Elastic Steel Beams”, *Research Report 1239-I*, Center for Transportation Research, The University of Texas at Austin, Texas.
- Zhao, X. L., Hancock, G. J., and Trahair, N. S. (1994), “Lateral Buckling Tests of Cold-Formed RHS Beams”, *Research Report R699*, School of Civil and Mining Engineering, The University of Sydney, Australia.

## **VITA**

### **İLKER KALKAN**

İlker Kalkan was born on July 22<sup>nd</sup>, 1981 in Mardin, Turkey. He attended Middle East Technical University in Ankara, Turkey and received a B.S. degree in Civil Engineering with emphasis on Construction Management and Engineering in 2004. He earned an M.S. degree in 2006 and a Ph.D. degree in 2009 in Structural Engineering, Mechanics and Materials from Georgia Institute of Technology, Atlanta, Georgia. He took classes from the Daniel Guggenheim School of Aerospace Engineering at Georgia Institute of Technology as his minor field of study in Ph.D. In his doctoral studies, he investigated the lateral stability of rectangular reinforced concrete beams analytically and experimentally.